Nanoparticles and Nanostructured Surfaces: Novel Reporters with Biological Applications

Catherine J. Murphy
Chair/Editor

24–25 January 2001
San Jose, USA

20030106 121

Proceedings of SPIE
Volume 4258

REPORT DOCUMENTATION PAGE

AFRL-SR-AR-TR-02-

1. REPORT DATE (DD-MM-YYYY)	2. REPORT DATE	3. DATES COVERED (From - To)
17-07-2002	Final Technical Report	18-01-2001 – 17-01-2002

4. TITLE AND SUBTITLE	5a. CONTRACT NUMBER
Nanoparticles and Nanostructured Surfaces: Novel Reporters with Biological Applications	
	5b. GRANT NUMBER
	F49620-01-1-0153
	5c. PROGRAM ELEMENT NUMBER

6. AUTHOR(S)	5d. PROJECT NUMBER
Catherine J. Murphy	
	5e. TASK NUMBER
	5f. WORK UNIT NUMBER

7. PERFORMING ORGANIZATION NAME(S) AND ADDRESS(ES)	8. PERFORMING ORGANIZATION REPORT NUMBER
Society of Photo-Optical Instrumentation Engineers PO Box 10 Bellingham, WA 98227-0010	Volume 4258

9. SPONSORING/MONITORING AGENCY NAME(S) AND ADDRESS(ES)	10. SPONSOR/MONITOR'S ACRONYM(S)
Air Force Office of Scientific Research 801 N. Randolph Street, Room 732 Arlington, VA 22203-1977	AFOSR/NL
	11. SPONSORING/MONITORING AGENCY REPORT NUMBER

12. DISTRIBUTION AVAILABILITY STATEMENT

Approved for Public Release

13. SUPPLEMENTARY NOTES

ISBN 0-8194-3936-3

14. ABSTRACT

This proceedings contains papers on the following topics: quantum dots, Metallic nanoparticles and nanowires, nanoparticles for biology, nanostructured oxide surfaces.

15. SUBJECT TERMS

biomedical optics

16. SECURITY CLASSIFICATION OF:			17. LIMITATION OF ABSTRACT	18. NUMBER OF PAGES	19a. NAME OF RESPONSIBLE PERSON
a. REPORT	b. ABSTRACT	c. THIS PAGE			Janice Gaines Walker
Non-classified			SAR	108	**19b. TELEPONE NUMBER (Include area code)** (360)676-3290

Standard Form 298 (Rev. 8-98)
Prescribed by ANSI-Std Z39-18

Nanoparticles and Nanostructured Surfaces: Novel Reporters with Biological Applications

Catherine J. Murphy
Chair/Editor

24–25 January 2001
San Jose, USA

The papers appearing in this book compose the proceedings of the technical conference cited on the cover and title page of this volume. They reflect the authors' opinions and are published as presented, in the interests of timely dissemination. Their inclusion in this publication does not necessarily constitute endorsement by the editors or by SPIE. Papers were selected by the conference program committee to be presented in oral or poster format, and were subject to review by volume editors or program committees.

Please use the following format to cite material from this book:

Author(s), "Title of paper," in *Nanoparticles and Nanostructured Surfaces: Novel Reporters with Biological Applications*, Catherine J. Murphy, Editor, Proceedings of SPIE Vol. 4258, page numbers (2001).

Printed in the United States of America.

Contents

Conference Committee

Conference Chair

    Catherine J. Murphy, University of South Carolina/Columbia (USA)

Program Committee

    Marcel P. Bruchez, Jr., Quantum Dot Corporation (USA)
    Steven R. Emory, Los Alamos National Laboratory (USA)
    John L. Ferry, University of South Carolina/Columbia (USA)
    Raoul Kopelman, University of Michigan (USA)
    Joseph R. Lakowicz, University of Maryland/Baltimore School of Medicine (USA)
    Shuming Nie, Indiana University (USA)

Session Chairs

    1   Quantum Dots I
        Joseph R. Lakowicz, University of Maryland/Baltimore School of Medicine (USA)

    2   Quantum Dots II
        Marcel P. Bruchez, Jr., Quantum Dot Corporation (USA)

    3   Metallic Nanoparticles and Nanowires: Fundamentals
        Shuming Nie, Indiana University (USA)

    4   Metallic Nanoparticles for Biology I
        Steven R. Emory, Los Alamos National Laboratory (USA)

    5   Nanoparticles for Biology II
        Catherine J. Murphy, University of South Carolina/Columbia (USA)

    6   Nanoparticles for Biology III
        Raoul Kopelman, University of Michigan (USA)

    7   Nanostructured Oxide Surfaces: Biological Delivery and Reactivity
        Catherine J. Murphy, University of South Carolina/Columbia (USA)

Bioconjugates of luminescent CdSe-ZnS quantum dots with an engineered two-domain protein G for use in fluoro-immunoassays

Phan T. Tran,[‡] Ellen R. Goldman,[*] Hedi Mattoussi,[⊥] George P. Anderson,[‡] and J. Matthew Mauro[‡]

U.S. Naval Research Laboratory, [‡]Center for Bio/Molecular Science and Engineering, [⊥]Division of Optical Sciences Washington, DC 20375, U.S.A.; *Center for Bioresource Development, George Mason University, Fairfax, VA 22030, U.S.A.

ABSTRACT

Colloidal semiconductor quantum dots (QDs) seem suitable for labeling certain biomolecules for use in fluorescent tagging applications, such as fluoro-immunoassays. Compared to organic dye labels, QDs are resistant to photo-degradation, and these luminescent nanoparticles have size-dependent emission spectra spanning a wide range of wavelengths in the visible and near IR. We previously described an electrostatic self-assembly approach for conjugating highly luminescent colloidal CdSe-ZnS core-shell QDs with engineered two-domain recombinant proteins. Here we describe the application of this approach to prepare QD conjugates with the β2 immunoglobulin G (IgG) binding domain of streptococcal protein G (PG) appended with a basic lucine zipper attachment domain (PG-zb). We also demonstrate that the QD/PG conjugates retain their ability to bind IgG antibodies, and that a specific antibody coupled to QD via the PG functional domain efficiently binds its antigen. These preliminary results indicate that electrostatically self-assembled QD/PG-zb/IgG bioconjugates can be used in fluoro-immunoassays.

Key Words: semiconductor quantum dots, bioconjugates, immunoassay

INTRODUCTION

Fluorescent labeling of biological materials is a widely employed and very useful practice for biological applications. Commonly, organic dyes have been used in single and multiplex detection, as well as in biological imaging [1], but the characteristics of organic fluorophores provide some limitations to these techniques. Problems with organic labels include narrow excitation bands and broad emission bands with red spectral tails, which makes simultaneous evaluation of different probes difficult due to spectral overlap. Many organic fluorophores also exhibit low resistance to photo degradation [2]. There are substantial advantages in using luminescent colloidal semiconductor nanocrystals (quantum dots, QDs) to synthesize bioconjugates with potential use in diagnostics and biological imaging applications, because they have the potential to overcome some of the problems encountered by organic dyes. These nanoparticles combine size-dependent tunable photoluminescence and high quantum yield with resistance to photo-degradation. CdSe-ZnS core-shell QDs are tunable fluorophores with narrow emission bands (FWHM, of ~ 30-45 nm) spanning the visible spectrum, and broad absorption spectra, a property that allows simultaneous excitation of several particle sizes at a single wavelength [3-7]. Furthermore, these QDs can be detected at concentrations comparable to organic dyes by conventional fluorescence methods [8].

We have developed a conjugation strategy based on electrostatic interaction between negatively charged dihydrolipoic acid (DHLA) capped CdSe-ZnS core-shell QDs and the positively charged leucine zipper [9] interaction domain of engineered bifunctional recombinant proteins. Our bifunctional proteins are designed to possess at the N-terminus a functional domain with binding specificity towards a molecule of interest, while at their extreme C-terminus is a basic homodimeric leucine zipper-containing attachment domain. This C-terminal domain consists of 70 residues, one of which is a disulfide bond-forming cysteine, while 20 are positively charged lysine residues. The attachment domain adopts an S-S linked homodimeric structure that strongly favors interaction with the negatively charged surface of the DHLA-capped QDs in order to relieve intramolecular repulsions. Consequently, the assembly process simply involves adding the fusion protein to QDs, and the engineered two-domain proteins rapidly conjugate with the nanoparticles.

Our electrostatic self-assembly approach is fundamentally different from approaches that use either a covalent cross-linking employing 1-ethyl-3-(3-dimethylaminopropyl) carbodiimide hydrochloride (EDC) [10] condensation to

Nanoparticles and Nanostructured Surfaces: Novel Reporters with Biological Applications, Catherine J. Murphy, Editor, Proceedings of SPIE Vol. 4258 (2001)

© 2001 SPIE · 1605-7422/01/$15.00

1

conjugate the nanoparticles to IgG [11], or the avidin-biotin binding approach employed to attach QDs to actin fibers [12]. The biomolecule-nanocrystal conjugates produced using these techniques showed a substantial loss of luminescence efficiency. Our design for electrostatic self-assembly of bioconjugates aims to improve upon previous approaches in its simplicity and efficiency. Here we describe the preparation and characterization of CdSe-ZnS QDs conjugated with the immunoglobulin G (IgG)-binding β2 domain of streptococcal protein G (PG) fused to an electrostatic interaction leucine zipper attachment domain. We show that the PG-zb coated QDs bind efficiently to anti-SEB IgG, an antibody specific for the toxin staphylococcal enterotoxin B (SEB) [13]. Our preliminary findings demonstrate that this bioconjugate (QD/PG-zb/anti-SEB IgG) complex has sufficient antigen (SEB) recognition for potential use in fluoro-immunoassays.

MATERIALS PREPARATION AND EXPERIMENTAL DETAILS

QD preparation

Nanocrystalline CdSe cores were prepared using high temperature solution synthesis followed by a ZnS-overcoating layer and trioctyl phosphine/trioctyl phosphine oxide (TOP/TOPO) capping as described in previous works [3,6,7]. To make the core-shell QDs water-compatible, their TOP/TOPO-caps were exchanged with dihydrolipoic acid (DHLA) groups by suspending purified and dried nanocrystals in DHLA [14] and heating to ~ 60-70°C. Subsequent deprotonation using potassium-tert-butoxide (K-t-butoxide) permitted dispersion of the new materials in water. This procedure allowed preparation of stable aqueous solutions of DHLA-capped CdSe-ZnS nanocrystals that are stable and have photoluminescence quantum yields of ~ 10-20%.

DNA construction

The two-domain protein G-basic zipper (PG-zb) fusion protein (shown schematically in Fig. 1) was constructed using standard gene assembly and cloning techniques. Polymerase chain reaction (PCR) was employed to amplify the β2 IgG binding domain of streptococcal protein G (PG) [15] and to introduce restriction sites to be used for cloning. The following primers were used in the PCR reaction (Nco I, Kpn I, and Sac I sites are underlined) GNCO199: CAACGCTAAAATCGCCATGGCTTACAAACTTGTT-ATTAAT, and GSAC199: GGTACCAGATCACGAGCTCTCAGTTACCGTAAAGGTCTT. The reverse primer (GSAC199) was designed to contain a stop codon between the Sac I and Kpn I sites. The NcoI – KpnI fragment containing PG was gel purified from a 2% agarose gel using a QIAquick gel extraction kit (Qiagen) and then ligated into the expression vector, pBad/HisB (Invitrogen) was cut with the appropriate restriction endonucleases to produce plasmid pBadG. To produce the leucine zipper fusion construct (pBadGzb), gel purified Sac I-Hind III fragment containing the pMAL linker, leucine zipper, and His tag used in previous studies [8] was ligated into pBadG digested with SacI and Hind III.
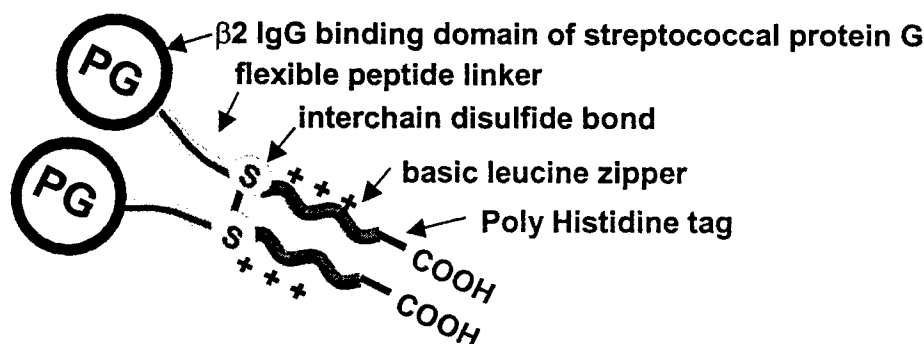
Figure 1. Schematic representation of the PG-zb fusion protein showing the components of the C-terminal interaction domain.

Protein purification

The initial purification step of the PG-zb protein from *E. coli* Top 10 (Invitrogen) cells was carried out under denaturing conditions using Ni-NTA agarose resin as described by the manufacturer (Qiagen) [16] with the following exceptions. After the denatured protein was loaded onto the column and washed with denaturing buffer, the protein was re-folded on the column during extensive washing with PBS, and then eluted with 50 mM NaH_2PO_4, 300 mM NaCl, 250 mM imidazole at pH 6.3. SDS gel electrophoresis under reducing and non-reducing conditions revealed the protein product to be a mix of monomer and dimer (about 25% and 75% respectively). A second purification step using SP Sepharose cation exchange resin was performed to separate the desired dimer product from the monomer contaminant. Sample was loaded onto the column in PBS, and eluted with an increasing NaCl gradient up to 1 M NaCl in PBS; dimer product was eluted at approximately 0.8M NaCl.

Conjugation of protein and QD

Conjugation of the chimeric PG-zb proteins and DHLA-capped CdSe-ZnS QDs was carried out in 10 mM sodium borate pH 9. Mixing dissolved fusion protein with QDs yielded self-assembled QD/protein conjugates free of obvious aggregates.

Gel shift electrophoresis assay

Samples containing ~ 11 picomoles of nanoparticles and variable QD:PG-zb molar ratios were prepared in 10 mM sodium borate, 10 mM EDTA at pH 9 in 30 μl reaction volume. Loading buffer, a 6X solution containing 0.2% each of bromophenol blue (Sigma) and xylene cyanole FF (Kodak) tracking dyes and 15% Ficoll (Sigma), was added to each sample, and samples were loaded into the wells of a 1.2% agarose gel in 1xTBE buffer (tris/borate/EDTA) [17], and run at 82 volts for 1 hour at ambient temperature. The fluorescent QD bands were visualized using UV epi-illumination excitation at 365 nm and a filter that blocks out wavelengths below 523 nm, utilizing a Kodak Image Station 440.

Labeling antibody with an organic fluorophore

Anti-SEB antibody (Toxin technology) was labeled with Cy-5 (Amersham Life Sciences) per the manufacturer instructions. The dye to protein molar ratio was determined spectrophometrically to be about 1.

Binding assays

Wells of black microtiter plates (FluoroNunc module Maxisorp surface, Nunc) were filled with 10-μg/ml goat IgG in 100 μl of 0.1 M $NaHCO_3$ (pH8.6), or 0.1 M $NaHCO_3$ containing no IgG, and incubated at 4°C overnight. After discarding unbound IgG (or blank solution for background) from the wells, plates were blocked at 4°C for 2 hours with PBS containing 4% powdered non-fat milk. Plates were then washed 2 times with PBS, and then PG-zb-conjugated QDs were added to IgG-adsorbed wells or control wells and incubated for 1-2 hours with gentle shaking at room temperature. Wells were then washed several times with 10 mM borate buffer at pH 9, and the fluorescence was measured utilizing a Spectra Fluor Plus microtiter plate reader (Tecan). A 25-nm band pass filter was used for excitation at 360 nm, and a long pass filter with a cut-off at 530 nm was used for measuring the photoluminescence. For data analysis, relative PL intensity was calculated by subtracting the appropriate background (blank solution for each conjugate concentration) signals from the florescence measured and expressed in plots as arbitrary fluorescence units.

A similar protocol was used to assess the binding of QD/PG-zb/anti-SEB-IgG conjugates to plate-immobilized SEB. SEB was immobilized onto the plate wells following the same overnight fixing procedure described above, either at a saturating concentration of 10 μg/ml or dilutions down to 0.014 μg/ml. PG-zb conjugated QDs that had been loaded with an anti-SEB antibody were incubated for 1-2 hours in SEB covered or control wells. Plates were then washed and the photoluminescence was measured as described above. Binding of Cy-5 labeled anti-SEB antibody to immobilized SEB was assayed using the same protocol, except that the fluorescence was measured using a 620nm, 10nm band pass excitation filter and a 670 nm, 10 nm band pass emission filter. Data analysis was also performed as described above.

RESULTS AND DISCUSSION

Conjugation of QD/PG-zb

Mixing the DHLA-capped CdSe-ZnS QDs and PG-zb two-domain proteins in borate buffer at pH 9 yielded QD/PG-zb bioconjugates free of any obvious macroscopic aggregates. Conjugating the DHLA-capped CdSe-ZnS nanocrystals to PG-zb enhanced the PL of the conjugates compared to unconjugated nanocrystals in basic solution, with a PL increase that exceeds a value of ~ 1.5 for PG-zb:QD molar ratio of ~ 20 [18]. This PL enhancement effect was also observed when the *E.coli* maltose binding protein (MBP) appended with an identical electrostatic interaction domain was used to form QD/MBP-zb bioconjugates [8].

QD/PG-zb conjugation was confirmed by a gel shift assay in which QDs incubated with increasing amounts of PG-zb were electrophoresed through an agarose gel (results shown in Figure 2). Due to a net negative charge from the DHLA cap on their surfaces, unconjugated QDs migrate towards the positive electrode in conventional agarose gel electrophoresis, with luminescent bands observable upon UV excitation (lane 1). As the QDs are conjugated with proteins, the size/charge of the QD/protein complexes and hence their migration through the gel change. For complexes in which ratios of PG-zb to QDs are smaller than 4, migration is essentially the same as for uncoated QDs; however, the readily observed increase in band luminescence intensity relative to unconjugated QDs suggests that interactions between PG-zb proteins and QDs do occur. No migration is observed when the ratio is increased to 12 or higher, indicating that the coating proteins have masked the charges of the QD and/or that the size of the formed bioconjugates prevents their entry into the gel matrix. At the intermediate ratio of approximately 8 proteins per nanocrystal, a smeared band is visible, suggesting a heterogeneous population of bioconjugates. These results, in addition to the increase in PL upon protein conjugation described above [8,18], indicate that an individual QD is capable of conjugation with several proteins.
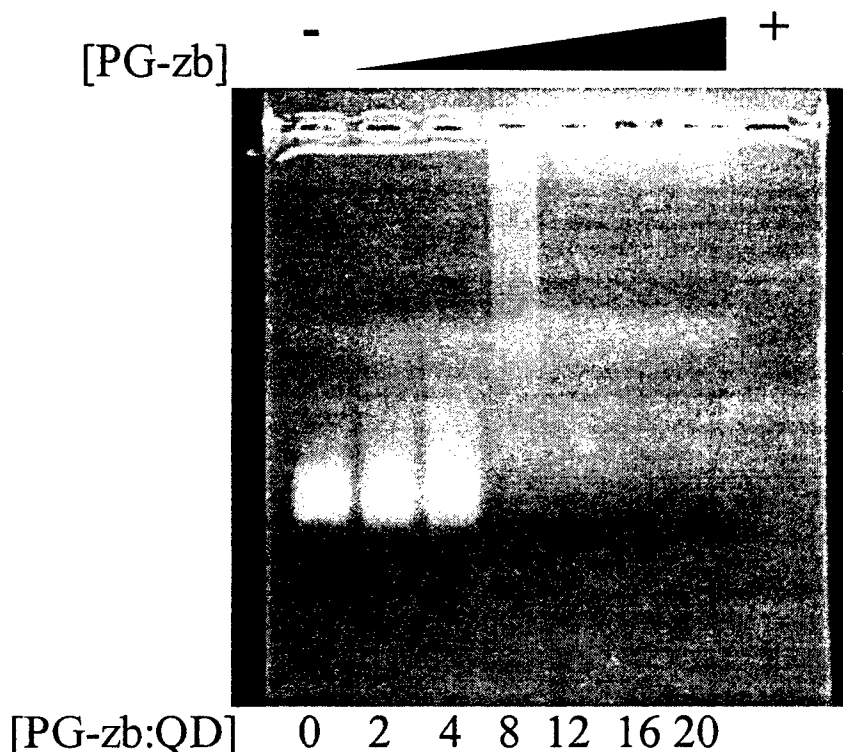
Figure 2. Gel shift as a function of PG-zb:QD molar ratio for a fixed QD concentration. The ratio of PG-zb:QD is shown at the bottom of each lane.

Direct binding of QD/PG-zb to IgG

Results from direct binding assays demonstrated that the QD/PG-zb bioinorganic conjugates retain their ability to bind IgG. When microtiter plate-immobilized goat IgG was exposed to a series of QD/PG-zb dispersions at increasing concentrations, wells that contain IgG exhibit photoluminescence after extensive well washing, indicative of stable interaction between QD/PG-zb and IgG. Plotting relative PL intensity, in fluorescence arbitrary units, as a function of the QD/PG-zb input concentration reveals a relatively linear relationship between conjugate concentration and PL output up to 20 nM of input QD/PG-zb (Figure 3). Above 20 nM conjugate concentration, the PL signal remains constant, presumably because all available Fc binding regions of immobilized IgG are occupied with QD/PG-zb conjugates. This experiment demonstrated that conjugate formation has no serious effect on the ability of the functional protein G domain of the fusion protein to bind IgG, and that much of the adsorbed IgG was oriented so that its Fc region was accessible to the QD/PG-zb conjugate. Retention of the QD/PG-zb conjugate ability to bind IgG suggests that fluoro-immunoassays can be designed using QD/PG-zb/IgG complexes.
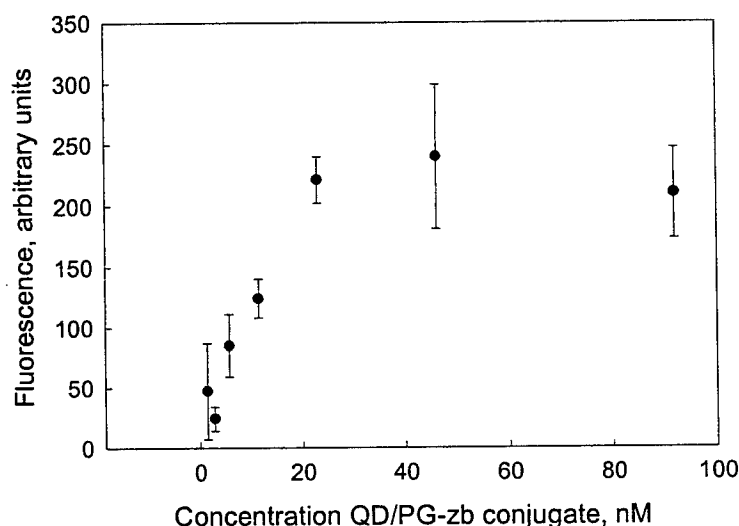
Figure 3. Direct binding assay to detect the binding of QD/PG-zb to IgG antibody. Relative PL intensity plotted as a function of concentration of QD/PG-zb added to the IgG covered wells; point 0 signal was from wells covered by a blank solution.

Fluoro-immunoassay

We explored the potential use of QD/PG-zb/antibody complexes in fluoro-immunoassays for detecting staphylococcal enterotoxin B (SEB). PG-zb conjugated QDs were coupled to a mouse monoclonal anti-SEB IgG via the PG functional domain and tested for their ability to bind to SEB immobilized in wells of a microtiter plate. Several experiments were performed to examine the effect of changing both the QD/PG-zb/anti-SEB-IgG concentration and the immobilized SEB concentration. At saturating amounts of SEB, a direct binding assay showed that the QD/PG-zb conjugated with anti-SEB IgG were able to bind SEB adsorbed onto the wells of microtiter plates. Relative PL intensity output at various QD/PG-zb/anti-SEB IgG input concentrations is shown in Figure 4. The signal increased linearly through the range of conjugate concentrations tested, indicating that the QD/PG-zb/IgG conjugates effectively bind to the adsorbed SEB. Under experimental conditions where the highest QD conjugate concentration examined was 33 nM, signal saturation was not reached. At a fixed QD-conjugate concentration of 90 nM, and various lowered SEB concentration, a saturation point was achieved (Figure 5). These results also give an indication of the detection limit of the assay at QD/PG-zb/IgG concentration of ~ 90 nM. Signal was observed through the entire toxin concentration range examined
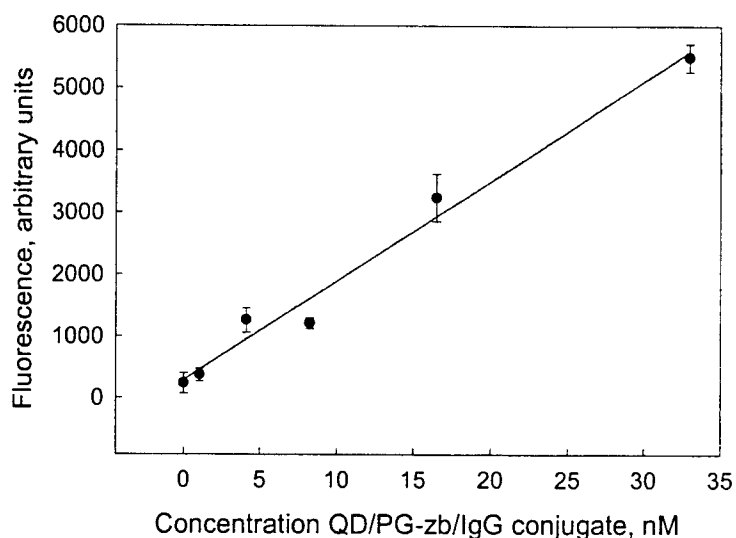
Figure 4. Direct binding detection of SEB by QD/PG-zb labeled anti-SEB antibody. PL intensity was measured for varying concentrations of QD/PG-zb/IgG binding to wells coated with a saturating amount of SEB (10 µg/ml).

(from 10 µg/ml down to 0.014 µg/ml). This is comparable to the results using anti-SEB antibody labeled with the dye Cy-5 and visualized utilizing the fluorescent plate reader [19]. These findings indicate that antigen detection with QD labeled antibodies can be at least as sensitive as detection using antibody labeled with a very bright commonly used organic fluorophore.
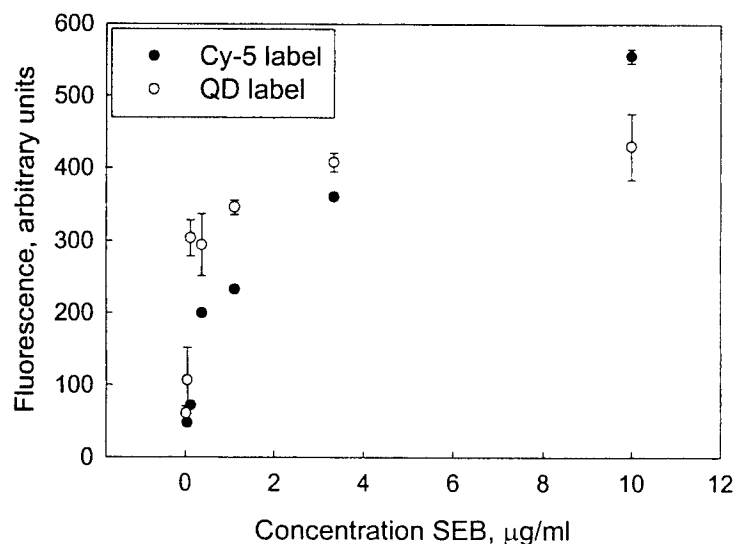
Figure 5. Fluoro-immunoassay for the detection of SEB. Wells coated with varying concentrations of SEB detected by an anti-SEB antibody conjugated to PG-zb linked QDs at a QD concentration of about 90 nM, and CY-5 labeled anti-SEB antibody at a CY-5 concentration of about 70 nM.

Conclusions

We have demonstrated effective non-covalent conjugation, driven by electrostatic self-assembly, between DHLA-capped CdSe-ZnS core-shell QDs and PG-zb. The resulting QD/PG-zb conjugates conserve both the properties of the QDs (absorption and PL) and PG (IgG binding). We were subsequently able to label anti-SEB antibody with QD/PG-zb, and incorporate the resulting QD/PG-zb/anti-SEB IgG into a plate fluoro-immunoassay. The preliminary results for detection of SEB using QD conjugated anti-SEB antibody were promising, with detection levels comparable with Cy-5 labeled anti-SEB antibody. Electrostatic self-assembly of spectrally tunable charged nanoparticle/engineered protein conjugates can be a general approach with a wide range of potential applications in biosensing, imaging, and diagnostics.

Acknowledgements

REFERENCES

1. E. Schröck, S. du Manoir, T. Veldman, B. Schoell, J. Wienberg, M.A. Ferguson-Smith, Y. Ning, D.H. Ledbetter, I. Bar-Am, D. Soenksen, Y. Garini and T. Ried, *Science* **273**, 494 (1996).
2. G.T. Hermanson, *Bioconjugate Techniques*, Academic Press, London (UK), 1996 (**chapter 8**).
3. C.B. Murray, D.J. Norris and M.G. Bawendi, *J. Am. Chem. Soc.* **115**, 8706 (1993).
4. H. Mattoussi, L.H. Radzilowski, B.O. Dabbousi, E.L. Thomas, M.G. Bawendi and M.F. Rubner, *J. Appl. Phys.* **83**, 7965 (1998).
5. J. Rodriguez-Viejo, H. Mattoussi, J.R. Heine, M.K. Kuno, J. Michel, M.G. Bawendi and K.F. Jensen, *J. Appl. Phys.* **87**, 8526 (2000).
6. M.A. Hines and P. Guyot-Sionnest, P. *J. Phys. Chem.* **100**, 468 (1996).
7. B.O. Dabbousi, J. Rodrigez-Viejo, F.V. Mikulec, J.R. Heine, H. Mattoussi, R. Ober, K.F. Jensen and M.G. Bawendi, *J. Phys. Chem.* **101**, 9463 (1997).
8. H. Mattoussi, J.M. Mauro, E.R. Goldman, G.P. Anderson, V.C. Sundar, F.V. Mikulec and M.G. Bawendi, *J. Am. Chem. Soc.* **122**, 12142 (2000).
9. E.K. O'Shea, K.J. Lumb and P.S. Kim, *Curr. Biol.* **3**, 658 (1993), and references therein.
10. G.T. Hermanson, *Bioconjugate Techniques*, Academic Press, London (UK), 1996 (**chapter 3**).
11. W.C.W. Chan and S. Nie, *Science* **281**, 2016 (1998).
12. M. Bruchez-Jr, M. Moronne, P. Gin, S. Weiss and A.P. Alivisatos, *Science* **281**, 2013 (1998).
13. L.A. Tempelman, K.D. King, G.P. Anderson and F.S. Ligler, *Anal. Biochem.* **233**, 50 (1996).
14. L.C. Gunzalus, L.S. Barton and W. Gruber, *J. Am. Chem. Soc.* **78**, 1763 (1956).
15. J. M. Mauro, L. K. Cao, L. M. Kondracki, S. E. Walz and J. R. Campbell Jr., *Analytical Biochemistry* **235**, 61 (1996).
16. *The QIAexpressionist*, fourth edition. January 2000 51-59, 68, 76, 89.
17. J. Sambrook, E.F. Fritsch, T. Maniatis, *Molecular Cloning A Laboratory Manual*, Cold Spring Harbor Laboratory Press, Plainview, New York, 1989 (chapter 6).
18. E. R. Goldman, H. Mattoussi, P. T. Tran, G. P. Anderson and J. M. Mauro, to appear in *Semiconductor Quantum Dots*, Materials Research Soc. Proceed., Ed. by S. Fafard, D. Huffaker, R. Leon, and R. Noetzel, Pittsburgh, 2001.
19. E.R. Goldman, M.P. Pazirandeh, J.M. Mauro, K.D. King, J.C. Frey and G.P. Anderson, *J. Mol. Recog.* **13**, 382 (2000).

Ultrahigh Resolution Multicolor Colocalization of Single Fluorescent Nanocrystals.

Xavier Michalet[a], Thilo D. Lacoste[a], Fabien Pinaud[a], Daniel S. Chemla[a,b], A. Paul Alivisatos[a,c], Shimon Weiss[a,b]

[a]Material Sciences Division and [b]Physical Biosciences Division, Lawrence Berkeley National Laboratory, 1 Cyclotron Road, Berkeley, CA 94720; [c]Department of Chemistry, University of California Berkeley, Berkeley, CA 94720

ABSTRACT

A new method for *in vitro* and possibly *in vivo* ultrahigh-resolution colocalization and distance measurement between biomolecules is described, based on semiconductor nanocrystal probes. This ruler bridges the gap between FRET and far-field (or near-field scanning optical microscope) imaging and has a dynamic range from few nanometers to tens of micrometers. The ruler is based on a stage–scanning confocal microscope that allows the simultaneous excitation and localization of the excitation point-spread-function (PSF) of various colors nanocrystals while maintaining perfect registry between the channels. Fit of the observed diffraction and photophysics-limited images of the PSFs with a two-dimensional Gaussian allows one to determine their position with nanometer accuracy. This new high-resolution tool opens new windows in various molecular, cell biology and biotechnology applications.

Keywords: Superresolution, diffraction limit, fluorescence, microscopy, confocal, single molecule, semiconductor nanocrystal, quantum dot.

1. INTRODUCTION

Fluorescence microscopy has become an indispensable tool for biologists, who can now label multiple molecular targets or subcellular compartments specifically using various methods (DNA specific intercalation, antibody recognition, *in vivo* expression of GFP-tagged proteins, etc). The variety of spectrally separated available fluorescent probes is indeed increasing at a constant pace, and the prospect of being able to observe the detailed functions of internal cellular machinery *in vivo* is looking closer. In addition, tremendous progresses have been performed in microscopy instrumentation and data analysis. For instance, laser, optical filter and detector developments have improved the quality and affordability of confocal microscopy, whereas 3D deconvolution techniques have reached a commercial stage and compete with confocal microscopy in terms of resolution, sensitivity and speed [1].

On the other hand, new challenges have to be faced if we are to study the actual spatial and temporal evolution of molecular species during signal transduction, gene expression or other aspects of metabolism at the proper nanometer scale. These goals indeed call for tools allowing the nanometer resolution localization of multicolor, individual fluorescent probes on a time scale compatible with biological phenomena.

Techniques to reach nanometer resolution imaging are still to be developed, but progress toward this goal is steadily made [2-6]. The main obstacle is namely the diffraction limitation of far-field microscopy, which results in a spot-like image (or point-spread-function, PSF) for a point source, the diameter of the spot being typically of the order of the excitation or emission wavelength. However, localization of sufficiently separated point-like sources can be determined with nanometer accuracy, as is well known in the literature [7, 8]. Normally, some care has to be taken of diverse aberrations coming from far-field optics (filters, dichroic mirrors, lenses, etc) and the inhomogeneity of the sample's index of refraction. We have recently demonstrated a method limiting the effect of these aberrations (called ultrahigh-resolution colocalization, UHRC) to a point where they can effectively be neglected.

A second critical aspect to obtain nanometer resolution localization of single fluorescent probes is the photophysics of probes. If observation of individual interacting molecules or organelles is to be achieved,

the fluorescent probes used to tag them have to be as small and non-perturbative as possible. Single molecule fluorescence (*in vivo* or not) is now a well established field, but nevertheless, one which is limited to very brief observations (at most a few seconds), due to photobleaching of the dyes used. In addition, the need for spectrally separated probes to detect different targets, requires the use of different laser excitation lines, or two-photon excitation, and usually suffers from broad emission spectra of organic dyes.

Semiconductor nanocrystals (NC) are very promising fluorescent probes in this respect [9-11]. They are small (a few nanometers in diameter, and thus comparable in size to an antibody), can be excited with a common wavelength and have narrow emission spectra (30 nm full width at half maximum, FWHM). Several groups including ours are working on NC functionalization in order to make them useful biological fluorescent probes. Here we show that in combination with our ultrahigh-resolution colocalization approach, they potentially could become the ideal probe for the goals set previously.

2. PRINCIPLE OF ULTRAHIGH-RESOLUTION MULTICOLOR COLOCALIZATION

The principle of ultrahigh-resolution colocalization we have recently presented [12] relies on using a closed-loop piezo-stage scanning confocal microscope, a single excitation wavelength and spectrally separable fluorescent probes, as illustrated on Figure 1.
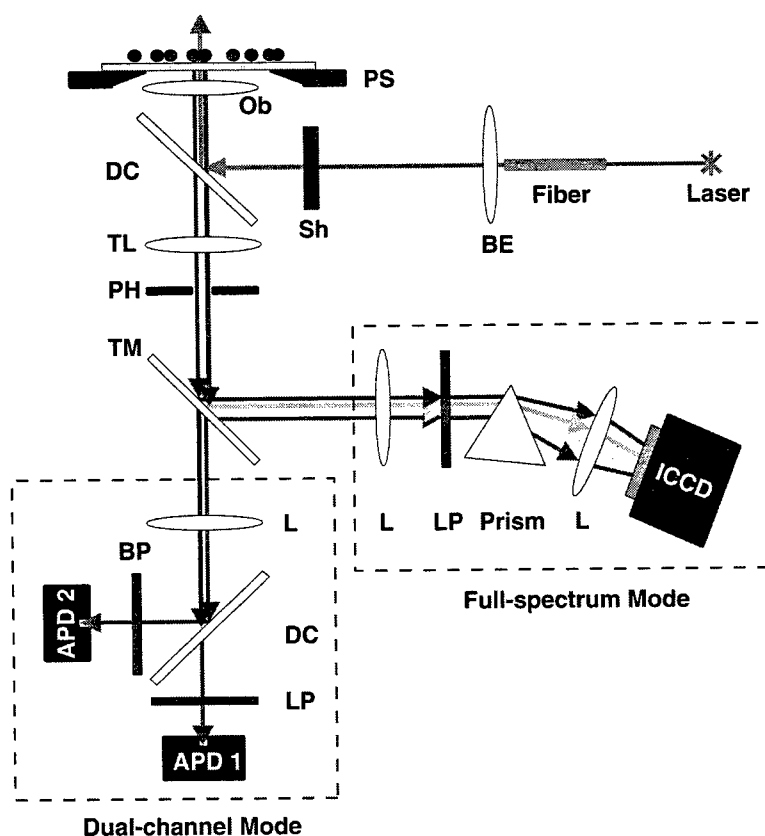
Figure 1: Setup used for ultrahigh-resolution colocalization of multicolor fluorescent probes. The microscope is a homemade stage-scanning confocal microscope using a nanometer-resolution closed-loop piezo-stage scanner (PS). A single laser line is brought via a fiber and a beam expander (BE) to the back focal plane of the objective (Ob) after reflection on a dichroic mirror (DC). Emission of the fluorescent probes is collected by the same objective, and either sent to a dual-channel recording arm using avalanche photodiodes (APD), or to a full-spectrum recording arm using a prism and an intensidifed CCD camera (ICCD). Sh: Shutter, TL: Tube lens, PH: Pinhole, TM: Tiltable Mirror, L: lens, LP: Longpass Filter, BP: Bandpass Filter.

Briefly, moving the sample with nanometer-resolution steps through the fixed on-axis excitation point-spread-function of the microscope objective, the emitted fluorescence is simultaneously recorded at different wavelengths, using either dichroic mirrors, emission filters and avalanche photodiodes (dual-channel mode) or a dispersive prism allowing the emitted spectrum to be focused and imaged onto the chip of an intensified CCD camera (ICCD). Since the excitation PSF is fixed on the optical axis, there is no contribution of off-axis aberrations encountered in beam-scanning confocal microscopy. Moreover, the recorded intensity for each channel is directly proportional to the excitation PSF, the effect of the imaging arm being constant for each emission wavelength, since this emission takes place on-axis.

In the dual-channel acquisition mode (lower part of Fig. 1), two-color APD images were constructed by overlaying the two independent, false-colored channel images. In the full-spectrum mode (lower right part of Fig. 1), the 3-dimensional data set (1 spectral + 2 spatial dimensions) had to be reduced in individual channel images for easier manipulation. A simple approach was used to detect individual spectra of many single NCs. For this, we scanned the spatial recording and summed the 10 nm-binned spectra of each block of $n \times n$ pixels, where n is chosen in such a way that the block covers an area corresponding to the PSF extension. We summed these histograms and used the spectral peaks observed in the resulting histogram as central wavelengths for the filtering step.

In the next step, spectral bands (typically 25 nm width) centered on the previously extracted peaks were used to generate images from the original data set. From these images, the binned spectra of detected NCs were determined as explained previously, with the block of pixels centered on the approximate position of the observed NCs.

In the third step, narrower spectral bands (5-20 nm) were chosen to define new color channels with reduced spectral overlaps (i.e. as 'orthogonal' as possible). In the fourth step, the above images were combined into a composite false-color image with perfect registry between each color plane. These composite images are the multicolor equivalent of the dual-color images obtained on the dual-channel APD detection mode.

The final steps of the UHRC analysis consist in determining the position of each PSF's center. This is done using a now classical 2D Gaussian fitting approach [8, 13-16]. Numerical simulations as well as theoretical arguments show that nanometer resolution can be achieved for sufficiently large signal-to-noise ratio (SNR), signal-to-background ratio (SBR) and small pixel size [7, 12, 17]. The corresponding uncertainty is estimated using bootstrap replicas of the original data set, as discussed elsewhere [12, 17, 18].

3. SPECTRAL PROPERTIES AND MULTICOLOR IMAGING OF NANOCRYSTAL

Core/shell (CdSe/ZnS) nanocrystals were synthesized as previously described [9, 19] and dissolved in butanol. We used different batches of different diameters, which are supposed to be defined to within 5% as checked by transmission electron microscopy [9, 19].

Mixture of diluted samples (down to 10^{-6} the stock concentration) were deposited on cleaned glass coverslip as previously described [12], resulting in random distribution of NCs. Semiconductor nanocrystals have broad excitation spectra that go far into the UV region, which allows the use of a common excitation wavelength well separated from the emission range. In the following experiments, we used the 488 nm laser line of an Argon ion laser source. In addition, their emission spectra are relatively narrow even at room temperature (on the order of 30-40 nm FWHM) and symmetric, as illustrated on Figure 2.

Individual nanocrystals of a given sample have even narrower emission spectra (15-25 nm), as illustrated by a few examples taken with the full-spectrum mode setup of Fig. 1. In practice, it is possible to separate two partially overlapping nanocrystal spectra by fitting two Lorentzian, if their peak emission wavelengths are distant by more than half their FWHM.
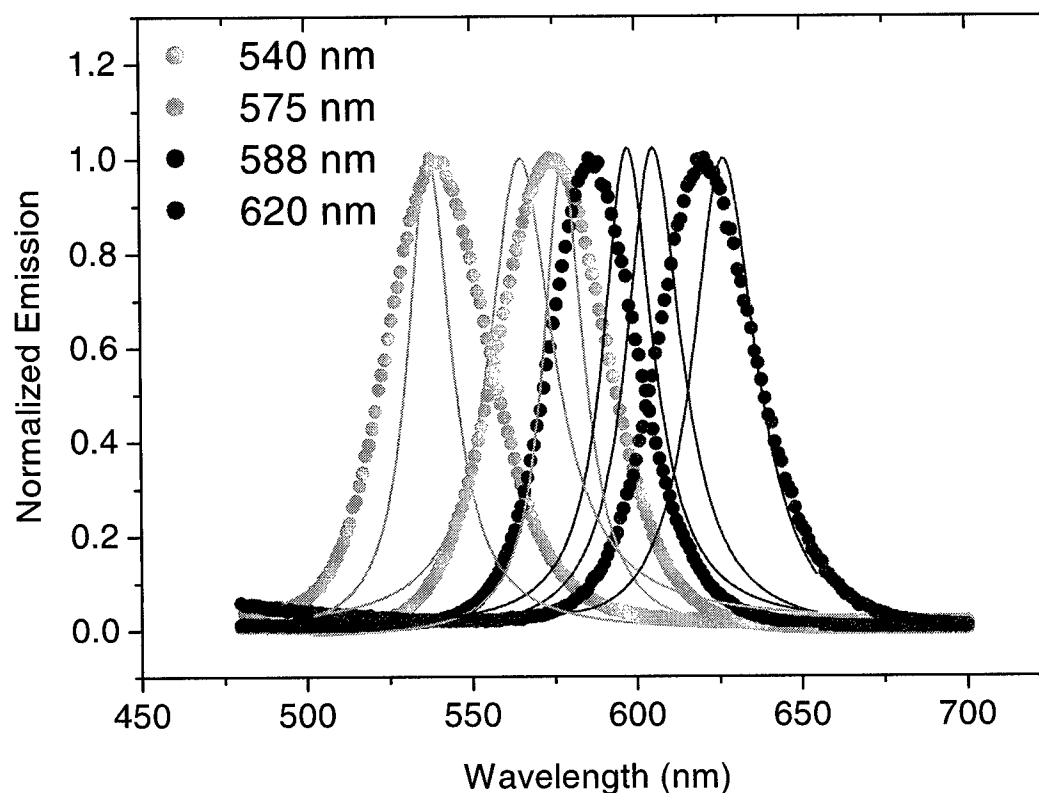
Figure 2: Normalized bulk emission spectra of 4 different NC samples (large dots) obtained with a standard spectrofluorimeter, superimposed with individual nanocrystals spectra (thin curves) as obtained with our multicolor imaging setup using the integrated data of 11x11 pixels and an integration time of 100 ms per pixel (200 nW incident excitation power). FWHM of bulk spectra are of the order of 30 nm: 34, 37, 34 and 32 nm, respectively for the 540, 575, 588 and 620 nm emissions. Peak ±FWHM of individual spectra from left to right (in nm): 537 ± 16, 565 ± 24, 578 ± 15, 598 ± 18, 605 ± 20, 627 ± 24.

However bright and resistant to photobleaching they might be, nanocrystals suffer from a major drawback for confocal (i.e. raster scanning) imaging. Indeed, they exhibit a complex pattern of intermittency [20-23], which results in a patchy image of the excitation PSF, as built up from the fluorescence emitted by a single nanocrystal. Figure 3 gives an example of multicolor imaging of a mixture of 4 batches exhibiting striking example of "blinking" nanocrystals.

Some ambiguity in this image results from the possible close spectra of nearby NCs, which would show up as overlapping PSFs. In order to distinguish this situation (of colocalization) from the mere observation of a single nanocrystal having a spectrum spread over the two selected spectral bands, it is necessary to take advantage of the full-spectrum information, as is illustrated for cases a and b in Fig. 3.

Spectra of two 11x11 pixels covering the two PSFs are shown on Figure 4. It is clear that case a corresponds to a single nanocrystal showing up in the false-color channel red and blue (spectrum: 586 ± 6 nm), whereas case b corresponds to two overlapping nanocrystals (spectra: 546 ± 10 and 602 ± 10 nm).
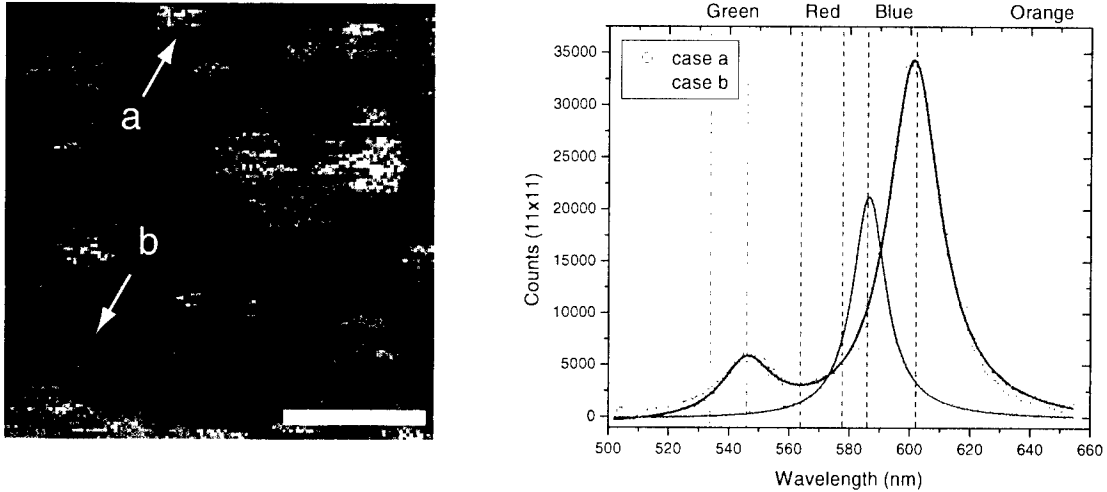
Figure 3: Multicolor imaging of a mixture of 4 NC batches (bulk spectra as indicated in Fig. 2). The area corresponds to a 3 x 3 µm² scan (bar indicates 1 µm) using 128 steps. Incident laser power: 200 nW, integration time: 100 ms per pixel. 4 spectral bands were selected as discussed in the text and false-colored (green: 540 ± 6, red: 571 ± 7, blue: 594 ± 8, orange: 643 ± 9). Some overlapping NCs are clearly visible in this contrast-enhanced image (case a, spectrum: 586 ± 6 nm), as well as cases of nanocrystals appearing simultaneously in the blue and red false-color channels (violet, case b, spectra: 546 ± 10 and 602 ± 10 nm).

Figure 4: Spectra of two different 11x11 pixels area of Fig. 3. Recorded spectra are displayed as scatter plots, with the best Lorentzian fits indicated by continuous curves. Boundaries of spectral bands used to build the false-color image planes of Fig. 3 are indicated by dashed vertical lines. Case a correspond to two nearby NCs whose PSFs overlap over most of their physical extension, but with clearly separated spectra (and different emission intensity). Case b corresponds to a single NC whose spectrum overlaps the two chosen bands used to build the red and blue image plane.
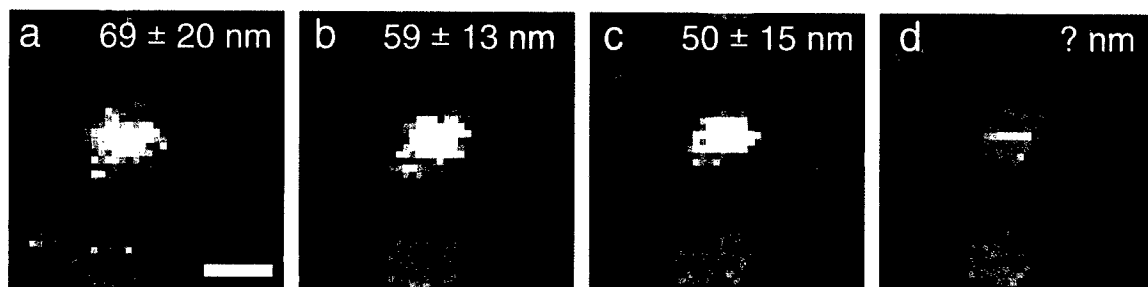
Figure 5: Repeated dual-color imaging of the same 2x2 µm² area of a mixture of green and red NCs, excited at 488 nm (incident excitation power: 200 nW, integration time: 50 ms, pixel size: 50 nm). The overall scan duration is about 80 s and the next scan is started almost immediately. Bar indicates 500 nm. The measured distance in each case is indicated with its corresponding 95 % confidence limit error bar as obtained with 1000 bootstrap simulations. Scan d gives a single stripe of signal for the red nanocrystal, so that no position can be determined for this NC. In subsequent scans, this NC gives more complete PSF images.

4. COLOCALIZATION RESULTS

Examples of NC colocalization using the approach exposed in this paper have already been presented elsewhere [12, 17]. Distance measurements down to 25 nm, with a resolution of a few nanometers can be achieved, as long as the scanned NCs do not exhibit too strong intermittency.

Intermittency of the fluorescence emitted by NCs leads to larger uncertainties on the position of the corresponding PSFs compared to non-blinking probes like fluorescent beads that we used in other demonstrations of ultrahigh-resolution colocalization [12, 17]. The reason is not only the reduction of the number of pixels above background available for the PSF fit, but rather more the complete change of probability distribution for each pixel value. This probability distribution is no more a Poisson distribution with mean equal to the value of the local excitation PSF, but a convolution of this and the "on" and "off" time probability distributions. Simulations performed using various probability distributions reported in the literature (exponential [22] or power law [23]), and as observed in our laboratory (data not shown), yielded uncertainties compatible with the values obtained by bootstrap estimation.

To experimentally assess the performance of colocalization studies using nanocrystals, we used the simpler APD (Fig. 1) setup that allows only dual-channel recording. As a consequence, we also limited ourselves to a mixture of green (Emission: 540 nm) and red (Emission: 620 nm) NCs. Since most NCs build up a patchy PSF due to blinking as illustrated in Fig. 3, we decided to estimate the uncertainty on the PSF position measurement by comparing several images of the same area recorded under the same conditions. Figure 5 shows a typical result of this kind of experiment.

The measured distances between the fitted position of each NC varies within the uncertainty computed in each case, which shows that our error bar estimation is robust. However, it also points to the serious problems that can be faced in case of severe blinking, if repeated imaging is not possible.

5. DISCUSSION

Nanocrystals are very attractive fluorescent probes for their ability to be excited by a common wavelength, their narrow spectra and seemingly immunization against photobleaching. Used in wide-field imaging, their intermittency would be of little influence, except to reduce their measured emission yield. In confocal microscopy, however, where the sample (or the beam) is raster scanned, "blinking" results in the diffraction spot corresponding to each individual NC to look patchy. In the worst case, position determination by fitting the PSF with a 2D Gaussian is impossible leading to a complete failure of the ultrahigh-resolution approach presented in this paper.

As rare cases of non-blinking, colocalized NCs, have convinced us, however, ultrahigh-resolution colocalization biological applications of NCs are promising if their photophysical properties can be improved. A possible way for reducing blinking would consist of artificially clustering NCs into aggregates of a few individuals, in order to average their intensity fluctuations. However, possible quenching or other photophysical effects could be introduced [24]. Progress in the synthesis of more efficient NCs is to be expected from the large community now involved in this type of research.

For static observations, the problems arising from severe blinking can be partially compensated for by the ability to scan precisely the same area with nanometer resolution, or use triangulation to fill gaps in a given UHRC measurement. We are currently using this approach to improve the resolution of gene mapping and DNA-binding proteins [25].

7. ACKNOWLEDGMENTS

8. REFERENCES

1. J. G. McNally, T. Karpova, J. Cooper, and J. A. Conchello, "Three-Dimensional Imaging by Deconvolution Microscopy,", *Methods* **19**, pp. 373-385, 1999.
2. E. G. Cragg and P. T. So, "Lateral resolution enhancement with standing evanescent waves," *Optics Letters* **25**, pp. 46-48, 2000.
3. P. Edelman and C. Cremer, "Improvement of confocal Spectral Precision Distance Microscopy (SPDM)," *SPIE Proceedings* **3921**, Optical Diagnostics of Living Cells III, 2000.
4. J. T. Frohn, H. F. Knapp, and A. Stemmer, "True optical resolution beyond the Rayleigh limit achieved by standing wave illumination," *Proceedings of the National Academy of Sciences USA* **97**, pp. 7232-7236, 2000.
5. M. G. L. Gustafsson, D. A. Agard, and J. W. Sedat, "I5M: 3D widefield light microscopy with better than 100 nm axial resolution," *Journal of Microscopy* **195**, pp. 10-16, 1999.
6. T. A. Klar, S. Jakobs, M. Dyba, A. Egner, and S. W. Hell, "Fluorescence microscopy with diffraction resolution barrier broken by stimulated emission," *Proceedings of the National Academy of Sciences USA* **97**, pp. 8206-8210, 2000.
7. N. Bobroff, "Position measurement with a noise-limited instrument," *Review of Scientific Instruments* **57**, pp. 1152-1157, 1986.
8. E. Betzig, "Proposed method for molecular optical imaging," *Optics Letters* **20**, pp. 237-239, 1995.
9. A. P. Alivisatos, "Semiconductor Clusters, Nanocrystals, and Quantum Dots," *Science* **271**, pp. 933-937, 1996.
10. M. J. Bruchez, M. M. Moronne, P. Gin, S. Weiss, and P. A. Alivisatos, "Semiconductor Nanocrystals as Fluorescent Biological Labels," *Science* **281**, pp. 2013-16, 1998.
11. W. C. W. Chan and S. Nie, "Quantum Dot Bioconjugates for Ultrasensitive Nonisotopic Detection," *Science* **281**, pp. 2016-18, 1998.
12. T. D. Lacoste, X. Michalet, F. Pinaud, D. S. Chemla, A. P. Alivisatos, and S. Weiss, "Ultrahigh-resolution multicolor colocalization of single fluorescent probes," *Proceedings of the National Academy of Sciences USA* **97**, pp. 9461–9466, 2000.
13. T. Schmidt, G. J. Schütz, W. Baumgartner, H. J. Gruber, and H. Schindler, "Characterization of Photophysics and Mobility of Single Molecules in a Fluid Lipid Membrane.," *Journal of Physical Chemistry* **99**, pp. 17662-17668, 1995.
14. T. Schmidt, G. J. Schütz, W. Baumgartner, H. J. Gruber, and H. Schindler, "Imaging of single molecule diffusion," *Proceedings of the National Academy of Sciences USA* **93**, pp. 2926-2929, 1996.
15. T. Ha, T. Enderle, D. S. Chemla, and S. Weiss, "Dual-molecule spectroscopy: Molecular rulers for the study of biological macromolecules," *IEEE Journal of Selected Topics in Quantum Electronics* **2**, pp. 1115-1128, 1996.
16. U. Kubitscheck, T. Kues, and R. Peters, "Visualization of Nuclear Pore Complex and Its Distribution by Confocal Laser Scanning Microscopy," in *Confocal Microscopy, Methods in Enzymology* **307**, P. M. Conn, Ed. San Diego: Academic Press, 1999, pp. 207-230.
17. X. Michalet, T. D. Lacoste, and S. Weiss, "Ultrahigh-resolution colocalization of single fluorescent probes," *Methods*, in press.
18. B. Efron and R. J. Tibshirani, *An Introduction to the Bootstrap*, vol. 57: CRC Press, 1994.
19. X. G. Peng, M. C. Schlamp, A. V. Kadavanich, and A. P. Alivisatos, "Epitaxial growth of highly luminescent CdSe/CdS core/shell nanocrystals with photostability and electronic accessibility," *Journal of the American Chemical Society* **119**, pp. 7019-7029, 1997.
20. S. A. Empedocles, D. J. Norris, and M. G. Bawendi, "Photoluminescence Spectroscopy of Single CdSe Nanocrystallite Quantum Dots," *Physical Review Letters* **77**, pp. 3873-3876, 1996.
21. A. L. Efros and M. Rosen, "Random telegraph signal in the photoluminescence intensity of a single quantum dot," *Physical Review Letters* **78**, pp. 1110-13, 1997.
22. U. Banin, M. Bruchez, A. P. Alivisatos, T. Ha, S. Weiss, and D. S. Chemla, "Evidence for a thermal contribution to emission intermittency in single CdSe/CdS core/shell nanocrystals," *Journal of Chemical Physics* **10**, pp. 1-7, 1999.
23. M. Kuno, D. P. Fromm, H. F. Hamann, A. Gallagher, and D. J. Nesbitt, "Nonexponential "blinking" kinetics of single CdSe quantum dots: A universal power law behavior," *Journal of Chemical Physics* **112**, pp. 3117-3120, 2000.

24. C. R. Kagan, C. B. Murray, M. Nirmal, and M. G. Bawendi, "Electronic Energy Transfer in CdSe Quantum Dot Solids," *Physical Review Letters* **76**, pp. 1517-1520, 1996.
25. X. Michalet, R. Ekong, F. Fougerousse, S. Rousseaux, C. Schurra, N. Hornigold, M. v. Slegtenhorst, J. Wolfe, S. Povey, and A. Bensimon, "Dynamic Molecular Combing: Stretching the Whole Human Genome for High-Resolution Studies," *Science* **277**, pp. 1518-1523, 1997.

Probing Specific DNA Sequences with Luminescent Semiconductor Quantum Dots

Jason Taylor and Shuming Nie

Department of Chemistry,Indiana University, Bloomington, IN 47405

ABSTRACT

The development of new fluorescent probes has impacted many areas of research such as medical diagnostics, high-speed drug screening, and basic molecular biology. Main limitations to traditional organic fluorophores are their relatively weak intensities, short life times (eg., photobleaching), and broad emission spectra. The desire for more intense fluorescent probes with higher photostability and narrow emission wavelengths has led to the development and utilization of semiconductor quantum dots as a new label. In this work, we have modified semiconductor quantum dots (QD's) with synthetic oligonucleotides to probe a specific DNA target sequence both in solution as well as immobilized on a solid substrate. In the first approach, specific target sequences are detected in solution by using short oligonucleotide probes, which are covalently linked to semiconductor quantum dots. In the second approach, DNA target sequences are covalently attached to a glass substrate and detected using oligonucleotides linked to semiconductor quantum dots.

Keywords: Quantum dots, fluorescence, DNA, Hybridization

1. INTRODUCTION

The development of new sensitive fluorescent tags utilized in biological detection has significantly impacted a variety of areas including medical diagnostics and molecular biology[1-3]. Current detection methods, however, are based mainly on the use of organic fluorophores that often suffer from photobleaching, low signals, narrow excitation spectra, and broad emission bands. The desire for more intense fluorescent probes with higher photostability, narrow emission bands, and broad excitation profiles has led to the continued development and utilization of new labels. Because of their optical properties, colloidal semiconductor QD's have the potential to overcome some of the problems present when using organic dye labels. The unique optical properties of QD's result from quantum confinement, which occurs when metal and semiconductor particles are smaller than their exciton Bohr radii[4-6]. Luminescent QD's are more advantageous as a label over typical organic dye molecules because they have narrow, symmetric, and size-tunable emissions, which are excitable at a single wavelength. The luminescent QD's are prepared by enclosing a core CdSe nanocrystal with a larger bandgap ZnS shell. Thus,

nonradiative relaxation pathways and photochemical degradation are prevented by confining the excitation to the core[7-8].

Because QD's are synthesized in an organic media and stablized by tri-n-octyl phosphine oxide molecules [9-10], rendering them water-soluble is necessary for biological applications. Various methods have been reported to make QD's water-soluble, allowing the immobilization of protein structures[11-13] and DNA molecules[14] onto the QD surface. Here we report alternative methods for linking short oligonucleotides to the QD surface. The QD's are passivated with a pyridine layer, which is subsequently removed by exchanging mercaptosuccinic acid molecules onto the surface to render them water-soluble. Our initial results indicate that short oligonucleotides can be linked to the QD surface and these QD bioconjugates can be used to probe specific DNA sequences. The ability to target specific sequences on a single DNA molecule could have implications in several research areas such as ultrasensitive medical diagnostics, high-speed genome mapping, and the fundamental studies of DNA molecules.

2. PROCEDURE

2.1 Materials

All chemicals and biochemicals used in this work were obtained from commercial sources. Acetone, ethanol, pyridine, hexanes, mercaptoacetic acid, PBS, CdCl, 2-mercaptoethanol, 1-ethyl-3-(3-dimethyl-aminopropyl)-carbodiimide (EDAC), polyethyleneglycol (PEG), polyvinylpyrrolidone, formamide, SSC, salmon sperm DNA, streptavidin, and bovine serum albumin were purchased from Sigma Chemical Co. (St. Louis, MO). Dimethylcadmium ($Cd(CH_3)_2$) and tributylphosphine (TBP) were purchased from Strem. Selenium (Se), tri-n-octylphosphine oxide (TOPO), dimethylzinc ($Zn(CH_3)_2$), Hexamethyldisilathiane (($TMS)_2S$) were purchased from Aldrich. Methanol, chloroform, and HCl were purchased from EM. NaOH was purchased from Bakers. EZ link TFP-PEO-biotin was purchased from Pierce (Rockford, IL). 5'-alkylthiol-, 3'alkylthiol-, 5'-alkylamine-, 3'-alkylamine and 30 mer target oligonucleotides were purchased from Midland Certified. Microscope cover slips (0.13 mm thick) were purchased from Fisher Scientific (Pittsburgh, PA). Ultrapure water was prepared by a Milli-Q purification system from Millipore (Bedford, MA).

2.2 Synthesis of ZnS-capped CdSe quantum dots

ZnS-capped CdSe QDs were prepared as described by Peng et al and Hines and Guyot-Sionnest[7-8]. Briefly, 12.5 g of tri-n-octylphosphine oxide (TOPO) was heated to 360°C inside a drybox purged with N_2. Then, an aliquot of CdSe stock solution (0.7 mmol Se/ 1.0 mmol Cd^{2+}) was injected into the hot TOPO solution. The solution was quickly lowered to 310°C and the size was monitored with a UV/Vis spectrometer (Shimadzu, Columbia, MD). The temperature was then lowered to below 300°C, and small aliquots (2 mL) of ZnS (0.23 M of Zn^{2+} and 0.16 M of Se in TBP) were injected to cap the CdSe QDs. The amount of ZnS injected was dependent upon the size of the CdSe core. Next,

the temperature was lowered to 100°C and stirred for an hour. Finally, the QDs were precipitated and washed three times with methanol to remove excess TOPO.

2.3 Optical characterization

UV-vis absorption spectra were acquired with a Shimadzu UV-2401 PC spectrophotometer (Columbia, MD). 1 mL quartz cuvettes were used for the measurements of all UV-vis spectra. The photoluminescence spectra were taken with a SPEX fluoromax-2 spectrometer (Edison, NJ). 1.5 mL acrylic (PGC Scientific, Frederick, MD) square cuvettes were used for the photoluminescence measurements of water-soluble quantum dots. For organic-soluble QDs, a 1.0 mL quartz cuvette was used.

2.4 Adsorption of DNA molecules onto the QD surface

Chloroform solvated QD's were washed to remove excess TOPO molecules by precipitatating with MeOH and resuspending the pellet in chloroform several times. After the final precipitation, the QD pellet was dissolved in excess pyridine and refluxed overnight at 60-70°C. The pyridine QDs were purified by hexane precipitation (70% hexane / 30% pyridine Q-dots) several times to remove excess pyridine. The final pyridine QD pellet was dissolved in mercaptosuccinic acid (0.5g/mL) at pH 9.0 and allowed to mix for 15-30 minutes (Figure 1).
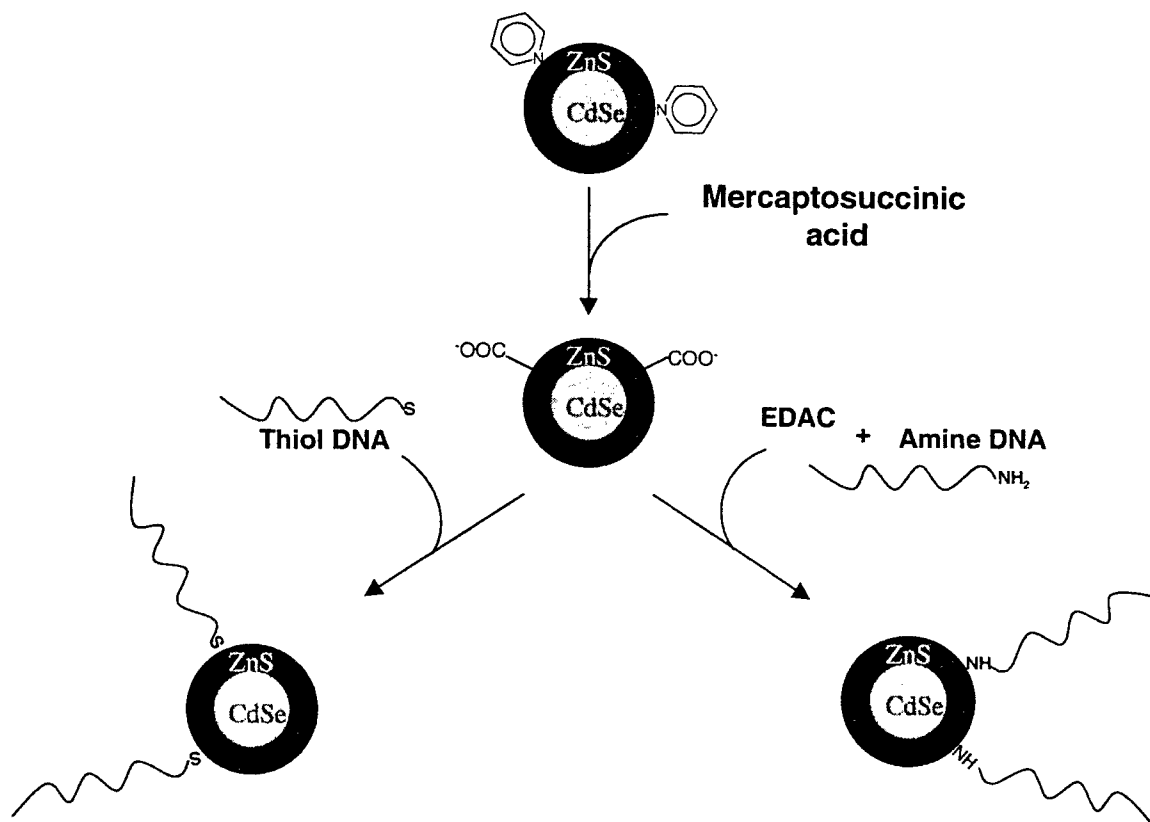
Figure 1: Schematic demonstrating the aggregation of DNA functionalized QD's

Amine-terminated oligo conjugates. QD's with adsorbed mercaptosuccinic acid molecules were purified from solution by either by a series of acetone precipitations (30% acetone / 70 % Q-dot solution) or by centrifuging the QD's at 60,000 rpm. The final mercaptosuccinic acid QD pellet was dissolved in a 15 mM buffered EDAC solution at pH 6.0. An aliquot of an amine-terminated oligonucleotide (15mer) was added to the QD solution at a final concentration of ~25-35 µg/ml and incubated for ~2 hours. The DNA QD conjugates were then purified from solution again either by acetone precipitation (30% acetone/70% Q-dot conjugates) or by ultracentrifugation at 50,000 rpm. The DNA QD conjugates are then dissolved and stored in a hybridization buffer (0.4 M NaCl, pH 7.0). Two different Q-dot conjugates were prepared using this protocol. One contained a 3'-amine-terminated oligonucleotide (15-mer) with a C16 spacer [5'-TCGTCTCAACTCGTA(_Spa 9) (_3'Amino C7)-3'] (Figure 1). The second was a 5'-amine-terminated oligonucleotide (15 mer) with a C15 spacer [5'-(_C6Amino)(_Spa 9) ATGCTCAACTCTGCT-3'].

Thiol-terminated oligo conjugates. Mercaptosuccinic acid passivated QD's were purified as mentioned before and dissolved in a 10 mM PBS solution (pH 9.0) containing excess alkylthiol-terminated oligos (25-35 µg/ml) and incubated for 24 hours. The DNA functionalized QDs were then purified several times either by acetone precipitation (30% acetone/70% QD's) or by ultracentrifugation at 50,000 rpm. The DNA functionalized QDs were then dissolved and stored in a hybridization buffer (0.4M NaCl, 7 % SDS, 2mM EDTA, pH 7.0). QDs functionalized with two different oligonucleotides were prepared using this protocol (Figure 1). One contained a 3'-thiol-terminated oligonucleotide (15-mer) with a C12 spacer [5'-TCGTCTCAACTCGTA(_Spa 9) (_Thiol C3)-3'], and the other a 5'-thiol-terminated oligonucleotide with a C15 spacer [5'-(_C6Thiol)(_Spa 9)ATGCTCAACTCTGCT-3'].

2.5 Hybridization with DNA-modified QD's

Equal aliquots of QDs conjugated with 5' amine/or thiol oligos and 3' amine/or thiol oligos were added to a hybridization buffer (0.4 M NaCl, 7 % SDS, 2mM EDTA, pH 7.4). To the solution, a complimentary 30-mer linker [5'-TACGAGTTGAGACGA-AGCAGAGTTGAGCAT-3'] was added at a relative concentration of ~50% the DNA functionalized QDs to hybridize and link the functionalized QDs together (Figure 2). Hybridization was monitored for 1-12 hours.

2.6 QD Imaging

A 7 µl aliquot of QD solution was sandwiched between two coverslips and allowed to spread for a few minutes. The coverslips are separated, which allows the buffer to evaporate from the surface. Upon drying, the QD's are imaged using an inverted microscope (Olympus, IX70, Melville, NY) with a Hg-lamp excitation source (Ushio
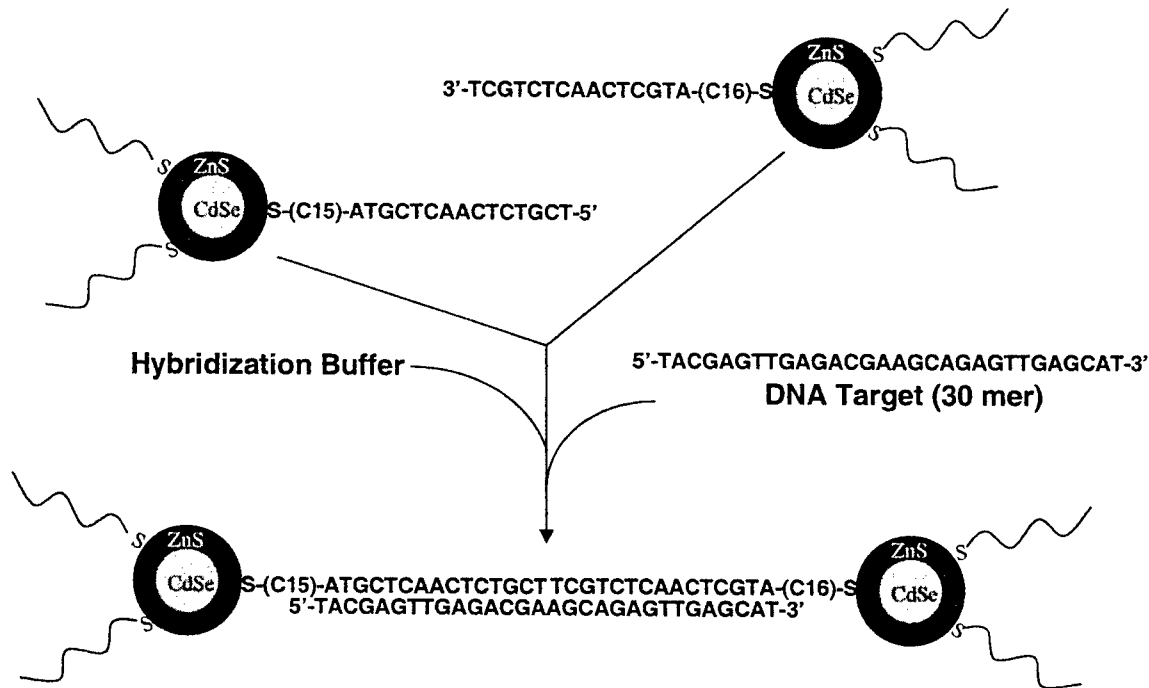
Figure 2: Schematic demonstrating the aggregation of DNA functionalized QD's

Inc., Tokyo, Japan). All images were collected using an oil-immersion objective (100X, N.A. = 1.4) and detected with a ultrasensitive CCD (Photometrics) or digital camera (Nikon).

3. Results and Discussion

3.1 Removal of surface TOPO molecules

ZnS-capped CdSe QD's are prepared in an organic media and stabilized by the TOPO molecules coordinated to the surface. The oxygen from the TOPO molecule is bound onto the surface Zn atoms, while the TOPO alkyl chains forms a network like structure around the QD [15-16]. Successful removal of surface TOPO molecules was accomplished by refluxing the QD's in excess pyridine. Because TOPO passivated QD's are insoluble in methanol, the exchange of pyridine for TOPO molecules on the QD surface is confirmed by their solubility in this solvent. In order to utilize these QD's as a biological label, they must be further modified to render them water-soluble.

3.2 Design of DNA-functionalized QD's

Mirkin and coworkers have demonstrated that QD's can be functionalized with DNA and used for programmed assembly[14]. Their work shows that QD's passivated with mercaptopropionic acid can be modified with alkylthiol-terminated oligonucleotides through an exchange reaction with the mercaptopropionic acid molecules on the QD surface. Here we demonstrate additional methods of linking oligos to the QD surface. We have used alkylthiol-terminated and alkylamine-terminated oligonucleotides to functionalize the QD surface and study the DNA-binding properties these bioconjugated nanoparticles. By passivating the QD surface with mercaptosuccinic acid after refluxing them in pyridine, the QD's become water-soluble and are stable for a few weeks. The mercaptosuccinic acid quickly exchanges with the pyridine molecules on the QD surface because its thiol group has a stronger binding affinity to zinc than the nitrogen of pyridine. Therefore, we were able to utilize these mercaptosuccinic acid molecules to functionalize the QD surface with DNA either by using conjugation chemistry with the free carboxylate groups of mercaptosuccinic acid or by directly exchanging alkylthiol-terminated oligonucleotides with the mercaptosuccinic acid molecules on the surface.

Our initial results show that it takes less than an hour to completely passivate the QD surface with mercaptosuccinic acid. We can then functionalize the QDs with alkylamine oligonucleotides through bioconjugate chemistry in less than 2 hours using 1-ethyl-3-(3-dimethyl-aminopropyl) carbodiimide (EDAC). This compound reacts with surface carboxylate (-COOH) groups on the QD's to yield an O-acyl-isourea active intermediate, which is reactive to the terminal primary amines of the oligos [17]. One drawback to this procedure is that the intermediate formed in the EDAC reaction is subject to hydrolysis in aqueous media [18]. To increase the reaction yield, we added a second reagent N-hydroxysulfosuccinimide (sulfo-NHS) to form a more stable active ester intermediate. This intermediate is less susceptible to hydrolysis while at the same time, reacts more rapidly with amines [19]. Alternatively, we also developed a method to directly link the oligos to the surface similar to that of Mirkin and coworkers. We find that thiol-terminated oligos when in excess will exchange with mercaptosuccinic acid molecules on the QD surface at a high pH (~9-10). The DNA binding capabilities of these DNA-QD bioconjugates confirms the presence of oligos on their surface.

3.3 Probing DNA target with DNA-QD bioconjugates

To investigate whether the conjugated nanoparticles would bind to DNA, approximately equal aliquots of QD's conjugated to 5'-amine oligonucleotides and 3'-amine oligonucleotides were incubated with a DNA linker capture sequence for 1-10 hours in a hybridization buffer at room temperature. The 30 mer linker was designed so that the first 15 nucleotides were complimentary to 5'-amine oligonucleotide conjugated QD's and the remaining 15 nucleotides complementary to the 3'-amine oligonucleotide conjugated QD's. Figure 3 shows the aggregation that occurs due to hybridization with the complimentary DNA linker molecules. It should be pointed out that these

nanoparticles (4-5 nm) are larger than single organic fluorophores. This could create problems in terms of binding kinetics and steric hindrance due to the bulkiness of the nanoparticle attached to the oligo. We have observed aggregation taking place as early as 1-2 hours after incubation, which demonstrates that hybridization can still occur fairly quickly with the oligos attached to nanoparticles. However, longer incubation times leads to an increase in size and number of aggregates observed. Because each QD contains several conjugated amine oligonucleotides, several conjugated QDs can be joined together through consecutive hybridizations and thus, large aggregates can form as demonstrated in the figure. In order to verify that the aggregation was due to hybridization with the linker, several experiments were set up. First, by placing equal amounts of the two different conjugated QD's in a hybridization buffer, we set a control study without the target sequence (linker) in solution. As expected, very little nonspecific aggregation is observed between the QD bioconjugates when the linker molecule is missing (Figure 3). Second, the aggregated sample in Figure 3 was heated to 100°C which is above the melting point of the DNA linker hybridization ($T_m = 84$°C). If the QD aggregation was due to hybridization with the linker, then the aggregation should disappear with an increase in temperature. As the solution was raised to 100°C, almost all of the QD aggregates become single QD's dispersed on the slide as indicated by their characteristic blinking behavior when single. Similar results were also obtained utilizing the thiol-terminated DNA-QD bioconjugates. Therefore, we believe our initial results have demonstrated that the synthetic oligonucleotides have been conjugated to the QD's and they are capable of probing specific DNA sequences.
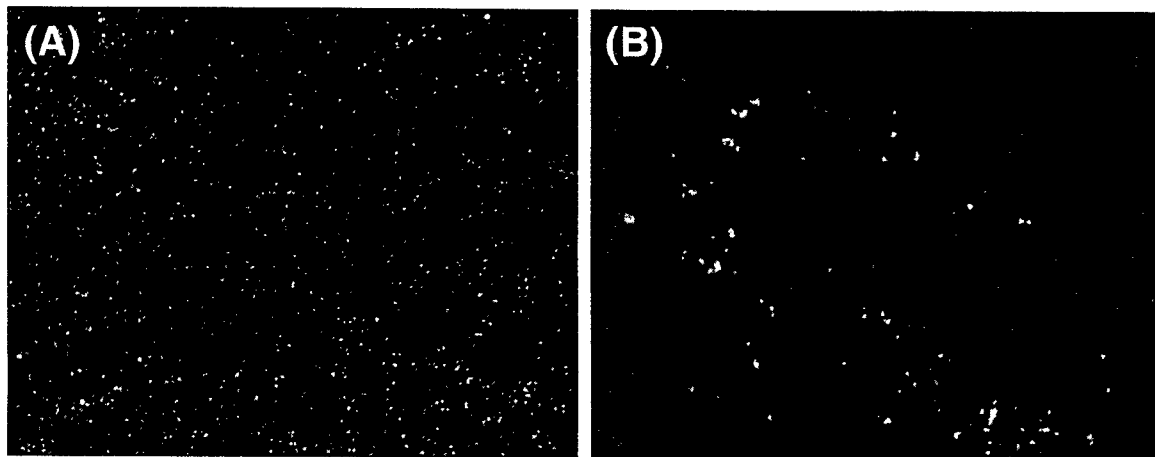
Figure 3. Equal aliquots of QD's conjugated to 5'-amine oligonucleotides and 3'-amine oligonucleotides incubated without (A) and with (B) the DNA target sequence.

4. CONCLUSIONS

Luminescent QD's are advantageous as a label over typical organic dye molecules because they offer narrow spectral linewidths, greater photostability, and symmetric, size-tunable emissions excitable at a single wavelength. However, the ability to manipulate the QD surface is key to controlling their solubilization and thus, will affect bioconjugation onto the surface. We have demonstrated two different methods for linking synthetic oligonucleotides to the QD surface. Amine-terminated oligonucleotides can be covalently linked to surface mercaptosuccinic acid groups through the carbodiimide EDC. Alternatively, thiol terminated oligos can be directly adsorbed onto the surface Zn atoms through a S-Zn bond under basic pH's.

We have demonstrated that the oligos linked to the QD's remain active. The DNA-QD bioconjugates are capable of probing a specific target DNA sequence in solution. used to target a specific DNA capture sequence. These DNA-QD bioconjugate probes have potential to find use in multicolor experiments due to their size-tunable emissions, real time studies due their long photostability, and medical diagnostics as a result of their specific DNA binding capabilities.

4. Acknowledgements

5. References

1. E. Pennisi, *Science* **275**, pp. 480-481, 1997.
2. T. Gura, *Science* **276**, pp. 1988-1990, 1997.
3. D. Sidransky, *Science* **278**, pp.1054-1058.
4. Alivisatos, A. P. *Science* **271**, pp. 933-936, 1996; *J Phys. Chem.* **100**, pp. 13226, 1996.
5. Brus. L.E., *Appl. Phys. A* **53**, pp. 465-460, 1991; Wilson, W. L.; Szajowski, P. F.; Brus, L. E., *Science* **262**, pp. 1242-1246, 1993.
6. Henglein, A., *Chem. Rev.* **89**, pp. 1861-1868, 1989.
7. Hines, M. A. and Guyot-Sionnest, P., *J. Phys. Chem.* **100**, pp. 468-471, 1996.
8. Peng, X. G.; Shlamp, M. C.; Kadavanich, A. V.; Alivisatos, A. P., *J. Am. Chem. Soc.* **119**, pp. 7019-24, 1997.
9. H. Weller, *Angew.Chem. Int. Ed. Engl.* **32**, pp. 41-53, 1993.
10. H. Weller, *Advanced Materials* **5**, pp.88-95, 1993.
11. W. C. W. Chan and S. Nie, *Science* **281**, pp. 2016-2018, 1998.
12. A.P. Alivisatos, *Science* **281**, pp.2013-2016, 1998.

13. H. Mattoussi, J. M. Mauro, E. R. Goldman, G. P. Anderson, V. C. Sundar, F. V. Mikulec, and M G. Bawendi, *J. Am. Chem. Soc.* **133**, 10258-10263, 2000.
14. G.P. Mitchell, C.A. Mirkin, and R. L. Letsinger, *J. Am. Chem. Soc.* 8122-8123, 1999.
15. L. R. Beccerra, C, B, Murray, R. G. Griffin, M. G. Bawendi, *J. Chem. Phys.* **100,** pp. 3297-3300, 1994.
16. J. K. Lorenz and A. B. Ellis, *J. Am. Chem. Soc.* **120**, pp. 10970-10975, 1998.
17. Hermanson, G. T. *Bioconjugate Techniques*, Academic Press, New York, 1996.
18. Gilles, M. A., Hudson, A. Q. & Borders, C. L., *Anal. Biochem.* **184**, 244-248,1990.
19. Staros, J. V., Wright, R. W. & Swingle, D. M., Anal. Biochem. **156**, 220-222, 1986.

Inorganic Nanoparticles as Optical Sensors of DNA

Catherine J. Murphy*, Rahina Mahtab, Kimberlyn Caswell, Latha Gearheart, Nikhil R. Jana,
Samyah Hammami, Derek D. Best

Department of Chemistry and Biochemistry, University of South Carolina, Columbia SC 29208

ABSTRACT

The 1 – 100 nanometer size range encompasses the dimensions of proteins and DNA. In this size range the bulk properties of inorganic materials become influenced by quantum mechanical effects and become size-dependent. Semiconductor nanoparticles are photoluminescent throughout the visible; the emission maximum is dictated by particle size, nature of the surface, and nature of the bulk material. We have used the photoluminescence of semiconductor nanoparticles to infer how oligonucleotides with unusual structure bind to the nanoparticles, providing insight into local structure and flexibility of the DNA. More recently we have examined the effects of base modifications on these binding events. Metallic nanoparticles can also interact with DNA, and these interactions can be monitored by the visible absorbance spectrum of the nanoparticles and by surface-enhanced Raman spectroscopy (SERS). Metallic surfaces that are rough on the nanometer scale are known to enhance the Raman signals of adsorbates by up to a million-fold. The result of photoluminescence titrations of abasic DNA and SERS DNA-nanoparticle studies will be reported.

Keywords: DNA, oligonucleotide, CdS, photoluminescence, quantum dot, nanoparticle, SERS, dimers, gold, silver

1. INTRODUCTION

A rapidly expanding division of nanoscience and nanotechnology includes research in which inorganic materials and biological molecules converge. Of particular interest are areas involving DNA and metal or semiconductor nanoparticles, where the nanoparticle either directly or indirectly provide an optical means of monitoring DNA-nanoparticle interactions.[1-12] In the past, we have employed photoluminescent quantum dot CdS as "inorganic proteins" to detect intrinsic DNA curvature in 16 base-pair oligonucleotides and more recently to differentiate between higher order DNA structures associated with disease. We have shown that quenching of CdS luminescence is an indirect approach to detecting DNA structure and is dependent on nanoparticle surface charge and functionality.[1,2,13] However, the luminescence signal does not provide direct molecular information. A technique, which provides chemical information about adsorbates at nanosize metallic surfaces, is surface-enhanced Raman scattering (SERS) spectroscopy. Gold and silver nanoparticles are two excellent SERS substrates that can be easily synthesized within the size regime of proteins. Our endeavors here have been to detect and differentiate between unusual DNA structures using inorganic molecules; and to develop new inorganic nanoparticle probes for detecting such molecules. The research presented here can be divided into three sections. First, we demonstrate the use of quantum dot CdS in detecting abasic DNA. Second, we show the potential of applying SERS spectroscopy to differentiate between thymine dinucleotides that have and have not been exposed to UV radiation. Finally, we examine the substrate size dependence on SERS signal intensity of an intrinsically bent sequence of DNA adsorbed to gold nanoparticles and explore the potential of employing dendrimer-gold nanocomposites as SERS substrates for DNA.

2. EXPERIMENTAL METHODS

2.1 CdS with Abasic and "Kinked" DNA

The two oligonucleotides used, 5'-GGCACATG*CCATTGG-3' and complement 5'-CCAATGGCCATGTGCC-3'as an abasic duplex, and the self complementary 5'-GGCACATGGCCATTGG3'as a "kinked duplex" were synthesized by standard phosphoramidite methods at the USC Institute for Biological Research and Technology's Oligonucleotide Synthesis Facility. Oligonucleotides were purified by reverse- phase high-pressure liquid chromatography and dissolved in tris-buffer (5 mM tris hydrochloride, 5 mM NaCl, pH 7.2).

Cd(II)- activated CdS nanoparticles, 45 Å in diameter and surface- enriched with Cd(II), were synthesized as previously described as a colloidal dispersion in water.[1] Nanoparticles were characterized by transmission electron microscopy and absorption and photoluminescent spectroscopy.

Photoluminescence titrations were performed by adding small aliquots (~5 μL) of ~mM (nucleotide) DNA solutions to 300 μL of a 2 x 10^{-4} M (Cd) Cd(II)-CdS solution. Emission spectra were acquired after ~30 minutes after each DNA aliquot was added to ensure equilibrium was reached. Blank titrations of buffer without DNA were also performed and used to correct the data for subsequent analysis.

2.2 Thymine dinucleotides and thymine dimers on silver nanoparticles

Thymine dinucleotides (highly purified salt free) were purchased from MWG Biotech Inc. The dinucleotides were dissolved in 5 mM Tris 5 mM NaCl pH 7.2-7.4 buffer. The dinucleotide/buffer stock was split into four equal samples: (1) DNA/buffer no acetophenone no UV-irradiation (2) DNA/buffer acetophenone no UV-irradiation (3) DNA/buffer no acetophenone UV-irradiation (4) DNA/buffer acetophenone UV-irradiation. UV-irradiation provided the impetus necessary to produce the desired photoproducts. Acetophenone (3 x 10^{-3} mM) functioned as a photosensitizer. The light source for UV-irradiation was that of the spectrofluorometer described below using 330 nm excitation for 6 hours with 15 minute agitation intervals.

Silver nanoparticles were prepared according to the seeded-growth method by Schneider.[14] The method involves growing larger particles from preformed silver seeds. The seed solution was prepared as follows: a 10 mL aqueous solution containing 1 mM NaOH and 0.1 mM NaBH$_4$, *solution 1*; and a 0.6 mM AgNO$_3$ solution, *solution 2*. While vigorously stirring *solution 1*, 10 mL of *solution 2* was added to *solution 1* all at once. The solution turned yellow. Stirring was allowed to continue 2-3 min after the color change.

The seed was then used to grow larger silver particles as follows: a 10 mL solution containing 0.3 mM AgNO$_3$ was added slowly (within 60 sec) to a 20 mL solution containing 0.25 mM NaOH, 0.15 mM ascorbic acid, and, 0.3 mL, from stock seed prepared according to the procedure above while stirring vigorously. Immediately, 1 mL of 100 mM KCl was added for stability. Particles prepared in this way were roughly spherical with an average diameter of 44 nm as judged by transmission electron microscopy. Utilizing 100 μL of Ag colloid with 10 μL of 1 M KCL and 10 μL DNA sample provided the most stable and well-defined SERS peaks for all dinucleotide samples.

2.3 "Kinked" DNA on different size gold particles

Gold colloids were prepared using the citrate-reduction method developed by Frens.[15] A 150 mL solution of 0.01% gold chloride was heated and either 1 mL or 3 mL of sodium citrate solution were added directly into the solution upon boiling. Approximately 10-15 seconds after addition of the sodium citrate, the solution changed color form clear, pale-yellow to dark-gray, and finally to a red-wine color, indicating reduction of the gold chloride into monodisperse, spherical particles. The solution was boiled for an additional 10-15 minutes to complete reduction. Using 1 mL of citrate produced ~29 nm particles and using 3 mL of citrate produced ~12 nm particles

Four fresh sets of 12 nm citrate-reduced gold particles were prepared according to the Frens method.[15] These particles were used as seeds to prepare three sets (Sets a, b, and c) of larger size ascorbic acid-reduced gold particles (four sets each). Each set was prepared by adding an appropriate amount of 10 mM ascorbic acid to solutions containing 2 mL of seed, an appropriate amount of 2.5 mM HAuCl$_4$, and an appropriate amount of H$_2$O. The volumes of HAuCl$_4$, H$_2$O, and ascorbic acid used are given for each set. Set A: 1.8 mL of HAuCl$_4$, 94 mL of H$_2$O, 1.4 mL of ascorbic acid for 43 nm particles; Set B: 7.8 mL of HAuCl$_4$, 84 mL of H$_2$O, 5.9 mL of ascorbic acid for 75 nm particles; Set C: 15.8 mL of HAuCl$_4$, 70 mL of H$_2$O, 15.8 mL of ascorbic for 100 nm particles.

SERS of "kinked" DNA was measured for all four batches of each size particle, including the 12 nm seed. The 12 nm seed was diluted appropriately (2 mL of seed in to 98 mL H$_2$O) so that the particle concentrations would be equal for each set. For the SERS measurements, 5 μL of 2.6 mM "kinked" DNA (concentration in nucleotide) was mixed with 100 μL of 0.1 M KCl and added to 200 μL of the gold particle solutions.

2.4 Gold-dendrimer nanocomposites

Au particles were prepared by the Frens method and had an average diameter of 29 nm as judged by transmission electron microscopy.[15] Au/COOH-dendrimer nanocomposites were prepared by adding 10 μL of a 0.05 mM dendrimer solution to

approximately 0.7 mL of citrate-reduced Au colloids (approximately 0.7 µM dendrimer). Addition of dendrimer to Au particles resulted in a color change from wine-red to purple.

The calf-thymus (CT) DNA used in the SERS experiments was purified by the phenol-chloroform extraction method and dissolved in 5 mM tris 5 mM NaCl buffer. SERS spectra of 700 µL of the gold-dendrimer nanocomposite solutions (0.05 mM COOH-dendrimer) containing 10 µL of CT DNA (9.1 x 10^{-3} M) in tris buffer were recorded.

2.5 Instrumentation
High pressure liquid chromatography was performed on a Beckman Gold System with an UV-vis absorption detector module. The stationary phase was a Hamilton PRP-1 reverse-phase column, the liquid phase was an acetonitrile/triethylammonium acetate aqueous buffer (pH 7.0) gradient. Absorption spectra were acquired with a Cary 500 Scan UV-VIS-NIR spectrophotometer. Photoluminescence spectra were acquired with an SLM-Aminco 8100 spectrofluorometer, with excitation at 350nm and 4 nm slit widths. Transmission electron microscopy (TEM) was performed on a Hitachi H-8000 electron microscope. All SERS measurements were performed using a Detection Limit Solution 633 Raman System. The system utilizes a filtered fiber-optic probe equipped with a microscope objective to focus radiation from a 633 nm helium neon laser on to the sample and collect the 180° Raman backscatter. Laser power at the sample was 25 mW. Spectral acquisition and processing were enabled with DLSPEC and GRAMS/32 (Galactic Industries) software.

3. RESULTS AND DISCUSSION

3.1 CdS Luminescence Titrations with Abasic DNA
Abasic DNA is thought to be one of the most frequent occurrences of cellular DNA damage and can cause Parkinson's disease, has been linked to causing some types of cancer and even death in humans due to prevention of DNA replication.[16-19] Abasic sites, which are the result from the loss of a base in DNA, can occur by spontaneous hydrolysis with a relatively high frequency, enzymatically in the course of the repair of changed or abnormal bases as a result of chemotherapy, anti-tumor medications, radiation, and carcinogens.[20-22] Abasic site formation is noticeably increased during the repair of damaged nucleic bases.[23] In our laboratory we have developed semiconductor nanomaterials as luminescent probes of intrinsic DNA structure and/ or flexibility.[1-4,13,24] These nanoparticles emit visible light when irradiated, and this photoluminescence is exquisitely sensitive to the nature of adsorbed species in solution.[1,25-28] The DNA can wrap around these nanoparticles, and to gain insight into sequence-directed DNA structure, we have considered these quantum dots to be generic curved surfaces, so that any specificity in the binding process is coming from the DNA.[1,2,4,13,24] Previously we have examined the binding of semiconductor CdS nanoparticles with 'straight', 'bent', and 'kinked' DNA.[1,2] Damaged DNA, such as abasic DNA, is considered more flexible than normal DNA and may have different binding properties. In this paper we examined the binding of protein-sized CdS quantum dots to abasic DNA and compare their binding with that of a 'kinked' DNA.[29,30]

Figure 1 shows the luminescence spectra of CdS as either 'abasic' or 'kinked' DNA is added to solution. Both the 'abasic' and the 'kinked' DNA quenched the photoluminescence of 45 Å Cd(II)-CdS. Our experimental results are consistent with DNA titrations previously performed in our laboratory.[1-4,13,24] The 'kinked' DNA quenched the photoluminescence more efficiently than the 'abasic' DNA. The details of the quenching mechanism is not very well known, and we have suggested that the photoluminescence quenching is due to adduct formation between the oligonucleotides and the nanoparticles; after the titrations no permanent base modifications are made on the DNA and hence any consequent redox damage is negligible.[1]

We have used the Frisch-Simha-Eirich theory of a long polymer adsorbing in segments onto a locally flat surface to obtain relative equilibrium binding constants,[31]

$$[\theta \exp(2K_1\theta)] / (1 - \theta) = (KC)^{1/\nu}$$

where θ, the fractional surface coverage, is equated to fractional change in luminescence ($\theta = (PL - PL_0)/ (PL_f - PL_0)$, where PL is the intensity of photoluminescence at an arbitrary point in the titration, PL_0 is the initial photoluminescence intensity before DNA is added, and PL_f is the photoluminescence intensity at which no further change takes place as DNA is added); K_1 is a constant that is a function of the interaction of adsorbed polymer segments(set equal to 0.5 here, which we have empirically found to give best fits to the data); K is the equilibrium constant for binding; and ν is the average number of segments attached to the surface. C is the DNA concentration in nucleotides.[27] We assume a two-state model for the nanoparticle-DNA interaction for our definition of θ; the quantum dot is either bound to the DNA (and emits with intensity PL_0 to PL_f depending on DNA concentration), or free of DNA (and emits with intensity PL_0). We find good fits to the

model (Figure   ). The binding constants for binding to the 45 Å Cd(II)- rich CdS nanoparticles are 23,800 M^{-1} for the 'kinked' DNA and 17,800 M^{-1} for the 'abasic' DNA.
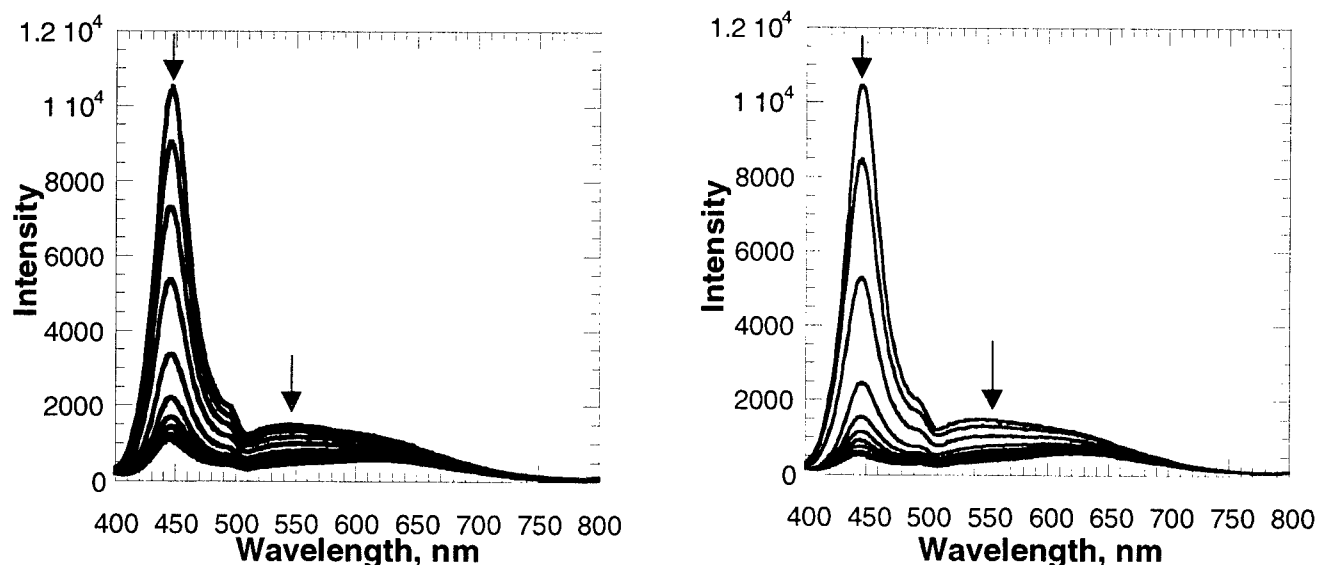
Figure 1. Photoluminescence titration data for the binding of abasic(left) and (kinked) DNA to 45 Å Cd(II)- rich CdS nanoparticles. DNA concentrations are from 0 – 300 μM nucleotide.
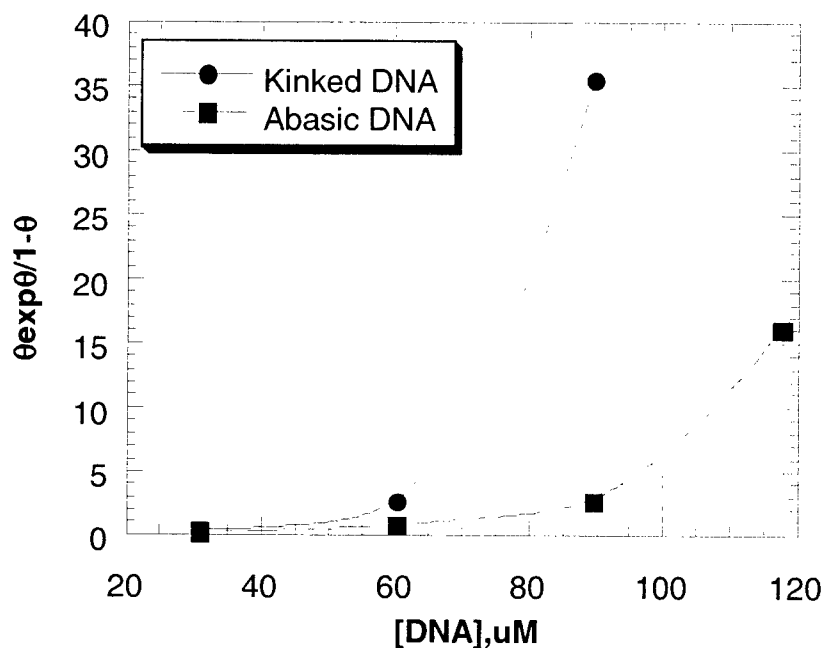
Figure 2. Frisch-Simha-Eirich plot for the binding of abasic and kinked DNA to 45 Å Cd(II)-rich CdS nanoparticles. Filled circles: kinked DNA; filled boxes : abasic DNA.

The results of our luminescence titrations show that the 'kinked' DNA quenches the nanoparticle emission more efficiently than the 'abasic' DNA . The sequence 5`-d(CATGGCCATG)-3` has been crystallized as a self-complementary duplex and shows a definite kink of 23° across the central 5`-GGCC-3`.[32] Fluorescence resonance energy transfer(FRET) studies have confirmed this intrinsic bending in the solution structure of GGCC tracts.[33] Other workers have suggested that the energetic

cost of bending DNA by proteins could be reduced if the DNA was already bent (or more likely to be bent).[34] Thus the 'kinked' DNA might bind better and faster because its static curved shape matches more closely the curved surface, and wraps the particle substrate more often upon collision in solution, than the 'abasic' DNA, which is supposed to be more flexible.[30]

3.2 SERS of Thymine Dinucleotide and Dimerized Thymine Dinucleotide on Silver Nanoparticles

Cyclobutane pyrimidine dimers (CPDs), particularly thymine dimers, are the predominant UV-induced photoproducts, constituting ~75-80% of DNA lesions.[35-41] Dimer formation has been implicated, with crucial importance, in the initiation of skin cancer through a close linking of the generation of mutations in tumor-suppressor genes expressed in UV-induced skin cancer.[37,38,42] The frequency of skin cancers induced by sunlight in the United States approaches that of all other cancers combined and is doubling each decade.[42] Increased exposure time, depletion of the ozone layer, and diseases associated with photosensitivity (e.g., xeroderma pigmentosa) are thought to be the primary reasons for the increased rate of incidence.[37,43-48] Cyclobutane thymine dimers are DNA lesions that are a result of a [2+2] photocycloaddition between adjacent thymine bases on the same polynucleotide strand.[49]

Other groups have demonstrated SERS of free base thymine; however, to the best of our knowledge, there are no reports on SERS of thymine photoproducts.[50-53] These photoproducts would be expected to produce new SERS peaks, which our spectra confirm. Figure 3 reveals distinct differences (denoted by arrows) between thymine dinucleotides and the UV-irradiated photoproducts. A detailed assignment of the vibrational modes of the thymine dinucleotide photoproducts is underway. The new bands in the SERS spectrum of thymine dinucleotide photoproducts are likely attributed to new bond formation and reorientation of the molecule on the silver surface.
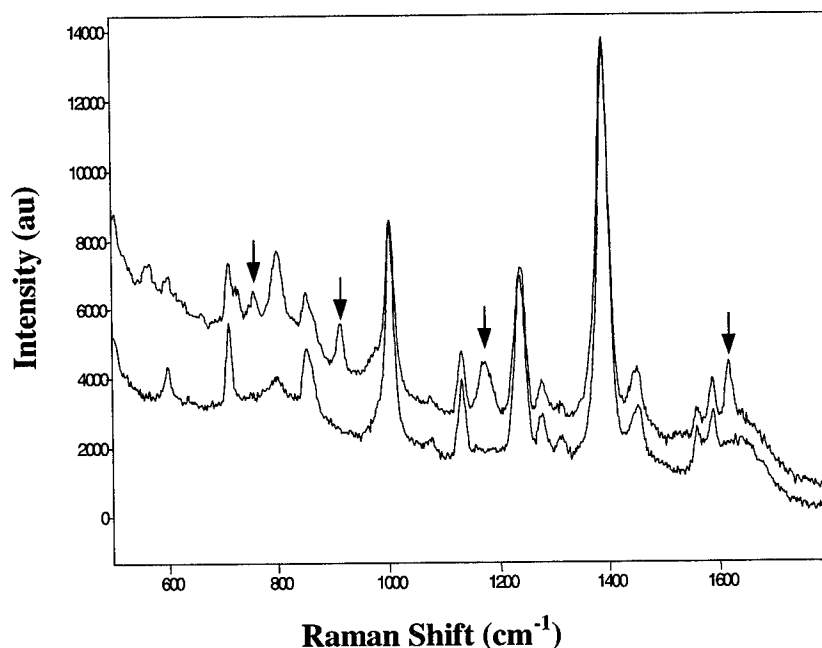
Figure 3. SERS of Thymine photoproduct (top) and dinucleotide (bottom) 100 µL Ag colloid, 5 µL 1 M KCl, and 15 µL 6.1 mM DNA.

3.4 SERS of DNA on Different Sized Gold Nanoparticles

The dimensions and homogeneity of SERS substrates heavily influence analyte signal enhancement and reproducibility, and as a result of advances in instrumentation and substrate preparation, groups are making significant headway into understanding the importance of substrate morphology.[14,54-59] Nie observed optimum Raman enhancement for 90-100 nm citrate-reduced silver nanoparticles, but only 0.1-1 % of the total nanoparticles in the heterogeneous solution were optically active.[54] Using a particle-filtration screening method, the concentration of SERS active nanoparticles was increased to 10-15%.[54] Though a considerable increase over 0.1%, the importance of developing new synthetic routes for more uniform metal nanoparticles was recognized.

A considerable amount of SERS research on DNA has been conducted dating back to the early 1980's; however, most work employed silver particles. Gold particles are less reactive than silver and hence are better suited for biological applications. In addition, gold particle preparations typically produce more homogeneous samples than those do for silver particles, and their sizes can be easily controlled.[60] We tested 12, 43, 75, and 100 nm gold nanoparticles as SERS substrates for 16 base pair double-stranded 'kinked' DNA in order to determine which size produced the greatest enhancement. Figure 4. compares the SERS spectra of a given concentration of DNA on the four different size sets of nanoparticles. The concentration of the nanoparticles was held constant. Optimum enhancement was observed on gold nanoparticles 75 nm in diameter after adding KCl (Figure 4). Without KCl, the SERS signals were very weak for all size particles. The SERS measurements were repeated four times with freshly prepared solutions of each size. The integrated intensity was calculated for the 735 cm[1] peak of the DNA (corresponding to the ring breathing vibrations of adenine) in order to determine the reproducibility associated with the different size particles. The percent relative standard deviation was the largest at 20% for the 75 and 43 nm particles and smallest at 10% for the 12 and 100 nm particles. These preliminary results indicate that the size of the nanoparticles plays a significant role in the enhancement of oligonucleotides on gold nanoparticles.

We also measured SERS spectra of a solution containing Au/COOH-dendrimer nanocomposites before and after addition of double-stranded CT DNA (Figure 5). Without DNA, several dendrimer vibrational bands were enhanced. Upon addition of the CT DNA, the SERS bands due to the dendrimer decreased, an indication that the CT DNA was displacing the dendrimer. Enhancement of the vibrational modes of CT DNA were not observed due to the notoriously weak SERS signal from CT DNA.[6,61]
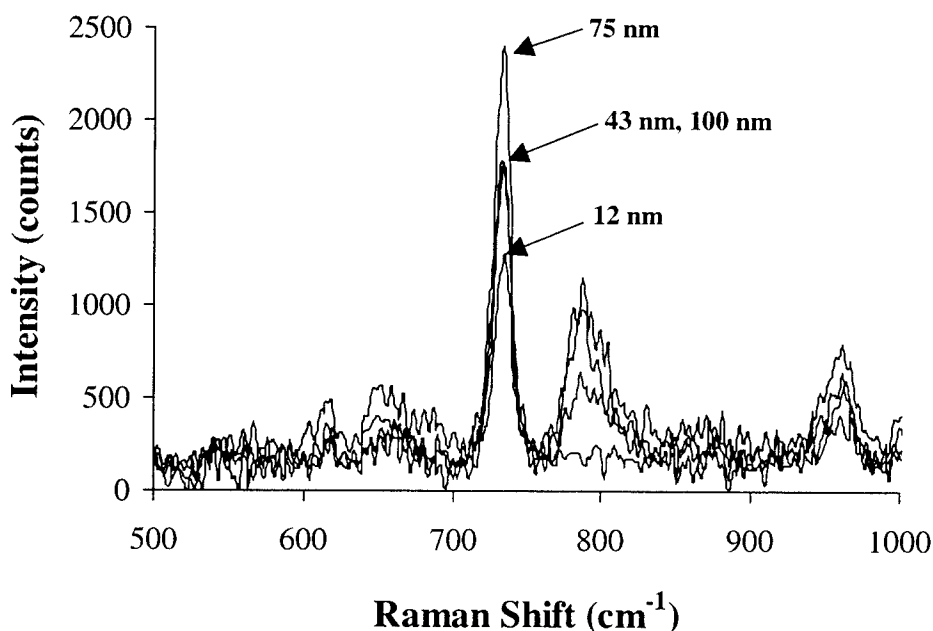
Figure 4. Comparison of surface-enhanced Raman scattering intensities of 43 µM "kinked" DNA on 12, 43, 75, and 100 nm size gold nanoparticles.
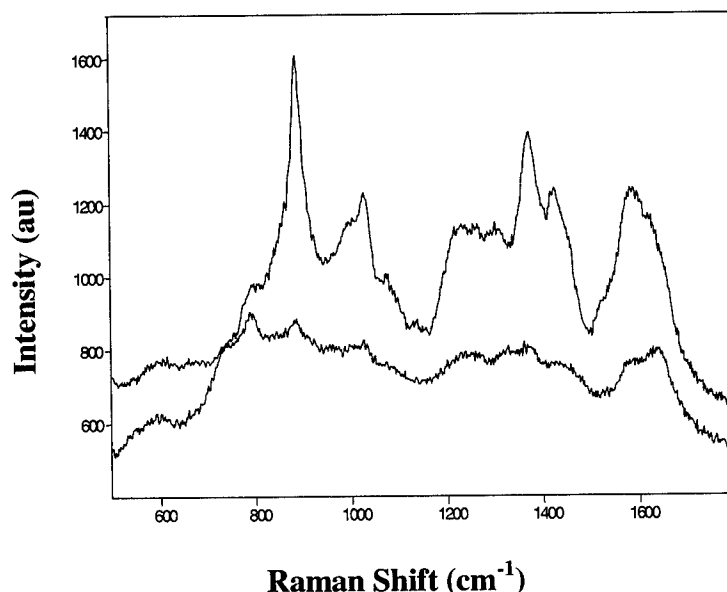
Figure 5. SERS spectra of COOH-dendrimer on gold particles before (top) and after (bottom) addition of 10 mL of 9.1 x 10^{-3} M calf-thymus DNA.

4. CONCLUSIONS

We have employed silver and gold nanoparticles as SERS substrates and CdS nanoparticles as luminescence substrates to study DNA. The luminescence titrations involving CdS and DNA, showed the 'kinked' sequence quenching more of the CdS luminescence than the 'abasic' sequence. The quenching events were interpreted as shape selective binding, where the curvature of the 'kinked' sequence more closely matched the curvature of the CdS nanoparticle compared to the 'abasic' sequence. The SERS spectra of thymine dinucleotides showed that new bands were present for the photoproducts of the dinucleotide. Our results show great promise and seem to confirm that silver nanoparticles used in conjunction with SERS is a viable method to detect anomalous DNA structures (DNA lesions) associated with disease. Though much work still needs to be accomplished in this area this method could prove to be an expedient and more direct alternative to existing techniques. A definite substrate-size dependence was observed for SERS of 'kinked' DNA on gold nanoparticles. Gold particles with 75 nm average diameter showed greatest enhancement but worst reproducibility of the different size gold particles tested.

AKNOWLEDGEMENTS

REFERENCES

1. Mahtab, R.; Rogers, J. P.; Murphy, C. J. "Protein-sized quantum-dot luminescence can distinguish between straight, bent, and kinked oligonucleotides" *J. Am. Chem. Soc.* **117**, 9099-9100, 1995.

2. Mahtab, R.; Rogers, J. P.; Singleton, C. P.; Murphy, C. J. "Preferential adsorption of a "kinked" DNA to a neutral curved surface: Comparisons to and implications for nonspecific DNA- protein interactions" *J. Am. Chem. Soc.* **118**, 7028-7032, 1996.

3. Mahtab, R.; Harden, H. H.; Murphy, C. J. "Temperature- and salt-dependent binding of long DNA to protein- sized quantum dots: Thermodynamics of "inorganic protein"-DNA interactions" *J. Am. Chem. Soc.* **122**, 14-17, 2000.

4. Murphy, C. J.; Brauns, E. B.; Gearheart, L. "Quantum dots as inorganic DNA-binding proteins" *Mat. Res. Soc. Synp. Proc.* **452**, 597-600, 1997.

5. Nabiev, I. R.; Sokolov, K. V.; Voloshin, O. N. "Surface-enhanced Raman-spectroscopy of biomolecules .3. Determination of the local destabilization regions in the double helix" *J. Raman Spectrosc.* **21**, 333-336, 1990.

6. Kneipp, K.; Pohle, W.; Fabian, H. "Surface-enhanced Raman spectroscopy on nucleic acids and related compounds adsorbed on colloidal silver particles" *J. Mol. Struct.* **244**, 183-192, 1991.

7. Kneipp, K.; Kneipp, H.; Kartha, V. B.; Manoharan, R.; Deinum, G.; Itzkan, I.; Dasari, R. R.; Feld, M. S. "Detection and identification of a single DNA base molecule using surface-enhanced Raman scattering (SERS)" *Phys. Rev. E* **57**, R6281-R6284, 1998.

8. Mirkin, C. A.; Letsinger, R. L.; Mucic, R. C.; Storhoff, J. J. "A DNA-based method for rationally assembling nanoparticles into macroscopic materials" *Nature* **382**, 607-609, 1996.

9. Storhoff, J. J.; Elghanian, R.; Mucic, R. C.; Mirkin, C. A.; Letsinger, R. L. "One-pot colorimetric differentiation of polynucleotides with single base imperfections using gold nanoparticle probes" *J. Am. Chem. Soc.* **120**, 1959-1964, 1998.

10. Taylor, J. R.; Fang, M. M.; Nie, S. M. "Probing specific sequences on single DNA molecules with bioconjugated fluorescent nanoparticles" *Anal. Chem.* **72**, 1979-1986, 2000.

11. Taton, T. A.; Mirkin, C. A.; Letsinger, R. L. "Scanometric DNA array detection with nanoparticle probes" *Science* **289**, 1757-1760, 2000.

12. Vo-Dinh, T.; Stokes, D. L.; Griffin, G. D.; Volkan, M.; Kim, U. J.; Simon, M. I. "Surface-enhanced Raman scattering (SERS) method and instrumentation for genomics and biomedical analysis" *J. Raman Spectrosc.* **30**, 785-793, 1999.

13. Gearheart, L.; Caswell, K. K.; Murphy, C. J. "Recognition of hypermethylated triplet repeats in vitro by cationic nanoparticles" *J. Biomed. Optics* 2000.

14. Schneider, S.; Halbig, P.; Grau, H.; Nickel, U. "Reproducible Preparation of Silver Sols with Uniform Particle Size for Application in Surface-Enhanced Raman Spectroscopy" *Photochem. Photobiol.* **60**, 605-610, 1994.

15. Frens, G. "Controlled nucleation for the regulation of te particle size in mondisperse gold suspensions" *Nature* **241**, 20-22, 1973.

16. Ayadi, L.; Coulombeau, C.; Lavery, R. "Abasic sites in duplex DNA: Molecular modeling of sequence- dependent effects on conformation" *Biophys. J.* **77**, 3218-3226, 1999.

17. Rossi, O.; Carrozzino, F.; Cappelli, E.; Carli, F.; Frosina, G. "Analysis of repair of abasic sites in early onset breast cancer patients" *Int. J. Cancer* **85**, 21-26, 2000.

18. Belmont, P.; Alarcon, K.; Demeunynck, M.; Lhomme, J. "Synthesis of an imidazo[1,2-e]purine-acridine heterodimer for targeting abasic sites in DNA" *Bioorg. Med. Chem. Lett.* **9**, 233-236, 1999.

19. Pinz, K. G.; Bogenhagen, D. F. "Efficient repair of abasic sites in DNA by mitochondrial enzymes" *Mol. Cell. Biol.* **18**, 1257-1265, 1998.

20. Ayadi, L.; Coulombeau, C. "Molecular modeling study of an abasic DNA undecamer duplex: d(GCGTGOGTGCG)center dot d(CGCACTCACGC)" *Theor. Chem. Acc.* **101**, 121-125, 1999.

21. Lindahl, T. "Instability and Decay of the Primary Structure of Dna" *Nature* **362**, 709-715, 1993.

22. Boturyn, D.; Constant, J. F.; Defrancq, E.; Lhomme, J.; Barbin, A.; Wild, C. P. "A simple and sensitive method for in vitro quantitation of abasic sites in DNA" *Chem. Res. Toxicol.* **12**, 476-482, 1999.

23. Lhomme, J.; Constant, J. F.; Demeunynck, M. "Abasic DNA structure, reactivity, and recognition" *Biopolymers* **52**, 65-83, 1999.

24. Murphy, C. J.; Mahtab, R. "Detection of unusual DNA structures with nanoparticles" *Proc. SPIE* **3924**, 10-16, 2000.

25. Dannhauser, T.; O'Neil, M.; Johansson, K.; Whitten, D.; McLendon, G. "Photophysics of Quantized Colloidal Semiconductors: Dramatice Luminescence Enhancement by Binding of Simple Amines" *J. Phys. Chem.* **90**, 6074, 1986.

26. Spanhel, L.; Haase, M.; Weller, H.; Henglein, A. "Photochemistry of colloidal semiconductors .20. Surface modification and stability of strong luminescing CdS particles" *J. Am. Chem. Soc.* **109**, 5649-5655, 1987.

27. Lisensky, G. C.; Penn, R. L.; Murphy, C. J.; Ellis, A. B. "Electrooptical evidence for the chelate effect at semiconductor surfaces" *Science* **248**, 840-843, 1990.

28. Bigham, S. R.; Coffer, J. L. "Deactivation of Q-CdS photoluminescence through polynucleotide surface binding" *J. Phys. Chem.* **96**, 10581-10584, 1992.

29. Mills, J. B.; Cooper, J. P.; Hagerman, P. J. "Electrophoretic evidence that single-stranded regions of one or more nucleotides dramatically increase the flexibility of DNA" *Biochemistry* **33**, 1797-1803, 1994.

30. Marathias, V. M.; Jerkovic, B.; Bolton, P. H. "Damage increases the flexibility of duplex DNA" *Nucleic Acids Res.* **27**, 1854-1858, 1999.

31. Simha, R.; Frish, H. L.; Eirich, R. R. "The adsorption of flexible macromolecules" *J. Phys. Chem.* **57**, 584, 1953.

32. Goodsell, D. S.; Kopka, M. L.; Cascio, D.; Dickerson, R. E. "Crystal structure of CATGGCCATG and its implications for A-tract bending models" *Proc. Natl. Acad. Sci. USA* **90**, 2930-2934, 1993.

33. Wildeson, J.; Murphy, C. J. "Intrinsic bending in GGCC tracts as probed by fluorescence resonance energy transfer" *Anal. Biochem.* **284**, 99-106, 2000.

34. Erie, D. A.; Yang, G. L.; Schultz, H. C.; Bustamante, C. "Dna Bending By Cro Protein in Specific and Nonspecific Complexes - Implications For Protein Site Recognition and Specificity" *Science* **266**, 1562-1566, 1994.

35. Perdiz, D.; Grof, P.; Mezzina, M.; Nikaido, O.; Moustacchi, E.; Sage, E. "Distribution and repair of bipyrimidine photoproducts in solar UV-irradiated mammalian cells - Possible role of Dewar photoproducts in solar mutagenesis" *J. Biol. Chem.* **275**, 26732-26742, 2000.

36. Goukassian, D.; Gad, F.; Yaar, M.; Eller, M. S.; Nehal, U. S.; Gilchrest, B. A. "Mechanisms and implications of the age-associated decrease in DNA repair capacity" *Faseb J.* **14**, 1325-1334, 2000.

37. Stege, H.; Roza, L.; Vink, A. A.; Grewe, M.; Ruzicka, T.; Grether-Beck, S.; Krutmann, J. "Enzyme plus light therapy to repair DNA damage in ultraviolet- B-irradiated human skin" *Proc. Natl. Acad. Sci. USA* **97**, 1790-1795, 2000.

38. Ensch-Simon, I.; Burgers, P. M. J.; Taylor, J. S. "Bypass of a site-specific cis-syn thymine dimer in an SV40 vector during in vitro replication by HeLa and XPV cell-free extracts" *Biochemistry* **37**, 8218-8226, 1998.

39. Clingen, P. H.; Arlett, C. F.; Cole, J.; Waugh, A. P. W.; Lowe, J. E.; Harcourt, S. A.; Hermanova, N.; Roza, L.; Mori, T.; Nikaido, O.; Green, M. H. L. "Correlation of UVC and UVB cytotoxicity with the induction of specific photoproducts in t-lymphocytes and fibroblasts from normal human donors" *Photochem. Photobiol.* **61**, 163-170, 1995.

40. Husain, I.; Griffith, J.; Sancar, A. "Thymine dimers bend DNA" *Proc. Natl. Acad. Sci. USA* **85**, 2558-2562, 1988.

41. Hurks, H. P. H.; Out-Luiting, C.; Vermeer, B.; Claas, F. H. H.; Mommaas, A. M. "In situr action spectra suggest that DNA damage is involved in ultraviolet radiation-induced immunosuppression in humans" *Photochem. Photobiol.* **66**, 76-81, 1997.

42. Brash, D. E.; Rudolph, J. A.; Simon, J. A.; Lin, A.; McKenna, G. J.; Baden, H. P.; Halperin, A. J.; Ponten, J. "A role For sunlight in skin-cancer - UV-induced P53 mutations in squamous-cell carcinoma" *Proc. Natl. Acad. Sci. USA* **88**, 10124-10128, 1991.

43. Hurks, H. M. H.; Outluiting, C.; Vermeer, B. J.; Class, F. H. J.; Mommaas, A. M. "The action spectra for UV-induced suppression of Mlr and Meclr show that immunosuppression is mediated by DNA-damage" *Photochem. Photobiol.* **62**, 449-453, 1995.

44. Freeman, S. E.; Hacham, H.; Gange, R. W.; Maytum, D. J.; Sutherland, J. C.; Sutherland, B. M. "Wavelength dependence of pyrimidine dimer formation in DNA of human-skinirradiated *in situ* with ultraviolet-light" *Proc. Natl. Acad. Sci. USA* **86**, 5605-5609, 1989.

45. Palmer, C. M.; Serafini, D. M.; Schellhorn, H. E. "Near ultraviolet radiation (UVA and UVB) causes a formamidopyrimidine glycosylase-dependent increase in G to T transversions" *Photochem. Photobiol.* **65**, 543-549, 1997.

46. Rockx, D. A. P.; Mason, R.; van Hoffen, A.; Barton, M. C.; Citterio, E.; Bregman, D. B.; van Zeeland, A. A.; Vrieling, H.; Mullenders, L. H. F. "UV-induced inhibition of transcription involves repression of transcription initiation and phosphorylation of RNA polymerase II" *Proc. Natl. Acad. Sci. USA* **97**, 10503-10508, 2000.

47. Nichols, A. F.; Itoh, T.; Graham, J. A.; Liu, W.; Yamaizumi, M.; Linn, S. "Human damage-specific DNA-binding protein p48 - Characterization of XPE mutations and regulation following UV irradiation" *J. Biol. Chem.* **275**, 21422-21428, 2000.

48. Kubitschek, H. E.; Hacham, H.; Gange, R. W.; Maytum, D. J.; Sutherland, J. C.; Sutherland, B. M. "Wavelength dependence of pyrimidine dimer formation in DNA of human skin irradiated in situ with ultraviolet light" *Photochem. Photobiol.* **43**, 443-447, 1986.

49. Dandliker, P. J.; Holmlin, R. E.; Barton, J. K. "Oxidative thymine dimer repair in the DNA helix" *Science* **275**, 1465-1468, 1997.

50. Koglin, E.; Sequaris, J.-M.; Valenta, P. "Surface enhanced Raman spectrosocpy of nucleic acid bases on Ag electrodes" *J. Mol. Struct.* **79**, 185-189, 1982.

51. Otto, C.; van den Tweel, T. J. J.; de Mul, F. F. M.; Greve, J. "Surface-enhanaced Raman spectroscopy of DNA bases" *J. Raman Spectrosc.* **17**, 289-298, 1986.

52. Thornton, J.; Force, R. K. "Surface-Enhanced Raman-Spectroscopy of Nucleic-Acid Compounds and Their Mixtures" *Appl. Spectrosc.* **45**, 1522-1526, 1991.

53. Aroca, R.; Bujalski, R. "Surface enhanced vibrational spectra of thymine" *Vib. Spectosc.* **19**, 11-21, 1999.

54. Emory, S. R.; Nie, S. "Screening and enrichment of metal nanoparticles with novel optical properties" *J. Phys. Chem. B* **102**, 493-497, 1998.

55. Nie, S. M.; Emory, S. R. "Probing single molecules and single nanoparticles by surface- enhanced Raman scattering" *Science* **275**, 1102-1106, 1997.

56. Krug, J. T.; Wang, G. D.; Emory, S. R.; Nie, S. M. "Efficient Raman enhancement and intermittent light emission observed in single gold nanocrystals" *J. Am. Chem. Soc.* **121**, 9208-9214, 1999.

57. Michaels, A. M.; Nirmal, J.; Brus, L. E. "Surface enhanced Raman spectroscopy of individual rhodamine 6G molecules on large Ag nanocrystals" *J. Am. Chem. Soc.* **121**, 9932-9939, 1999.

58. Moyer, P. J.; Schmidt, J.; Lukas M. Eng; Meixner, A. "Surface-enhanced Raman scattering spectrocopy of single carbon domains on individual Ag nanoparticles on a 25 ms time scale" *J. Am. Chem. Soc.* **122**, 5409-5410, 2000.

59. Freeman, R. G.; Bright, R. M.; Hommer, M. B.; Natan, M. J. "Size selection of colloidal gold aggregates by filtration: Effect on surface-enhanced Raman scattering intensities" *J. Raman Spectrosc.* **30**, 733-738, 1999.

60. Brown, K. R.; Walter, D. G.; Natan, M. J. "Seeding of colloidal Au nanoparticle solutions. 2. Improved control of particle size and shape" *Chem. Mater.* **12**, 306-313, 2000.

61. Lecomte, S.; Baron, M. H. "Surface-enhanced Raman spectroscopy investigation of fluoroquinolones-DNA-DNA gyrase-Mg^{2+} interactions .2. Interaction of pefloxacin with Mg^{2+} and DNA" *Biospectroscopy* **3**, 31-45, 1997.

Interparticle coupling effects in surface-enhanced Raman scattering

Hongxing Xu, Erik J. Bjerneld, Javier Aizpurua, Peter Apell, Linda Gunnarsson, Sarunas Petronis, Bengt Kasemo, Charlotte Larsson, Fredrik Höök, and Mikael Käll*

Dep. of Applied Physics, Chalmers Univ. of Technology, S-412 96 Göteborg, Sweden

ABSTRACT

We report experimental and theoretical results on the effect of electromagnetic coupling between metal particles in surface-enhanced Raman scattering (SERS). Model calculations of the near-field optical properties of Ag and Au nanoparticle-aggregates show that the electromagnetic surface-enhancement factor can reach 11 orders-of-magnitude in gaps between nearly touching particles. Single particles exhibit a much weaker enhancement, unless the particles contain extremely sharp surface protrusions. Data on spectral fluctuations in single-molecule SERS and measurements on the efficiency of nanofabricated SERS substrates give experimental support for the idea that an efficient interparticle coupling is a necessary requirement for an ultra-high surface-enhancement. We suggest a route for biorecognition induced coupling of metal particles for use in biosensing applications.

- nanoparticles, surface-enhanced Raman scattering, Mie theory, biosensors

1. INTRODUCTION

The spectacular optical effects associated with systems of metallic nanoparticles have fascinated scientists and laymen alike for centuries [1]. These properties are due to collective electron-photon resonances (surface plasmon polaritons) in the confined geometry defined by the size and shape of the nanoparticle. The optical properties thus vary with particle morphology, as well as with the dielectric properties of the particle itself and the medium immediately surrounding it. If several particles are close together, the single-particle resonances couple and the optical properties change. A prototypical example of a far-field interparticle coupling effect is the color change of a gold hydrosol upon aggregation, a phenomenon that has been used e.g. for the recent realization of an ultrasensitive polynucleotide optical detection method [2].

Surface-enhanced spectroscopies, such as surface-enhanced Raman scattering (SERS), rely on the near-field optical properties of metal nanoparticles or nanostructures, in particular on the increase in the electromagnetic field strength that occurs close to the metal particle surface when a collective resonance is excited. It is well known that aggregation effects can increase the SERS efficiency of colloidal nanoparticle systems substantially, indicating the importance of interparticle coupling effects for the surface-enhancement [3,4]. However, recent SERS reports on enormous enhancement-factors (14-15 orders-of-magnitude) and single-molecule detection efficiency [5] have caused a renewed interest into the basic mechanisms and requirements of SERS. This presentation, which is based on ref. [6-11], summarizes some of our work on SERS with a focus on electromagnetic coupling between metal particles.

2. MODELLING INTERPARTICLE COUPLING EFFECTS IN SERS

Consider an electromagnetic field E_0 interacting with a small metal sphere of radius a and complex dielectric function $\varepsilon(\omega) = \varepsilon_1(\omega) + i\varepsilon_2(\omega)$ embedded in a uniform medium of dielectric constant ε_m. In the Rayleigh size-regime ($a \ll \lambda$), we can treat the incident field as a plane wave. The induced dipole moment P in the sphere will be directed along the incident polarization vector and have a magnitude:

$$P = \varepsilon_m \alpha E_0 = 4\pi\varepsilon_0\varepsilon_m \frac{\varepsilon - \varepsilon_m}{\varepsilon + 2\varepsilon_m} a^3 E_0 \tag{1}$$

A surface-plasmon resonance occurs when $\varepsilon + 2\varepsilon_m = 0$, which for the case of Ag in air happens at a wavelength of around 380 nm ($\varepsilon \approx -2 + i0.2$). The local field at a distance r from the center of the sphere, in a direction parallel to the incident polarization, will be a sum of the incident field and the induced field from the dipole: $E_{loc} = E_0 + P/2\pi\varepsilon_0 r^3$. A molecule positioned at r will thus experience a "driving" field E_{loc} that is higher than the original field E_0, especially when the incident wavelength coincides with the surface-plasmon resonance. Similarly, a Raman scattered field, emitted by the molecule at r, can reach a detector either directly or via elastic scattering off the metal sphere. These two effects combined constitute the essence of the "classical" electromagnetic theory of SERS. Furthermore, if a complete "symmetry" between the excitation and the emission channel in the Raman scattering process is assumed, the net effect of the presence of the sphere will be an enhancement of the apparent Raman scattering cross-section by a factor:

$$M = \left[\frac{|E_{loc}(\omega_L)|}{|E_0(\omega_L)|}\right]^2 \left[\frac{|E_{loc}(\omega_L - \omega_v)|}{|E_0(\omega_L - \omega_v)|}\right]^2 \tag{2}$$

where ω_L is the incident (laser) frequency and ω_v is a vibrational frequency of the molecule. The assumptions behind eq. 2, which have been discussed in detail in [3,4], include for example a completely isotropic molecular polarizability tensor. Eq. 2 thus gives an estimated upper limit for the "classical" surface-enhancement. This limit should be the relevant quantity for models of electromagnetic contributions to single-molecule sensitivity in SERS, as outlined in [6]. Note that if the vibrational frequency is assumed much smaller than the laser frequency, then the enhancement factor scales as the *fourth power* of the local field. It is also interesting to note that the enhancement factor for surface-enhanced *fluorescence* is similar to eq. 2, but with the second part replaced by a factor that for example takes into account non-radiative energy transfer to the metal sphere (i.e. fluorescence quenching) [12].
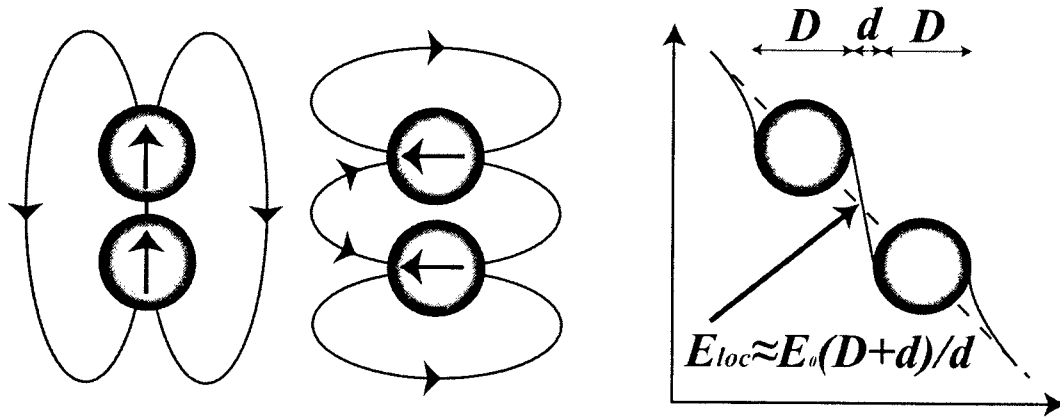

Figure 1: Illustration of electromagnetic coupling between metal particles. An electromagnetic field that interacts with a two-particle system induces two in-phase dipole-moments that reinforce each other if the field is polarized parallel to the main symmetry axis (left) or weaken each other in the perpendicular polarization configuration (center). The coupled-particle surface-plasmon resonances corresponding to these two cases will be red-shifted and blue-shifted, respectively, compared to the single-particle resonance. The figure to the right illustrates the increase of the local field in the interparticle region that occurs for the parallel polarization configuration. Two perfectly conducting particles of diameter D are situated in an electrostatic field of strength E_0. The electrostatic potential drop will be concentrated to the interparticle region of length d, leading to a large increase in the local field for $D/d \gg 1$.

If we now have an "aggregate" of two spheres of radii a_i and a_j separated by a surface-to-surface gap d, an electric field will induce two *in-phase* dipoles oriented along the incident polarization. The induced dipole moment of sphere i in the presence of sphere j now becomes:

$$P_i^* = P_i \frac{1 + c\alpha_j}{1 - c^2 \alpha_i \alpha_j}, \qquad i,j = 1,2, \qquad c = \gamma \Big/ 4\pi\varepsilon_0 (d + a_1 + a_2)^3 \tag{3}$$

where $\alpha_{i,j}$ and $P_{i,j}$ refer to the isolated spheres (eq.1), and $\gamma = -1, 2$ for the perpendicular / parallel polarization configurations shown schematically in Fig.1. The resonance positions of the two modes, determined by $1 - c^2 \alpha_i \alpha_j = 0$, will be blue-shifted and red-shifted, respectively, compared to the single sphere resonances. From Fig. 1 we see that, depending on the angle between the polarization and the "dimer-axis", the two dipoles will either strengthen or weaken each-other. Specifically, the induced field *between* the spheres will be dramatically enhanced in the longitudinal polarization configuration. We can make a rough estimate of this effect through a simple electrostatic model, as shown in the right part of Fig. 1. Imagine two particles of diameter D separated by a distance d and arranged with the "dimer-axis" parallel to a uniform electrostatic field E_0. If the particles are perfectly conducting, the electrostatic potential drop will be concentrated to the interparticle region, resulting in a local field $E_{loc} = E_0 (D + d)/d$ obtained from simple geometrical considerations. A molecule situated between the particles thus experiences a SERS enhancement-factor of the order $M = (D/d + 1)^4$, which in general is much higher than what is obtained for a single particle. The simple electrostatic picture can also be used to estimate the *volume* that is affected by the interparticle coupling. For spherical particles one obtains $V \propto d^2 D$, which for small separation distances can be of nanometric dimensions [6].

The simplistic discussion above illustrates the main effects of interparticle coupling in SERS, namely a shift in plasmon resonance positions and a polarization dependent increase of the enhancement factor in a highly localized region between particles. However, in order to make quantitative predictions it is necessary to perform more advanced calculations. We have utilized Generalized Mie Theory following the calculational procedure described by Inoue and Ohtaka [13] for the case of spherical particles. GMT yields an essentially exact solution to Maxwell's equations for the chosen configuration, including retardation effects and contributions from multipolar resonances. The importance of going beyond the dipole approximation in the case of strongly interacting particles is illustrated in Fig.2. The method allows us to calculate e.g SERS excitation profiles, based on eq. 2, and extinction spectra for linear aggregates of spherical particles of arbitrary sizes and composition and with spherical surface layers of arbitrary thickness and refractive index. A simple example is given in Fig. 3, which shows the variation in the SERS enhancement factor with interparticle separation distance for a system of two interacting Ag spheres in air. The most surprising result in Fig. 3 is perhaps that the simple electrostatic model $M = (D/d + 1)^4$ gives an excellent *quantitative* estimate of the interparticle coupling effect. We refer the reader to ref. [6] for further details and calculations, including wavelength dependencies.
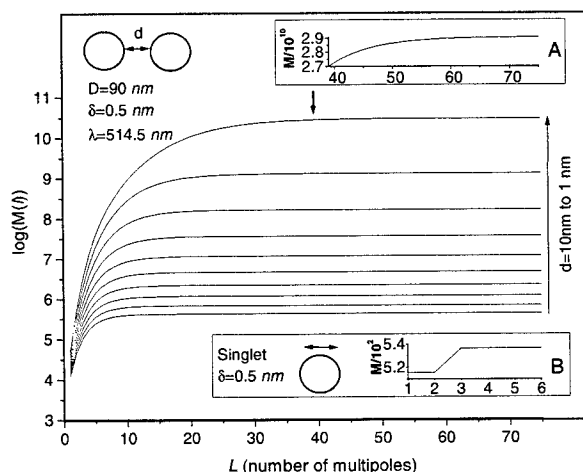
Figure 2: Illustration of multipolar effects in SERS. The figure shows the calculated SERS enhancement-factor, approximated as $M = |E_{loc}/E_0|^4$, for two Ag spheres of diameter $D = 90$ nm separated by a gap d as a function of the number of multipolar terms L that are included in the calculation. The calculations have been performed for the parallel polarization configuration at $\lambda = 514.5$ nm and at a gap-position δ located 0.5 nm outside one of the surfaces along the dimer axis. As shown in inset A, more than 50 multipolar terms are needed for convergence at the smallest interparticle distance. In contrast, the dipole approximation ($L=1$) gives a good estimate of the enhancement-factor outside an isolated particle, as shown in inset B.

The most serious drawback of the GMT is probably the restriction to spherical particle shapes. The colloidal metal particles used in SERS are actually small crystallites with well-defined facets, as shown in Fig.4. The question is then to what extent sharp edges, surface protrusions etc. affect the near-field optical properties. We analyzed a few non-spherical shapes by the Boundary Charge Method (BMT), excluding retardation effects [6]. An example is given in Fig. 4, which shows the variation in the SERS enhancement-factor in a cross-section through a system of two rotationally symmetric polygons with edge-angles similar to what is observed experimentally. The conclusion from these investigations was that the estimated enhancement-factors for fairly open-angled "crystallite-shaped" particle-dimers did not differ substantially from the spherical case. Both the GMT and the BMT calculations predicted maximum enhancement-factors of the order 10^{11} in narrow gaps between particles, for the right choice of wavelength, polarization and particle size. Only in the case of very sharp surface protrusions did we find a similar level of enhancement for single isolated particles. These results indicate that interparticle coupling gives the dominant contribution to single-molecule sensitivity in SERS.
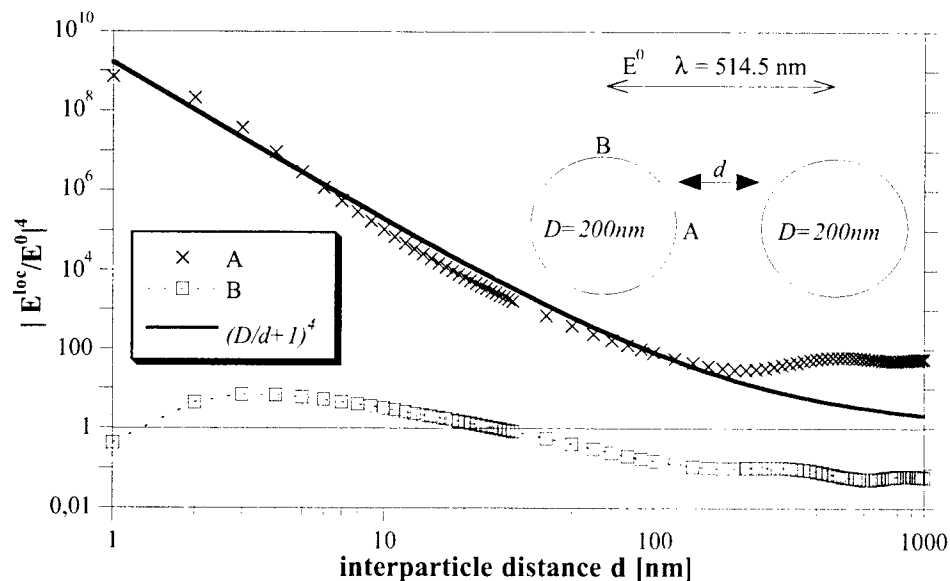
Figure 3: Calculated SERS enhancement-factor for a Ag dimer system in the parallel polarization configuration as a function of interparticle separation d. The calculations have been performed for two positions, A and B, located 0.5 nm from the surface of one of the spheres and at λ = 514.5 nm. The electrostatic model of interparticle coupling illustrated in Fig.1 can quantitatively explain the dramatic increase in enhancement that occurs when $D/d > 1$. Note that the enhancement at the off axis position B is almost always below unity (i.e. no enhancement).
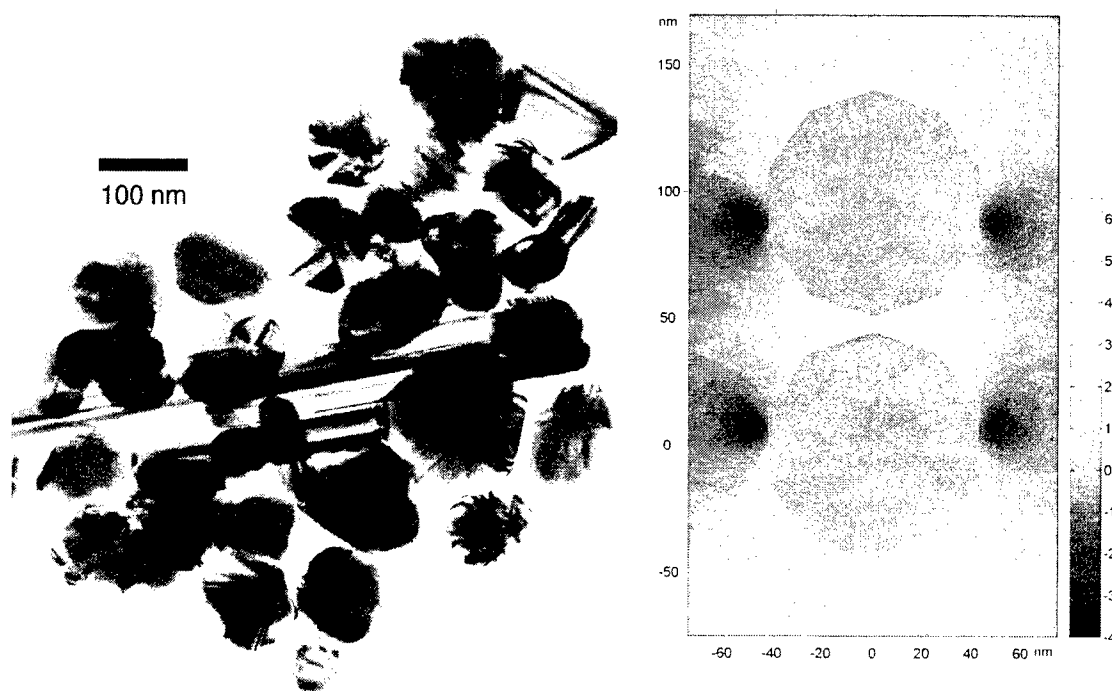
Figure 4: Transmission electron microscopy image of Ag nano-particles (left). This type of particles is found to be efficient substrates for single-molecule SERS [9,10]. Note the heterogeneous distribution of non-spherical shapes. The figure to the right shows the spatial variation of the SERS enhancement-factor in a plane through two interacting rotationally symmetric polygons of largest dimension 90 nm. The interparticle separation is 5.5 nm. The grey-scale gives M in orders-of-magnitude on a logarithmic scale. Note the region of high enhancement in the inter-particle region (adapted from ref. [6]).

3. EXPERIMENTAL RESULTS

3.1 Interparticle coupling effects in nanostructured SERS substrates

As noted in the introduction, a large body of experimental results point towards the importance of interparticle coupling effects in SERS. However, for "traditional" SERS systems, such as metal colloids or roughened electrodes, it is very difficult to actually control the degree electromagnetic coupling, as this would imply a tuning of e.g. interparticle separations. This section describes an effort to achieve such control through nanofabrication [7,8].

The technique utilized here is based on electron-beam lithography in conjunction with the so-called lift-off procedure. A resist is spin-coated on an oxidized Si wafer and an electron beam draws the predefined pattern. A developer then removes the exposed resist and a thin metal layer is vapor-deposited on top of the surface. The metal that covers unexposed resist is removed in a suitable solvent ("lift-off"). The manufacturing process is described in greater detail in [8]. The technique allows us to produce uniform arrays of 30-50 nm thick Ag or Au particles in various shapes and with lateral dimensions D down to ~100 nm. The interparticle separation d can be varied *independently* of other parameters down to $d \approx 30$ nm. Fig. 5 shows some examples of the patterns produced.

The efficiencies of the SERS substrates were evaluated by adsorbing a probe-molecule on a sample consisting of a set of 100 μm^2 arrays with different morphology (D, shape) and interparticle separation. The different arrays were then investigated in succession in a notch-filter based single-grating Raman spectrometer equipped with NA=0.95 microscope optics and a CCD detector. All measurements were performed in the back-scattering configuration using the 514.5 nm Ar$^+$-line for excitation. The incident power ranged between 0.2 and 1 mW and the probe-area was 1-2 μm in diameter.

The plot in Fig. 5 shows results obtained for tiophenol adsorbed to arrays of $D = 200$ nm wide square-shaped Ag-particles. It is clear that the relative SERS intensity increases strongly for interparticle separations d below ~100 nm. We analyzed the data with the function:

$$I^{SERS} \propto \frac{A(D/d+1)^4 + B}{(d+D)^2} \qquad (4)$$

where A and B are fitting constants determining the contributions from molecules adsorbed to the particle edges and to the upper particle surfaces, respectively. The former contribution is assumed to vary with particle separation according to the electrostatic model described previously, while the latter is assumed independent of d. These assumptions are motivated by the calculations for spherical particles shown in Fig. 3. The denominator in eq. 4 takes into account the fact that the number of molecules within the probe area varies with d, as tiophenol adsorbs specifically to Ag and not to the Si surface. The best fit to the data set in Fig. 5 is achieved for $B = 0$, indicating a *dominant* interparticle coupling contribution to the overall SERS efficiency in this case. This result illustrates the potential of nanofabrication as a route for controlling and optimizing electromagnetic surface-enhancement effects in optical spectroscopy.
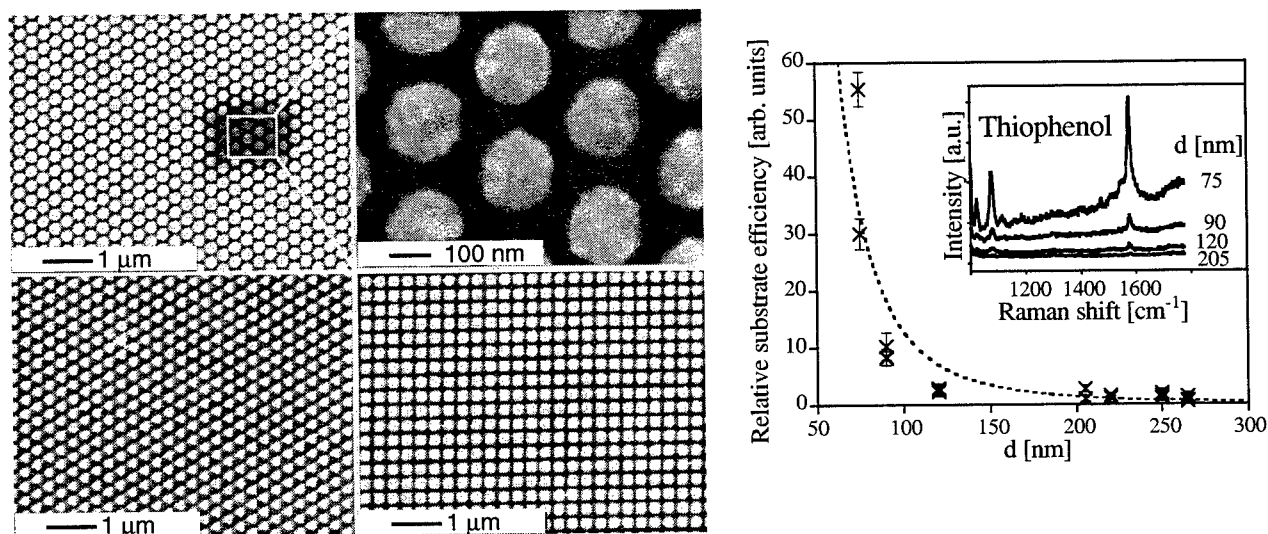
Figure 5: Interparticle coupling effects in SERS substrates prepared by electron-beam lithography (reproduced from ref. [7]) Figure to the left shows scanning electron microscopy images of SERS-substrates consisting of circular, triangular and square 30 nm thin Ag particles on Si. Figure to the right shows the relative SERS-substrate efficiency versus edge-to-edge distance d, quantified as $I^{SERS}(d)/I^{SERS}(d_{max})$, for tiophenol adsorbed to a substrate of square particles of width $D = 200$ nm. Inset shows examples of SERS spectra for different d-values. The dashed line is a single-parameter fit to eq. 4.

3.2 Single-molecule fluctuations as a probe of "hot sites" in SERS

Following the reports by Nie and Emory [14] and Kneipp et al. [15], there has been an increasing interest in SERS as a method for single-molecule detection and spectroscopy. Whereas Kneipp et al. found single-molecule sensitivity for freely diffusing particle clusters in solution, Nie and Emory reported "hot sites" on isolated and immobilized particles. Both groups reported enhancement factors of the order 10^{14}-10^{15}, i.e. at least three orders-of-magnitude higher than the estimated maximum electromagnetic enhancement effect for particle dimers or sharp surface-protrusions [6]. Indications for a dominant interparticle coupling effect in single-molecule SERS came from our study on hemoglobin, for which the "hot sites" corresponded to Ag particle dimers with a size that was close to the calculated optimum dimension at the laser wavelength used [9]. Still, the calculated enhancement factor for the appropriate particle size and separation fell short of the experimental value by about two orders-of-magnitude also in this case. These discrepancies of course raise important questions concerning the origin of single-molecule sensitivity in SERS. This paragraph suggests a somewhat different approach to this problem [10].

The occurrence of spectral fluctuations, i.e. stochastic variations in band positions and intensities, is the perhaps most spectacular "feature" of single-molecule SERS on immobilized particles [9,10]. Although a detailed understanding of this effect is lacking at present, the existence of spectral fluctuations is a strong evidence for extremely localized regions of ultra-high enhancement that effectively block normal ensemble-averaging. An example is given in Fig. 6 A. In this case we have immobilized a monolayer of large Ag-particles ($D \approx 90$ nm) on a substrate and added a *dense* solution of the aromatic amino-acid tyrosine ([Tyr] = 0.1 mM final concentration) in order to occupy as many "hot sites" as possible. Raman measurements were performed with microscope optics as in the previous paragraph. The measurement area ($\Phi \approx 1$-2 μm) thus includes around 100-150 Ag particles. Despite the comparatively large number of particles and the huge number of Tyr molecules present, there are enormous spectral fluctuations indicating a limiting number of "hot sites". In Fig. 6 B, we have repeated the experiment under identical conditions but with *small* $D \approx 30$ nm particles, in which case one expects an order of magnitude more particles within the measurement area. In this case we do *not* observe any spectral fluctuations, indicating a large number of contributing "hot sites". This indicates that the number of probed "hot sites" scale with the average particle size and not with the total Ag area, as would be the case if the "hot sites" were only due to atomic-scale features (e.g. ad-atoms or ion-complexes) or a localized "chemical" enhancement. On the other hand, a mechanism based on electromagnetic enhancement in gaps between particles would predict of the order ~50 and ~500 "hot sites" for the D = 90 nm and D = 30 nm particle layers, respectively, if approximately half of the gaps were oriented parallel to the incident polarization. This difference would then explain the difference in "ensemble averaging efficiency" for the two cases [10].
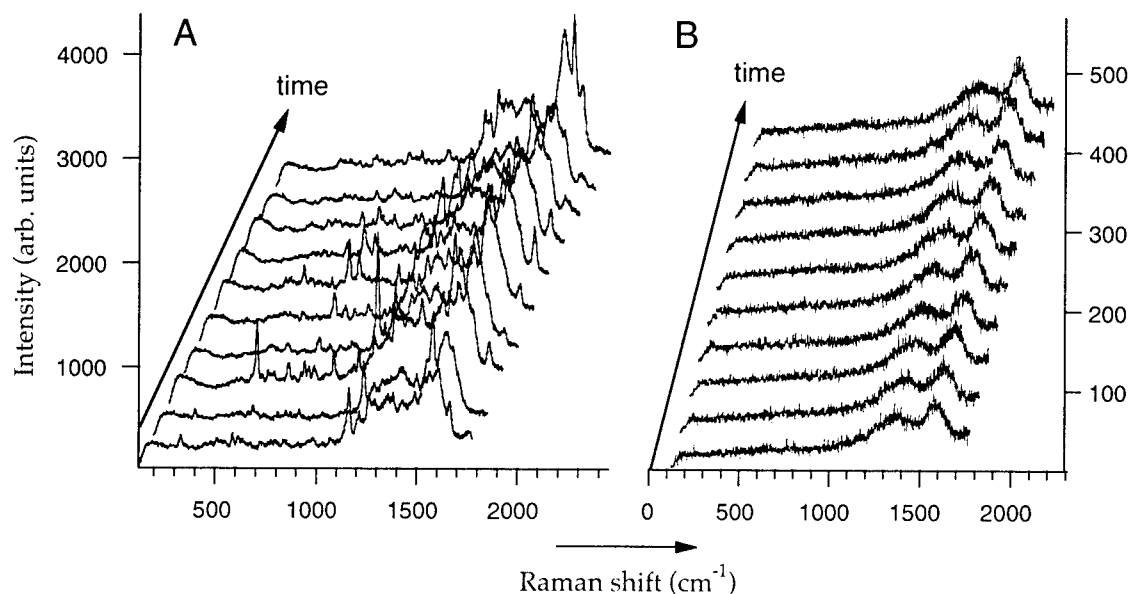
Figure 6: Temporal spectral fluctuations in SERS. **A**: series of consecutive 5-second spectra of tyrosine adsorbed to a layer of 90-nm Ag particles in water. Spectral fluctuations occurred despite the large number of Tyr molecules present in solution (0.1 mM). **B**: same as in A, but for a layer of 30-nm Ag particles. No fluctuations are observed in this case. Except for the particle size, all experimental parameters were the same in the two experiments (laser-power: 2.5 μW, laser spot-size: 1-2 μm, λ = 514.5 nm). Data adapted from ref. [10].

3.3 Biorecognition induced coupling between metal nanoparticles

In the previous paragraphs, we have presented some theoretical and experimental evidence that indicate that electromagnetic coupling between metal particles is a key-factor in SERS. In colloidal nanoparticle systems, interparticle coupling is achieved through aggregation. This can be induced by disturbing the stability of the colloid, e.g. by adding salt [15] or by adding the probe molecule itself [9]. However, this method is usually too unspecific for analytical purposes. Instead it would be desirable with a highly stable colloid, in which aggregation is induced only by a specific target molecule. This paragraph gives a preliminary account of a method for stabilizing colloidal metal particles and enabling biorecognition-induced coupling through self assembled coating with phospholipids [11].

The main reason for producing lipid-coated nanoparticles is that such a coating would mimic the natural surface properties of living cells, with potential to improve the colloidal stability, and at the same time decrease the influence of the metal surface on the integrity and function of immobilized bio(macro)molecules. It is for example well known that lipid coatings of planar surfaces allow controlled attachment of both transmembrane and water-soluble proteins. Moreover, this method is generic in the sense that a large variety of biological functionalization strategies are available for lipids. Since lipid bilayers do not form spontaneously on neither Au nor Ag, we transferred the procedure to create phosphatidylcholine (PC) lipid monolayers on hydrophobic surfaces to methyl-terminated thiolated metal particles, as illustrated in Fig. 7. We used gold particles with an average diameter of 25 nm. Specific biorecognition induced coupling was induced by incorporating 5% biotinylated lipids in the PC coating followed by addition of streptavidin. A full account of the preparation protocols will be given in a separate publication [11].

The spectra in Fig. 7 illustrate the far-field optical properties of the colloidal systems. The typical extinction spectrum of the bare Au colloid is dominated by the dipolar surface-plasmon resonance at around 525 nm, giving the solution a clear pinkish color. The lipid coated particles exhibit a slightly red-shifted peak-position, induced partly by the change in refractive index of the surface layer and partly by a weak unspecific aggregation. However, addition of streptavidin causes a much more dramatic color change, from bright pink to turbid purple, occurring in a few seconds. This effect is caused by the biorecognition induced formation of *large* nanoparticle clusters that support a set of plasmon resonance pushed far towards the red side of the original dipolar resonance of the isolated Au nanoparticles. We have not yet investigated the SERS characteristics of the present system, but the extinction spectra in Fig. 7 indicate that the enhancement-factor in the 650-800 nm range should increase dramatically due to streptavidin induced aggregation. This may allow for the production of SERS-based biosensors, possibly with sensitivity down to the single-molecule limit.
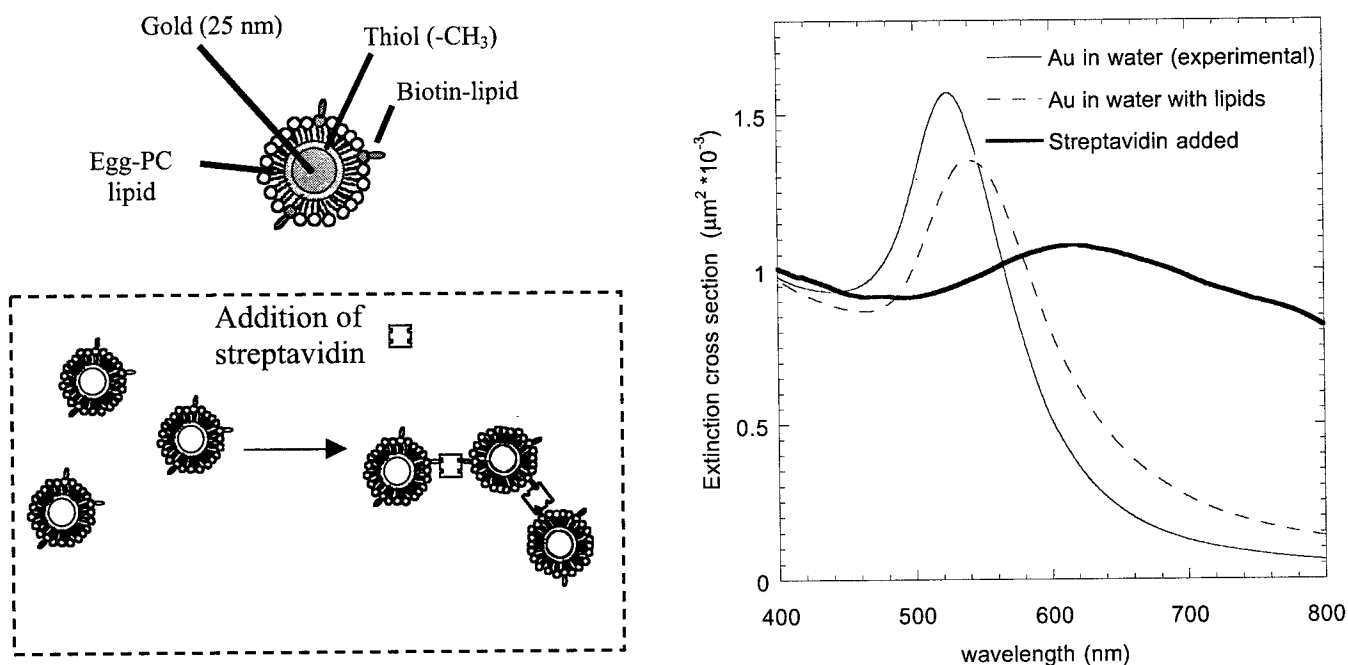
Figure 7: The schematic pictures to the left illustrate the functionalization of Au nanoparticles. The particles are thiolated in order to produce a hydrophobic surface, on which a lipid monolayer can self-assemble. A fraction of the lipids are functionalized by a biotin termination, allowing streptavidin induced aggregation. With slight excess of lipids in the solution, the colloid was sufficiently stable in room temperature for about one week. The figure to the right shows examples of extinction spectra in the visible range. Addition of streptavidin (80 nM final concentration) induces an instant color change from pink to purple.

CONCLUSIONS

Experiments and theory indicate that electromagnetic coupling between metal nanoparticles gives a dominant contribution to the surface-enhanced Raman scattering (SERS) effect, especially in the case of single molecule SERS. Electromagnetic coupling can be achieved in nanofabricated SERS substrates, although the effect is much more efficient in aggregated colloidal systems for which intreparticle distances can be of molecular dimensions. Biorecognition induced coupling of lipid-coated nanoparticles is suggested as a route towards highly efficient SERS-based biosensors.

ACKNOWLEDGEMENTS

REFERENCES

*Corresponding author. E-mail adress: kall@fy.chalmers.se, phone: +46-31-7723119, fax: +46-31-7722090.

[1] U. Kreibig and M. Wollmer, *Optical Properties of Metal Clusters*, Springer Verlag, Berlin 1995.

[2] R. Elghanian, J.J. Storhoff, R.C. Mucic, R.L. Letsinger, and C.A. Mirkin, "Selective colorimetric detection of polynucleotides based on the distance-dependent optical properties of gold nanoparticles", Science **277**, pp. 1078-1081, 1997.

[3] A. Otto, "Surface-enhanced Raman scattering: "classical" and "chemical" origins", in *Light Scattering in Solids IV*, pp. 289-411, edited by M. Cardona and G. Güntherodt, Springer Verlag, Berlin 1984.

[4] M. Moskovits, "Surface-enhanced spectroscopy", Rev. Mod. Phys. **57**, pp. 783-826, 1985.

[5] K. Kneipp, H. Kneipp, I. Itzkan, R.R. Dasari, and M.S. Feld, "Ultransensitive chemical analysis by Raman spectroscopy", Chem. Rev. **99**, pp. 2957-2975, 1999.

[6] H. Xu, J. Aizpurua, M. Käll, and P. Apell, "Electromagnetic contributions to single-molecule sensitivity in surface-enhanced Raman scattering", Phys. Rev. E **62**, pp. 4318-4324, 2000.

[7] L. Gunarsson, E.J. Bjerneld, H. Xu, S. Petronis, B. Kasemo, and M. Käll, "Interparticle coupling effects in nanofabricated substrates for Surface-enhanced Raman scattering", Applied Phys. Lett. *to appear*.

[8] L. Gunnarsson, S. Petronis, B. Kasemo, H. Xu, E.J. Bjerneld, and M. Käll, "Optimizing nanofabricated substrates for surface-enhanced Raman scattering", NanoStructured Materials **12**, pp. 783-788, 1999.

[9] H. Xu, E.J. Bjerneld, M. Käll, and L. Börjesson, "Spectroscopy of single hemoglobin molecules by surface-enhanced Raman scattering", Phys. Rev. Lett. **83**, pp. 4357-4360, 1999.

[10] E.J. Bjerneld, P. Johansson, and M. Käll, "Single molecule vibrational fine-structure of tyrosine adsorbed on Ag nano-crystals", Single Molecules **1**, pp. 239-248, 2000.

[11] C. Larsson, H. Xu, M. Käll, and F. Höök, manuscript in preparation.

[12] K. Sokolov, G. Chumanov, and T.M. Cotton, "Enhancement of Molecular Fluorescence near the Surface of Colloidal Metal Films", Anal. Chem. **70**, pp. 3898-3905, 1998.

[13] M. Inoue and K. Ohtaka, "Surface enhanced Raman scattering by metal spheres. I. Cluster effect", J. Phys. Soc. Japan **52**, pp. 3853-3864, 1983.

[14] S.M. Nie and S.R. Emory, "Probing Single Molecules and Single Nanoparticles by Surface-Enhanced Raman-Scattering", Science **275**, pp. 1102-1106, 1997.

[15] K. Kneipp, Y. Wang, H. Kneipp, L.T. Perelman, I. Itzkan, R. R. Dasari, and M.S. Feld, "Single Molecule Detection using Surface-Enhanced Raman Scattering", Phys. Rev. Lett. **78** pp. 1667-1671, 1997.

SERS and the Single Molecule: Near Field Microscopy and Spectroscopy

Martin Moskovits*, Li-Lin Tay, Jody Yang and Thomas Haslett
Deparment of Chemistry, University of Toronto Toronto M5S 3H6, Canada
*Current address: Department of Chemistry and Biochemistry, University of California, Santa
Barbara, CA 93106

ABSTRACT

Recent results suggest that surface-enhanced Raman Spectroscopy (SERS) of single adsorbate
molecules is possible under appropriate circumstances. We propose that this phenomenon is
associated with very intense enhancements available at interstitial sites (hot spots) of nanoparticle
assemblies (either colloid particle aggregates or rough surfaces) illuminated with light of an
appropriate wavelength so as to excite surface plasmons, coupled with additional resonance
enhancements due to a judicious choice of ad-molecule. The former contribution, known as
electromagnetic (EM) enhancement, has been known for years to be capable of producing EM hot
spots where the enhancement can top 10^{11}. This fact seems to have been rediscovered recently. It is
also known that the fields at the surface of fractal aggregates commonly show hot spots. These are
also, at times, capable of such high local enhancements. On fractals, the location of these hot spots
are, however, highly dependent on parameters such as the excitation wavelength. In contrast, small
compact clusters (when properly designed) have the benefit of a wavelength-independent hot spot
where a small number of molecules could be (chemically) directed and detected. This insight
suggests an eventual optimally engineered single-molecule SERS system with predictable
enhancement capabilities and optimal adsorption (i.e. chemical) characteristics at the hot spot.

Surface enhanced Raman Scattering spectroscopy (SERS) is now a well-established
phenomenon having been extensively studied for over two decades by several dozen groups [1]. Its
attributes have attracted the attention of physicists, chemists and engineers and its potential as an
analytical tool for detecting molecules at the subpicomolar level has kept SERS a vibrant field of
inquiry. More recently, the prospect of detecting SERS from single adsorbed molecules [2,3,4] has
invigorated the field enormously. Some aspects of the interpretation of those observations have
created some controversy. For example, Nie reported the existence of *individual* "hot" silver and
gold particles capable of SERS enhancements in excess of 10^{14} [2a]. Although originally the
authors of 2a concluded that the hot particles were individual particles of low aspect ratio, they
have softened that conclusion recently in light of more recent observations by Käll [2b] and Brus
[4] and now suggest that the hot "particles" might, in fact, be small compact clusters. The intriguing
properties of the hot particles include a very rapid saturation as a function of surface coverage by
adsorbate implying that only a small fraction of the surface of a hot particle manifests such large
enhancements. Only a small fraction of a give ensemble of particles is "hot". The excitation spectra
associated with the large enhancements are narrowly peaked at particle-size-dependent
wavelengths. The aspect ratio of the particles, moreover, does not seem to correlate well with its
giant enhancement abilities.

Kneipp and co-workers report an elegant series of experiments from which she argues two novel
effects, both implying very large enhancements, again exceeding 10^{14}. These large enhancements

are reckoned in two ways. First, Kneipp observes unusually intense antistokes Raman emission [3a] implying a strongly non-Boltzmann population in vibrationally excited states of the adsorbed molecules studied. She interprets this to be indicative of optical pumping by the Raman process itself. Normally Raman is orders of magnitude too weak to produce such pumping. A simple analysis of these observations suggests that for such an effect to be observed the overall emission cross-section must be enhanced by some 15 orders of magnitude or alternatively the local radiative intensity must be increased by an equivalent extent, or some of both mechanisms must occur whose total contribution produces a 15-order of magnitude increase over ordinary Raman. There are no known phenomena that would boost the Raman cross-section so extraordinarily. If, on the other hand, one ascribes the effect to field-enhancement the resultant local field would not be tolerated by ordinary samples.

In another series of elegant experiments Kneipp measures SERS from silver colloid aggregates dosed with so small a quantity of adsorbate that, on average, only a single adsorbate molecule resides on any given silver aggregate [3]. A statistical analysis of the time series of the observed Raman intensities suggests that essentially every adsorbate molecule introduced into the system can be accounted for in the resulting Poisson statistics of the Raman signal suggesting that, in very case, the single adsorbate molecule riding on a silver aggregate, occupies a high-enhancement location. This contrasts with Nie's observation that very few particles are capable of ultra-high enhancement. Recently Käll and coworkers [2a] reported single molecule SERS from hemoglobin adsorbed on silver colloid. In most other respects their observations paralleled those of Nie and members of his group. However, Käll's group concluded that the hot particles were dimers or small clusters of silver colloid particles and that most of the enhancement could be accounted for by the very strong fields that are thought to exist in the interstices or sharp clefts in the dimers. Michaels et al [4] repeated some of the experiments of Nie on silver and obtained phenomenologically the same results. Additionally, Michaels et al. measured the resonant Rayleigh spectra of the particles and concluded that intense Rayleigh and SERS scattering did not correlate.

Although some of the above observations appear to challenge the conventional understanding of SERS. One can, in fact that they accord with our present understanding of SERS.

As it is currently understood SERS is primarily a phenomenon associated with the enhancement of the electromagnetic field surrounding small metal (or other) objects optically excited near an intense and sharp (high Q), dipolar resonance such as a surface-plasmon polariton. The enhanced re-radiated dipolar fields excite the adsorbate, and, if the resulting molecular radiation remains at or near resonance with the enhancing object, the scattered radiation will again be enhanced (hence the most intense SERS is really frequency-shifted elastic scattering by the metal). Under appropriate circumstances the field enhancement will scale as E_L^4, where E_L is the local optical field. A great deal of early SERS literature dealt with this phenomenon [5]. For particles with regions of very high curvature (ellipsoidal or rod-shaped particles) the enhancement near those sharp regions can be very much greater than for spherical or near-spherical particles.

Another contribution to the observed SERS intensity is generally referred to as "chemical enhancement". This comes about from the fact that many adsorbates bind sufficiently strongly to the SERS-active surface that the Raman scatterer cannot properly be construed to be the adsorbate alone, but rather an adsorbate-surface complex, more or less analogous to a metal-ligand or perhaps

cluster-ligand coordination complex. As a result, the Raman cross-section of the scatterer might be increased in much the same way as the Raman cross-section of ligand vibrational modes is often increased in coordination complexes over that of the free ligand. The creation of a surface complex might, moreover, lead to resonances in the visible region of the spectrum even for colorless adsorbates due to metal-to-molecule or molecule-to-metal transitions owing to the convenient location of the Fermi energy of most metals in an energy region intermediate between the energy of the HOMO and the LUMO of many molecules. These new states can contribute resonantly to the Raman cross-section of the surface complex increasing its magnitude further. Although most workers in the field recognize these two contributions to SERS with the electromagnetic contribution being the dominant (indeed, the contribution that defines the salient features of SERS, after all, all metal/ligand systems can, in principle, engage in "chemical enhancement" yet SERS is a phenomenon that is robust only with a few metals and with systems comprised predominantly of nanoparticles) the antipathy of some groups to the electromagnetic (em) contribution [6] has obscured the origin of SERS over the past two decades. However, attempts to account for the major aspects of SERS primarily in terms of chemical contributions have not been successful.
A more subtle SERS mechanism (also often referred to as chemical enhancement), proposed by Otto [6] and Persson [7] suggests that the SERS enhancement results from the interaction of chemisorbed molecules with ballistic electrons that arise through plasmon excitations.

An em model in terms of single particles is, in most cases, a poor model for real SERS-active systems. Most SERS-active systems are actually assemblies, sometimes very large assemblies, of coupled nanoparticles. The em fields associated with such assemblies have been approximated in a variety of ways: gratings, fractal aggregates, small compact clusters and periodic superlattices. For compact or periodic systems of particles one has shown that the em field strength at interstitial locations in the aggregate can be greatly increased over the field surrounding a single constituent particle in the aggregate [8]. Interstitial sites might also correspond to the chemically most active surface sites. An adsorbate molecule landing on a randomly rough surface might remain strongly bound to such chemically active sites after diffusing on the surface.

Many SERS-active systems, such as colloid clusters that have aggregated via so-called cluster-cluster aggregation or randomly rough surfaces produced by restricted diffusion on cold surfaces have been shown to possess scaling or fractal symmetry [9]. Stockman [10] and Shalaev [11] and coworkers have predicted a number of novel optical properties for such aggregates resulting from their fractality. The approach taken by those groups is to consider the cluster or the surface to be composed of a large number of individual particles each interacting through dipole-dipole coupling. The dipolar field em fields in the vicinity of such surfaces will be those corresponding to the normal modes of the interacting dipoles. (This problem is isomorphic, to a great extent, with vibrational excitation, except that here we are dealing with plasmon "oscillations".)
Among the robust optical features of these fractal systems that distinguish them from the optical behavior of compact clusters are: (1) the optically allowed normal modes span a broad range of wavelengths, while in compact or periodic clusters most modes would not be dipole active. Hence the absorption spectrum of a fractal aggregate (or surface) is in general broad while that of a compact aggregate much narrower. (2) Many of the normal modes will be highly localized in regions of the aggregate small with respect to the overall size of the aggregate and the wavelength of the exciting light. Although some normal modes of some compact clusters will be localized, this would be an accidental feature of those compact clusters. In general, for compact or periodic

aggregates the normal modes are delocalized over all or most of the volume of the cluster. (3) Most optical properties of fractal clusters, such as their absorption and their SERS excitation spectra, rapidly approach a size-independent form which will also be independent of the cluster's specific shape so long as it belongs to the same class of fractal.
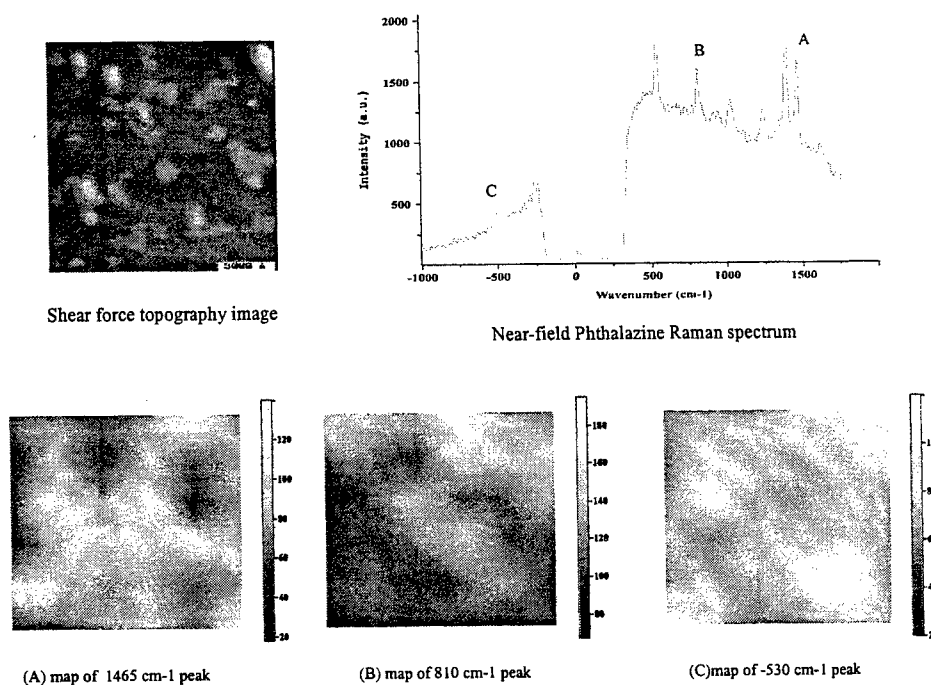
For compact clusters, size-independence is approached slowly and the absorption spectrum will depend critically on cluster geometry. Of these three properties the second - excitation localization - is the most intriguing. What it implies, is that for essentially all fractal clusters many of the normal modes will be so localized that the enhancement resulting from the interaction of all of the particles comprising the cluster will be concentrated in very small regions of the cluster, in so-called hot spots, where the enhancement can reach many orders of magnitude higher than the average enhancement. Local enhancements $\sim 10^{11}$ have been predicted in these hot spots [11]. Because the normal mode patterns corresponding to even closely located excitation wavelengths can be quite different, the hot spots will not, in general, reflect local geometrical features of the cluster. Hence, for some normal modes the hot spots will correspond to interstitial surface sites for others to hilltops. In cases where the aggregate is dosed with very few molecules, as one might do in attempting to measure SERS from single molecules, an aggregate might seem "cold" or "hot" depending on whether the normal mode has a hot spot where the molecule happens to be for the excitation wavelengths used. If the molecule binds strongly to the surface, then, in general, few aggregates will seem hot. Contrariwise, a molecule that is mobile can diffuse in and out of the hot spot. It may even be trapped in the hot spot by the strong dipolar field gradients at the periphery of the hot spots.

For compact clusters the situation is more unpredictable. Because compact clusters have few normal modes for which the fields are highly concentrated only few in an ensemble of compact clusters will appear hot and only for a narrow range of wavelengths. However, one can, in principle, find some sites, normally interstitial sites, where the electromagnetic enhancement could be such that, locally, SERS intensities $\sim 10^{11}$ are encountered. We believe that a great deal of the giant enhancements reported by Nie and Kneipp and others are due to the field-concentrating properties of aggregates. It is also clear, however, that another effect contributes as well to raise the observed enhancement to the reported $\sim 10^{14}$. We note that almost all of the results reported so far have been with molecules with a rich spectrum in the visible region of the spectrum. The added enhancement may be due to some form of resonance.

Many of the salient features of the em theory of fractals have been corroborated using near-field microscopy and spectroscopy [12]. For example, the em fields near the surfaces of self-affine, randomly rough surfaces

Figure 1

Top left: shear-force topographic image of a silver film produced by collapsing phthalazine-covered silver colloid aggregates gravitationally onto a pyrex cover slide. Top right: the near-field SERS spectrum of phthalazine measured on the film imaged in the previous panel. A, B, C: near-field Raman intensity maps of the SERS bands shown in the previous spectrum measured over a 3 μm × 3 μm portion of the colloidal silver film

Shear force topography image

Near-field Phthalazine Raman spectrum

(A) map of 1465 cm-1 peak

(B) map of 810 cm-1 peak

(C)map of -530 cm-1 peak

produced by collapsing colloidal metal aggregates under the influence of gravity, have been shown to be highly localized. More recently we were able to measure good quality near-field SERS spectra from which one could construct near-field Raman maps of SERS transitions in which the hot spots are also visible. For example, Figure 1 shows a scanning electron micrograph of a sample produced by allowing colloidal silver particles to aggregate then settle gravitationally on a glass plate. The silver aggregate was exposed to phthalazine. The near-field SERS spectrum measured at the surface of that sample with a sharpened optical fiber tip with a resolution <100nm is shown in Figure 1. A number of maps of the SERS intensities of a number of Raman bands were obtained by manually moving the tip to lattice points over a 3μm × 3μm grid, measuring the near-field SERS spectrum at each point, fitting a Lorentzian under the band in each spectrum, then plotting the result. A shear-force topographic image was taken before and after each set of measurements. The resulting map is shown in Figure 1. Hot spots with dimensions < 1 μm are clearly visible. We have also shown that the excitation spectra measured by probing the near field in very small regions of such samples display a number of narrow lines corresponding to the normal modes of surface plasmon excitation to which the region of the aggregate being probed participated.

Careful experiments in which the Stokes and antistokes intensities in the SERS spectra of several molecules were measured over five orders of magnitude of laser excitation and showed (i) that while large antistokes intensities were observed (for dye molecules) as previously reported, the antistokes intensity depended linearly on laser power over many orders of magnitude, (ii) adsorbed small, colorless molecules, while showing intense SERS spectra, showed no unusual antistokes intensities, and (iii) a careful analysis of the physics of the proposed Raman pumping would imply local radiative intensity (i.e. $<|E_L^2|>$) enhancements ~ 10^{14} which would imply a staggering expected SERS enhancement ~10^{28}.

We, therefore, believe that the results reported by Nie and Kneipp so far can be accounted for by a combination of strong local em excitation in colloidal metal aggregates (generally small compact

aggregates) with added contributions from resonance enhancements. The fact that, so far, the reports have largely focused on adsorbed dye molecules is, in our view, not a coincidence. One needed the opportunity for additional resonance enhancement that those systems provide, on top of electromagnetic enhancement. Because AFM images tend to show the particles as "compact" we propose that the particles involved are either compact colloidal aggregates or "failed fractals" [14]. Such aggregates would possess few plasmon normal modes that would have highly localized and concentrated fields (hot spots). Because of the high localization of the fields only a few aggregates would manifest a SERS spectrum under circumstances where only one or very few adsorbate molecules decorate a given cluster. Only those clusters in which the adsorbed molecule is coincidentally bound at a location on the cluster corresponding to a hot spot would show inordinate SERS intensities. This explains the rarity of hot particles and the sharpness of the excitation spectrum for a given group of hot particles. This also accounts for the fact that as one continues to add adorbate to a sample of particles, progressively more particles become "hot". Adding adsorbate increases the probability that an ad-molecule eventually binds to a location on the aggregate where the field is concentrated. This also explains the fact that for a given particle the SERS intensity saturates rapidly and then becomes roughly independent of further coverage. Once the surface sites within the hot spots on an aggregate are populated further surface coverage would not add significantly to the SERS intensity.

According to this explanation, localization of the em field due to particle-particle interactions in an aggregate results in a SERS enhancement of the order of 10^{11} [11] the remaining enhancement arises from resonance Raman and other so-called chemical enhancement effects. The fact that resonant Rayleigh and SERS scattering do not correlate also accords well with this view. Rayleigh scattering is a coherent process that depends on averaging a two-point field correlation over the entire volume of the aggregate. Rayleigh scattering is phase-dependent and the variation in the field's phase and amplitude from point to point on the aggregate is important. Raman is an incoherent, phase-independent process in which the enhancement is defined by the one-point correlation: $<|E(r)^4>$. The very intense fields that exist at hot spots would dominate this average [15]. Hence the aggregates that show intense Rayleigh scattering need not be those manifesting the most intense SERS signals or vice versa. Our explanation also does away with the implied requirement that there are very special and rare adsorption sites on a particle where the adsorbate molecule binds chemically. Although we recognize the known fact that some surface sites can be more reactive than others, the very early saturation of the SERS signal with added adsorbate [4] suggests that surface sites suitable for chemisorption are very rare indeed. There is no reason to suppose that silver aggregates possess such rare, highly reactive adsorption sites. The model we propose does not require such highly site selective surface chemistry.

REFERENCES

1. M. Moskovits, Rev. Mod. Phys., **57**, 783 (1985); R. K. Chang, Ber. Bunsen-Ges. Phys. Chem., **91**, 296 (1987).
2. a: Krug JT, Wang GD, Emory SR, Nie SM, J. Amer. Chem. Soc., **121**, 9208 (1999); Emery SR, Haskins WE, Nie SM, J. Amer. Chem. Soc., **120**, 8009 (1998); Lyon WA, Nie SM, Anal. Chem., 69, 3400 (1997); Nie SM, Emery SR, SCIENCE , 275, 1102 (1997); b: H. Xu, E. J. Bjerneld, M. Käll and L. Börjesson, Phys. Rev. Lett. **83,** 4357 (1999).

3. a: Kneipp K, Wang Y, Kneipp H, Itzkan I, Dasari RR, Feld MS, Phys. Rev. Lett., **76**, 2444 (1996);
b: Kneipp K, Kneipp H, Itzkan I, Dasari RR, Feld MS, Chem. Phys. 247, 155 (1999); Kneipp K, Kneipp H, Manoharan R, Hanlon EB, Itzkan I, Dasari RR, Feld MS, Appl. Spectrosc., 52, 1493 (1998); Kneipp K, Kneipp H, Manoharan R, Itzkan I, Dasari RR, Feld MS, J. Raman Spectrosc., 29, 743 (1998); Kneipp K, Kneipp H, Kartha VB, Manoharan R, Deinum G, Itzkan I, Dasari RR, Feld MS, Phys. Rev. E, 57, R6281 (1998); Kneipp K, Wang Y, Kneipp H, Perelman LT, Itzkan I, Dasari R, Feld MS, Phys. Rev. Lett., 78, 1667 (1997).
4. A. M. Michaels, M. Nirmal and L. E. Brus, J. Amer. Chem. Soc. 121, 9932 (1999).
5. Kerker M, Wang D, Chew H, Appl. Opt. 19, 4159 (1980).
6. A. Otto, in Light Scattering in Solids IV, M. Cardona and G Gundtherodt, Eds, Springer-Veralg: Berlin, 1984, pp 289-418.
7. B. N. Persson, Chem. Phys. Lett., 82, 561 (1981).
8. P. K. Aravind et al., Surf. Sci. 110, 189 (1981); N. Liver et al., Chem. Phys. Lett. 111, 449 (1984); A. Wirgin and T. López-Ríos, Opt. Commun. 48, 416 (1984); N. Garcia et al., Surf. Sci. 143, 342 (1984); P. A. Kneipp and T. L. Reinecke, Phys. Rev. B 45, 9091 (1992); F. J. García-Vidal and J. B. Pendry Phys. Rev. L 77, 1163-1166 (1996).
9. D. A. Weitz and M. Oliveria, Phys. Rev. Lett. 52, 1433 (1984).
10. M. I. Stockman, Phys. Rev. E 56 6494 (1997).
11. V. M. Shalaev, R. Botet, J. Mercer and E. B. Stechel, Phys. Rev. B 54, 8235 (1996); E. Y. Poliakov, V. M. Shalaev, V. A. Markel and R. Botet, Opt. Lett. 21, 1628 (1996); V. M. Shalaev and A. K. Sarychev, Phys. Rev. B 57, 13265 (1998); S. Grésillon, L. Aigouy, A. C. Boccara, J. C. Rivoal, X. Quelin, C. Desmarest, P. Gadenne, V. A. Shubin, A. K. Sarychev and V. M. Shalaev, Phys. Rev. Lett. 82, 4520 (1999).
12. V. A. Markel, V. M. Shalaev, P. Zhang, W. Huynh, L. Tay, T. L. Haslett, M. Moskovits, Phys. Rev. B 16, 8080 (1999); P. Zhang, T. Haslett, C. Douketis and M. Moskovits, Phys. Rev. B 57, 15513 (1998); D.P. Tsai, J. Kovacs, Z. Wang, M. Moskovits, V. Shalaev, J.S. Suh and R. Botet, Phys. Rev. Lett., 72 4149 (1994).
13. T. L. Haslett, L. Tay and M. Moskovits, J. Chem. Phys. 113, 1641 (2000).
14. A. M. Michaels, J. Yang and L. Brus, unpublished.
15. V. M. Shalaev, personal communication.

OPTICAL SPECTROSCOPY OF MOLECULES ON METALLIC NANOPARTICLES AND ON NANOSTRUCTURED METALLIC SURFACES

Katrin Kneipp[a,b], Harald Kneipp[a], Irving Itzkan[b], Ramachandra R. Dasari[b], Michael S. Feld[b]

[a]Department of Physics, Technical University Berlin, D 10623 Berlin, Germany
[b]George R. Harrison Spectroscopy Laboratory,
Massachusetts Institute of Technology, Cambridge, MA 02139

ABSTRACT

In the vicinity of small metal particles in dimensions of tens of nanometers or close to nanostructured metallic surfaces, local optical fields can be strongly enhanced due to resonances with the collective excitation of the conduction electrons in these metallic nanostructures. These enhanced local fields open up exciting opportunities for enhancing spectroscopic signals and to perform spectroscopy on single molecules. We report surface-enhanced Raman studies on silver and gold nanostructures. The field strengths in the "hot spots" on silver and gold colloidal cluster structures are inferred to be enhanced on the order of 10^3 resulting in field enhancement factors for Raman scattering up to 10^{12}. Simultaneously, as a further advantage for Raman spectroscopy, the fluorescence of the target molecules is quenched by new non-radiative decay channels to the metal.

Keywords: Single molecules, Raman, SERS, nanostructures, colloidal gold, colloidal silver

1. INTRODUCTION

The unexpectedly high Raman scattering signal from molecules attached to a metal substrate with nanometer scaled structure or "roughness" [1-4] might be one of the most impressive effects for demonstrating the interesting optical properties of metallic nano structures, which occur due to resonances with the plasmon excitations in the metal. In particular, strong enhancement of the Raman scattering has been observed when molecules are attached to silver or gold colloidal clusters or to island structures of these metals, even when excitation light non-resonant to molecular electronic transitions was used [5-9]. Similar enhancement factors are reported for surface-enhanced resonance Raman scattering of Rhodamine 6G on isolated highly SERS-active silver particles [10]. For resonant surface-enhanced Raman scattering of Rhodamine 6G on small silver colloidal clusters even 1 order of magnitude higher enhancement factors are reported [11, 12].

In particular, Raman cross sections of the order of 10^{-16} cm^2 per molecule, corresponding to enhancement factors of about 10^{14} can be inferred also for adenine adsorbed on silver colloidal clusters at near infrared excitation [8]. Adenine has absorption bands in the ultraviolet. Therefore, at 830 nm excitation, no molecular resonance Raman effect can contribute to the observed large Raman cross section.

The high local optical fields in the hot spots of silver cluster structures provide a rationale for the high enhancement level, which is necessary for non-resonant single molecule Raman spectroscopy [13]. On the other hand, an additional "chemical effect" must be operative in order to account for the gap of 2 - 3 orders of magnitude between the best estimated electromagnetic field enhancement for Raman scattering and the experimentally verified non-resonant SERS enhancement factor of 10^{14}. Another strong argument for a "chemical" enhancement mechanism is the molecular selectivity of the effect.

Of course, strong field enhancement does not rule out, and may even support a simultaneous "chemical" enhancement, which may be present in the SERS effect. Therefore, the "electronic" interaction between molecule and the metallic nanoparticle is an important issue that needs to be studied in more detail in the future.

2. SILVER AND GOLD COLLOIDAL NANOSTRUCTURES

The plasmon resonance frequency and also the size of the electromagnetic field enhancement factor depend on the size, shape, and of course, the material of the metallic nanoparticles and their environment. Electromagnetic field enhancement and surface plasmon resonance can also explain the initial discovery of surface-enhanced Raman scattering. This observation was possible because the blue and green emission lines of the Ar$^+$ laser accidentally fell in the excitation range of surface plasmons due to the bumps on the electrochemically roughened silver electrode.

Theory predicts strong enhancement of electromagnetic fields for sharp features and large curvature regions, which may exist on silver and gold nano structures. For example, it was recently shown, that the electromagnetic SERS enhancement factor can be increased up to nearly 10^{11} when the sphere degenerates and becomes "sharper" at one edge. Also, closely spaced interacting particles can provide extra field enhancement, particularly near the gap sites between two particles in proximity. Recently, electromagnetic enhancement factors up to 10^{11} have been estimated for the midpoint between two silver or gold spherical particles separated by a gap of 1 nm [14].
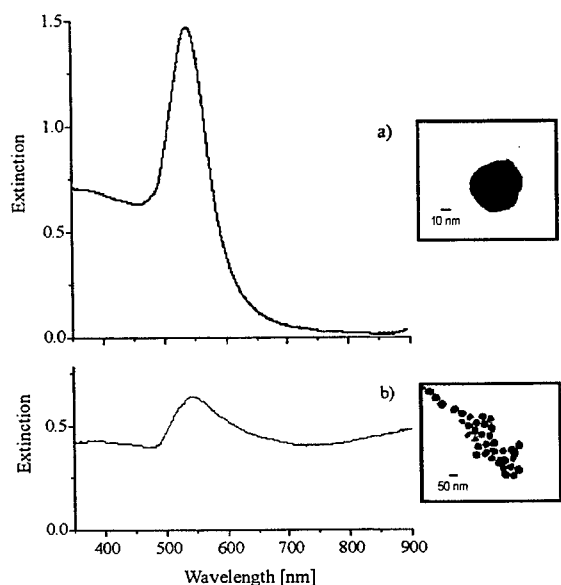
Fig. 1: Isolated colloidal gold particles and a gold colloidal cluster.

Figure 1 shows typical gold colloidal structures and their extinction spectra.

Maximum values for electromagnetic enhancement for isolated single colloidal silver and gold spheroids are on the order of 10^6 and 10^4, respectively[2].

In many experiments, SERS-active substrates consist of a collection of silver or gold nanoparticles exhibiting fractal properties, such as colloidal clusters formed by aggregation of colloidal particles or metal island films.
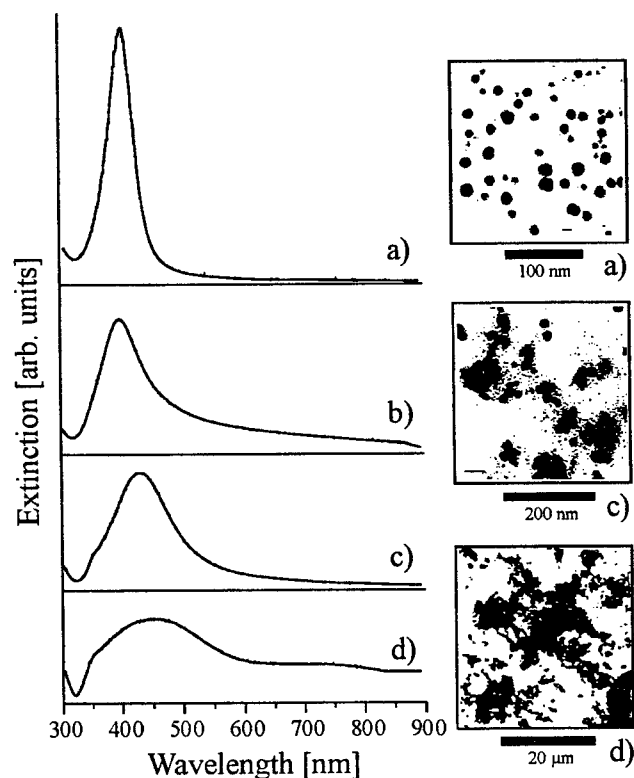

Fig. 2: Colloidal silver particles in different aggregation stages and the extinction spectra of their aqueous solutions

Figure 2 shows SERS-active colloidal silver particles in different aggregation stages.

The changes in the extinction spectra reflect the changes of the plasmon resonances, which depend on the particle aggregation.

A comparison between the electron microscope view (200 nm scale) and the light microscope view (20 μm scale) shows strong similarities and demonstrates the fractal nature of these structures.

SERS-active silver colloidal clusters can be also generated in silver halide emulsions by laser illumination [15, 16].
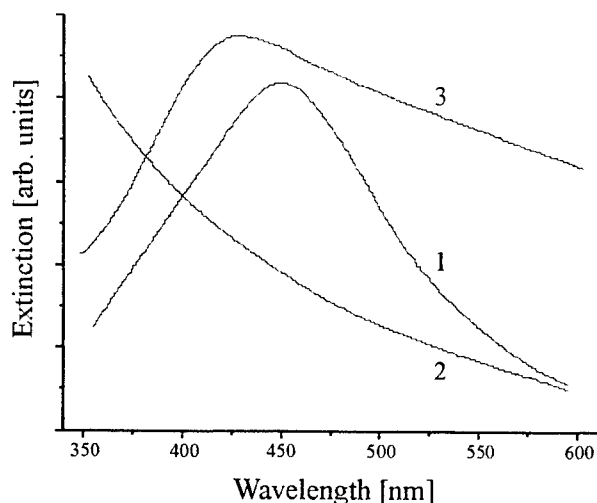
Fig. 3a: Extinction spectra of a silver chloride emulsion (2), silver chloride emulsion with print out silver (3) and colloidal silver solution (1)
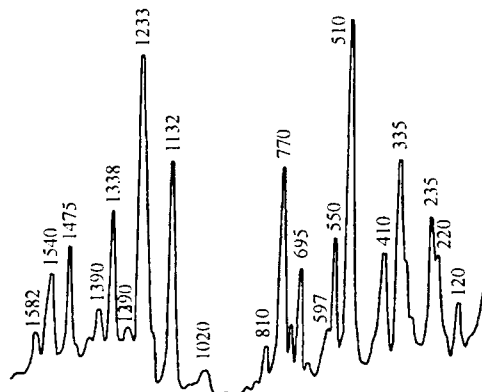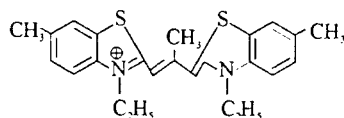

Fig. 3b: SERS spectrum of a 10-9 M dye in silver chloride emulsion after 5 minutes laser illumination.

Figure 3a shows for comparison the extinction spectra of a silver chloride emulsion (curve 2). After a few minutes of laser illumination, print out silver is formed and gives rise to a broad absorption band with a maximum at about 415 nm (curve 3), which is very similar to the extinction spectrum of colloidal silver solution (curve 1). The silver particles in the silver halide emulsion result in total (RRS + SERS) enhancement factors on the order of 1011. Fig. 3b shows the SERRS spectrum of a sensitizing polymethine dye in nanomolar concentration. Since the SERS enhancement factor of small silver particles depends on their sizes, the increase of the SERS signal can be used as probe for monitoring the growth of the silver particles in the photographic emulsion. Furthermore, relative intensities of Raman lines can show a dependence on the potential of the SERS-active surface. Therefore, changes in the relative intensities of Raman lines suggest changes in the surface potential of the silver clusters during the growing process [16].

3. SERS EXPERIMENTS ON ISOLATED SILVER AND GOLD SPHERES AND ON COLLOIDAL CLUSTERS

The electromagnetic contribution to the SERS enhancement strongly depends on the morphology of the metal nanostructures. In the following, we discuss some experimental observations on SERS performed on isolated nanospheres of silver and gold and on colloidal clusters structures of these metals.

Stokes Shift [cm⁻¹]   Anti Stokes Shift [cm⁻¹]
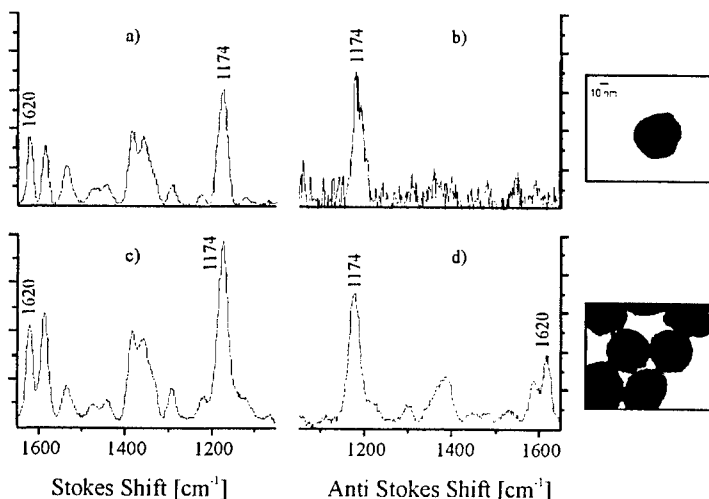
Fig. 4. Stokes and anti Stokes SERS spectra of crystal violet attached to isolated and aggregated colloidal gold, excitation at 830nm

Figures 4a and 4b display Stokes and anti Stokes SERS spectra of crystal violet attached to isolated colloidal gold spheres in aqueous solution. NaCl was added to the aqueous solution in order to induce aggregation of the spheres, but spectra in Figs. 4a and 4b were measured in the first minutes after addition of the salt. No changes in the extinction spectrum of the colloidal solution were observed indicating that no aggregation occurred during this time.

Therefore, the electromagnetic SERS enhancement should be mainly related to isolated gold spheres of about 60 nm dimension. On the other hand, if there is any additional "chemical" enhancement related to NaCl induced "active sites" [17], that effect should already exist. After several minutes, when changes in the extinction spectrum from curve a to curve b in Fig. 1 indicated the formation of colloidal gold clusters, the SERS Stokes signal strongly increased (Fig. 4c). Now also a strong anti-Stokes spectrum occurs, as it is shown in Fig. 4d. Particularly, higher frequency modes appear at unexpectedly high signal levels in the anti-Stokes spectrum. This behavior indicates a very high SERS-enhancement since molecules, which are "pumped" to the first excited vibrational levels due to the strong Raman process now contribute to the anti Stokes signal in addition to the thermally excited molecules [5].

For comparison, Fig. 4b shows the anti-Stokes SERS spectrum measured from crystal violet on isolated gold spheres. The higher frequency anti Stokes bands do not appear in this spectrum due to their weak thermal population. The anti-Stokes to Stokes signal ratio of the 1174 cm-1 crystal violet SERS line measured in Fig. 4a and 4b is in agreement with the ratio measured for 1211 cm-1 line of toluene, which represents the Boltzmann population of the vibrational levels. That means that no vibrational pumping due to SERS can be observed for the smaller enhancement factors of isolated gold colloidal spheres, since the effective Raman cross section is not large enough for measurably populating the first vibrational levels. Estimates show, that effective SERS cross sections on the order of 10^{-16} cm^2 per molecule must be operative, in order to generate a measurable population of the first excited vibrational levels.

Deviations of the anti Stokes to Stokes signal ratios from those expected from a Boltzmann population can also be observed when the resonance Raman conditions for anti Stokes and Stokes scattering are different. Since the resonance Raman effect depends on resonance conditions of both excitation laser and the scattered light, the anti Stokes scattering may benefit in some special circumstances from some pre resonance Raman effect. This can occur in particularly at excitation wavelengths in the NIR for molecules with absorption bands in the visible. In that case, the anti Stokes to Stokes signal ratio also shows deviations from the Boltzmann ratio [18]. Vibrational pumping can be separated from this effect by checking the dependence on the excitation laser intensity. Whereas the selective resonance Raman effect for the anti Stokes scattering is independent on the excitation laser intensity, indication for vibrational pumping is also a linear increase of the anti Stokes to Stokes signal ratio or a quadratic dependence of the anti Stokes signal power vs. the excitation laser intensity [5, 19].

Vibrational population pumping effects of comparable size have been also found in SERS experiments on colloidal silver clusters [5-8].

In order to study the dependence of the enhancement factor on cluster size, Fig. 5 shows Stokes and anti Stokes SERS spectra measured from crystal violet on silver colloidal clusters of about 5 μm in size and from "a few" small 100 – 500 nm clusters (see circles a and b in the microscope view).
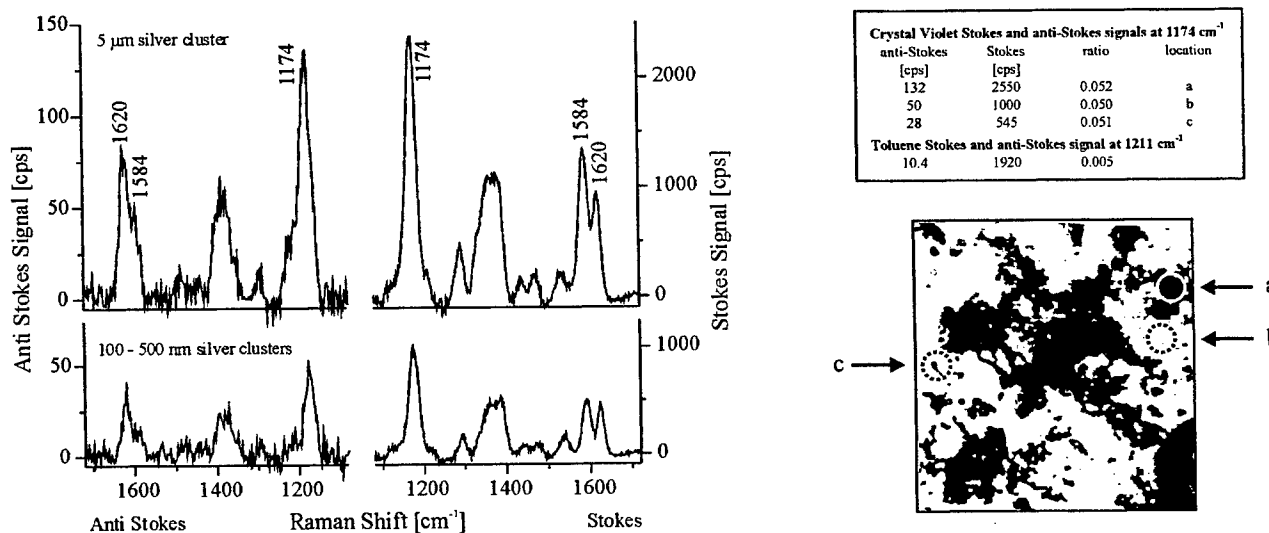

Fig. 5: Stokes and anti Stokes SERS spectra measured from crystal violet on silver colloidal clusters of different sizes as shown in the microscope view, excitation at 830 nm. The table shows the measured anti-Stokes to Stokes signal power ratios, for comparison the same ratio is given for a toluene line.

The table in figure 5 gives anti-Stokes to Stokes ratios measured from crystal violet on clusters of different sizes shown in Fig. 5. The ratios are constant within the accuracy of our measurement implying effective SERS cross sections independent of cluster size.

This might give the explanation for perhaps the most surprising experimental observation in single molecule Raman measurements, namely the relatively uniform enhancement observed despite the non-uniform shape and size of the silver particles forming the clusters. In this "cluster-based enhancement" model, a molecule "feels" an enhancement in the hot spots of the clusters, which can be independent of the individual particles in the cluster, and also independent of the size of the cluster.

At near infrared excitation, gold colloidal clusters provide as good SERS enhancement factors as silver colloidal clusters [20].

4. REFERENCES

1. A. Otto, "Light Scattering in solids", M. Cardona, G. Guentherodt, Eds., Springer, Berlin, Heidelberg, New York 1984, p. 289
2. M. Moskovits, Surface-enhanced spectroscopy, Rev. Mod. Phys. 57, p. 783, 1985
3. A. Campion, P. Kambhampati, Surface-enhanced Raman scattering, Chem. Soc. Reviews 27, p. 241, 1998
4. K. Kneipp, H. Kneipp, I. Itzkan, R.R. Dasari, M.S. Feld, Ultrasensitive Chemical Analysis by Raman Spectroscopy, Chem. Rev. 99, p. 2957, 1999
5. K. Kneipp, Y. Wang, H. Kneipp, I. Itzkan, R.R. Dasari, M. S. Feld, Population Pumping of Ecited Vibrational States by Spontaneous Surface-Enhanced Raman Scattering, Phys. Rev. Lett. 76, p. 2444, 1996
6. K. Kneipp, Y. Wang, H. Kneipp, L. T. Perelman, I. Itzkan, R.R.Dasari, M. S. Feld, Single Molecule Detection Using Surface-Enhanced Raman Scattering (SERS),Phys. Rev. Lett. 78, p. 1667, 1997
7. K. Kneipp, H. Kneipp, G. Deinum, I. Itzkan, R.R. Dasari, M.S. Feld, Single-Molecule Detection of a Cyanine Dye in Silver Colloidal Solution Using Near-Infrared Surface-Enhanced Raman Scattering, Appl. Spectr. 52, p. 175, 1998
8. K. Kneipp, H. Kneipp, V.B. Kartha, R. Manoharan, G. Deinum, I. Itzkan, R.R. Dasari, M.S. Feld, Detection and identification of a single DNA base molecule using surface-enhanced Raman scattering (SERS), Phys. Rev. E57, p. R6281, 1998
9. E. Bjernheld, P. Johansson, M. Kall: private communication, 2000
10. S. Nie, S.R. Emory, Probing single molecules and single nanoparticles by surface-enhanced Raman scattering, Science 275, p. 1102, 1997
11. M. Michaels, M. Nirmal, and L. E. Brus, Surface-enhanced Raman spectroscopy of individual Rhodamine 6G molecules on large Ag nanocrystals ,J. Am. Chem. Soc. 121, p. 9932, 1999
12. M. Michaels, J. Jiang, and L. E. Brus, Ag nanocrystal junctions as the site for Surface-enhanced Raman scattering of single Rhodamine 6G molecules, J. Phys. Chem. B104, p. 11965, 2000
13. V. A. Markel, V.M. Shalaev, P. Zhang, W. Huynh, L. Tay, T.L. Haslett, M. Moskovits, Near-field optical spectroscopy of individual surface-plasmon modes in colloid clusters, Phys. Rev. B 59, p. 10903, 1999
14. H. Xu, J. Aizpurua, M. Kaell, P. Apell, Electromagnetic contribution to single-molecule sensitivity in surface- enhanced Raman scattering, Phys. Rev. E 62, p. 4318, 2000
15. K.Kneipp, Application of SERS in photographic science, J.Mol.Struct. 218, p. 357, 1990
16. K. Kneipp, H. Kneipp, Time-dependent SERS of pseudoisocyanine on silver particles generated in silver bromide sol by laser illumination, Spectrochim. Acta 49A, p. 167, 1993
17. P. Hildebrandt, M. Stockburger, Surface-enhanced resonance Raman spectroscopy of rhodamine 6G adsorbed on colloidal silver, J. Phys. Chem. 88, p. 5935, 1984
18. T. L. Haslett, L. Tay, and M. Moskovits, Can surface-enhanced Raman scattering serve as a channel for strong optical pumping?, J. Chem. Phys. 113, p. 1641, 2000
19. K. Kneipp, H. Kneipp, I. Itzkan, R.R. Dasari, M. S. Feld, Surface-enhanced non-linear Raman scattering at the single-molecule level, Chem.Phys. 247, p. 155, 1999
20. K. Kneipp, H. Kneipp, E.B.Hanlon, I. Itzkan, R.R. Dasari, M. S. Feld, Extremely Large Enhancement Factors in Surface-Enhanced Raman Scattering for Molecules on Colloidal Gold Clusters, Appl. Spectroscopy 52, p. 1493, 1998

SERS-Active Nanoaggregates Observed with Near-Infrared Laser Excitation

Dustin J. Maxwell[1] and Shuming Nie[2]

Department of Chemistry, Indiana University, Bloomington, IN 47405

ABSTRACT

Using wide-field illumination, optically active "hot" particles can be screened from a heterogeneous colloid using a near-IR excitation source. Atomic force microscopy (AFM) correlated with surface-enhanced Raman scattering (SERS) measurements reveal that the majority of these particles are small nanoparticle aggregates. This finding indicates a strong dependence between particle size and Raman enhancement. Furthermore, these "hot" nanoaggregates display an intermittent on-off emission behavior similar to "blinking" SERS exhibited at 488 nm and 514 nm laser excitation. This behavior, not observed in bulk SERS studies, can only be examined at the single particle level because of variations in particle size, shape, and surface defects. Further examination at the single particle level using a near–IR excitation source could led to new insights regarding the fundamental nature of "hot" particles as well as the SERS mechanism.

Keywords: Nanoparticles, surface-enhanced Raman scattering, SERS, near-infrared.

1. INTRODUCTION

Raman spectroscopy is an inelastic light scattering method that is capable of providing highly resolved vibrational information. In the case of normal Raman scattering, molecules are excited from the ground state to an intermediate level (a virtual state), which does not correspond to a real energy level of the molecule. After reaching the virtual state, a photon is emitted and the molecule returns to a different vibrational level. However, because of its small cross-sections (10^{-30} cm^2/molecule), Raman scattering is an extremely inefficient process.

This situation is dramatically improved if the analyte is adsorbed on a metallic surface, a process known as surface-enhanced Raman scattering (SERS).[1] In 1977, Jeanmaire and Van Duyne[2] and Albrecht and Creighton[3] independently reported that molecules adsorbed on roughened silver surfaces exhibit a surface enhancement effect. The increased Raman signals could not be attributed by an increase in the surface area, but by some enhancement mechanism. While Jeanmaire and VanDuyne proposed a mechanism based on electromagnetic field enhancement, their counterparts, Albrecht and Creighton, suggested a resonance Raman effect. This initial work started a renaissance in Raman spectroscopy. Thousands of papers were published within the next ten years offering new insights into the SERS mechanism. By 1985, two fundamental mechanisms[4-6] were proposed to explain the SERS process, a short-range chemical effect and a long range-electromagnetic effect. The electromagnetic enhancement mechanism can be explained by surface plasmon resonance, a process in which an incident light produces intense electromagnetic fields at the surface of metals. The experimental evidence for the electromagnetic theory includes the observation of surfaced-enhanced Raman signals placed near the surface of the metal, but not in direct contact,[7] and from molecules with different chemical properties.[8]

---

[1] D.J.M. E-mail: dumaxwel@indiana.edu; Telephone: (812) 856-5185
[2] S.N. (correspondence) E-mail: nie@indiana.edu; Telephone: (812) 855-6620

On the other hand, there is direct evidence for a chemical enhancement mechanism involving a charge transfer between the metal and adsorbate molecule.[9] The most revealing evidence includes: (1) the electrode potential at which the optimal SERS intensity obtained shifts with excitation frequency[10]; and (2) different molecules with the similar cross-sections can show different enhancements.

Although twenty years have passed, the controversy surrounding the SERS mechanism continues. All previous estimates of the enhancement surface enhancement factors were derived from ensemble averages of molecules and particles. Recently this problem has been overcome by the discovery of optically active nanoparticles and nanoaggregates. Two research groups. Katrin Kneipp's group and our research group, have detected single molecules adsorbed onto nanoparticles.[11,12] To achieve single-molecule sensitivity, the Raman scattering cross sections must be on the order of 10^{-16} cm^2 per molecule, comparable to the fluorescence cross-sections of fluorescent dye molecules. By coupling single molecules to nanometer-sized particles, the spectroscopic signatures of single molecules can be amplified by exploiting the surface-enhancement and resonance effects. This enhancement, on the order of 10^{14} or more, overcomes the inefficiencies of Raman scattering and leads to the detection of single molecules at room temperature. These nanoparticles, called "hot" particles, exhibit enormous enhancement, emit Stokes shifted light, and display intermittent "on/off" photon emission behavior.

Following these initial studies, two other groups have detected single-molecules using SERS. Kall and co-workers have studied the SERS mechanism using biological molecules such as hemoglobin.[13] According to their calculations a strong electromagnetic effect field dominates the surface enhancements. However, they suggest a single hemoglobin molecule can only be detected when situated between two nanoparticles. Also new results presented by Brus and coworkers demonstrate using large silver particles to detect single molecules.[14]

In this paper, we report the existence of optically "hot" silver particles using near-infrared laser excitation. It has been reported that large metallic clusters are extremely efficient for surface-enhancement using near-infrared excitation. However, the method employed required the SERS-active particle diffusing through the probe volume. Using wide-field illumination and confocal spectroscopy, it is possible to screen for immobilized SERS-active particles and then examine the morphology, size, and Raman scattering of an individual particle. One important finding is that only large aggregated particles exhibit SERS-activity. A significant advantage of studying Raman using a near-infrared excitation is that the fluorescent background is reduced. Although fluorescence background is not an inherent problem with SERS because the adsorbed molecules are quenched by the metal's surface, the remaining background signal from the non-adsorbed species is virtually eliminated using a near-infrared laser source. Furthermore, measurements between the visible and near-infrared region can be compared to study their different contribution to the SERS enhancement factors. By identifying particles that are responsible for these enormous enhancements in the NIR, this work opens up new opportunities to study the fundamental mechanism of SERS.

2. EXPERIMENTAL

2.1 Reagents

All chemicals and materials were used as received: crystal violet (Sigma), 1,2-bis(4-pyridyl)ethylene (Aldrich), polylysine hydrobromide (Sigma). sodium chloride (99.8% Mallinckrodt), silver nitrate (99+% Aldrich), and sodium citrate (J. T. Baker). Stock solutions of 1,2-bis-(4-pyridl)ethylene(Aldrich) and crystal violet were prepared in spectrophotometric-grade methanol (99.9% Aldrich) before being diluted in water to the required concentrations. Ultrapure water (Millipore, Bedford, MA) was used throughout the experiment.

2.2 Colloid Preparation and Characterization.

Silver colloids were prepared using the standard procedure of Lee and Miesel.[15] Morphological measurements by transmission electron microscopy (TEM) reveal that the majority of the particles are small spheres 30-50 nm diameter. This heterogeneous mixture display a characteristic absorption

maximum at 420 nm and has a typical concentration of ~$10^{10\text{-}11}$ particles/mL. These values are in agreement with previous reports on silver colloids.[16]

To activate the particles, an aliquot of colloid is incubated with a reporter molecule (e.g. crystal violet, BPE) for 1 hr at room temperature. To this sample, small amounts of 50 mM sodium chloride were added to aggregate the particles. The aggregated colloid was then diluted in water and immobilized on a glass coverslip treated with poly-l-lysine. The poly-l-lysine gives the glass surface a positive charge that holds the negatively charged nanoparticles in place.[17] Other methods using silane and thiol groups have been used to attach nanoparticles to glass supports.[18]
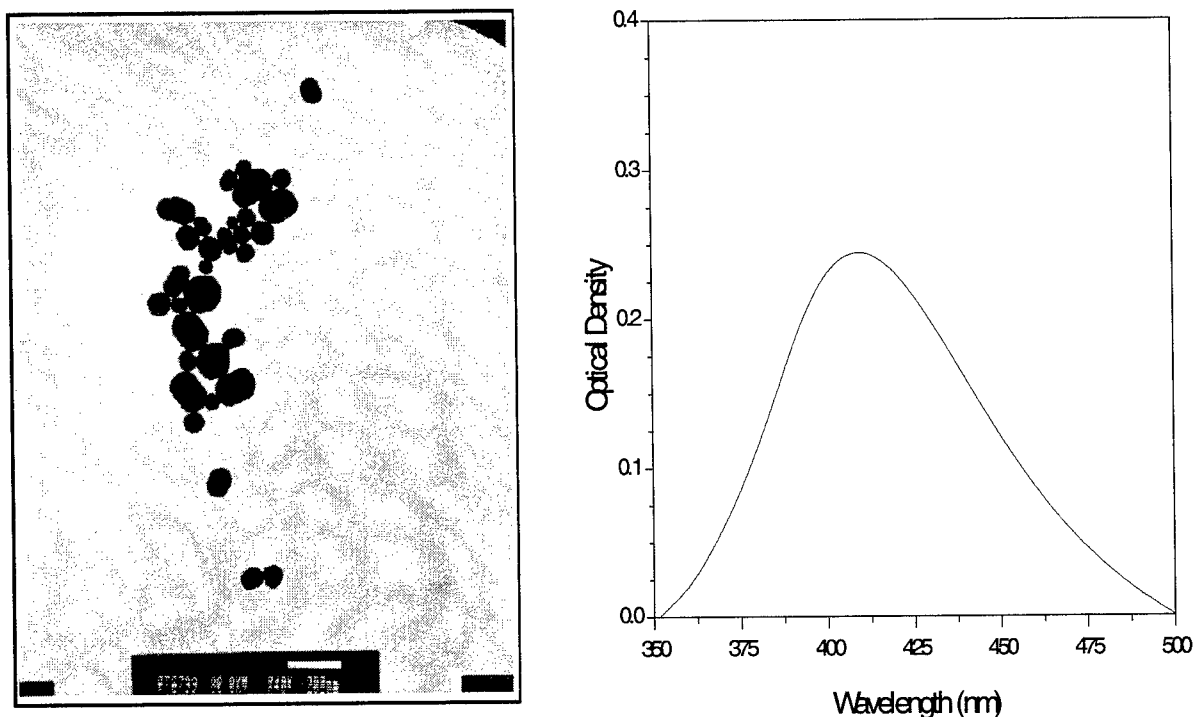

Figure 1. LEFT: Transmission electron microscope (TEM) image of a heterogeneous silver colloid. RIGHT: optical absorption spectrum of the colloid.

2.3 Instrumentation.

An inverted microscope (Nikkon Diaphot 200) coupled to a near-infrared diode laser (Power technology Inc., Mabelvale, AR) centered at 830 nm was used to examine the immobilized nanoparticles. A detailed schematic of this instrumentation is shown in Figure 2. Using wide-field illumination, nanoparticles could be rapidly screened using a video-rate intensified-charge coupled device (ICCD) (Photon Technology, Couth Brunswick, NJ) camera mounted to the front microscope port. Once identified, the wide-field optics are removed and a confocal laser beam is used to probe the SERS-active nanoparticles. The back-scattered photons emitted from the particle surface were collected by a 100X objective and passed through a spatially isolated pinhole before: (a) entering a spectrograph coupled to a

back-thin CCD camera (Princeton Instruments, Trenton, NJ) to detect the Raman scattered photons or (b) striking an avalanche photo diode (APD) (EG&G ORTEC, Oak Ridge, TN) to measure the number of emitted photons.

Simultaneously, an atomic force microscope (AFM) (Digital Instruments, Santa Barbara, CA) stage mounted on top of the inverted microscope can examine the nanoparticle morphology. By probing "hot" areas with an AFM tip, a SERS-active nanoparticle could be distinguished from inactive ones. Therefore, the instrument allows a real-time analysis of SERS-active nanoparticles while providing morphological measurements.
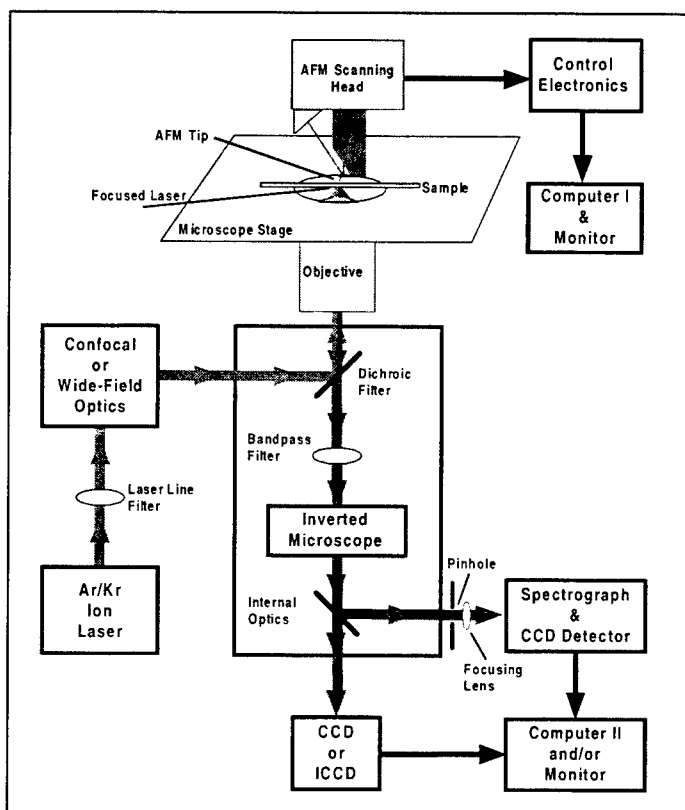
Figure 2: Schematic diagram of an integrated optical and atomic force microscope.

3. RESULTS AND DISCUSSION

3.1 SERS Active Nanoaggregates.

Surfaced enhanced Raman scattering (SERS) and silver nanoparticles has been used to examine the relationship between particle size and optical excitation wavelength.[19, 20] Figure 3 is a plot of particle size as a function of excitation wavelength. Although this plot reveals detailed information of optimum particle size in the visible region of the electromagnetic spectrum, it gives little insight to the near infrared region. According to the electromagnetic theory proposed by Schatz,[21] larger particles should give the largest Raman enhancements at longer wavelengths, where the relationship between particle size and wavelength becomes roughly linear. Kneipp and coworkers have demonstrated that near-infrared excitation coupled with large nanoparticle clusters can detect single molecules in solution.[12]

A common practice in SERS is to activate the colloid with 1 mM sodium chloride. At this

concentration, nanoparticles become activated, but remain as single particles. By increasing the sodium chloride concentration to 50 mM a majority of the particles can couple together to form aggregates. Aggregates created by salt induced aggregation are believed to be more efficient for Raman enhancement. Brus and coworkers[14] suggest that the number of SERS-active particles can be increased with higher concentrations of sodium chloride.
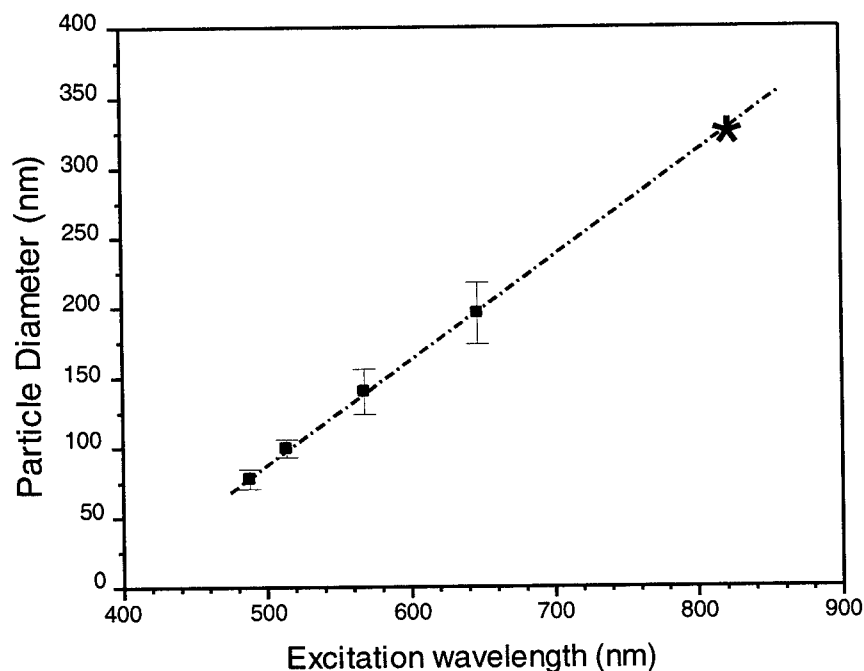
Figure 3. Plot of particle size as a function of excitation wavelength. The particle size values are an average of several measurements determined previously. By extending the line out from previous visible region measurements, one can roughly predict the particle size from an 830 nm excitation source (indicated by the asterisk).

According to Figure 3, if the dashed line were extended linearly out into the near-infrared region, the optimum particle size using a 830 nm excitation source is roughly 300 nm in diameter. However, large metal nanoparticles are difficult to prepare, and in a heterogeneous silver colloid, particles begin to precipitate out of solution around 200 nm. To form large particles, 50 mM sodium chloride was used to cause the smaller particles to aggregate. In theory, the only the aggregated particles would be "hot" or SERS-active. Figure 4 shows a wide-field image of a sample treated with and without 50 mM sodium chloride. As shown, the number of "hot" particles clearly increases through electrolyte induced aggregation. Although a few "hot" particles are visible in the untreated sample, they are not as frequent or as intense and are likely random aggregates formed in the colloidal solution.
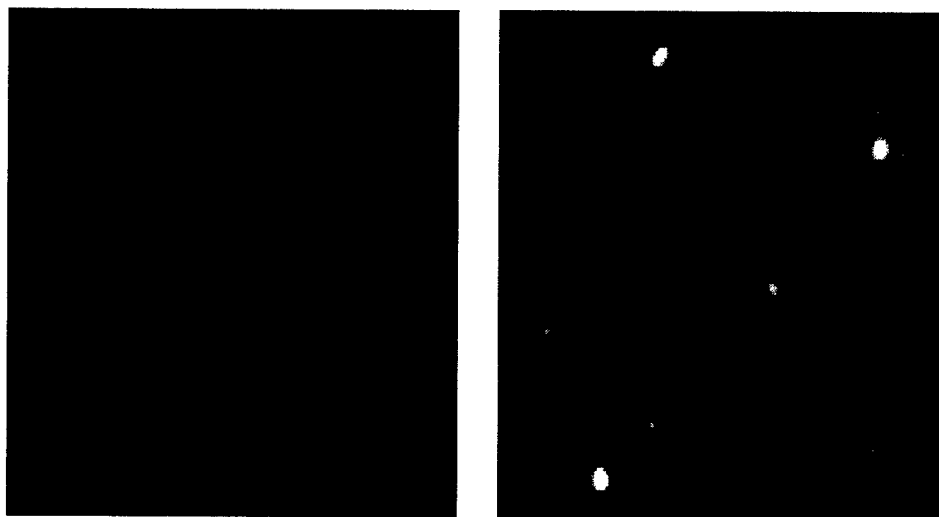
Figure 4. An optical image of SERS-active nanoaggregates recorded by an intensified charged-coupled device. Raman images were obtained from two sets of colloid containing 1 x 10^{-7} M crystal violet. The SERS-active nanoparticles are observed as bright spots. LEFT: a colloid sample activated with sodium chloride (<1 mM added) RIGHT: an aggregated sample. Notice the increase in the number of particles as well as the overall intensity.

3.2 AFM Image of a "Hot" Particle

Figure 5. Detailed AFM image of a typical SERS-active nanoparticle. This particular nanoaggregate consisted of approximately 30 nanoparticles with an average diameter of 35 nm.

Figure 5 shows detailed AFM image of an optically active nanoparticle excited at 830 nm. Only particles that were Stoke-shifted were studied by AFM. As shown several individual nanoparticles (approximately 35 nm in size) compose an active aggregate. These smaller particles appear to form random nanostructures that can come in a variety of shapes in sizes. The average active nanostructure had a cross-section of 290 nm, an average over 10 lateral measurements. We find that these results correlate well with previous single particle measurements (**Figure 3.**). However, it should be mentioned that the previous single particle results were based on height measurements, which are more accurate than lateral measurements.

3.3 SERS Spectrum of an Individual Nanoagregate

To determine if the nanoaggregates examined by AFM are SERS-active, a large number of isolated aggregates were identified by wide-field screening and probed by confocal microscopy. SERS signals were recorded using two different analyte molecules, crystal violet and BPE. **Figure 6** displays the Raman-active vibrational modes of BPE molecules adsorbed onto silver nanoparticles. These signals are in agreement with other reported signals for BPE adsorbed onto silver nanoparticles. [23] It should be noted that no SERS signals could be detected in the absence of sodium chloride.
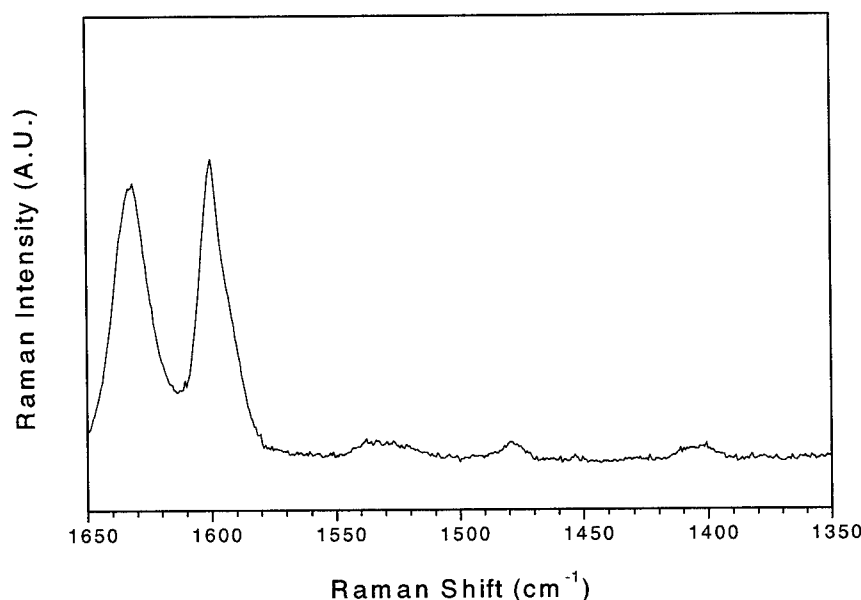
Figure 6. Surface-enhanced Raman scattering spectra of BPE molecules adsorbed on a silver nanoaggregate. Laser wavelength = 830 nm; confocal excitation power = 0.4 mW; data integration time = 1 s; and BPE concentration = 1 x 10^{-5} M.

4. CONCLUSION

In conclusion, we have detected optically "hot" nanoparticles using wide-field illumination and a near-infrared excitation source. AFM images reveal that the SERS-active particles are large aggregates composed of several small particles. This finding is in agreement with previous near-infrared results and gives us a better understanding of the size-tunable optical properties of small metal nanoparticles. However, the SERS-active particles are large aggregates formed by electrolyte addition. This procedure offers little control over regulating particle size, shape and SERS activity. The origin of what makes a particle SERS-active is still a mystery and will require more research to study the intrinsic behavior of nanoparticles at the single particle level. Therefore, a new challenge in nanometer size architecture is to rationally design SERS-active structures. One approach is to use biological materials to selectively construct small nanostructures. Recently Mirkin and coworkers have linked together individual nanoparticles using complementary strands of DNA. [24] Therefore, it might be possible to link several inactive nanoparticles to assemble SERS-active nanoaggregates of particular shapes and sizes to further study the fundamentals of the SERS mechanism.

5. REFERENCES

1. For reviews see: (a) Campion, A.; Kambhampati, P. *Chem Soc. Rev.* **1998**, 27, 241-250. (b) Moskovits, M. *Rev. Mod. Phys.* **1985**, *47*, 783-826.
2. Jeanmaire, D. L.; Van Duyne, R. P. *J. Electroanal. Chem.* **1977**, *1*, 84.
3. Albrecht, M. G.; Creighton, J. A. *J. Am Chem. Soc.* **1977**, *99*, 5215.
4. Moskovits, M. *Rev. Mod. Phys.* **1985**, *57*, 783.
5. Otto, A.; Mrozek, I.; Grabbhorn, H.; Akemann, W. *J. Phys. Condens. Matter* **1992**, *4*, 1143.
6. Schatz, G. C. *Acc. Chem. Res.* **1984**, *17*, 370.
7. (a) Tadayoni, M. A.; Farquharson, S.; Weaver, M. J. *J. Chem. Phys.* **1984**, *80*, 1363. (b) Koglin, E.; Lewinsky, H. H.; Sequaris, J. M. *Surf. Sci.* **1985**, *158*, 370.
8. Zeman, E. J.; Schatz, G. C.; Van Duyne, R. P. *J. Chem. Phys.* **1987**, *87*, 4189.
9. Lombardi, J. R.; Birke, R. L.; Lu, T.; Xu, J. *J. Chem. Phys.* **1986**, *84*, 4174.
10. Hansma, P. K.; Elings, V. B.; Marti, O. *Science* **1988**, *242*, 209.
11. Nie, S.; Emory, S. R. *Science* **1997**, *275*, 1102-1106.
12. (a) Kneipp, K.; Wang, Y.; Kneipp, H.; Perelman, L. T.; Itzkan, I.; Dasari, R. R.; Feld, M. S. *Phys. ReV. Lett.* **1997**, *78*, 1667-1670. (b) Kneipp, K.; Wang, Y.; Kneipp, H.; Itzkan, I.; Dasari, R. R.; Feld, M. S. *Phys. Rev. Lett.* **1996**, *76*, 2444-2447.
13. Xu, H.; Bjerneld, E. J.; Kall, M.; Borjesson, L. *Phys. Rev. Lett.* **1999**, 83(21), 4357-4360.
14. Micheals, A. M.; Nirmal, M.; Brus, L. E.; *J. Amer. Chem. Soc.* **1999**, 12, 9932-9939.
15. Lee, P. C.; Meisel, D. *J. Phys. Chem.* **1982**, 86, 3391-3395.
16. Hildebrandt, P.; Stockburger, M. *J. Phys. Chem.* **1984**, 88, 5935.
17. Emory, S. R.; Nie, S. *J. Phys. Chem B* **1998**, 102, 493-497.
18. Freeman, R.G. et al. *Science* **1995**, 267, 1629. (b) Chumanov, G.; Sokolov, K.; Gregory, B. W.; Cotton, T. M. *J. Phys. Chem.* **1995**, 99, 9466-9471.
19. Emory, S. R.; Haskins, W. E.; Nie, S. *J. Am. Chem. Soc.* **1998**, *120*, 8009-8010.
20. Vlckova, B.; Gu, X. J.; Moskovits, M. *J. Phys. Chem. B* **1997**, 101, 1588-1593.
21. Schatz, G. C. *Acc. Chem. Res.* **1984**, 17, 370-376.
22. Graber, K. C.; Smith, P. C.; Musick, M. D.; Davis, J. A.; Walter, D. G.;Jackson, M. A.; Guthrie, A. P.; Natan, M. J. *J. Amer. Chem. Soc.* **1996**, 118, 1148-1153.
23. (a) Mucic, R. C., Storhoff, J. J., Mirkin, C. A., Letsinger, R. L., *J. Amer. Chem. Soc.* **1998**; 120; 12674-12675. (b) Storhoff, J. J., Elghanian, R., Mucic, R. C., Mirkin, C. A., Letsinger, R. L., *J. Amer. Chem. Soc.* **1998**, 120, 1959-1964. (c) Elghanian, R.; Storhoff, J. J.; Mucic, R. C.; Letsinger, R. L.; Mirkin, C. A. *Science* **1997**, 277, 1078-1081.

Observing single molecule chemical reactions
on metal nanoparticles

Steven R. Emory, W. Patrick Ambrose, Peter M. Goodwin, and Richard A. Keller

Bioscience Division, Los Alamos National Laboratory, MS M888, Los Alamos, NM 87545

ABSTRACT

We report the study of the photodecomposition of single Rhodamine 6G (R6G) dye molecules adsorbed on silver nanoparticles. The nanoparticles were immobilized and spatially isolated on polylysine-derivatized glass coverslips, and confocal laser microspectroscopy was used to obtain surface-enhanced Raman scattering (SERS) spectra from individual R6G molecules. The photodecomposition of these molecules was observed with 150-ms temporal resolution. The photoproduct was identified as graphitic carbon based on the appearance of broad SERS vibrational bands at 1592 cm^{-1} and 1340 cm^{-1} observed in both bulk and averaged single-molecule photoproduct spectra. In contrast, when observed at the single-molecule level, the photoproduct yielded sharp SERS spectra. The inhomogeneous broadening of the bulk SERS spectra is due to a variety of photoproducts in different surface orientations and is a characteristic of ensemble-averaged measurements of disordered systems. These single-molecule studies indicate a photodecomposition pathway by which the R6G molecule desorbs from the metal surface, an excited-state photoreaction occurs, and the R6G photoproduct(s) readsorbs to the surface. A SERS spectrum is obtained when either the intact R6G or the R6G photoproduct(s) are adsorbed on a SERS-active site. This work further illustrates the power of single-molecule spectroscopy (SMS) to reveal unique behaviors of single molecules that are not discernable with bulk measurements.

Keywords: surface-enhanced Raman scattering (SERS), nanoparticles, single-molecule detection (SMD), single-molecule spectroscopy (SMS), Rhodamine 6G (R6G).

1. INTRODUCTION

There have been many recent reports of surface-enhanced Raman scattering (SERS) at the single-molecule level. These new results have generated considerable excitement in both the Raman and single-molecule spectroscopy communities.[1] The observed enhancement factors are on the order of 10^{14} to 10^{15},[2-5] which are much larger than ensemble-averaged values (10^6 to 10^8) obtained with conventional SERS measurements[6]. Both electromagnetic and chemical enhancement mechanisms have been proposed to explain the SERS phenomenon.[6] An additional finding of these new studies is the presence of optically "hot" nanoparticles that are highly efficient for surface enhancement.[2-5,7] Raman scattering from these optically "hot" nanoparticles occurs intermittently.[2,4,5] This blinking behavior is similar in appearance to discontinuous fluorescence emission observed for single dye molecules[8-10] and single semiconductor quantum dots,[11-13] but the fundamental mechanisms have yet to be definitively determined in many cases. By probing one nanoparticle at a time, these studies have overcome the effects of ensemble averaging and have revealed the intrinsic properties associated with single nanoparticles.

A major advantage of single-molecule detection (SMD) and spectroscopy (SMS) is the ability to reveal events masked by ensemble-averaging inherent in bulk measurements. Various groups have successfully exploited this using laser-induced fluorescence (LIF) to study single-molecule photodynamics, photochemistry, and molecular dynamics.[8-10,14-20] An extension of these studies is to follow a complete chemical reaction at the single-molecule level. This has been accomplished to a limited degree by LIF. For example, the photobleaching of fluorescent molecules such as B-phycoerythrin,[17] R6G,[18,19] and allophycocyanin trimers[20] have been studied. However, SMD by LIF is limited to the study of highly fluorescent molecules and often does not provide sufficient spectral information for chemical identification. In the case of photobleaching, only the disappearance of the analyte is observed and the identity of the

Further author information:
S.R.E. (correspondence): E-mail: semory@lanl.gov; Telephone: (505) 665-2092; Fax: (505) 665-3024
W.P.A.: E-mail: wpa@lanl.gov; Telephone: (505) 665-2092; Fax: (505) 665-3024
P.M.G: E-mail: pmg@lanl.gov; Telephone: (505) 665-2092; Fax: (505) 665-3024
R.A.K.: E-mail: keller@lanl.gov; Telephone: (505) 667-3018; Fax (505) 665-3024

nonfluorescent photoproduct(s) must be determined by other means. An ideal SMD method would allow the detection and identification of both the reactant and product molecules. Single-molecule SERS spectroscopy has the potential to provide such information via a vibrational fingerprint and, unlike LIF, does not require the analyte to be fluorescent.

In this work, we take advantage of the single-molecule sensitivity and structural information provided by SERS to follow the photodecomposition reaction of individual R6G molecules adsorbed on silver nanoparticles. In the case of R6G, there is an abundance of SERS studies in the literature including studies at the single-molecule level.[1] Photochemistry of molecules adsorbed on metal surfaces, such as silver, has also been studied extensively by SERS. In some cases, surface-enhanced photochemistry has been observed. The concept of surface-enhanced photochemistry was first outlined by Nitzan and Brus[21] and has since been extended by other groups.[22,23] Experimental studies, lead by Moskovits and coworkers,[24] have reported this phenomenon for a wide range of adsorbed species.[24-26] The fundamental conclusion is that the same electromagnetic field enhancement involved in SERS is also capable of enhancing photochemical reactions on SERS-active substrates. Experimental and theoretical studies have determined the most efficient location for surface-enhanced photochemistry is not on the metal surface, but rather a short distance away from the surface. Although the electromagnetic field decreases as a function of distance from the surface, the excited-state lifetime increases as the molecule moves away. Therefore, at a position slightly above the surface, a maximum photochemical rate can be reached where the two competing effects are balanced. In the case of R6G, the increased photostability on metal surfaces was attributed to efficient nonradiative damping of electronic excited states.[18,27] However, as is described in this report, R6G does undergo photodecomposition on silver nanoparticles, albeit at a reduced rate. Our single-molecule SERS data provides important new information that aids in understanding the photodecomposition and blinking mechanisms observed for R6G on silver.

2. EXPERIMENTAL

2.1 Materials
Silver nitrate (analytical grade, Aldrich), sodium citrate (analytical grade, Fisher), sodium chloride (biological grade, Fisher), Rhodamine 6G perchlorate (Molecular Probes), and poly-L-lysine hydrobromide (molecular weight 2.5×10^6 g/mole, Sigma) were used as received. Ultrapure water (18 MΩ·cm, Millipore) was used to prepare all aqueous solutions. Pure ethanol (99+%, Quantum Chemical) was used for diluting the R6G stock solution. Glass microscope coverslips (No. 1, 25 x 25 mm, Corning) were cleaned in concentrated sulfuric acid for approximately one minute, rinsed with copious amounts of ultrapure water, and dried with nitrogen.

2.2 Colloidal Silver Synthesis
The silver colloid was prepared by the citrate reduction method outlined by Lee and Meisel.[28] Colloid concentration was determined to be 3×10^{11} nanoparticles/mL and the absorbance spectrum showed a maximum at ~420 nm, characteristic of ~35 nm diameter silver nanoparticles. The colloid was stored in a sealed Erlenmeyer flask and was stable for several months.

2.3 Preparation of Samples for Single-Molecule SERS Studies
For single-molecule studies, a 5-μL aliquot of 1 nM R6G in ethanol was added directly to 250 μL of silver colloid in a 500-μL polypropylene microcentrifuge tube. This corresponds to ~0.1 R6G molecules per nanoparticle. The mixture was immediately mixed with a pipette and then vortexed for approximately 10 seconds. After 10 minutes, 9.4 μL of 20 mM sodium chloride was added and mixed to activate the colloid as described in previous studies.[2,29] The R6G/colloid mixture was allowed to incubate at room temperature for at least 30 minutes prior to immobilization on polylysine-coated glass coverslips for analysis.

The nanoparticles were immobilized on polylysine-coated glass coverslips using the following procedure:[2,7] 5 μL of the R6G/colloid mixture was placed on a polylysine-coated glass coverslip (~2 nanoparticles per μm^2). An uncoated glass coverslip was used to spread evenly the solution between the two coverslips. The negatively charged nanoparticles (the citrate that stabilizes the colloid is negatively charged) electrostatically bind to the positively charged surface. After approximately 10 minutes, the two coverslips were pulled apart. The polylysine-coated coverslip was then air-dried prior to analysis. A majority of the nanoparticles was sufficiently spatially isolated (>1 μm apart) to allow far-field microscopy to interrogate single nanoparticles or nanoaggregates (2 to 5 nanoparticles) at a time. The sample was then positioned on the microscope stage (Section 2.5) for analysis, and no further characterization was performed to determine if single nanoparticles or nanoaggregates were probed.

2.4 Preparation of Samples for Ensemble-Averaged SERS Studies

More concentrated samples for ensemble-averaged measurements were prepared in the same manner as described for single-molecule SERS samples (Section 2.3) with the following changes: a 5-µL aliquot of 10 µM R6G in ethanol was added to the colloid (to yield ~1000 R6G molecules per nanoparticle); 20 µL of the R6G/colloid mixture was placed and air-dried onto a polylysine-coated coverslip with a spot diameter of approximately 5 mm. This corresponds to a density of approximately 300 nanoparticles per μm^2. The sample was then positioned on the microscope stage (Section 2.5) for analysis.

2.5 Instrumentation

A confocal Raman microscope was constructed to obtain SERS spectra from single isolated nanoparticles or nanoaggregates (Figure 1). The 514.5-nm laser line from an argon ion laser (Innova 90, Coherent) was used for excitation. Approximately 5 mW of laser light was focused to a spot ~600 nm in diameter[30] yielding an irradiance of 2 MW/cm^2 or 5×10^{24} photons/(s·cm²). A mechanical shutter (SH) was used to minimize laser-induced damage to the sample when spectra were not being collected. A laser line notch-filter (F1, 514LF, Omega Optical) was used to filter the
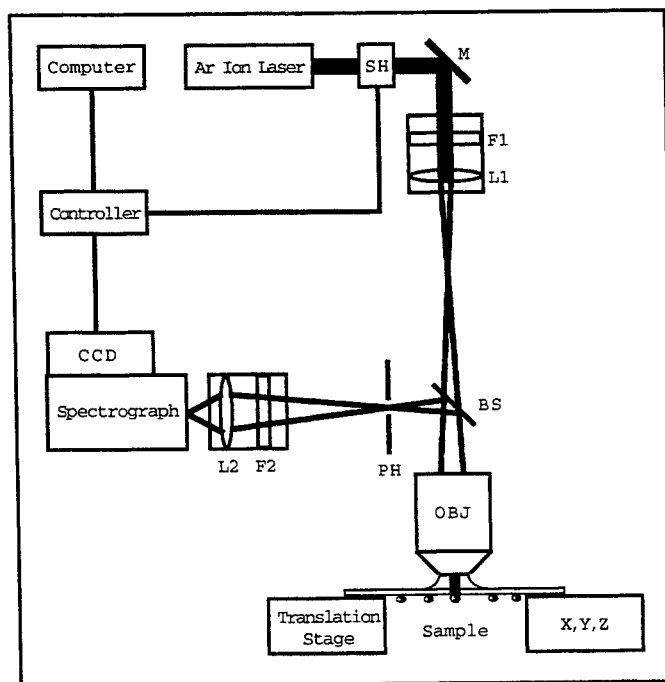

Figure 1. Diagram of confocal Raman microscope. See text for discussion.

background from the plasma discharge. An achromatic, plano-convex focusing lens (L1, f = 150 mm, aperture = 21.5 mm, Melles Griot) was used to expand the beam to fill the back aperture of an oil immersion objective (100x, 1.1NA, Zeiss). The sample coverslip was mounted horizontally on an x,y,z-translation stage using Scotch™ tape. Immersion oil (Type DF, η_D = 1.5150 +/- 0.0002, Cargille) was placed directly between the objective and the glass coverslip. Stokes-shifted Raman light was collected in an epi-illumination geometry. A dichroic reflector (BS, 525DRSP, Omega Optical) directed the collected light to a pinhole (PH, diameter = 1 mm) for stray-light rejection. An angle-tunable holographic Raman notch filter (F2, HSPF-515.5-1.0, Kaiser Optical) filtered out the reflected or Rayleigh backscattered excitation photons. An aspheric lens (L2, C220TM-A, f = 11.0 mm, 0.25NA, Thorlabs) focused the light onto the entrance slit (500 µm) of a high-throughput imaging spectrograph (f-number = 2.2, Holospec, Kaiser Optical). Spectra were acquired with a thermoelectrically-cooled CCD camera (Model number TWA/CCD-1242-EM-1, Roper Scientific [formerly Princeton Instruments]) operated at 1 MHz (12 bits) and optimized for rapid spectral acquisition. Spectra were processed with *Winspec* software (v. 1.6, Princeton Instruments). A 100 x 1152 strip was selected out of the total 1242 x 1152 pixel CCD chip. The pixels where the analyte spectrum was focused (10 x 1152) were binned vertically to a final configuration of 1 x 1152. The detector readout time was measured with an oscilloscope to be 50 ms. An integration time of 100 ms was necessary to acquire single-molecule SERS spectra with reasonable signal to noise. Thus for a given spectrum, a total of 150 ms (100 ms integration plus 50 ms deadtime readout) was required for spectral acquisition. CCD detector counts were converted to photoelectrons (pe) by multiplying by 35 photoelectrons/count (manufacturer's

specification). For displayed spectra, intensity was calculated as pe/(s·bin) obtained by dividing the pe/bin by the integration time.

# 3. RESULTS

3.1 Ensemble-Averaged SERS Spectra

Figure 2 shows the photodecomposition SERS spectra of an ensemble of R6G molecules adsorbed on an aggregate of silver nanoparticles. Approximately 1000 R6G molecules were adsorbed on each nanoparticle and there were approximately 300 nanoparticles in the confocal laser spot (~3 x 10^5 molecules probed). Because the absorption band of the analyte was in resonance with the excitation frequency, excited-state photodecomposition can occur.[31] The gradual progression from the narrow SERS peaks (<20 cm^{-1} FWHM) of the intact R6G to the broad SERS peaks (>100 cm^{-1} FWHM) of the photoproduct is observed. The final SERS spectrum (t = 30.00 s) is a sum of SERS spectra from intact R6G and R6G photoproduct(s). The photoproduct's two major SERS peaks at 1592 cm^{-1} and 1340 cm^{-1} are labeled in Figure 2.

To determine the rate of the photochemical reaction, the disappearance of the 1648 cm^{-1} R6G SERS peak was monitored because it is virtually free of interference from SERS bands of the photoproduct(s). The area of this peak (A$_{1648}$), which is proportional to the concentration of intact R6G, was plotted as a function of time (t) as shown in Figure 3. The following exponential decay function was used to determine the photochemical rate constant (k) where t is time, B is the area of the 1648 cm^{-1} peak at t = 0, and C is a constant used to correct for the background offset:

$$A_{1648} = Be^{-kt} + C \qquad (1)$$

The rate of photodecomposition of R6G (k) was determined under the set of experimental conditions described in Figure 2 to be 0.156 ± 0.007 s^{-1}. The photochemical rate constant was then determined in the same manner for a series of excitation powers. A log/log plot of the photochemical rate versus the excitation power yields a line with a slope of 0.9 ± 0.1 with a correlation coeffecient (R) of 0.98 (data not shown) demonstrating that the photodestruction is a first-order process.

A photodecomposition quantum yield (ϕ_d) has been used to assess the photostability of fluorescent dyes.[32] This value is defined as the fraction of absorbed photons that cause a photodestruction event, and typically ranges from 10^{-5} to 10^{-7} for relatively photostable dye molecules in solution. A similar value can be calculated for the photostability of R6G on silver (ϕ_{dSERS}) using the experimentally determined SERS photochemical rate constant (k) and the photon excitation rate (k_{ex}). k_{ex} was calculated using Equation (2) where M is the irradiance of the laser spot in photons/(s·cm^2) and σ_{SERS} is the surface-enhanced Raman scattering cross section. The
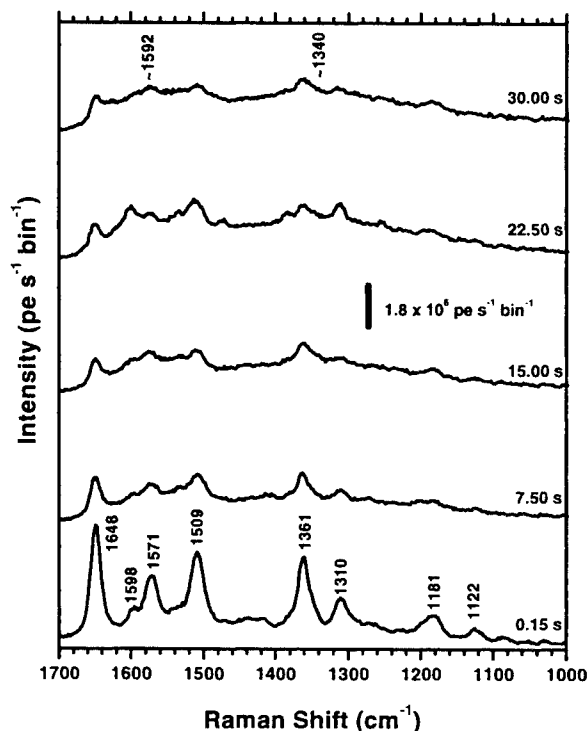
Figure 2. Bulk ensemble-averaged photodecomposition SERS spectra of R6G on silver nanoparticles. Five SERS spectra that highlight spectral changes are displayed with elapsed time noted. The scale bar represents 1.8 x 10^6 pe/(s·bin). There are 2.3 cm^{-1}/bin. The R6G concentration was 20 x 10^{-8} M corresponding to ~1000 R6G molecules per nanoparticle and there were ~300 nanoparticles in the laser spot. λ_{ex} = 514.5 nm; t$_{int}$ = 100 ms; t$_{readout}$ = 50 ms; M = 5 x 10^{24} photons/(s· cm^2). Spectra are offset for clarity.
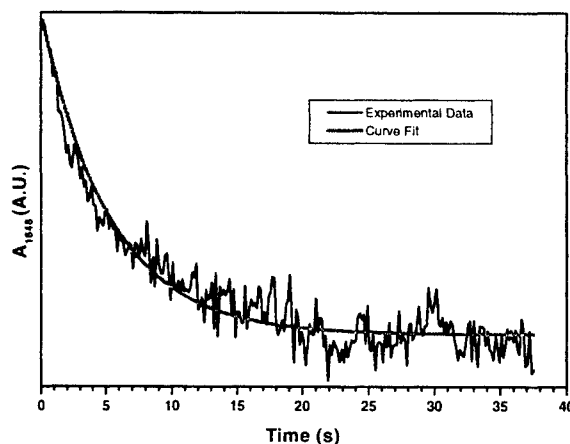
Figure 3. Bulk photodecomposition of R6G on silver nanoparticles. The area of the 1648 cm^{-1} R6G peak (A$_{1648}$) is plotted vs. time. The R6G concentration is 20 x 10^{-8} M corresponding to ~ 1000 R6G molecules per nanoparticle. λ_{ex} = 514.5 nm; t$_{int}$ = 100 ms; t$_{readout}$ = 50 ms; M = 5 x 10^{24} photons/(s· cm^2). The experimental data was fitted using Equation (1) with a reduced chi-squared value of 0.73. A photochemical rate constant (k) of 0.156 ± 0.007 s^{-1} was determined from the fit.

σ_{SERS} replaces the absorption cross section that would be used to determine k_{ex} for fluorescence. For R6G on silver, σ_{SERS} has been estimated to be between 10^{-16} and 10^{-15} cm^2/molecule using 514.5-nm excitation. [2-5]

$$k_{ex} = M\sigma_{SERS} \qquad (2)$$

With an M of 5 x 10^{24} photons/(s·cm^2), k_{ex} ranges from 500 to 5000 MHz depending on the value of σ_{SERS}. ϕ_{dSERS} calculated from Equation (3) was in the range of 10^{-11} and 10^{-10} using k obtained from the curve fit (Figure 3) and the calculated k_{ex}.

$$\phi_{dSERS} = k/k_{ex} \qquad (3)$$

3.2 Single-Molecule SERS Spectra

In contrast to the ensemble-averaged SERS spectra described in Section 3.1, SERS spectra during the photodecomposition of a single R6G molecule are shown in Figure 4. At the single-molecule level, the transition from the intact R6G molecule to the R6G photoproduct can be seen to occur in discrete steps. In the beginning, fluctuations in the R6G spectral intensity were observed that have previously been reported (Figure 4a-e). [2,4,5] The intact R6G SERS spectra survived for approximately 12.90 s (Figure 4e) before it disappeared (Figure 4f). After a delay of approximately 3 seconds, a significantly altered SERS spectrum appeared (Figure 4g) and was followed by similar SERS spectra (Figure 4h-j). These spectra are believed to arise from the R6G photoproduct(s). The curiously long absence of SERS spectra (13.05 s to 15.90 s) before the observation of a photoproduct SERS spectrum was consistently observed with delays ranging from a few seconds to over ten seconds (50 total observations). The single-molecule SERS bands of the photoproduct were broader (~20 to 100 cm^{-1} FWHM) than those observed for the intact R6G (<20 cm^{-1} FWHM); however, the SERS spectra of single-molecule photoproducts were narrower than those found for the bulk ensemble-averaged spectra (>100 cm^{-1} FWHM, Figure 2). The photoproduct SERS spectra also exhibited increased intensity fluctuations and a wide variability in the SERS peak frequencies.
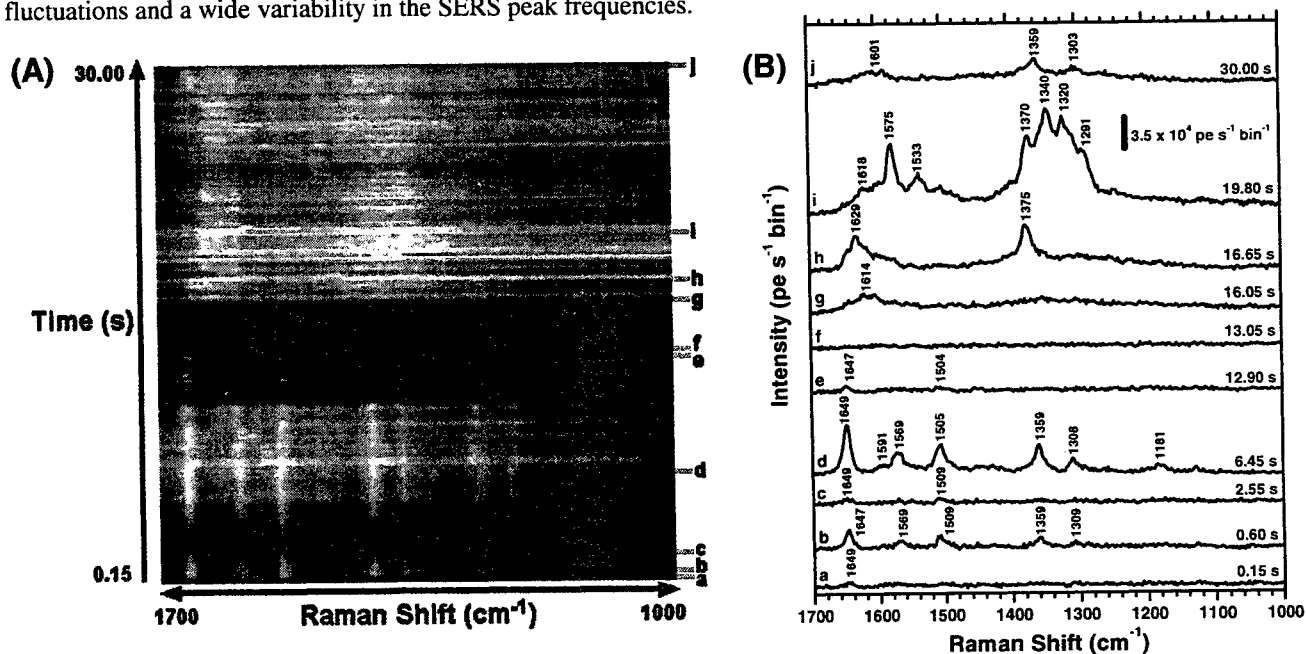

Figure 4. Photodecomposition of a single R6G molecule adsorbed on a silver nanoparticle. (A) Gray-scale intensity plot of 200 consecutive SERS spectra collected during the photodecomposition of a single R6G molecule. Intensity increases from black to white. Letters on the right side of the plot indicate the position of the corresponding SERS spectra shown in (B). Fluctuations in the SERS intensity can clearly be observed for both R6G and R6G photoproduct(s). The R6G SERS spectra (a to e) disappeared (f) and did not return after 13.05 s. After a delay of ~3 s it was followed by a photoproduct SERS spectrum (g) at 16.05 s. Significant changes in the SERS peak frequencies were observed in both R6G and photoproduct(s) SERS spectra. (B) Ten selected SERS spectra (from the 200 spectra in A) are displayed to highlight spectral changes. The letters correspond to the letters in (A) and the acquisition time of each spectrum is displayed on the right. The scale bar represents 3.5 x 10^4 pe/(s·bin). There are 2.3 cm^{-1}/bin. Spectra are offset for clarity. Small changes in peak frequencies were observed in the R6G SERS spectra (a to e) and are attributed to changes in the orientation and local environment. Larger changes in the photoproduct SERS spectra (g to j) were observed and are attributed to changes in orientation, local environment, and the formation of additional photoproducts. Spectra were obtained under the following experimental conditions: R6G concentration was 20 x 10^{-12} M corresponding to ~ 0.1 R6G molecules per nanoparticle. λ_{ex} = 514.5 nm; t_{int} = 100 ms; $t_{readout}$ = 50 ms; M = 5 x 10^{24} photons/(s·cm^2).

The photochemical rate constant (k) was calculated using the survival times ($t_{survival}$) obtained for individual R6G molecules on silver. A similar method has been used to determine photobleaching rates for fluorescent molecules using LIF.[16b,17] The $t_{survival}$ of a single molecule was defined as the time when the R6G SERS spectrum dropped to the background level and was followed by a subsequent photoproduct SERS spectrum. Figure 5 shows a histogram of compiled survival times for fifty individual R6G molecules. The data were fitted to Equation (1), with C constrained to zero, and a rate constant of 0.13 ± 0.02 s^{-1} was obtained from the fit. Because of the sparse nature of the data, k was also calculated using a maximum likelihood estimator (MLE) method[33] to verify the results obtained from the least squares fit. Since all the observed R6G molecules photodecomposed during the observation time, k was determined using Equation (4) where N is the number of observed events divided by the sum of $t_{survival}$.

$$k = N/\Sigma\ t_{survival} \qquad (4)$$

The MLE method yielded a $k = 0.16 \pm 0.02$ s^{-1} that is in agreement with the value obtained from the least squares fit (Figure 5). ϕ_{dSERS} was then calculated with Equation (3) to be between 10^{-10} and 10^{-11} and is in good agreement with the values obtained from ensemble-averaged measurements (Section 3.1).
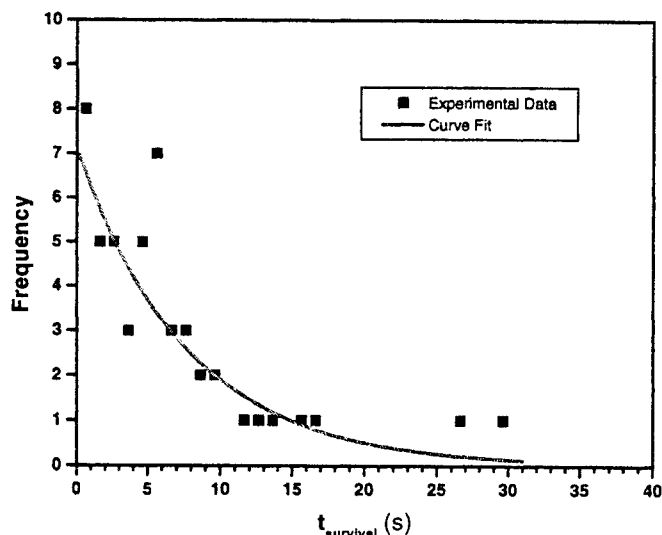

Figure 5. Histogram of individual survival times (squares). The data were binned using 1-s intervals and were fitted to Equation (1) with C constrained to zero (reduced chi-squared = 0.34). k was determined to be 0.13 ± 0.02 s^{-1} from the fit. The following experimental conditions were used for all 50 samples observed: R6G concentration was 20 x 10^{-12} M corresponding to ~ 0.1 R6G molecules per nanoparticle. λ_{ex} = 514.5 nm; t_{int} = 100 ms; $t_{readout}$ = 50 ms; M = 5 x 10^{24} photons/(s·cm^2).

4. DISCUSSION

4.1 Identification of R6G Photoproduct

The photoproduct SERS spectrum can be obtained either from an ensemble-averaged SERS spectrum that has the intact R6G spectrum subtracted out, or by adding a number of single-molecule R6G photoproduct SERS spectra (Figure 6). For simplicity, the identification of the R6G photoproduct was determined from these spectra that show broad peaks at 1592 cm^{-1} and 1340 cm^{-1} because of the complexity and variety of the single-molecule R6G photoproduct SERS spectra. However, the individual photoproducts could conceivably be identified using molecular models for SERS.[34] The SERS spectra shown in Figure 6 have been attributed to graphitic carbon.[35,36] Highly ordered macroscopic graphite crystals exhibit a narrow Raman band at 1575 cm^{-1}. This is attributed to in-plane atomic displacement and is of E_{2g}-symmetry. This band shifts slightly to higher frequencies (~1590 cm^{-1}) for very small graphite crystals. A Raman peak at approximately 1355 cm^{-1} arises from the symmetry forbidden A_{1g} mode of small crystallites or boundaries found in larger crystals. The ratio of the intensities of these two peaks can be used to estimate the size of the graphitic carbon photoproduct. Using the linear relationship developed by Tuinstra and Koenig,[35] we conservatively estimate the graphite
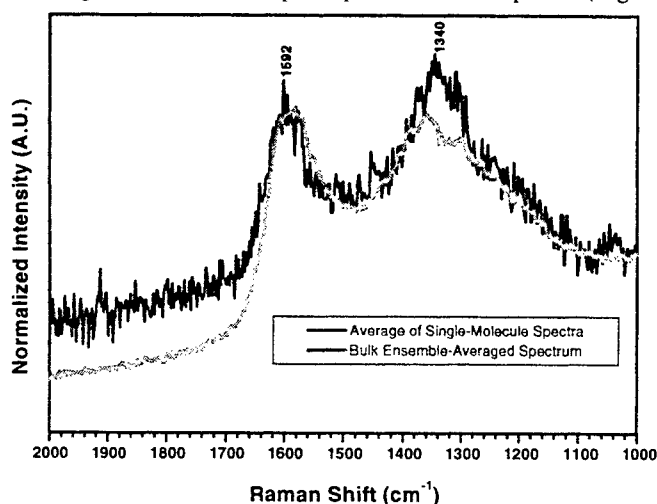

Figure 6. SERS spectra of R6G photoproduct(s). The solid line is a sum of 500 individual R6G photoproduct(s) SERS spectra. The gray line is from an ensemble-averaged measurement with the intact R6G SERS spectrum subtracted. For ease of comparison, both spectra are normalized to the 1592 cm^{-1} peak.

fragments to be less than 5 nm in diameter. Our spectra with peaks at 1592 cm^{-1} and 1340 cm^{-1} are also consistent with the presence of extremely small graphite fragments. The individual R6G photoproduct(s) (Figure 4g-j) are believed to be various forms of graphitic carbon fragments that are the result of excited-state photochemical reaction(s) of R6G.

We were initially concerned that the observed graphitic carbon SERS spectrum could be the result of either carbon contamination[37] or possibly the citrate ions used to stabilize the colloidal nanoparticles.[38] However, blank samples under the same conditions yielded no detectable graphitic carbon SERS spectra. Additionally, the SERS spectrum of citrate ions consists of a weak peak at 1580 cm^{-1} (carboxylate group asymmetric stretch) and a strong peak at 1415 cm^{-1} (carboxylate symmetric stretch). Therefore, we have excluded carbon contamination and citrate ions as possible sources of the observed graphitic carbon SERS spectrum.

4.2 Photodecomposition Reaction Pathway

A striking difference between the ensemble-averaged and single-molecule data sets is the appearance of "off" times in the single-molecule SERS spectral traces (Figure 7A). This phenomenon has previously been reported for R6G on silver and has been only observed in single-molecule studies.[2,5] Brus and coworkers proposed that these "on" and "off" times are the result of a single R6G molecule adsorbing and desorbing from a SERS-active site repeatedly.[5] This
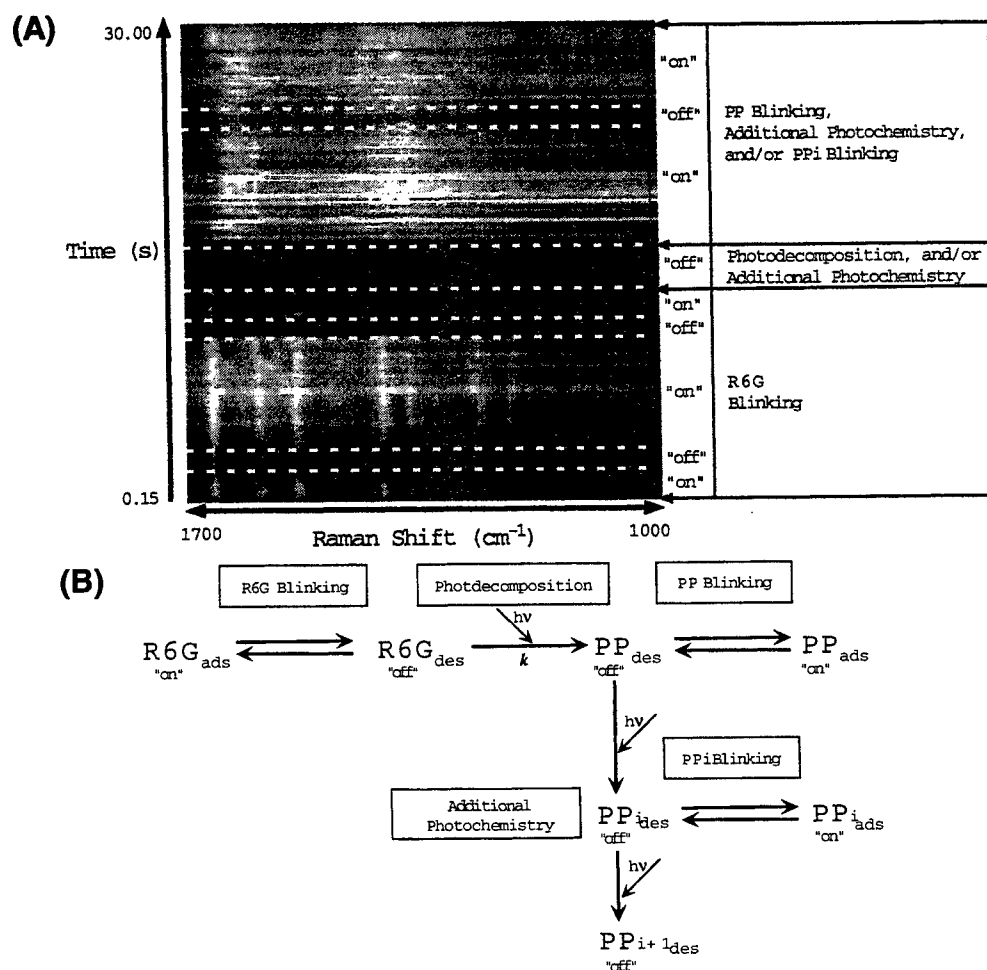
Figure 7. (A) The same gray-scale intensity plot in Figure 4 is shown with the reaction steps of the proposed photodecomposition pathway labeled on the right. Adsorption or "on" periods when SERS spectra were detected are labeled "on". Desorption or "off" periods when no SERS spectra were detected are labeled "off". Dashed lines indicate transitions between the "on" and "off" states. (B) A proposed pathway for the photodecomposition of R6G on silver. The blinking observed for the intact R6G SERS spectra is explained by reversible adsorption (R6G$_{ads}$) and desorption (R6G$_{des}$) of the R6G to and from a SERS-active site (R6G Blinking). Only when R6G is adsorbed to an active-site are R6G SERS spectra observed. During the desorption time, R6G may undergo irreversible excited-state photodecomposition (Photodecomposition). After photodecomposition, the photoproduct (PP) may readsorb to a SERS-active site (PP Blinking) or undergo additional photodecomposition (Additional Photochemistry) before readsorbing to a SERS-active (PPi Blinking). Upon adsorption, PP SERS spectra may be obtained.

behavior cannot be observed with ensemble-averaged measurements because the asynchronous adsorption and desorption of many molecules occurs simultaneously. When the R6G is slightly removed from the surface during these "off" or desorption times, it is more susceptible to excited-state photoreactions. This is because the local electromagnetic field is enhanced and the R6G molecular excited-states are not as efficiently quenched by the metal surface.[21-24] Based on the adsorption/desorption "blinking" theory and the model of surface-enhanced photochemistry, we propose a pathway by which the photodecomposition of R6G occurs during this desorption or "off" time and the graphitic carbon photoproduct (PP) SERS spectra are obtained when the PP adsorbs to a SERS-active site.

Figure 7B outlines the proposed photodecomposition pathway for R6G on silver and Figure 7A relates the proposed pathway to our single-molecule SERS data. The first step in the pathway involves the reversible adsorption and desorption of R6G to and from a SERS-active site (Figure 7B, R6G Blinking). When chemisorbed to an active-site ($R6G_{ads}$), a strong SERS spectrum is obtained because both chemical and electromagnetic enhancements are active.[2,5,6] Upon desorption ($R6G_{des}$), chemical enhancement ceases while electromagnetic enhancement is diminished. The molecule may move onto a layer of condensate or molecular ions such as citrate that act as a spacer layer. No SERS spectrum is detected because of the decrease in enhancement and the period is said to "off". It should be stated that although a diminished electromagnetic field enhancement may be sufficient to obtain a SERS spectrum from a large ensemble of desorbed species, the loss of chemical enhancement renders a single molecule undetectable with current instrument limitations. The $R6G_{des}$ is able to readsorb to the SERS-active site before photodecomposing and thus another R6G SERS spectrum can be obtained (Figure 7A, R6G Blinking). However, the $R6G_{des}$ can undergo irreversible excited-state photodecomposition in the desorbed state (Figure 7A, Photodecomposition). After photodecomposition, the PP can either adsorb to a SERS-active site to yield a PP SERS spectrum (Figure 7A, PP Blinking) or undergo further photodestruction (Figure 7A, Additional Photochemistry) before adsorbing and yielding a PPi SERS spectrum (Figure 7A, PPi Blinking). The presence of an "off" time prior to the appearance of the first PP SERS spectrum (Figure 4 and Figure 7B) is consistent with photodecomposition occurring in the desorbed state. However, the length of this "off" time (~seconds) is surprisingly long and warrants further study.

4.3 Inhomogeneous Broadening of Photoproduct SERS Spectra

Another difference between the ensemble-averaged and single-molecule spectra was in the SERS linewidths of the graphitic carbon photoproduct(s). Single-molecule photoproduct SERS spectra were narrower (~20 to 100 cm^{-1} FWHM, Figure 4) than the bulk ensemble-averaged spectra (>100 cm^{-1} FWHM, Figure 6). However, when single-molecule photoproduct spectra are added together, the result is an ensemble-like spectrum (Figure 6). This is consistent with an inhomogeneously broadened bulk ensemble-averaged photoproduct SERS spectrum due to a distribution of photoproducts in varying surface environments and orientations.[39]

An additional finding was that the photoproduct(s) exhibited greater temporal fluctuations in SERS intensity compared to R6G (data not shown); we attribute this to a difference in the strength of adsorption of R6G and graphitic carbon to silver. R6G adsorbs strongly to silver in the presence of chloride ions via a Ag-N bond ($|\Delta H_{ads}| = 65$ kJ/mol),[29] while graphitic carbon only weakly physisorbs to silver ($|\Delta H_{ads}| < 40$ kJ/mol). The difference in ΔH_{ads} means it is easier for graphitic carbon to desorb from the surface and, as a result, it blinks "on" and "off" faster than the chemisorbed R6G. This behavior inhomogeneously broadens the SERS spectra in two ways: (1) the photoproduct may undergo additional photodecomposition when it desorbs and thus its SERS spectrum will change; and (2) the photoproduct may rapidly change surface orientation resulting in an altered SERS spectrum.

4.4 Photostability of R6G on Silver Nanoparticles

It is important to note that the exceptional photostability of R6G on silver nanoparticles allows the photodecomposition reaction to occur on an observable time scale. The experimentally determined ϕ_{dSERS} is between 10^{-11} and 10^{-10} that is *3 to 4 orders* of magnitude more stable than the best fluorescent dye molecules in solution.[32] It should also be stated that there may be additional photodecomposition pathways that are too fast (k > 1 s^{-1}) for our present system to monitor. However, the initial R6G ensemble-averaged SERS spectrum (Figure 2) did not display significant signs of photodecomposition that would be present if a faster reaction was occurring. Additionally, the fact that the ensemble-averaged ($k = 0.156 \pm 0.007$ s^{-1}) and single-molecule ($k = 0.13 \pm 0.02$ s^{-1}) photodecomposition rate constants are in agreement suggests that we are monitoring the dominant photodecomposition pathway.

5. CONCLUSIONS

This work demonstrates that single-molecule measurements can provide valuable new insights into chemical reactions by removing the mask of ensemble averaging. Based on the observed single-molecule SERS spectra, we postulate that the photodecomposition of R6G to graphitic carbon occurs when the R6G desorbs from the SERS-active site. The observation of long "off" times prior to the detection of photoproduct spectra is in accord with the hypothesis that the blinking behavior is caused by adsorption/desorption of R6G to and from SERS-active sites. This pathway is also consistent with theoretical predictions of photochemistry occurring slightly above the metal surface where a balance is struck between the enhanced electromagnetic field and the excited-state lifetime. These results further demonstrate how single-molecule SERS spectroscopy may be used to study chemical reactions at the single-molecule level. In the future, single-molecule SERS studies may be expanded to study biological or catalytic reactions to gain further insight into diverse reaction pathways.

REFERENCES

1. For recent reviews: (a) Kneipp, K.; Kneipp, H.; Itzkan, I.; Dasari, R. R.; Feld, M. S. "Ultrasensitive Chemical Analysis by Raman Spectroscopy," *Chem. Rev.* **1999**, *99*, 2957. (b) Campion, A.; Kambhampati, P. "Surface-enhanced Raman scattering," *Chem. Soc. Rev.* **1998**, 27, 241.
2. (a) Nie, S.; Emory, S. R. "Probing single molecules and single nanoparticles by surface-enhanced Raman scattering," *Science* **1997**, 275, 1102. (b) Krug II, J. T.; Wang, J. D.; Emory, S. R.; Nie, S. "Efficient Raman enhancement and intermittent light emission observed in single gold nanocrystals," *J. Am. Chem. Soc.* **1999**, *121*, 9208.
3. (a) Kneipp, K.; Wang, Y.; Kneipp, H.; Perelman, L. T.; Itzkan, I.; Dasari, R. R.; Feld, M. S. "Single molecule detection using surface-enhanced Raman scattering (SERS)," *Phys. Rev. Lett.* **1997**, 78, 1667. (b) Kneipp, K.; Wang, Y.; Kneipp, H.; Itzkan, I.; Dasari, R. R.; Feld, M. S. "Population pumping of excited vibrational states by spontaneous surface-enhanced Raman scattering," *Phys. Rev. Lett.* **1996**, 76, 2444. (c) Kneipp, K.; Kneipp, H.; Kartha, V. B.; Manoharan, R.; Deinum, G.; Itzkan, I.; Dasari, R. R.; Feld, M. S. "Detection and identification of a single DNA base molecule using surface-enhanced Raman scattering (SERS)," *Phys. Rev. E* **1998**, 57, R6281.
4. Xu, H.; Bjerneld, E. J.; Kall, M.; Borjesson, L. "Spectroscopy of single hemoglobin molecules by surface enhanced Raman scattering," *Phys. Rev. Lett.* **1999**, 83, 4357.
5. Michaels, A. M.; Nirmal, M.; Brus, L. E. "Surface enhanced Raman spectroscopy of individual Rhodamine 6G molecules on large Ag nanocrystals," *J. Am. Chem. Soc.* **1999**, *121*, 9932.
6. For general SERS reviews: (a) Moskovits, M. "Surface-enhanced spectroscopy," *Rev. Mod. Phys.* **1985**, *57*, 783. (b) Otto, A.; Mrozek, I.; Grabhorn, B.; Akemann, W. "Surface-enhanced Raman scattering" *J. Phys. Condens. Matt.* **1992**, *4*, 1143. (c) Schatz, G. C. "Theoretical studies of surface-enhanced Raman scattering" *Acc. Chem. Res.* **1984**, *17*, 370. (d) Vo-Dinh, T. "Surface-enhanced Raman spectroscopy using metallic nanostructures," *Trends Anal. Chem.* **1998**, *17*, 557.
7. (a) Emory, S. R.; Haskins, W. E.; Nie, S. "Direct observation of size-dependent optical enhancement in single metal nanoparticles," *J. Am. Chem. Soc.* **1998**, 120, 8009. (b) Emory, S. R.; Nie, S. "Screening and enrichment of metal nanoparticles with novel optical properties," *J. Phys. Chem. B* **1998**, 102, 493.
8. (a) Trautman, J. K.; Macklin, J. J.; Brus, L. E.; Betzig, E. "Near-field spectroscopy of single molecules at room temperature," *Nature* **1994**, *369*, 40. (b) Ambrose, W. P.; Goodwin, P. M.; Martin, J. C.; Keller, R. A. "Alterations of single-molecule fluorescence lifetimes in near-field optical microscopy," *Science* **1994**, *265*, 364. (c) Lu, H. P.; Xie, X. S. "Single-molecule spectral fluctuations at room temperature," *Nature (London)* **1997**, *385*, 143.
9. Dickson, R. M.; Cubitt, A. B.; Tsien, R. Y.; Moerner, W. E. "On/off blinking and switching behaviour of single molecules of green fluorescent protein," *Nature (London)* **1997**, *388*, 355.
10. (a) Vanden Bout, D. A.; Yip, W.-T.; Hu, D.; Fu, D.-K.; Swager, T. M.; Barbara, P. F. "Discrete intensity jumps and intramolecular electronic energy transfer in the spectroscopy of single conjugated polymer molecules," *Science* **1997**, *277*, 1074. (b) Yip, W.-T.; Hu, D.; Yu, J.; Vanden Bout, D. A.; Barbara, P. F. "Classifying the photophysical dynamics of single- and multiple-chromophoric molecules by single molecule spectroscopy," *J. Phys. Chem. A* **1998**, *102*, 7564.
11. Nirmal, M.; Dabbousi, B. O.; Bawendi, M. G.; Macklin, J. J.; Trautman, J. K.; Harris, T. D.; Brus, L. E. "Fluorescence intermittency in single cadmium selenide nanocrystals," *Nature* **1996**, *383*, 802.
12. S. A. Empedocles, S. A.; Bawendi, M. G. "Quantum-confined stark effect in single CdSe nanocrystallite quantum dots," *Science* **1997**, *278*, 2114.
13. Blanton, S. A.; Hines, M. A.; Guyot-Sionnest, P. "Photoluminescence wandering in single CdSe nanocrystals," *Appl. Phys. Lett.* **1996**, *69*, 3905.
14. Wazawa, T.; Ishii, Y.; Funatsu, T.; Yanagida, T. "Spectral fluctuation of a single fluorophore conjugated to a protein molecule," *Biophys. J.* **2000**, *78*, 1561.

15. Talaga, D. S.; Lau,W. L.; Roder, H.; Tang, J. Y.; Jia, Y. W.; DeGrado, W. F.; Hochstrasser, R. M. "Dynamics and folding of single two-stranded coiled-coil peptides studied by fluorescent energy transfer confocal microscopy," *Proc. Nat. Acad. Sci. (U.S.A.)* **2000**, *97*, 13021.

16. (a) Edman, L.; FoldesPapp, Z.; Wennmalm , S.; Rigler, R. "The fluctuating enzyme: a single molecule approach," *Chem. Phys.* **1999**, *247*, 11. (b) Wennmalm, S.; Rigler, R. "On death numbers and survival times of single dye molecules," *J. Phys. Chem. B* **1999**, *103*, 2516.

17. Wu, M.; Goodwin, P. M.; Ambrose, W. P.; Keller, R. A. "Photochemistry and fluorescence emission dynamics of single molecules in solution: B-phycoerythrin," *J. Phys. Chem.* **1996**, *100*, 17406.

18. Ambrose, W. P.; Goodwin, P. M.; Martin, J. C.; Keller, R. A. "Single molecule detection and photochemistry on a surface using near-field optical excitation," *Phys. Rev. Lett.* **1994**, *72*, 160.

19. Eggeling, C.; Wedengren, J.; Rigler, R., Seidel, C. A. M. "Photobleaching of fluorescent dyes under conditions used for single-molecule detection: evidence of two-step photolysis," *Anal. Chem.* **1998**, *70*, 2651.

20. Ying, L.; Xie, X. S. "Fluorescence spectroscopy, exciton dynamics, and photochemistry of single allophycocyanin trimers," *J. Phys. Chem. B* **1998**, *50*, 10399.

21. Nitzan, A.; Brus, L. E. "Theoretical model for enhanced photochemistry on rough surfaces," *J. Chem. Phys.* **1981**, *75*, 2205.

22. Das, P.; Metiu, H. "Enhancement of molecular fluorescence and photochemistry by small metal particles," *J. Phys. Chem.* **1985**, *89*, 4680.

23. Goncher, G. M.; Parsons, C. A.; Harris, C. B. "Photochemistry on rough metal surfaces," *J. Phys. Chem.* **1984**, *88*, 4200.

24. (a) Jeong, D. H.; Suh, J. S.; Moskovits, M. "Photochemical reactions of phenazine and acridine adsorbed on silver colloid surfaces," *J. Phys. Chem. B.* **2000**, *104*, 7462. (b) Jeong, D. H.; Jang, N. H.; Suh, J. S.; Moskovits, M. "Photodecomposition of diazanaphthalenes adsorbed on silver colloid surfaces," *J. Phys. Chem. B.* **2000**, *104*, 3594. (c) Jang, N. H.; Suh, J. S.; Moskovits, M. "Effect of surface geometry on the photochemical reaction of 1,10-phenanthroline adsorbed on silver colloid surfaces," *J. Phys. Chem. B.* **1997**, *101*, 8279. (d) Suh, J. S.; Jang, N. H.; Jeong, D. H.; Moskovits, M. "Adsorbate photochemistry on a colloid surface: phthalazine on silver," *J. Phys. Chem.* **1996**, *100*, 805. (e) Suh, J. S.; Moskovits, M.; Shakhesemampour, J. "Photochemical decomposition at colloid surfaces," *J. Phys. Chem.* **1993**, *97*, 1678. (f) Wolkow, R. A.; Moskovits, M. "Enhanced photochemistry on silver surfaces," *J. Phys. Chem.* **1987**, *87*, 5858.

25. Jang, N. H.; Suh, J. S.; Moskovits, M. "Photochemical desorption of 4-vinylbenzoic acid adsorbed on silver colloid surfaces," *J. Phys. Chem. B.* **1997**, *101*, 1649.

26. (a) Suh, J. S.; Jeong, D. H.; Lee, M. S. "Effect of inhomogeneous broadening on the surface photochemistry of pthalazine," *J. Raman Spec.* **1999**, *30*, 595. (b) McMahon, J. J.; Gergel, T. J.; Otterson, D. M.; McMahon, C. R.; Kabbani, R. M. "Photochemical charge transfer excitation of trans-4-stilbazole at a silver electrode," *Surf. Sci.* **1999**, *440*, 357. (c) Kidd, R. T.; Meech, S. R.; Lennon, D. "Enhanced photodesorption of NO on roughened silver surfaces," *Chem. Phys. Lett.* **1996**, *262*, 142. (d)Azim, S. A.; El-Daly, H. A.; El-Daly, S. A.; Abou-Zeid, Kh. A.; Ebeid, E. M.; Heldt, J. R. "Energy transfer and photodecomposition of anthracene laser dyes," *J. Chem. Soc. Faraday Trans.* **1996**, *92*, 2685.

27. (a) Garoff, S.; Weitz, D. A.; Alverez, M. S. "Photochemistry of molecules adsorbed on silver-island films: effects of the spatially inhomogeneous environment," *Chem. Phys. Lett.* **1982**, *93*, 283. (b) Waldeck, D. H.; Alivisatos, A. P.; Harris, C. B. "Nonradiative damping of molecular electronic excited states by metal surfaces," *Surf. Sci.* **1985**, *158*, 103.

28. Lee, P. C.; Meisel, D. "Adsorption and surface-enhanced Raman of dyes on silver and gold sols" *J. Phys. Chem.* **1982**, *86*, 3391.

29. Hildebrandt, P.; Stockburger, M. "Surface-enhanced resonance Raman spectroscopy of Rhodamine 6G adsorbed on colloidal silver," *J. Phys. Chem.* **1984**, *88*, 5935.

30. Keller, H. E. "Objective lenses for confocal microscopy," In *Handbook of Confocal Microscopy*, Pawley, J. B., Ed.; Plenum Press: New York, **1995**, 111.

31. (a) George, N. A.; Aneeshkumar, B.; Radhakrishnan, P.; Vallabhan, C. P. G. "Photoacoustic study on photobleaching of Rhodamine 6G doped in poly(methyl methacrylate)," *J. Phys. D: Appl. Phys.* **1999**, *32*, 1745. (b) Mialocq, J. C.; Hebert, Ph.; Armand, X.; Bonneau, R.; Morand, J. P. "Photophysical and photochemical properties of Rhodamine 6G in alcoholic and aqueous sodium dodecylsuphate micellar solutions," *J. Photochem. Photobiol. A: Chem.* **1991**, *56*, 323.

32. Soper, S. A.; Nutter, H. L.; Keller, R. A.; Davis, L. M.; Shera, E. B. "The photophysical constants of several fluorescent dyes pertaining to ultrasensitive fluorescence spectrscopy," *Photochem. Photobiol.* **1993**, *57*, 972.

33. Tellinghuisen, J.; Wilkerson, C. W., Jr. "Bias and precision in the estimation of exponential decay parameters from sparse data," *Anal. Chem.* **1993**, *65*, 1240.

34. Sagmuller, B.; Freunscht, P.; Schneider, S. "The assignment of the vibrations of substituted mercaptotetrazoles based on quantum chemical calculations," *J. Mol. Struct.* **1999**, *483*, 231.

35. Tuinstra, F.; Koenig, J. L. "Raman spectrum of graphite," *J. Chem. Phys.* **1970**, *53*, 1126.

36. (a) Moyer, P. J.; Schmidt, J.; Eng, L. M.; Meixner, A. J. "Surface-enhanced Raman scattering spectroscopy of single carbon domains on individual Ag nanoparticles on a 25 ms time scale," *J. Am. Chem. Soc.* **2000**, *122*, 5409. (b) Kudelski, A.; Pettinger, B. "SERS on carbon chain segments: monitoring locally surface chemistry," *Chem. Phys. Lett.* **2000**, *321*, 356.

37. (a) Taylor, C. E.; Garvey, S. D.; Pemberton, J. E. "Carbon contamination at silver surfaces: surface preparation procedures evaluated by Raman spectrscopy and x-ray photoelectron spectroscopy," *Anal. Chem.* **1996**, *68*, 2401. (b) Norrod, K. L.; Rowlen, K. L. "Removal of carbonaceous contamination from SERS-active silver by self-assembly of decanethiol," *Anal. Chem.* **1998**, *70*, 4218.

38. (a) Kerker, M.; Siiman, O.; Bumm, L. A.; Wang, D.-S. "Surface enhanced Raman scattering (SERS) of citrate ion adsorbed on colloidal silver," *Appl. Opt.* **1980**, *19*, 3253. (b) Siiman, O.; Bumm, L. A.; Callaghan, R., Blatchford, C. G.; Kerker, M. "Surface-enhanced Raman scattering by citrate on colloidal silver," *J. Phys. Chem.* **1983**, *87*, 1014.

39. Kudelski, A.; Pettinger, B. "SERS on carbon chain segments: monitoring locally surface chemistry," *Chem. Phys. Lett.* **2000**, *321*, 356.

Detection of DNA and P-450s on silver colloidal nanoparticles by surface-enhanced resonance Raman scattering (SERRS)

W. Ewen Smith[*], Ewan Polwart, Clare McLaughlin, Benjamin J. Mallinder, Susan J. Smith, Duncan Graham

Department of Pure and Applied Chemistry, University of Strathclyde, Glasgow, Scotland, UK

ABSTRACT

Surface-enhanced resonance Raman scattering (SERRS) is a very sensitive and selective detection method that can be used for the analysis of both DNA and P-450s. A number of factors have limited the broader application of the technique. These limitations are described and addressed. An approach to reduce the problems associated with variation of the silver colloids used to provide surface enhancement and chemical methodologies that ensure surface adsorption are presented. A practical approach was used to investigate the nature of the effect. This approach has highlighted the importance of resonance enhancement for ultimate sensitivity. Two approaches to achieve successful detection of DNA using SERRS are described, and, using these two approaches, the possibility of multiplexing is also demonstrated. The analysis of proteins by SERRS is discussed and P-450 is presented as a specific example of the information that may be gained from SERRS of proteins.

Keywords: surface-enhanced Raman scattering (SERS), surface-enhanced resonance Raman scattering (SERRS), silver colloid, DNA, P-450

1. INTRODUCTION

Surface-enhanced resonance Raman scattering (SERRS) is a very sensitive and selective detection method. The method requires that an analyte is chosen which has an absorption band close to the frequency of the laser to be used for Raman excitation and that the analyte is adsorbed onto a roughened metal surface, typically silver or gold. Excitation of the sample with the laser provides enhanced Raman scattering both from molecular resonance with the analyte and from surface enhancement, resulting in selective enhancement of the signal of the chosen analyte. Despite the very great potential of the method, its use has been inhibited by difficulties with regard to reproducibility and quantitation. The work reported here uses aggregated colloidal suspensions as the roughened metal surface for the analysis of biological molecules and indicates solutions to the main problems limiting the wider application of the technique. The main factors limiting the use of the technique for quantitative analysis are: the effect of particle shape and size, and state of aggregation of the colloid; uncertainties with regard to the nature of the surface adsorption mechanism; and uncertainties with regard to the actual mechanism of enhancement. These three main problems have been addressed to improve the technique.

2. SILVER COLLOIDAL NANOPARTICLES

2.1 Colloid variation

We have eliminated some of these difficulties associated with reproducibility of the SERRS signal from analytes adsorbed on silver colloids by careful preparation of the colloid in a standard manner. The initial decision as to whether or not a particular batch of colloid is acceptable is taken on the basis of the UV-visible extinction spectrum. This spectrum is related

* w.e.smith@strath.ac.uk; phone +44 141 548- 2615; fax +44 141 552- 0876; Department of Pure and Applied Chemistry, University of Strathclyde, 295 Cathedral Street, Glasgow, Scotland, UK, G1 1XL

in a complex manner to the particle size and shape, and state of aggregation of the colloid. Whilst the spectrum alone is not a sufficient test to define these characteristics, by combining such results with the standard method of colloid production, the effect of variability on the substrate is largely eliminated.

2.2 Surface adsorption

The second major practical difficulty is in ensuring effective surface adsorption. Early experiments with rhodamine give curved concentration dependent profiles suggesting adsorption of the rhodamine onto the walls of the vessel as well as onto the particles.[1,2] New ligands—azo-dyes which contain the benzotriazole (BT) group—were designed to provide effective surface adsorption. BT is an anti-corrosion agent for copper and an anti-tarnish agent for silver. It is believed to function by forming a polymeric array by complexation with silver ions on the surface of the metal,[3] thus preventing desorption. Aggregation studies using these ligands have shown that a number of inorganic and organic aggregating agents can be used. The concentration of the aggregation agent can be set so that the aggregated colloid remains stable and in suspension. Over-aggregation provides bigger signals but reduces reproducibility, as the colloid becomes unstable in the aqueous suspension. Aggregation with reagents such as sodium chloride takes a few minutes to develop. Following that, stability is obtained for over 20 minutes. In Figure 1, a BT-dye (GM19) is illustrated along with the spectrum obtained in an experiment using sodium chloride as aggregating agent. The time stability is also shown.
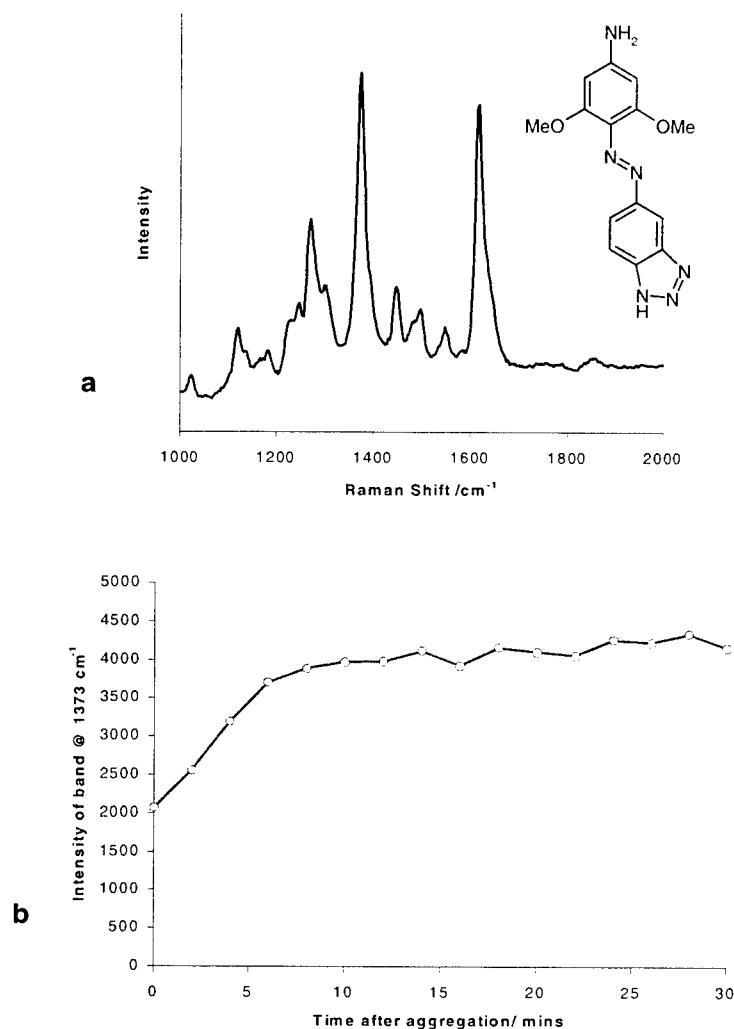

Figure 1. (a) SERRS spectrum and chemical structure of a BT-azo-dye (GM19) on aggregated silver colloid, and (b) a plot of the time dependence of the intensity of the largest peak after aggregation with sodium chloride.

To determine the reproducibility of the colloidal suspension, 6 batches were prepared, and with this dye, at a concentration of 10^{-8} M, the SERRS measured gave an inter-batch variability of ±25 %. This result indicates that semi-quantitative analysis is possible using SERRS and this may well be sufficient for many practical purposes. Other experiments in this laboratory have indicated that much better RSDs can be obtained using flowcell technology.[4]

2.3 The nature of the effect

The third major difficulty with the more general application of the technique is the lack of understanding of the effect. In recent experiments, we have addressed the problem from a practical point of view. Using the specially synthesised dye (GM19) described above, concentration dependent studies were carried out using 457.9 nm excitation, which is close in energy to the absorption maximum of the dye (which is at 450 nm), 514.5 nm excitation, which is pre-resonant with the dye, and 632.8 nm excitiation, which is further from the absorption maximum of the dye. Addition of GM19 to silver colloid produces aggregation so there is no need for an additional aggregating agent that would increase the complexity of the experiment. It was found in log-log plots of the normalised intensity against concentration—Figure 2—that the signal decreases at concentrations above ~10^{-6} M. It is thought that this concentration corresponds to monolayer coverage. Signals from molecules not on the first monolayer are much weaker and the high concentrations of dye may lead to over-aggregation of the colloid. However, significantly, at concentrations below this coverage, it was found that with the different excitation frequencies there were very considerable differences in slope of the calibration graph. With excitation at 457.9 nm the gradient is approximately 1.1 and is close to linear although the concentration profile is probably best defined by to two slopes within the concentration range studied. One gradient is found where the dye concentration is greater than 10^{-8} M and one where the dye is at a concentration of 10^{-8} M or less. With 514.5 nm excitation no signal was detected below 10^{-8} M and a much steeper gradient is obtained above this concentration. For excitation at 632.8 nm, the limit at which a signal is observed is ~10^{-7} M, and a profile steeper than that observed at either 457.9 nm or 514.5 nm is observed. At 10^{-6} M, the normalised signal with 457.9 nm excitation is approximately four times that obtained with either 514.5 nm or 632.8 nm excitation. The difference between resonance and non-resonant conditions at 10^{-6} M is remarkably small since SERRS is regularly quoted as being 10^3 times more sensitive than surface-enhanced Raman scattering (SERS) without resonant enhancement. These experiments clearly show this to be concentration dependent, with the biggest differences being obtained where the molecule is in molecular resonance and is at low concentration.
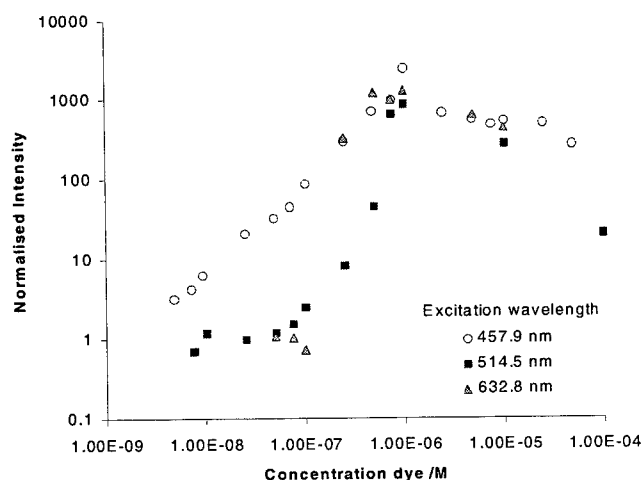

Figure 2. Plot of the concentration dependence of the intensity of the SERRS of GM19 at three different excitation wavelengths.

Two Raman maps of the same area, but with excitation at 514.5 nm and 632.8 nm respectively, are shown in Figure 3(a) and (b). These maps represent the intensity of the GM19 signal obtained from colloid adsorbed onto an amine-derivatised glass surface. It can be seen that there is significant variation in Raman signal across the surface with excitation at both 514.5 nm and 632.8 nm. The areas of high intensity (lighter shades) are thought to result from large enhancements at large colloidal aggregates that are randomly spatially distributed. An additional important observation is the fact that a significant Raman signal is obtained across the whole area examined with 514.5 nm excitation but not 632.8 nm excitation. There appears to be significant scattering from the areas of lower density of immobilised colloid, thought to consist of single particles and small aggregates when the exciting frequency is close to resonance. The explanation for this result appears to be that there is a significant enhancement closer to resonance. This supports the observation of much steeper concentration profiles and higher limits of sensitivity further from resonance. It is clear that this effect is only obtained on resonance. The slope obtained with 457.9 nm excitation is consistent with the fact that there is a single particle enhancement mechanism in SERRS but not in SERS as the data collected with 632.8 nm excitation show.
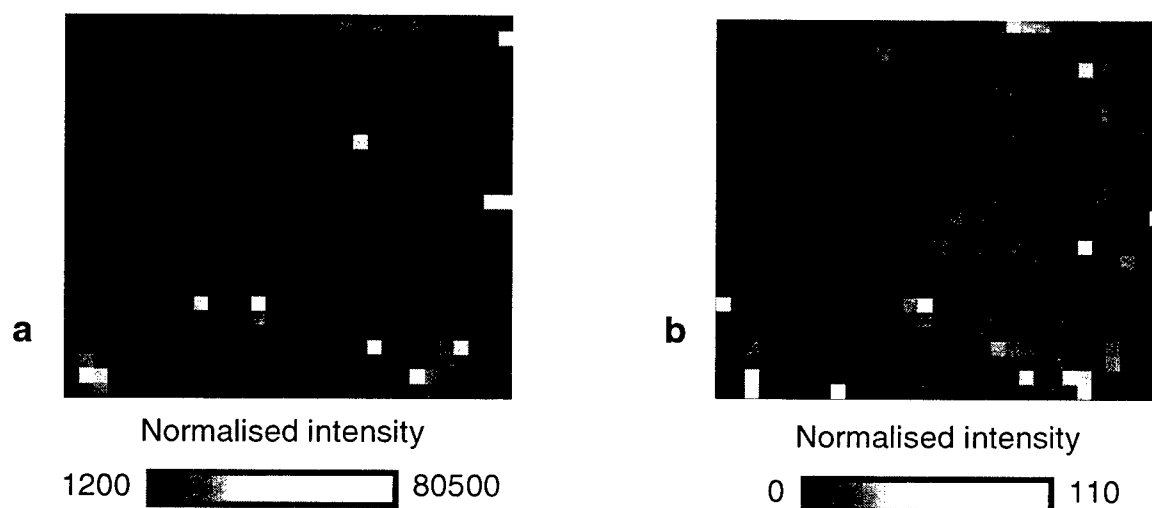

Figure 3. Raman maps of the SERRS intensity of the signal from GM19 taken from the same 62 × 56 μm area of immobilsed silver colloid collected with excitation at (a) 514.5 nm and (b) 632.8 nm.

3. DETECTION OF DNA AND PROTEINS

3.1 DNA detection

An area in which sensitive and selective detection of molecules would provide meaningful results is in DNA detection. DNA detection at low concentration is often carried out by the use of fluorescent tags. Since SERRS is reported to have single molecule detection limits, it should be possible to use SERRS active tags in place of fluorescent tags.[5,6] The advantage is that a vibrational spectrum is obtained from the tag giving much better molecular specificity, and the greater ability to discriminate between tags enables multiplex analysis. A further major advantage in SERRS is that there is a fluorescence quenching mechanism at the surface. This means that both non-fluorophores and fluorophores can be used as tags. This greatly extends the range of taggants that can be used. However, initial experiments using fluorophores as potential SERRS ligands were unsuccessful. The reason for this is that both the DNA, through its phosphate backbone, and the silver colloidal particles are negatively charged. The result is that good surface adsorption of the DNA dyes cannot be readily achieved.

New probe molecules were therefore designed for the SERRS approach. In one approach, a tail of propargyl amines was added to the DNA chain containing the fluorophore. These propargyl groups exist with the amine in the protonated form at neutral pH and consequently add a tail of positive charge to the DNA chain. In an alternative approach, a number of positively charged dyes were added at the end of the chain. Another advantage of SERRS is illustrated by this approach since the problem of fluorescence quenching which can arise with multiple fluorescent tags does not apply to SERRS. Consequently, the use of multiple dye labels closely spaced together on one end of the chain, to increase signal strength while leaving the rest of the probe sequence for molecular biology, is more effective with SERRS than fluorescence. The addition of these probes to colloid did produce some evidence of surface enhanced resonance Raman scattering but the technique was ineffective in that it was very irreproducible. A second problem had to be overcome in that the negative charge on the DNA was preventing effective aggregation of a DNA/silver colloidal cluster. To overcome this, the DNA charge reduction agent spermine was added. It proved to be effective both in reducing DNA charge and as an aggregating agent for the silver particles. Thus, the addition of the specially designed tails and spermine generate effective surface adsorption and therefore allow detection by SERRS. The limits of sensitivity obtained in this experiment are comparable to those of fluorescence, or better. Figure 4(a) illustrates the probe tails designed for the two approaches described above and Figure 4(b) illustrates the ability of SERRS to discriminate between the two tags. These are early examples and expansion of the chemistry will provide many more examples of multiplexing, using methodologies unique to SERRS.

Figure 4. (a) Design of the probe tails used for DNA detection by SERRS—HEX and RHOD are dye labels—and (b) SERRS of mixtures of the two probes at a range of ratios, RHOD:HEX.

3.2 Protein Analysis

SERRS can also be applied effectively in protein analysis. In this case, interest is mainly in the nature of the chromophore in the protein rather than in the quantitation of the amount of protein. This can be illustrated with reference to P-450 proteins that contain a haem chromophore as part of their structure. By using laser excitation of the correct frequency to be resonant with one of the adsorption bands of this chromophore, the resonance effect enhances only the vibrational spectrum from the haem. This provides selective information concerning the active pocket. The effect of substrate addition can be seen by following oxidation and spin state markers. This information can be obtained by resonance Raman spectroscopy

and this technique is preferred, where practical, for studies of protein function, since adsorption of a protein on a metal surface can cause deformation and change in activity. However, there are specific advantages in SERRS over resonance. Firstly, some of the key proteins tended to fluoresce and in these circumstances, the fluorescence quenching of SERRS is very effective. This applies to some of the P-450s although protein purification can also overcome some of these problems. However, resonance also uses higher powers and requires more concentrated samples and consequently the effect of the exciting radiation on the protein can be much greater. Additionally, the adsorption of proteins on metal surfaces is of specific importance in biotechnology and in some occasions the effect of adsorption is not key to the application required. Thus, in the protein analysis field, SERRS still has a specific niche. This is strengthened by the much greater sensitivity that it offers compared to resonance Raman scattering. A typical SERRS spectrum of P-450 is indicated in Figure 5 and the oxidation state marker band, v_4, is indicated. With different excitation wavelengths the spin state, v_{10}, marker band is clearly resolved. We have demonstrated previously that even for substrates that do not directly complex with the iron, there is an allosteric effect on the pocket that can be reflected particularly in the vinyl groups present on the haems. In a further extension of this work, we have indicated the advantage of SERRS in selective nitration of the tyrosine groups of proteins. In this case, the sharp nature of the signals provides an indication of whether the nitrated tyrosine is present in a hydrophilic or hydrophobic environment.[7]
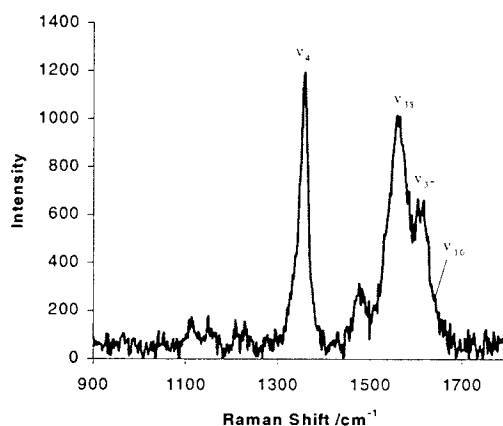
Figure 5. SERRS of P-450 on aggregated silver colloid, collected with excitation at 457.9 nm .

4. CONCLUSIONS

As a technique, SERRS is now well enough understood and a number of chemical methodologies have been introduced to control a number problematic variations to allow semi-quantitative, or quantitative, measurements to be made. This is achieved by firstly ensuring strong surface adsorption. Furthermore, the analyte should preferably have a molecular absorbance, and an exciting frequency close to the maximum should be chosen to provide the maximum sensitivity. The understanding of the effect is still primitive, but at a practical level SERRS can be manipulated in a controlled fashion to provide useful results from a number of analytes, including DNA and proteins.

ACKNOWLEDGEMENTS

REFERENCES

1. C. Rodger, W. E. Smith, G. Dent, and M. Edmondson, "Surface-enhanced resonance-Raman scattering: An informative probe of surfaces", *J. Chem. Soc., Dalton Trans.*, pp. 791-799, 1996.
2. P. Hildebrandt and M. Stockburger, "Surface-Enhanced Resonance Raman-Spectroscopy of Rhodamine-6G Adsorbed On Colloidal Silver", *J. Phys. Chem.* 88, pp. 5935-5944, 1984.
3. D. Graham, C. McLaughlin, G. D. McAnally, J. C. Jones, P. C. White, and W. E. Smith, "Synthesis of novel monoazo benzotriazole dyes specifically for surface enhanced resonance Raman scattering", *J. Chem. Soc., Chem. Commun.*, pp. 1187-1188 , 1998.
4. R. L. Keir, C. McLaughlin, J. C. Jones, and W. E. Smith, unpublished results.
5. D. Graham, W. E. Smith, A. M. T. Linacre, C. H. Munro, N. D. Watson, and P. C. White, "Selective Detection of Deoxyribonucleic Acid at Ultralow Concentrations by SERRS", *Anal. Chem.* 69, pp. 4703-4707, 1997.
6. D. Graham, B. J. Mallinder, and W. E. Smith, "Surface-enhanced Resonance Raman Scattering as a Novel Method of DNA Discrimination", *Angew. Chem. Int. Ed.* 39, pp. 1061-1063, 2000.
7. L. Quarioni and W. E. Smith, "Nitration of internal tyrosine of cytochrome c probed by resonance Raman scattering" Biospectrosc. 5, pp. S71-S76, 1999.

Nanoparticle-amplified surface plasmon resonance for detection of DNA hybridization

G.P. Goodrich[a], S.R. Nicewarner[a], L. He[b], M.J. Natan[b], C.D. Keating[a]

[a]The Pennsylvania State University, University Park, PA 16802
[b]SurroMed Inc. , Palo Alto, CA 94503

ABSTRACT

In recent years there has been a great deal of interest in the measurement of DNA hybridization at surfaces. Surface-confined DNA hybridization has been used to monitor gene expression, to detect the presence of a particular DNA sequence and determine single nucleotide polymorphisms (SNPs). DNA microarrays, which can contain thousands of discrete DNA sequences on a single surface, have become widely used for hybridization studies. While a powerful technique, this technology is limited by the stability of the fluorescent dyes used to label the DNA, and the need to perform measurements ex-situ to reduce the fluorescence background. In this report, we describe the use of colloid-amplified surface plasmon resonance (SPR) to measure DNA hybridization at surfaces. SPR is a surface sensitive technique, which can be used to study hybridization in situ, and the use of colloidal metal tags provides excellent sensitivity. Angle-scanning SPR has been used to study oligonucleotide hybridization to surface confined probes, and work is underway to apply SPR imaging to study DNA hybridization in macro- and microarray formats.

Keywords: Surface plasmon resonance, DNA, hybridization, Au colloid, nanoparticle

1. INTRODUCTION

The ability to detect the hybridization of complementary DNA strands provides a powerful tool for medical diagnostics and gene expression analysis. The selectivity of the hybridization process allows for the detection of a particular sequence in a mixture of hundreds or thousands of other sequences. Hybridization analysis can be used to diagnose genetic diseases based on either the presence or absence of a particular sequence, and can also be used to monitor changes in the expression levels of certain sequences to better understand the response of an organism to external stress.

Recently, fluorescence microarray technology has become a powerful new technology for hybridization analysis.[1,2] In this technology DNA is immobilized in spatially defined arrays on a solid substrate. The surface is then exposed to a solution of fluorescently labeled DNA. The DNA in solution will hybridize to the spot containing the complementary sequence on the surface. Using a confocal fluorescence scanner, it is possible to determine which sequences were present in the solution of labeled DNA. With the advent of microarray technology, it has become possible to monitor the hybridization for an entire genome simultaneously.[2,3] However, the fluorescent technology has some serious limitations. First, the fluorescent dyes used to label the DNA strands suffer from photobleaching and oxidation, causing a loss in signal, and limiting the lifetime of the labeled DNA. The labeling process, which is usually performed during PCR amplification can lead to uncertainty in the amount of fluorophore incorporated into each DNA strand, making it difficult to quantitate the actual amount of DNA in a sample. Finally, fluorescence techniques cannot observe the hybridization reaction in real-time, due to high fluorescent background from the labeled DNA in solution. In order to address these limitations to the fluorescent techniques, we have developed a system for measuring DNA hybridization using particle-amplified surface plasmon resonance.

Surface plasmon resonance is a surface sensitive analytical technique based on the measurement of the dielectric constant at the surface of a thin noble metal film.[4] Adsorption of molecules on the SPR active film and subsequent modification of that material can be detected as a change in the dielectric at the surface. As SPR is an evanescent wave phenomenon, only the area directly adjacent to the metal surface is interrogated. This has allowed the technique to be widely used for real-time studies of biomolecular interactions between unlabeled biomolecules, including antibodies and DNA [5-10]

While it is possible to make unlabeled measurements, the sensitivity of these measurements is limited due to the relatively small change in dielectric resulting from each binding event. In order to detect extremely low numbers of binding events, it

is necessary to increase the sensitivity of the technique. Toward this end, a number of external tags such as latex beads,[11,12] liposomes,[13] and colloidal metal particles[14-18] have been investigated. The external tag provides a much larger change in the dielectric at the surface for a single binding event. We have previously reported the use of colloidal Au tags as an amplification tag for SPR based immunoassays and DNA hybridization assays.[16,17] In these experiments, a sandwich assay is used in which the analyte binds to an antibody or oligonucleotide immobilized on the surface, and is then detected by exposure of the surface to a secondary antibody or oligo conjugated to a Au particle. The SPR technique is also readily applied to an imaging format where the reflectivity of an entire surface is monitored simultaneously. SPR imaging has been used to measure hybridization of DNA and RNA to a photolithographically patterned surface.[8,19] Our goal is to develop SPR imaging as an alternative technique for the measurement of gene expression using microarray technology.

2. MATERIALS AND METHODS

2.1 Materials
Trisodium citrate dihydrate, poly(ethylene glycol) bis(3-aminopropyl) terminated (PEG), 16-mercaptohexadecanoic acid (90%) (MHA), 3-mercaptopropionic acid (MPA) and NaOH were obtained from Aldrich. $HAuCl_4 \cdot 3H_2O$ was from Acros. NaH_2PO_4, Na_2HPO_4, NaCl, KCl, concentrated HCl, HNO_3, H_2SO_4, and 30% H_2O_2 were purchased from J. T. Baker Inc. 3-Mercaptopropylmethyldimethoxysilane (MPMDMS) and (3-aminopropyl)trimethoxysilane (APTMS) were purchased from United Chemical Technologies. Spectrophotometric grade CH_3OH, and CH_3OCH_3 were obtained from EM Science. CH_3CH_2OH was purchased from Pharmco. 1-Ethyl-3-(3-dimethyl-aminopropyl)carbodiimide (EDC), N-hydroxysulfosuccinimide (sulfo-NHS), and streptavidin were from Pierce. HPLC-purified oligonucleotides were purchased from Integrated DNA Technology or from the Pennsylvania State University Nucleic Acid Facility. cDNA fragments were obtained from Prof. N.V. Fedoroffs group at Penn State. All reagents were used as received without further purification. H_2O used was distilled and subsequently purified using a Barnstead Nanopure system. Au (99.99%) shots and Cr wires used for evaporation were obtained from Johnson-Matthey Corp. SF11 glass slides (Schott Glass Technologies, n = 1.78) were used in the SPR scanning experiments, and Fisher Precleaned microscope slides (BK7, n = 1.515) were used in the imaging experiments.

2.2 DNA: Au conjugate preparation
Colloidal Au (12-nm diameter) was prepared via citrate reduction of $HAuCl_4 \cdot 3H_2O$ as described previously. Average particle diameter was determined using transmission electron microscopy, and showed a standard deviation less that 10%. Optical spectra of the colloid solutions were recorded using a HP 8453 spectrophotometer. Thiolated DNA:Au conjugates were prepared according to procedures developed by Mirkin and co-workers.[20-22] Biotinylated conjugates were prepared as described previously. In brief, 12-nm particles were derivatized with streptavidin. The protein:colloid conjugates were then modified using a biotinylated oligonucleotide. Excess DNA was removed by centrifugation. Optical spectra were recorded for all conjugate solutions to ensure consistent particle concentrations.

2.3 SPR Substrate Preparation
All glass substrates were cleaned using Aqua Regia (3:1 $HCl:HNO_3$) and Piranha (3:2 $H_2SO_4:H_2O_2$). For scanning experiments, clean glass slides were modified in 5% silane for 1 hr prior to evaporation. Approximately 48 nm of Au was deposited using an Edwards Auto 306 thermal evaporator at a rate of 0.2 nm/sec determined by an internal quartz crystal microbalance and a pressure of 2×10^{-6} millibar. Films were then annealed using a home-built tube oven. For imaging experiments an adhesion layer consisting of ~1nm of Cr was evaporated onto clean glass slides followed by ~48 nm of Au.

2.4 Instrumentation
The home-built scanning SPR apparatus used in this investigation has been previously described.[17,23,24] Briefly, a 1 inch diameter hemispherical prism (SF11 glass, EscoProducts) was index-matched to the SPR surface in a Kreschmann geometry setup, with a He-Ne laser (632.8 nm, Melles Griot) used as the excitation source. A silicon photodiode detector (Thorlabs) collected the reflected laser light. Angular positioning of the sample was accomplished using a θ-2θ rotation stage with the prism/sample mounted on the top. A miniature peristaltic pump (Instech Laboratories, Inc.) was used to deliver analyte solutions to the sample cell at 0.1 mL/min.

An imaging instrument was constructed as previously reported.[25] Two minor modifications to the optical path and sample cell were made to accommodate multiwavelength excitation and fine angle adjustments. The 5 mW He-Ne laser was replaced with a Coherent I-70 Ar^+/Kr^+ laser that permits excitation at multiple wavelengths. Also, the prism assembly was mounted on a rotation stage to accommodate adjustment in the incident angle. Sample cells were fabricated by punching 16 4.5-mm-

diameter holes in a 4 x 4 geometry in 0.5-mm-thick sheets of "press to seal" silicone (Molecular Probes). The polarizer was repositioned after the beam expander and the CCD was fitted with a Nikon 60 mm/f = 2.8 Macro lens. Data were plotted as spatial intensity maps of the SPR substrate surface, where an increase in intensity indicates an increase in SPR response. A commercial software package, NIH Image, was used for image analysis. From the spatial intensity map the integrated intensity from each sample cell was calculated, a baseline intensity was subtracted, and each signal was normalized for the area of the sample cell. AFM images of samples were measured after collecting SPR curves. Images were captured in the tapping mode on a Digital Nanoscope IIIa instrument (Digital Instruments, CA). Two 5 x 5 μm images and three 1 x 1 μm images were collected for each surface. The surface coverage was calculated by manually counting particles.

2.5 Hybridization experiments

The basic system used for DNA hybridization is illustrated in Scheme 1. Briefly, a gold surface is modified with a self-assembled monolayer of mercaptohexadecanoic acid. The carboxyl groups on the terminal end of the thiol molecules are then activated using EDC/NHS and crosslinked to an amine modified 12-mer oligonucleotide (A). The surface is then exposed to a solution containing an unmodified "linking" oligonucleotide (B). The linker used was a 24-mer; half of which
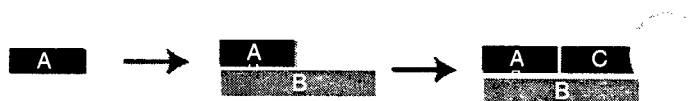
Scheme 1. Sandwich assay used in hybridization experiments

was complementary to the surface bound DNA strand. The other half of the linker was complementary to the DNA strand (C) conjugated to Au colloids. All hybridizations were carried out in hybridization buffer (0.3 M NaCl, 10 mM Phosphate, pH 7) for 1 hour. After hybridization the surface was rinsed extensively with buffer to remove any nonspecifically attached DNA.

3. RESULTS AND DISCUSSION

3.1 Hybridization detection by scanning SPR

We have used colloid amplified SPR to detect hybridization of short oligonucleotides. Figure 1 illustrates the effect of colloid amplification on detection sensitivity. Curve A is the SPR curve from a Au film modified with a 12-mer
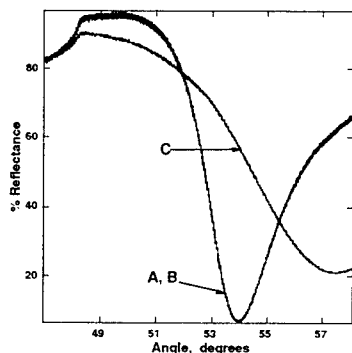
Fig 1. SPR curves for detection of oligonucleotide hybridization. Curve labels correspond to labels in Scheme 1.
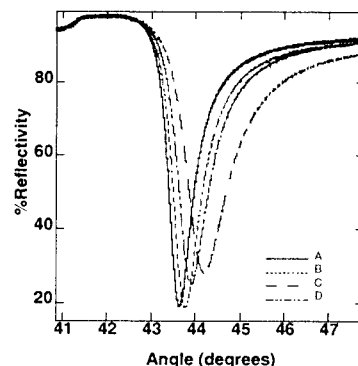
Figure 2. SPR curves for cDNA hybridization experiments. A: Bare Au, B: Single stranded cDNA fragment. C: Non-specific conjugate D: specific conjugate

oligonucleotide. The film was then exposed to a solution of linking oligonucleotide (10 μM) for 1 hr. The shift in the SPR curve resulting from the binding of the 24-mer linking oligonucleotide is shown in curve B. Under these experimental conditions, the shift in SPR curve is negligible. After subsequent hybridization with a 12-mer conjugated to a 12-nm particle through biotin:streptavidin interactions a large shift in the SPR curve is observed (Curve C). The sensitivity afforded by

particle amplification has allowed for the ultra-sensitive detection of DNA hybridization. We have previously reported picomolar quantitation limits for short oligonucleotides.[16]

In addition to hybridization using short synthetic oligonucleotides, we have studied the detection of hybridization to fragments of cDNA obtained from *Aribidopsis thaliana* (Fig 2). In this system the 5' end of a ~200 base-pair cDNA fragment is modified with a thiol moiety. This modified double stranded cDNA is then immobilized through the thiol group to a Au surface. After thermal denaturation, a single stranded DNA fragment remains (Fig 2 B) available for hybridization. A colloid conjugate, prepared using 12-nm Au particles and either a complementary 18-mer or a noncomplementary 18-mer is then introduced into the system. Figure 2 shows the curves for both the complementary conjugate (D) and the nonspecific binding due to the non-complementary conjugate (C). While the nonspecific signal is significant in these experiments, it is important to realize that none of the prehybridization steps normally used in cDNA hybridization were used in these preliminary experiments. The addition of a prehybridization step should significantly reduce the amount of non-specific binding.

3.2 Particle-amplified Imaging SPR

The SPR response for colloid amplification using scanning SPR has been reported previously.[17,24,26] In order to determine the analytical sensitivity and the dynamic range of colloid amplified imaging SPR, The SPR response, measured as a change in reflectivity was measured for 12-nm and 45-nm Au particles. Figure 3 shows representative SPR images of films modified with spots of 12-nm (A) and 45-nm (B) Au colloids. In the 12-nm case, the surface was exposed to colloid
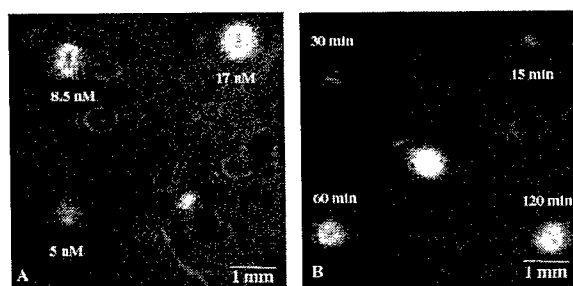
Fig. 3 SPR images of surfaces modified with 12-nm colloids (A) and 45-nm colloids (B) Dark spots on surface are a result of irregularities in the immersion oil layer

solutions of varied concentrations for a set time, in the 45-nm case the time of exposure was varied to achieve different surface coverage of particles. One advantage of particle amplified SPR is the unique ability to determine the absolute number of binding events by counting the particles using AFM. Fig. 4 shows the calibration curve constructed by counting surface coverage of particles for films modified with 12 and 45-nm particles. It can be seen from this graph that the SPR
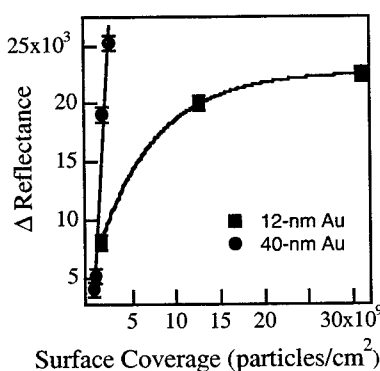
Fig 4 Plot of change in reflectance as a function of surface coverage for the images in Fig 3. Solid lines are added to guide the eye

response is greater for larger particles at a given coverage than for the smaller particles. It is also apparent that the SPR response is linear at low surface coverages of particles. Both of these effects have been studied previously using scanning

SPR. [26]Using 12-nm particles, surface coverages of 2×10^9 particles/cm^2 can easily be detected, with S/N ratio of 10. The use of larger particles allows for the reliable detection of coverages as low as 5×10^7 particles/cm^2.

Imaging SPR was used to study DNA hybridization in macroscopic sized wells (Fig 5). In this experiment, the surface was modified with a 12-mer oligo. Each spot in the array was then exposed to solutions of various concentrations of linking oligonucleotide for 1 hr. After rinsing, the surface was exposed to 12-nm colloid conjugates. The amount of DNA available
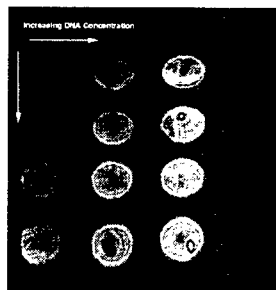
Figure 5. SPR Image of film after hybridization with DNA:Au colloid conjugates.

for hybridization to the colloid conjugate is a function of the initial solution concentration of linking oligonucleotide. We have previously reported the use of this system for ultrasensitive detection of the linking oligonucleotide, with detection limits in the low picomolar range.[16]

4. CONCLUSIONS

We have demonstrated the excellent sensitivity provided by particle-amplified SPR. Using this technique picomolar quantitation limits for oligonucleotides have been achieved in both scanning and imaging formats. The SPR response for both 12-nm and 45-nm particles has been studied, giving limits of detection in imaging mode of 2×10^9 and 5×10^7 particles/cm^2 respectively.

5. ACKNOWLEDGEMENTS

6. REFERENCES

1. Schena, M.; Shalon, D.; Davis, R. W.; Brown, P. O.,"Quantitative Monitoring of Gene Expression Patterns with a Complementary DNA Microarray" *Science,* **270,** 467-470 1995.

2. DeRisi, J. L.; Iyer, V. R.; Brown, P. O.,"Exploring the Metabolic and Genetic Control of Gene Expression on a Genomic Scale" *Science,* **278,** 680-470 1997.

3. Lashkari, D. A.; DeRisi.J.L.; McCusker, J., H.; Namath, A. F.; Gentile, C.: Hwang, S. Y.; Brown, P. O.; Davis, R. W.,"Yeast microarrays for genome wide parallel genetic and gene expression analysis" *Proc. Natl. Acad. Sci.,* **94,** 13057-13062 1997.

4. Raether, H. *Surface plasmon on smooth and rough surfaces and on gratings;* Springer-Verlag: Berlin, New York, 1988; Vol. 111.

5. Thiel, A. J.; Frutos, A. G.; Jordan, C. E.; Corn, R. M.; Smith, L. M.,"In situ surface plasmon resonance imaging detection of DNA hybridization to oligonucleotide arrays on gold surfaces" *Anal. Chem.,* **69,** 4948-4956 1997.

6. Pockrand, I.; Swalen, J. D.; II, J. G. G.; Philpott, M. R.,"Surface Plasmon Spectroscopy of Organic Monolayer Assemblies" *Surf. Sci.*, **74**, 237-244 1977.

7. Peterlinz, K. A.; Georgiadis, R. M.; Herne, T. M.; Tarlov, M. J.,"Observation of Hybridization and Dehybridization of thiol-tethered DNA using 2-color Surface plasmon Resonance Spectroscopy" *J. Am. Chem. Soc.*, **119**, 3401-3402 1997.

8. Nelson, B. P.; Grimsrud, T. E.; Liles, M. R.; Goodman, R. M.; Corn, R. M.,"Surface Plasmon Resonance Imaging Measurements of DNA and RNA Hybridization Adsorption onto DNA microarrays" *Anal. Chem*, **ASAP Article**, 2000.

9. Löfas, S.; Malmqvist, M.; Ronnberg, I.; Stenberg, E.; Liedberg, B.; Lundstorm, I.,"Bioanalysis with surface-plasmon resonance" *Sensor Actuator B-Chem.*, **5**, 79-84 1991.

10. Jordan, C. E.; Frutos, A. G.; A.J., T.; Corn, R. M.,"Surface plasmon resonance imaging measurements of DNA hybridization adsorption and streptavidin/DNA multilayer formation at chemically modified gold surfaces" *Anal. Chem.*, **69**, 4939-4947 1997.

11. Severs, A. H.; Schasfoort, R. B. M.,"Enhanced Surface Plasmon Resonance Inhibition test (ESPRIT) using latex particles" *Biosensors & Bioelectronics*, **8**, 365-370 1993.

12. de Vries, E. F. A.; Schasfoort, R. B. M.; Vanderplas, J.; Greve, J.,"Nucleic-Acid Detection with Surface Plasmon Resonance Using Cationic Latex" *Biosens. and Bioelectronics*, **9**, 509-514 1994.

13. Wink, T.; van Zuilen, S. J.; Bult, A.; van Bennekom, W. P.,"Liposome-mediate Enhancement of the Sensitivity in Immunoassays of Proteins and Peptides in Surface Plasmon Resonance Spectrometry" *Anal. Chem*, **70**, 827-832 1998.

14. Choi, K.; Youn, H. J.; Ha, Y. C.; Kim, K. J.; Choi, J. D.,"Detection of Cholera Cells Using Surface Plasmon Resonance Sensor" *J. Microbiology*, **36**, 43-48 1998.

15. Gu, J. H.; Lu, H.; Chen, Y. W.; Liu, L. Y.; Wang, P.; Ma, J. M.; Lu, Z. H.,"Enhancement of the Sensitivity of Surface Plasmon Resonance Biosensor with Colloidal Gold Labeling Technique" *Supremolecular Science*, **5**, 695-698 1998.

16. He, L.; Musick, M. D.; Nicewarner, S. R.; Salinas, F. G.; Benkovic, S. J.; Natan, M. J.; Keating, C. D.,"Colloidal Au-Enhanced Surface Plasmon Resonance for ultrasensitive detection of DNA hybridization" *JACS*, **in press**, 2000.

17. Lyon, L. A.; Musick, M. D.; Natan, M. J.,"Colloidal Au-enhanced surface plasmon resonance immunosensing" *Anal. Chem.*, **70**, 5177-5183 1998.

18. Sadeghi, H.; Wang, B. Enhancement of *BIAcore Sensitivity with Colloidal Gold Labeled Secondary Antibodies*; Pharmacia Biosensor: Piscataway, NJ, 1992.

19. Thiel, A. J.; Frutos, A. G.; Jordan, C. E.; Corn, R. M.; Smith, L. M.,"In situ surface resonance imaging detection of DNA hybridizaiton to olligonucleotide arrays on gold surfaces" *Anal. Chem.*, **69**, 4948-4956 1997.

20. Storhoff, J. J.; Elghanian, R.; Mucic, R. C.; Mirkin, C. A.; Letsinger, R. L.,"One-pot Colorimetric Differentiation of Polynucleotides with single base imperfections using gold nanoparticle probes" *J. Am. Chem. Soc.*, **120**, 1959-1964 1998.

21. Elghanian, R.; Storhoff, J. J.; Mucic, R. C.; Letsinger, R. L.; Mirkin, C. A.,"Selective Colorimetric Detection of Polynucleotides based on the Distance-dependent Optical properties of Gold nanoparticles" *Science*, **277**, 1078-1081 1997.

22. Mucic, R. C.; Storhoff, J. J.; Mirkin, C. A.; Letsinger, R. L.,"DNA-directed synthesis of binary network materials" *J. Amer. Chem. Soc.*, **120**, 12674-12675 1998.

23. Lyon, L. A.; Musick, M. D.; Smith , P. C.; Peña, D. J.; Natan, M. J.,"Surface plasmon resonance of colloidal Au-modified gold films" *Sensor Actuator B-Chem.*, **54**, 188-124 1999.

24. Lyon, L. A.; Musick, M. D.; Smith, P. C.; Reiss, B. D.; Peña, D. J.; Natan, M. J.,"Surface Plasmon Resonance of Colloidal Au-Modified Gold Films" *Sensors and Actuators B*, **54**, 118-124 1999.

25. Lyon, L. A.; Holliway, W. D.; Natan, M. J.,"An improved surface plasmon resonance imaging apparatus" *Rev. Sci. Instr.*, **70**, 2076-2081 1999.

26. Lyon, L. A.; Peña, D. P.; Natan, M. J.,"Surface Plasmon resonance of Au colloid-modified Au films: Particle size dependence" *J. Phys. Chem. B.*, **103**, 5826-5831 1999

Deleterious Effects of Sunscreen Titanium Dioxide Nanoparticles on DNA. Efforts to Limit DNA Damage by Particle Surface Modification

N. Serpone, A. Salinaro, and A. Emeline,

Department of Chemistry and Biochemistry, Concordia University,
1455 deMaisonneuve Blvd West, Montréal (Québec), Canada H3G 1M8.

ABSTRACT

Sunlight can have deleterious effects on humans: causes sunburns and is the principal cause of skin cancers. Usage of TiO_2 (and ZnO) in sunscreen lotions, widely used as UVA/UVB blockers, and intended to prevent sunburns and "to protect" consumers from skin cancers (carcinomas and melanomas) is examined. Although used to mineralize many undesirable organic pollutants, TiO_2 is considered to be a safe *physical* sunscreen agent because it reflects and scatters both UVB (290-320 nm) and UVA (320-400 nm) sunlight; however, it also absorbs substantial UV radiation which, in aqueous media, yields hydroxyl radical (•OH) species. These species cause substantial damage to DNA {*J.Photochem.Photobiol. A:Chem.*, **111** (1997) 205}. Most importantly, sunlight-illuminated sunscreen TiO_2 particles catalyze DNA damage both *in vitro* and in human cells {*FEBS Letters*, **418** (1997) 87}. These results raise concerns on the overall effects of sunscreens and raise the question on the suitability of photoactive TiO_2 as a sunscreen component without further studies. The photocatalytically active nature of these metal oxides necessitates some changes since even the TiO_2 specimens currently used in suncreams cause significant DNA strand breaks.

Keywords: DNA damage / titania / sunscreen agents / skin cancers

1. INTRODUCTION

1.1 Harmful Effects of Sunlight Radiation

Solar radiation reaching the Earth's surface is ~15% UV radiation (UVC, UVB and UVA), ca. 60% visible and ~25% infrared radiation (Figure 1). UV radiation can induce significant biological damage to living systems. The resulting overall
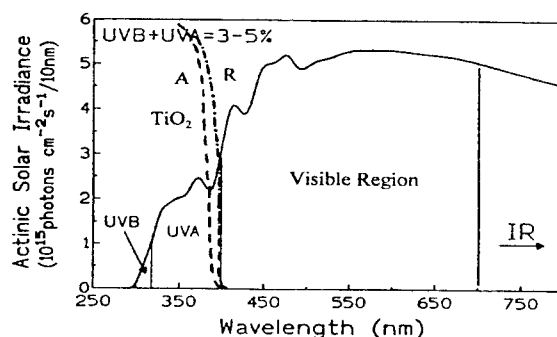
Figure 1 - Solar spectrum impinging on the Earth's surface and spectra of TiO_2 anatase (A) and rutile (R).

photochemical interactions and secondary reactions (e.g., generation of reactive species) are responsible for the UV-induced damage displayed in a wide variety of harmful clinical effects.[1]

UVB (290 to 320 nm) radiation is the principal component of sunlight that causes *erythema* of the skin; it can cause structural and cellular skin damage (e.g. elastosis, actinic keratosis, telangiectasis and skin cancers).[2] Various sunscreen lotions have been formulated and commercialized to protect human skin from such damage. Topical sunscreens are intended to provide a protective layer of exogeneous UV chromophores on the skin surface to absorb or block UV radiation before it can penetrate the epidermis and affect endogenous UV chromophores such as DNA (deoxyribonucleic acid). In doing so, sunscreens should substantially reduce endogenous photochemistry and subsequent photobiology.[3]

UVA sunlight (320 to 400 nm) contributes significantly to actinic premature skin ageing, dryness, and exfoliation, and to dermatological photosensitivity and skin cancer.[4,5] Repeated and chronic UV exposure leads to *photoaging* of the skin and initiation of skin cancers some incurable such as malignant melanomas. Photoaging is typically manifested as a leathery, thick and wrinkled appearance of the skin resulting from free radical oxidation of cell membrane lipids caused by the photogenerated reactive oxygen species (ROS).

Under "The Sun Wise School Program", the US Environmental Protection Agency has idendified some health effects from overexposure to the Sun:[6]
- Skin cancers (melanoma, basal-cell carcinoma, and qaumous-cell carcinoma).
- Premature aging of the skin and other skin problems (e.g., actinic keratoses).
- Cataracts and other eye damage (e.g., pterygium, skin cancer around the eyes and degeneration of the macula).
- Suppression of the immune system and the skin's natural defenses (e.g., impaired response to immunizations; increased sensitivity to sunlight; and reactions to certain medications), and this regardless of skin color

Consumers seek protection from the harmful effects of UVA/UVB radiation by applying a thin film of sunscreen lotion, an emulsion (oil-in water or water-in-oil) invariably composed of *physical* filters (e.g. TiO_2 and ZnO) in combination with (organic) *chemical* filters (see below).

2. SUNSCREEN ACTIVE INGREDIENTS

DNA is the most important target of UV-induced skin damage through direct or indirect absorption of UV radiation.[7] DNA bases (see Figure 2) absorb light directly in the UVB region and strongly in the UVC region (maximum absorption at 260nm) yielding various oxygen-independent reactions and photoproducts. UV radiation can also be absorbed by the DNA bases through energy transfer from sensitizers yielding oxygen-dependent reactions and formation of reactive oxygen species. There are two main types of skin cancers: squamous and basal cell carcinoma and malignant melanoma, the incidence of which has increased significantly in recent years.[8-10] This has been attributed to alterations in population behavior, e.g. to an increased exposure to sunlight is related to an increased desire for a tan. Some reports have even suggested that use of sunscreens may be associated with an increased risk of melanoma[11] attributable either to a smaller quantity of sunscreen than is recommended, 2 mg/cm^{2}, and used to determine the Sun Protection Factor (SPF) numbers, and/or to an increase in sunlight exposure when using a sunscreen because of the consumer's belief of long term protection. Sunscreen use in itself may also be a potential cause of increased incidence of carcinomas and melanomas.[12]

Sunscreens have been typically classified as (a) organic *chemical* sunscreen filters which absorb UV radiation and (b) *physical* sunscreen filters whose principal feature is to block the UV light through reflection and scattering (however see below and ref. 12. They must have three important properties if they are to prevent sunburns and protect people from skin cancers: (1) they must block UVB and UVA radiation effectively from reaching DNA in cell nuclei; (2) they must be photostable, ideally 100%; and (3) must dissipate the absorbed energy efficiently through photophysical and photochemical pathways that preclude formation of singlet oxygen, other ROS species and/or other deleterious intermediates. When excited, the active suncream ingredients likely undergo photochemical changes and energy and/or electron transfer. Such processes as photofragmentation and photoisomerization are typical. Photoisomerization may yield isomers that are less light absorbing than the parent species, and thus less useful as sunscreen agents. As well, reactive intermediates or photoproducts produced could potentially be toxic to DNA.[13]

A wide variety of organic chemicals are permitted in sunscreens, at least in Europe and elsewhere, but not in North America. Table1 lists those active sunscreen agents recognized and approved by the U.S. Food and Drug Administration for use in sunscreen lotions They all work by absorbing UVB and UVA sunlight energy. This of course raises the question of what happens

to that UV energy. In the case of Padimate-O, some of the UV radiation generates excited state species that can attack and damage DNA.[14]
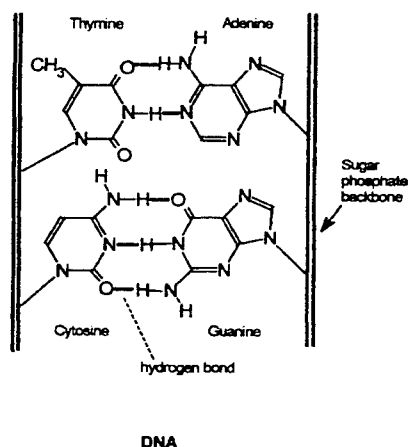
Figure 2 - Simplified DNA structure illustrating the pyrimidine and purine bases and the sugar phosphate backbone.

Commercial formulations typically employ a combination of *physical* filters (e.g. TiO_2 and ZnO) for protection over the UVA and UVB regions with *chemical* filters.[15-17] Table 2 summarizes some of the active ingredients in three well known commercial sunscreen lotions (purposely not identified). Currently, a widely used organic sunscreen active agent seems to be octylmethoxycinnamate (OMC).[3]

Table 1 - List of sunscreen active agents allowed under the U.S. Federal Register (May 21, 2000)

PABA ($\leq 15\%$)	Homosalate ($\leq 15\%$)	Octyl Salicylate ($\leq 5\%$)	Sulisobenzone ($\leq 10\%$)
Avobenzone ($\leq 3\%$)	Menthyl Anthranilate ($\leq 5\%$)	Oxybenzone ($\leq 6\%$)	**Titanium Dioxide** ($\leq 25\%$)
Cinoxate ($\leq 3\%$)	Octocrylene ($\leq 10\%$)	**Padimate-O** ($\leq 8\%$)	Trolamine Salicylate ($\leq 12\%$)
Dioxybenzone ($\leq 3\%$)	Octyl Methoxycinna- mate (OMC; $\leq 7.5\%$)	Phenylbenzimidazole Sulfonic acid ($\leq 4\%$)	Zinc Oxide ($\leq 25\%$)

Presumably the metal oxides TiO_2 and ZnO, which are both inert and nontoxic in the dark, attenuate light in these regions by simple reflection and scattering[12] (however, this is not the case; see e.g. Figure 1). Ultrafine TiO_2 irradiated with (simulated) sunlight is harmful to supercoiled plasmid DNA.[18] Specifically, irradiated TiO_2 causes single- and double-strand breaks in DNA, and photoexcited TiO_2 specimens extracted from commercial sunscreens show similar DNA damage (described later) and similar strand breaks in nuclei of whole human skin cells. TiO_2 is genotoxic to human skin.

The marketing strategy used by manufacturers is worth a brief discussion. In 1996, the focus of this strategy popularized the *micronized* TiO_2 particles: *"...protegge la pelle da scottature ed effetti dannosi provocati dal sole perche il suo sistema di protezione anti-UVA+UVB resistente all'acqua contiene Microriflettori™ che agiscono come minuscoli specchi per proteggere la pelle dai raggi solari dannosi"*. That is, *micronized* titania "... protects the skin against sunburns and harmful effects induced by the Sun because its water-resistant anti-UVA+UVB protective system contains Microreflectors™ which act as small reflectors to protect the skin from the Sun's harmful rays". The year after, publicity of sunscreen lotions was based on their containing Meroxyl as one of the active sunblock, whereas in 1998 marketing focused on the photostability of suncreams.

Table 2. - Typical active ingredients in three commercially popular sunscreen lotions.

Sunscreen 1	Sunscreen 2	Sunscreen 3
4-Methylbenzylidine camphor; 6% Parsol 1789; 1% Meroxyl SX; 1%	4-Methylbenzylidinecamphor; 6% Parsol 1789; 2% Meroxyl SX; 2%	Ethylhexyl-p-methoxycinnamate; 7.5% Oxybenzone; 5% 2-Phenylbenzimidazole-5-sulfonic acid triethanolamine salt; 2.3%
Titanium dioxide; 3.2%	**Titanium dioxide; 5%**	**Titanium dioxide; 4.5%**
Pure melanin Vegetable extracts		

Parsol 1789 = butylmethoxydibezoylmethane; Meroxyl SX = terephthalidine dicamphor sulfonic acid.

(A)

(B)

(C)

(D)
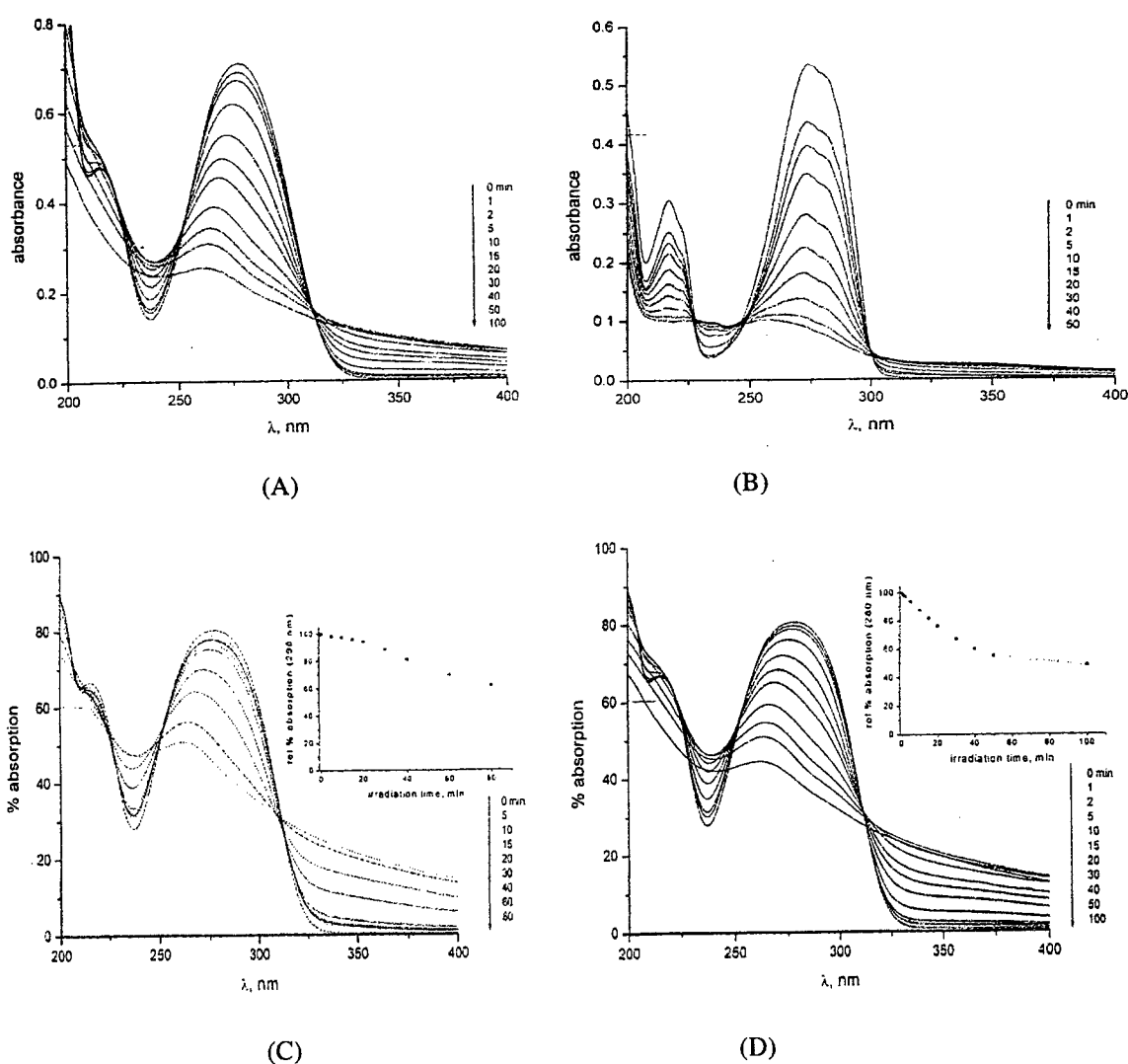
Figure 3 - Time dependent spectra of PABA either as absorbance versus wavelength or as percent absorption versus wavelength under various conditions: (A) PABA in aqueous media; (B) PABA in hexane; (C) PABA in water under anaerobic conditions; (D) PABA in water under aerobic conditions. Note the more rapid degradation of PABA in hexane by nearly a factor of two relative to PABA in aqueous media.

Figure 3 illustrates the temporal dependent spectra of PABA under various conditions. Figure 3A and 3B show the spectra of PABA in aqueous and in hexane media, respectively. In a non-polar solvent such as hexane, the long wavelength band is considerably shifted toward the blue to an extent that it no longer absorbs significant UVB radiation. Consequently one must question the usefulness of such a *chemical* UV filter in suncreams commercialized for over two decades. Figures 3C and 3D depict the effect of air oxygen when an aqueous PABA solution is illuminated with UVB radiation. Under aerobic conditions PABA degrades faster (Figure 3D) than in the absence of molecular oxygen (Figure 3C). This calls attention to the possibility of a reaction between the appropriate excited state(s) of PABA and molecular oxygen to yield singlet oxtgen (see below). As well, the absorption band blue-shifts decreasing the extent of absorption of UVB, but whatever photoproduct or intermediate is formed some UVA radiation is absorbed.

2.1 Organic Sunscreen Active Agents

Until recently, most commercial sunscreens depended entirely on organic UV-absorbing chemicals. One of the first commercially and widely used was p-aminobenzoic acid (PABA) which absorbs UV-B. Although not an ideal sunscreen, because of its crystalline nature and thus not easily incorporated into lotions, and also because it is soluble in water, PABA was thought to be quite effective at preventing sunburns. Potentially harmful side-effects of PABA were also known. In the late 1970's, Hodges et al.[19] showed that when bacteria were illuminated at 313 nm they were killed much more rapidly when PABA was present in the medium. Illumination at longer wavelengths reduced the effect. They attributed their results to increased formation of thymine dimers. When DNA absorbs UV-B radiation, thymine dimers form by reaction between two adjacent thymine residues on the same DNA strand. Unless repaired, thymine dimers lead to mutation when the cell divides. The work of Hodges et al. was later extended to human skin cells. Illumination in the presence of PABA produces thymine dimers and the cells exhibit abnormal growth characteristics.[20,21]
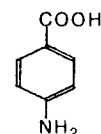
PABA = para-aminobenzoic acid

Among the PABA derivatives that were later introduced into sunscreens was the related ester 2-ethylhexyl-4-dimethylaminobenzoate (patented in 1968), known under various aliases as octyldimethyl-PABA, OD-PABA, O-PABA:, Escalol 507, and Padimate-O (Figure 4). It was an attractive sunscreen component because it is virtually insoluble in water and is a colorless oily liquid easily incorporated into sunscreen lotions; it clings well to the skin. Figure 4 summarizes some of the structures of popular chemical active agents in sunscreens.[14]
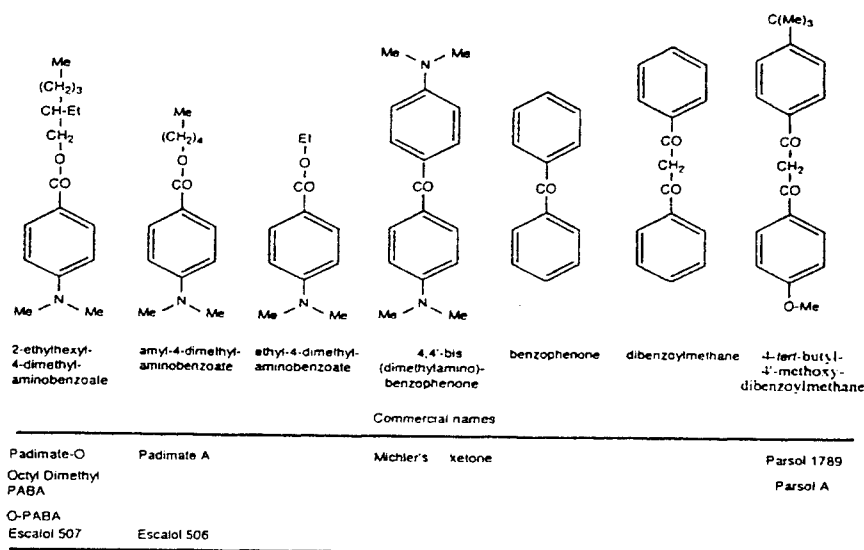
Figure 4. - Chemical structures of some of the organic *chemical* sunscreen active agents and their commercial names. From ref.[14].

Note the structural similarities between Padimate-O, Padimate-A and PABA, between benzophenone and Michler's ketone (a known carcinogen), and between Parsol 1789 and dibenzoylmethane (also a well known toxic product).

Chemically, Padimate-O is identical to the corresponding ethyl ester (ethyl-4-dimethylamino-benzoate) an industrial photo-initiator of polymerisation reactions. This ethyl ester generates carbon-centered radicals under illumination.[22] It is likely that Padimate-O behaves in a very similar fashion. In the presence of air and water, carbon-centered radicals generate peroxy radicals (•OOH) and hydroxyl radicals (•OH), both of which are very reactive and therefore expected to attack a wide variety of biologically important molecules, including DNA. It is not surprising that Padimate-O damages DNA as evidenced from studies of model systems. It kills dividing yeast cells, especially if they are incapable of repairing certain lesions; it also induces mutations.[14] Though the precise nature of the attacking species of Padimate-O remains elusive, it breaks single DNA strands and inflicts other damage as well, notably at GC (guanine-cytosine; see Figure 2) base pairs.[23] Unlike PABA, however, Padimate-O does not sensitise formation of thymine dimers. This has a potentially very important consequence. Sunscreens like Padimate-O that absorb UV-B light may actually reduce formation of direct photoproducts such as thymine dimers, while simultaneously sensitising other forms of damage that thus far have escaped intensive scrutiny.

Although Padimate-O has been in many ways a very successful sunscreen component, the related Padimate-A has been rather less so. Reports of photo-allergy and other skin problems associated with the use of sunscreens containing Padimate-A have led to its withdrawal from the European market in 1989.[1] Manufacturers gradually became wary of the effects of sunscreens that contain any compounds related to PABA. Not surprisingly, many sunscreens are marketed as PABA-free. Strictly speaking, PABA refers to *p-aminobenzoic acid*, so that although a PABA-free sunscreen may not contain *p*-aminobenzoic acid, it might still contain either or both Padimate-O and Padimate-A. In some instances, the term PABA-free comprises the absence of all three compounds, so that in practice a PABA-free sunscreen may contain none of the three related systems. Nonetheless, the consumer would be wise to read the labels (fine print).

Many of the sunscreen active ingredients, with PABA being the most efficient, are good triplet state sensitizers with the potential to convert harmless triplet oxygen, $^3O_2$, into singlet oxygen, $^1O_2$, a well-known cytotoxic species.[24] Some irradiated chemical sun-filters either increase the rate of formation of potentially carcinogenic DNA photoproducts (e.g. the cyclobutane-type pyrimidine dimers[25]) or undergo photochemical changes that result in a loss of UV-B blocking ability.[26]

There is of course no reason to believe that all organic *chemical* sunscreens behave in a like manner, but concern about their possible effects has to some extent fueled the search for inert alternatives. A UV protecting agent that is opaque to both UVA and UVB radiation, and that would be biologically inert, chemically inert, cosmetically acceptable, and compatible with conventional components of sunscreen formulations seems therefore desirable. Manufacturers have increasingly turned to inorganic materials rather than to organic compounds.[15-17] The most popular and widely used inorganic material is *micronized* titanium dioxide, TiO_2, particles. In so doing, it is interesting to note that several commercial sunscreen lotions are marketed by the claim that they contain *no chemical filters*.

2.2 Inorganic Sunscreen Active Agents

The maximal opacity of titanium dioxide particles to visible light occurs for sizes in the 180–220 nm (dia.) range. Light in this wavelength region is presumably attenuated mostly, but not completely, by reflection and scattering. Smaller particles transmit light. *Micronized* metal oxides are transparent to visible radiation and are the ones most currently used in cosmetic products. For these smaller particles, the mechanism of light attenuation is primarily due to Rayleigh scattering, with the intensity following the power law $I_{sc} \sim \lambda^{-4}$. Consequently, small particles scatter the UVB and UVA wavelengths more than the longer visible light wavelengths. However, TiO_2 also absorbs UVB and UVA light significantly,[27] a point not fully appreciated by the authors of ref [12]. For ZnO with particle size between 20 nm and 100 nm, UV radiation is scattered and absorbed by the particles. Recent work[28,29] has shown that the percent relative scattering (*versus* extent of absorption) at wavelengths below 400 nm decreases dramatically from about 80% at 390 nm to about 20% at 290 nm, i.e. in the wavelength region where UV sunlight is most damaging to human skin. Since sunscreen preparations are exposed to sunlight, the photocatalytic behavior of these *physical* UV blockers is indeed relevant.

The more common polymorphs of titanium dioxide are the two crystalline forms *anatase* and *rutile*. In the 400-700 nm region, titania particles only reflect and scatter light resulting in the expected $1/\lambda^4$ (where λ is the wavelength) dependence,[28] thereby making TiO_2 an excellent physical screen against certain photo-dermatoses (e.g. porphyria) that occur at the visible wavelengths.[30]
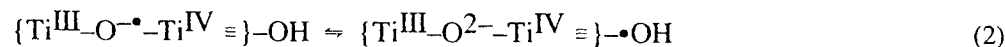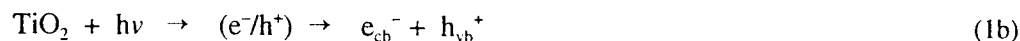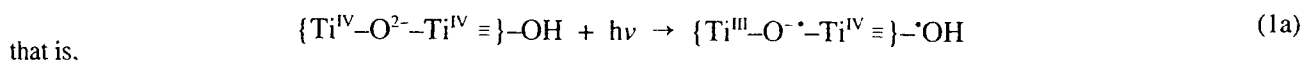
However, titania nano- and micro-crystallites absorb significantly and, to a lesser extent, scatter UVA and UVB radiation,[28] i.e. they absorb at wavelengths below 385 nm (absorption threshold: 3.20 eV; bandgap energy) for anatase and below ca. 405 nm (3.02 eV) for rutile. The anatase polymorph is a very photoactive UV semiconductor which has been used extensively as a photocatalyst to mineralize a variety of environmental organic pollutants.[31,32] The rutile TiO_2 polymorph is also a reasonably good photocatalyst under certain conditions.[33]

Absorption of radiation of suitable energy (Figure 5) by TiO_2 nano- and micro-crystallites leads to a low-energy non-vertical, indirect electronic transition from the valence band to the conduction band (indirect bandgap of anatase, 3.20 eV) and to direct, vertical transitions at higher energies (wavelengths < 385 nm).[34] These transitions form bound excitons (bound electron-hole
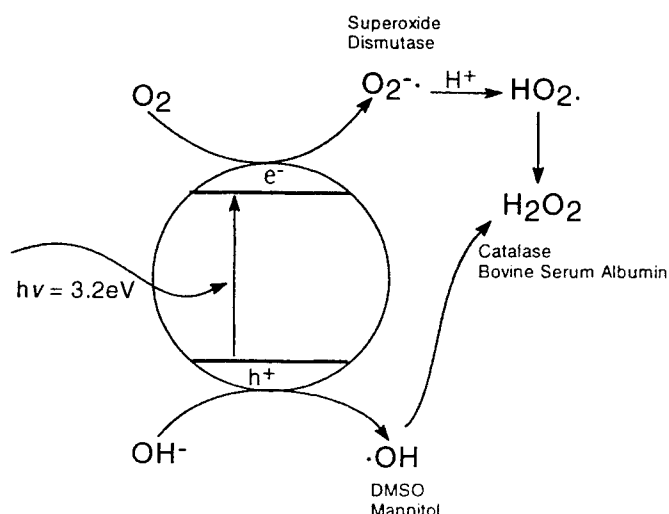
Figure 5 - Scheme illustrating the various events on illumination of a TiO_2 particle by UVB/UVA radiation together with formation of the superoxide radical anion, •OH radicals, and hydrogen peroxide. Also shown are the compounds that react with these reactive oxygen species.

pairs, eqn 1b), which subsequent to their separation and migration (eqn 1b) towards the crystallite surface, while spanning various lattice and surface defects, ultimately yield surface-trapped electrons (e_{tr}^-) and holes (h_{tr}^+) in very short time ($< 10^{-11}$ s[35]). These charge carriers are then poised to initiate photoreductions and photooxidations at the particle surface. The trapped holes (eqn 2) are identified with surface-bound •OH radicals which can combine to yield H_2O_2 (eqn. 3).[36,37]

that is,

$$\{Ti^{IV}-O^{2-}-Ti^{IV} \equiv\}-OH + h\nu \rightarrow \{Ti^{III}-O^{-\bullet}-Ti^{IV} \equiv\}-{}^\bullet OH \tag{1a}$$

$$TiO_2 + h\nu \rightarrow (e^-/h^+) \rightarrow e_{cb}^- + h_{vb}^+ \tag{1b}$$

$$e_{cb}^- \rightarrow e_{tr}^- \{as\ Ti^{III}\} \tag{1c}$$

$$h_{vb}^+ \rightarrow h_{tr}^+ \{as\ {}^\bullet OH_{surf}\} \tag{1d}$$

$$\{Ti^{III}-O^{-\bullet}-Ti^{IV} \equiv\}-OH \rightleftharpoons \{Ti^{III}-O^{2-}-Ti^{IV} \equiv\}-{}^\bullet OH \tag{2}$$

$$2\ \{Ti^{III}-O^{2-}-Ti^{IV} \equiv\}-{}^\bullet OH \rightarrow H_2O_2 \tag{3}$$

The •OH radical causes cellular damage *in vivo*[38] and although it does not diffuse from the surface of TiO_2 particles, its dimeric product H_2O_2 can diffuse to considerable distances and effect serious damage.[39] Some recent reports have even inferred formation of singlet oxygen when TiO_2 is UV-irradiated.[40,41]

To test for the formation of •OH radicals produced on irradiation of TiO_2 extracted from sunscreens and to verify their activity as initiators of harmful reactions inducing DNA damage, we examined the oxidation of organics by •OH radicals

produced on illuminated TiO_2.[18] Photodecomposition of a large variety of other organic compounds by irradiated TiO_2 has been reported extensively.[42] Table 3 lists results obtained from our study[18] of 10 different TiO_2 samples extracted from commercial sunscreen lotions for the photoxidative degradation of phenol. This photooxidation does not correlate with the fraction of anatase and rutile forms present in the TiO_2 specimens (rutile is ca. 10% as photocatalytically active as anatase[33]). Evidently, other factors influence the photodegradation, the most notable one being the very complex nature of the particle surface.

It is noteworthy that photoexcited titania particles are cytotoxic (*in vitro*) to HeLa cells and suppress their growth when implanted in nude mice; T-24 human cancer cells are destroyed *in vitro* and *in vivo* by illuminated titania.[43] Of greater import TiO_2 particles are located both on the surface of the cells and inside the cells.[44] This observation has important consequences.

Confirming the work of Fujishima and coworkers,[43,44] *in vitro* studies by Knowland[45] using human cells in culture and simulated sunlight irradiated TiO_2 suggested that DNA is damaged. Also, Wamer[46] found that UVA excited TiO_2 is photocytotoxic to skin fibroplasts and is accompanied by photooxidative damage to cellular RNA (ribonucleic acid). Such damage to endogenous chromophores appears to occur by a process involving radical species.

Table 3. - Relative rates of photodegradation of phenol by TiO_2 specimens and percent anatase and rutile forms present (from ref. [18]).

Specimen	% anatase	% rutile	Relative rates
Pure anatase	100	0	3803
pure rutile	0	100	427
SN1*	50	50	1.0
SN2	0	100	2.8
SN3	0	100	5.2
SN4	54	46	5.2
SN5	0	100	10.4
SN6	100	0	17.6
SN7*	0	100	22.7
SN8	100	0	53.3
SN9	63	37	134
SN10**	0	100	180

SN1-SN10: OTC sunscreen lotions. * Also contains $Al(OH)_3$; ** Also contains 1.95% ZnO.

To the extent that such radicals are produced when TiO_2 particles are illuminated with UV-A and/or UV-B light and that TiO_2 particles have been seen in the interior and exterior of cell walls,[44] the question about the *safe* utilization of this inorganic material in sunscreen lotions requires closer examination.

3. PHOTOACTIVITY OF SUNSCREEN TIO$_2$ ON DNA

Ultrafine titanium dioxide irradiated with simulated sunlight is harmful to supercoiled plasmid DNA owing to photogenerated •OH radicals on TiO_2. Figure 6 shows that TiO_2 causes single- and double-strand breaks, as evidenced by the change of the supercoiled form of DNA plasmids (S) to the relaxed form (R) after one nick, and then to the linear form (L) after two nicks. A TiO_2 specimen extracted from a commercial sunscreen showed similar results, consistent with the data obtained for the photodegradation of phenol (see Table 3).

Hydroxyl radicals can inflict direct strand breaks on DNA. To test for such damage supercoiled plasmids were illuminated with simulated sunlight and TiO_2. Plasmids were first converted to the relaxed form and then to the linear form, demonstrating strand breakage. Sunlight alone has very little effect, whereas anatase is more active than rutile, consistent with photochemical comparisons.[33] TiO_2 extracted from a sunscreen was also photoactive. Since the quantity of TiO_2 in sunscreens was less than in the pure anatase and rutile samples, the sunscreen titania is especially active. Damage is quenched[47] by DMSO and mannitol, strongly suggesting that damage is caused by direct attack by •OH radicals. DNA strand breaks are not caused by the superoxide $(O_2^-•)$ radical anion, an active oxygen species formed by reaction between $e^-(cb)$ and O_2, nor by hydrogen peroxide, an intermediate species from reaction between 2•OH radicals as evidenced by the fact that superoxide dismutase had no effect on

the degradative process. DNA damage was not confined solely to strand breaks.[18]
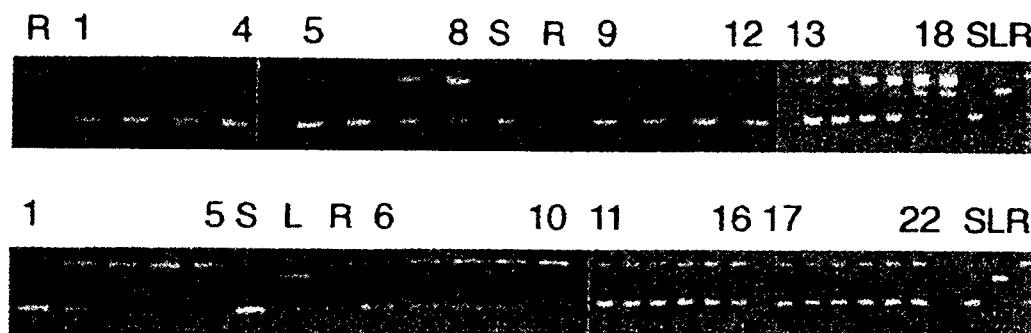
Figure 6. - Relaxation of plasmids caused by illuminated TiO_2 and ZnO, and suppression by DMSO and mannitol. In both panels, S, L, and R show migration of supercoiled (S), linear (L) and relaxed (R) plasmids. **Top panel**: plasmid relaxation found after ilumination with sunlight alone (lanes 1-4), with 1 wt.% anatase TiO_2 (lanes 5-8), and 1 wt.% rutile TiO_2 (lanes 9-12) for identical times as sunlight alone (0, 20, 40 and 60 min). Lanes 13-18 depict effect of illumination of TiO_2 extracted from a commercial sunscreen sample and irradiated for 0, 5, 10, 20, 40 and 60 min. **Bottom panel**: illumination of plasmids (0, 10, 20, 40, and 60 min) with 0.2 wt.% ZnO before (lanes 1-5) and after (lanes 6-10) addition of DMSO; and with 0.0125 wt.% sunscreen SN8 TiO_2 after addition of DMSO (200 mM; lanes 11-16) and mannitol (340 mM; lanes 17-22) for 0, 5, 10, 20, 40 and 60 min pf irradiation. From ref. [18].

DNA damage caused by illuminated TiO_2 is only slightly suppressed by catalase (Figure 7); heat-inactivated catalase and bovine serum albumin show similar effects. The limited quenching is caused by the surrounding protein and not by the catalase. In addition, superoxide dismutase does not suppress DNA damage. Consequently, any resulting DNA damage is not due to the superoxide radical anion, $O_2^{-\bullet}$, nor to the intermediate hydrogen peroxide, H_2O_2, formed by reaction between two •OH radicals
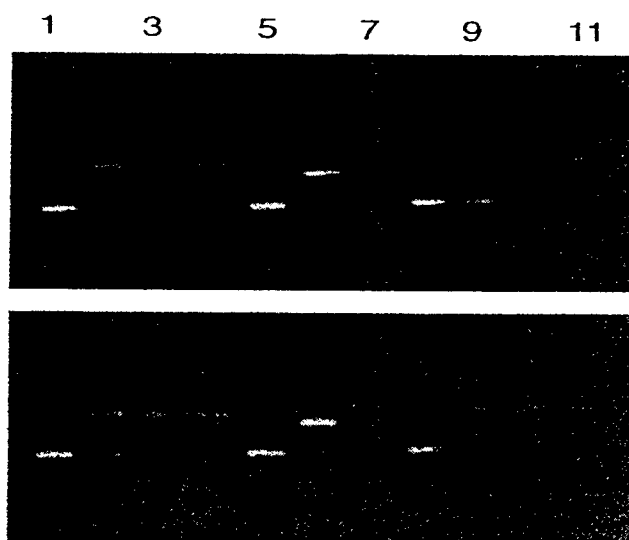
Figure 7. - Effect of catalase on DNA damage inflicted by illuminated TiO_2. **Top Panel** illustrates plasmid DNA illuminated in the presence of sunscreen SN8TiO_2 alone (lanes 1-4) and after addition of 2.5 units/μL of catalase (lanes 8-11; 0.1 mg/mL of protein) for 0, 20, 40 and 60 min. In lanes 5-7 of the panel are shown the supercoiled, linear and relaxed forms of the plasmid DNA. Lower panel shows plasmids illuminated as above after addition of boiled catalase (lanes 1-4) or 0.1 mg/ml of bovine serum albumin (lanes 8-11). From ref. [18].

(eqn. 3). The cause of the observed strand breaks produced in the plasmid molecule is caused by •OH radicals since the damage is suppressed by hydroxyl radical quenchers[52] such as DMSO and mannitol (Figure 7).

Comet assays are ideal to confirm whether photoexcited TiO_2 causes strand breaks in the nuclei of whole human skin cells, and to detect directly alkali-labile sites in DNA. These assays (Figure 8) provide a basis for assessing the potential genotoxicity of ultrafine TiO_2 on human skin. The assay is based on the effect that the introduction of strand breaks in DNA has on the supercoiling within the nucleus. Introducing a nick into supercoiled DNA causes relaxation and loss of supercoiling. If the nuclear membrane and most of the nuclear proteins are removed to create a nucleoid, the DNA strands that contain the nicks are released creating a so-called comet; otherwise the supercoil remains intact in undamaged nuclei and appears as a round whole circle (see Figure 8). The assays showed that human cell DNA can indeed be damaged by illuminated TiO_2 that can penetrate the cell membrane in the cytoplasm, and which is consistent with endocytosis of TiO_2.[48] Once again DMSO suppressed DNA damage thereby confirming the important role of •OH radicals.

Our recent results[18] show that sunscreen TiO_2 (and also ZnO) can also catalyze oxidative damage to DNA *in vitro* and in cultured human fibroblasts. However, the fate of these inorganic materials when applied to the skin remains controversial, even though there is supporting evidence[48] to show that TiO_2 and ZnO can penetrate human skin. Auto-radiographic studies using ^{65}ZnO noted that ZnO passes through rat[49] and rabbit[50] skin (probably) through hair follicles. Other reports have raised the possibility that ZnO [19] and pigmentary TiO_2 [51,52] can also pass though human skin. A recent study has even suggested that micronised TiO_2 in sunscreens does also.[53]
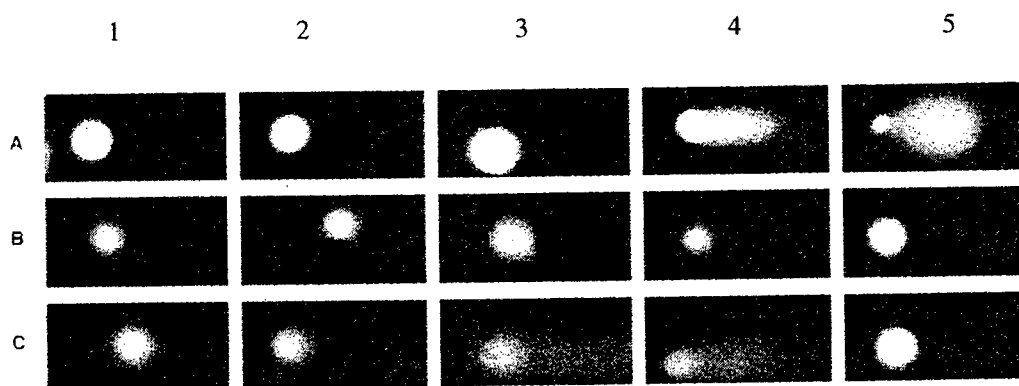
Figure 8. - Damage inflicted on human cells revealed by Comet assays. **Row A** shows comets obtained using X-rays from a Gravitron RX30 source; dose rate was 8.9 Gy/min and cells were exposed on ice for 0, 15, 30, and 60 s, giving comets falling into the 5 main standard classes shown: (1) class 0; (2) class I; (3) class II; (4) class III; (5) class IV. **Rows B and C** illustrate examples of comets obtained using simulated sunlight, MRC-5 fibroblasts and sunscreen TiO_2 (0.0125 wt.%). For each exposure, 100 cells were scored and comets were classified by comparison with the standards (row A). Row B: no treatment (1); sunlight alone for 20, 40 and 60 min (2-4); and effect of TiO_2 in the dark for 60 min (5). Row C: sunlight with TiO_2 for 0, 20, 40, and 60 min (1-4), and for 60 min with TiO_2 and 200 mM DMSO (5). From ref. [18].

DNA damage is typically assessed by classifying the comets produced into groups according to the length and area of the tail. The greater the area of the tail, the more damage has been caused (done visually using a fluorescence microscope). Figure 8 shows that light alone induces some breaks at 20,40 and 60 min of irradiation; TiO_2 (Degussa P-25) catalyzes this damage at identical irradiation times. Titanium dioxide specimens present in commercial sunscreens were also tested; results confirmed that ultrafine TiO_2 inflicts breaks in DNA.[18]

Whilst most researchers in heterogeneous photocatalysis have attempted to fabricate the most *photocatalytically active* TiO_2 system to degrade the most stubborn of environmentally harmful pollutants, our recent efforts[54] have focussed on producing the most *photocatalytically inactive* TiO_2 specimens for possible use in sunscreen lotions while retaining the spectroscopic features of TiO_2 that make it an excellent UVA/UVB blocker. We have fabricated some 20 or so specimens. Figure 9 illustrates the kinetic behavior of these specimens before and after inactivation of the particle surface for the photooxidative degradation of phenol.
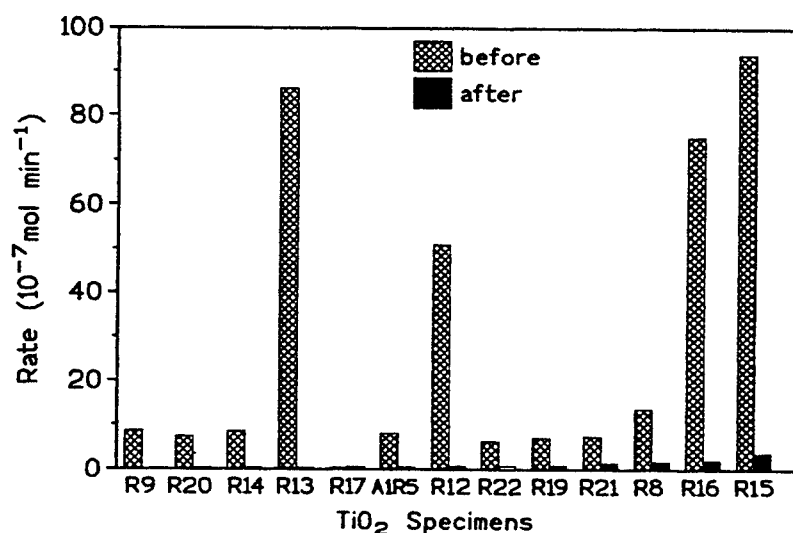
Figure 9. - Rates of photodegradation of phenol by several TiO$_2$ specimens before and after surface modification.

The method used has achieved the desired goal since the rate of photodegradation of phenol has been reduced dramatically for many of the specimens. Specimen R13 shows the largest drop in the rate of photooxidation of phenol, followed by R12, R16 and R15. Subsequently we examined the damaging effects of these samples on DNA plasmids. Figure 10 displays some of the results as the fraction of DNA plasmids remaining in the supercoiled state as a function of illumination time for a 1% by wt. concentration of TiO$_2$.

For pure anatase (Tioxide) and for the R12 and R19 specimens the data in Figure 10 show that after modification, the irradiated R12A specimen has no influence on DNA relative to a DNA sample subjected to otherwise identical UVA/UVB
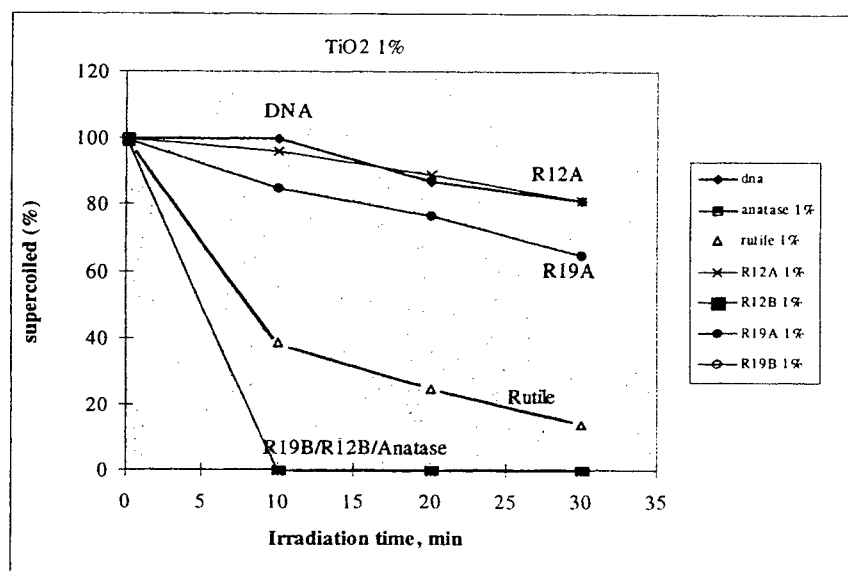
Figure 10. - Fraction of supercoiled DNA plasmids surviving the influence of various samples of irradiated TiO$_2$ (1 wt.%) for a 30-min period. From ref. [54].

illumination (calibrated solar simulator) and experimental conditions for a 30-min time period; note that R12A displays the same spectral features as specimen R12B. Figure 10 also demonstrates that anatase R19B and R12B specimens have in fact destroyed

nearly all the plasmids after only 10 min of irradiation; as well, the rutile form is less damaging than anatase (ca. 15% of the plasmids remain in the supercoiled state), as known from a multitude of studies on the photooxidation of environmental organic pollutants, and R19A is even better with ca. 65% of the plasmids surviving during the 30-min period.

3. CONCLUDING REMARKS

No doubt utilization of sunscreens helps to prevent sunburns, but does it reduce the risk of skin cancers? These have increased remarkably rapidly lately.[55,56] There is a need to characterise the fate and photochemical behavior of such sunscreens before commercial utilization. Though they can reduce the formation of cyclobutane dimers in DNA,[57] which are induced by direct absorption of UVB, the ability of TiO_2 and at least one organic *chemical* sunscreen to form reactive species such as •OH radicals that can inflict other forms of damage[14,23] emphasizes the importance of investigating the photobiological and photochemical aspects of sunscreen active components. These may themselves photochemically degrade and thereby reduce the UV blocking ability for times typically used in actual practice (tens of minutes to a few hours). Work along these lines is in progress.

ACKNOWLEDGEMENTS

REFERENCES

1. Official Journal of the European Communities (8 March 1989) No L64, 10-12.
2. M.W. Brown, E. Galley, *Cosmetics & Toiletries*, **105**, 69 (1990).
3. N.A. Shaath, "*Photochemistry and Photostability of Sunscreen Components, Mixtures, and Products*", Discussion of the Photochemistry and Photobiology of Sunscreens: Public Meeting and Reopening of the Administrative Record", U.S. Food and Drug Administration, Rockville, MD, September 19 & 20, (1996).
4. L.H. Kligman, *J.Invest.Dermatol.*, **84**, 274 (1985).
5. L.H. Kligman,.., *Dermatol.Clin.*, **4**, 517 (1986).
6. EPA's Sun Wise School Program: Health Effects of UV Radiation. U.S. Environmental Protection Agency, July 26, 2000.
7. N.A. Cridland, R.D. Saunders, "*Cellular and Molecular Effects of UVA and UVB*", NAPB-R269, HMSO, London, **1994**.
8. D. S. Preston, R. S. Stern, *New. Engl. J. Med.*, **327**, 1649 (1992).
9. P. Boyle, P. Maisonneuve, J. F. Dore, *Br.Med.Bull.*, **51**, 523 (1995).
10. (a) R. Marks, *Cancer*, **1995**, 75, 607; (b) A. Katsambas, E. Nicolaidou, *Arch.Dermatol.*, **132**, 444 (1996).
11. C. F. Garland, F. C. Garland, E. D. Gorham, *Am.J.Public Health*, **82**, 615 (1992).
12. U.S. Federal Register, Report 64 FR 27666, May 21, **2000**.
13. (a) B. Epe, *Chem-Biol.Interact.*, **80**, 239 (1991); (b) J.M. Allen, C.J. Gossett, S.K. Allen, *Chem.Res.Toxicol.*, **9**, 605 **(1996)**.
14. J. Knowland, E.A. McKenzie, P.J. McHugh, N.A. Cridland, *FEBS Letters*, **324**, 309 (1993).
15. B. Catlow, *Seifen Oele Fette Wachse J.*, **119**, 497 (1993).
16. P. Alexander, *Manufacturing Chemist*, **62**, 21 (1991).
17. "Formulators Fine-Tune TiO_2-Based Screens", *Manufacturing Chemist*, **64**, 26 (1993).
18. R. Dunford, A. Salinaro, L. Cai, N. Serpone, S. Horikoshi, H. Hidaka, J. Knowland, *FEBS Letts.*, **418**, 87 (1997).
19. N.D.M. Hodges, S.H. Moss, D.J.G. Davies, *Photochem. Photobiol.* **26**, 493 (1977).
20. B.M. Sutherland, *Photochem. Photobiol.* **36**, 95 (1982).
21. J.C. Sutherland, K.P. Griffin, *Photochem. Photobiol.* **40**, 391(1984).
22. M. Forster, R.E. Hester, *J. Chem. Soc. Faraday Trans. 2*, **77**, 1521 (1981).
23. P.J. McHugh, J. Knowland, *Photochem. Photobiol.* **66**, 276 (1997).
24. J.M. Allen, C.J. Gossett, S.K. Allen, "*Photochemical Formation of Singlet Molecular Oxygen ($^1O_2$) in Aqueous Solutions of Several Sunscreen Active Ingredients*", Discussion of the Photochemistry and Photobiology of Sunscreens: Public Meeting and Reopening of the Administrative Record, U.S. Food and Drug Administration, Rockville, MD, September 19 & 20, (1996).
25. S.Y. Wang,, Ed., "*Photochemistry and Photobiology of Nucleic Acids*", vol.I, Academic Press, New York, (1976).

26. B.S. Martincigh,, *"DNA Photodamage Induced by Sunscreen Absorbers"*, Discussion of the Photochemistry and Photo-biology of Sunscreens: Public Meeting and Reopening of the Administrative Record, U.S. FDA. Rockville, MD, September 19 & 20, 1996.

27. N. Serpone, A. Salinaro, H. Hidaka, S. Horikoshi, J. Knowland, R. Dunford, "Beneficial and Deleterious Effects of Solar Radiation", in *Solar Engineering 1998.*,J.M. Morehouse & R.E. Hogan, Eds., ASME, New York, **1998**, pp. 287-298.

28. N. Serpone, A. Salinaro, *Pure Appl.Chem.*, **1999**, *71*, 303.

29. A. Salinaro, A.V. Emeline, J. Zhao, H. Hidaka, V.K. Ryabchuk, N. Serpone, *Pure Appl.Chem.*, **1999**, *71*, 321.

30. T.M. Macleod, W. Fran-Bell, *British J.Dermatol.*, **92**, 149 (1975).

31. D.W. Bahnemann, J. Cunningham, M.A. Fox, E. Pelizzetti, P. Pichat, N. Serpone, in *"Aquatic and Surface Photochemistry"*, D. Crosby, G, Helz, and R.G. Zepp, Eds., Lewis Publishers, Boca Raton, FL., pp. 261-316 (1994).

32. N. Serpone, , in *"The Kirk-Othmer Encyclopedia of Chemical Technology"*, Wiley-Interscience, New York, vol.18, pp. 820-837 (1996).

33. A. Sclafani, J.-M. Herrmann,, *J.Phys.Chem.*, **100**, 13655 (1996).

34. N. Serpone, D. Lawless, R.F. Khairutdinov, *J.Phys.Chem.*, **99**, 16646 (1995) .

35. N. Serpone, D. Lawless, E. Pelizzetti, R.F. Khairutdinov, *J.Phys.Chem.*, **99**,16655 (1995) .

36. D. Lawless, N. Serpone, D. Meisel, *J.Phys.Chem.*, **95**, 5166 (1991).

37. J.H. Arbour, J. Tromp, M.L. Hair,, *Can.J.Chem.*, **63**, 204 (1985).

38. J. Russell, J. Ness, M. Chopra, J. McMurray, W.E. Smith, *J. Pharmaceut. Biomed. Anal.*, **12**, 863 (1994).

39. H.M. Swartz, *"The Significance of Free Radicals in the Pathophysiology of the Skin"*, Discussion of the Photochemistry and Photobiology of Sunscreens: Public Meeting and Reopening of the Administrative Record, U.S. FDA, Rockville, MD, September 19 & 20, 1996.

40. (a) W.C. Dunlap, Y. Yamamoto, M. Inoue, M. Kashiba-Iwatsuki, M. Yamaguchi, K. Tomita, *Int.J.Cosmetic Sci.*, **20**, 1 (1998); (b) R. Konaka, E. Kasahara, W.C. Dunlap, Y. Yamamoto, K.C. Chien, M. Inoue, *Free Radic.Biol.Med.*, **27**, 294 (1999).

41. Y. Yamamoto, N. Imai, R. Mashima, R. Konaka, M. Inoue, W.C. Dunlap, *Methods Enymol.*, **319**, 29 (2000).

42. N. Serpone and E. Pelizzetti, "Solar Photochemical Remediation of Air and Water", in *"Photochemical and Photoelectro-chemical Approaches to Solar Energy Conversion"*, M.D. Archer and A.J. Nozik, Eds., Imperial College Press, London, **2001**, vol. **III**, chapter 15.

43. R. Cai, Y. Kubota, T. Shuin, H. Sakai, K. Hashimoto, A. Fujishima, *Cancer Res.*, **52**, 2346 (1992).

44. Y. Kubota, T. Shuin, C. Kawasaki, M. Hosaka, H. Kitamura, R.Cai, H.Sakai, K. Hashimoto, A. Fujishima, *British J.Cancer*, **70**, 1107 (1994).

45. J. Knowland, *"Potential Genotoxicity of Inorganic Sunscreens"*, lecture presented at the Discussion of the Photochemistry and Photobiology of Sunscreens: Public Meeting and Reopening of the Administrative Record, U.S. FDA., Rockville, MD, September 19 & 20, 1996.

46. W. Warner, *"Oxidative Damage to Nucleic Acids Photosensitized by Titanium Dioxide"*, Discussion of the Photochemistry and Photobiology of Sunscreens: Public Meeting and Reopening of the Administrative Record, U.S. FDA, Rockville, MD, September 19 & 20, 1996.

47. B. Halliwell and J.M.C. Gutteridge, *"Free Radicals in Biology and Medecine"*, Clarendon Press, Oxford, UK., **1989**.

48. R. Cai, K. Hashimoto, K. Itoh, Y. Kubota, A. Fujishima, *Bull. Chem. Soc. Jpn.*, **64**, 1268 (1991).

49. G. Hallmans, S. Liden, *Acta. Derm. Venereol.* **59**, 105 (1979).

50. S.P. Kapur, B.R. Bhussry, S. Rao, E. Hormouth-Hoene, *Proc. Soc. Exp. Biol. Med.* **145**, 932 (1974).

51. A. Dupre, P. Touron, J. Daste, J. Lassere, J.L. Bonafe, R. Viraben, *Arch. Dermatol.* **121**, 656 (1985).

52. C.A Moran, F.G. Mullick, K.G. Ishak, F.B. Johnson, W.B. Hummer, *Hum. Pathol.* **22**, 450 (1991).

53. M-H. Tan, C.A. Commens, L. Burnett, P.J. Snitch, *Australas. J. Dermatol.* **37**, 185 (1996).

54. A. Salinaro, N. Serpone, J. Knowland, results **1998-2000**, to be published.

55. D.S. Preston,, R.S. Stern, *New Engl. J. Med.*, **327**, 1651 (1992).

56. P. Boyle, P. Maisonneuve, J-F. B. Dore, *Med. Bull.* **51** 523 (1995).

57. H.N. Ananthaswamy, et al., *Nature Medicine*, **3**, 510 (1997).

Nano-carriers of Fluorescent Probes and Enzymes

Qiang Wang[a], Xiaoyan Chen[a], Dan Meisel[b], Hiroshi Mizukami[c], Agnes Ostafin[1a],

[a]Department of Chemical Engineering, University of Notre Dame, Notre Dame, IN 46556.
[b]Department of Chemistry and Biochemistry & Radiation Laboratory, University of Notre Dame, Notre Dame, IN 46556.
[c]Department of Biological Science, Wayne State University, Detroit, MI 48202.

ABSTRACT

Cascade Blue, Sulforhodamine G and yeast alcohol dehydrogenase were encased inside nano-sized silicate shell and their absorption and fluorescence spectrophotometric properties, and the enzyme activity investigated. The stabilized molecules have potential as biosensors, in drug delivery, and recyclable catalysts.

Cascade Blue and Sulforhodamine G were attached to 85 nm diameter colloidal gold, encased with silicate, and the gold core dissolved. Fluorescence quenched by the gold was recovered for both dyes, but the peak emission was red-shifted from that in water for Cascade Blue and blue-shifted for Sulforhodamine G. The fluorescence excitation spectra of these dyes showed similar shifts, reflecting their interaction with the shell interior.

The spectrofluorometric results for alcohol dehydrogenase bound to 15 nm diameter colloidal gold were similar. The substrate ethanol and cofactor NAD were permeable to the silicate shell. Only 20% of enzyme activity of ADH was lost after binding to gold and an additional 20% lost by encasing with silicate. Subsequent rate of loss of activity was significantly lowered.

This study demonstrated that dyes and enzymes could be encased within silicate shells. Whether the shell protects these molecules from the environment, and how the thickness of silicate shell affects the rate of enzyme reaction remain to be investigated.

Keywords: Nano-carriers, nano-shells, colloidal silicate, colloidal gold, Cascade Blue, Sulforhodamine -G, alcohol dehydrogenase

1. INTRODUCTION

Colloidal chemistry enjoys one of the longest traditions among many fields of chemistry. While its primary interest in the bulk behavior of colloids remains strong, the properties and behavior of individual nano-scale colloidal particles are becoming another primary focus of the field. The applications for nano -sized colloidal particles are diverse, for example, they may be used as a primary host to capture specific molecules, or act as a template to form nano -shells of other materials around it. The focus of this work is to explore the method fo encasing probe molecules and enzymes within hollow nano-shells of silicate.

Several improved methods to coat nano-sized particles with silicate have been reported. Bi -functional amino or mercapto-silanes have been used to help nucleate the condensation of silicate around colloidal polystyrene [1] and colloidal gold [2-4]. Recently it has been shown that polyme -coated vesicles [5] can also be coated with a shell of silicate. The thickness of the shell and the size of the nanoparticle core may be adjusted by varying the conce trations of reagents, the pH, and amount of time allowed for silicate condensation, and thus silicate -coated

---

[1] Corresponding author aostafin@nd.edu; tel:1-219-631-3798; fax:1-219-631-8366; http://www.nd.edu/~aostafin; Department of Chemical Engineering, University of Notre Dame, Notre Dame IN 46556.

particles ranging from tens of nanometers to several hundreds of nanometers of relatively uniform size can now be made.

Once the condensation of silicate shell is completed, the template core may be dissolved leaving a hollow center. This center may be filled with materials of interest, adding chemical, as well as biological, functionality to the silicate shells. The silicate shells may provide a protective coat for sensitive encased materials, such as proteins, drugs, probes, etc., assuring their prolonged survival in harsh environments and use as chemical or biological sensors [6,7]. Earlier, fluorescein isothiocyanate was encased inside silicate nano-shells by Makarova, et al.[8]. Comparative fluorescence quenching experiments confirmed that the dye was indeed encased within a nano-shell of silicate, and the work suggested that it should be feasible to encapsulate other active molecules within these shells in a similar manner. In this paper, we will discuss a method for the encapsulation of two small dy molecules, Cascade Blue and Sulforhodamine-G, and a relatively large protein, yeast alcohol dehydrogenase. The chemical and biological activities of these two classes of molecules following the encapsulation are also examined.

2. METHODOLOGY

2.1 Materials.

Hydrogen tetrachloroaurate (III) hydrate ($HAuCl_4\cdot3H_2O$) (Sigma), sodium citrate ($Na_3C_6H_5O_7\cdot2H_2O$) (Fisher), hydroxyamine hydrochloride (NH_2OH-HCl) (Sigma), 3-aminopropyl trimethoxysilane (APS) (Sigma), sodium silicate solution ($Na_2O(SiO_2)_3$, (0.27 wt% SiO_2) (Sigma), sodium cyanide (NaCN) (Sigma), Cascade Blue and Sulforhodamine-G (Molecular Probes) were all us ed as received without further purification. Analytical grad ethanol (Sigma) and E -pure water (18 MOhm) were used in all preparations. Yeast alcohol dehydrogenase (Sigma) was used as received. All other chemicals were analytical grade and used without further purification.

2.2 Transmission Electron Microscopy

Transmission Electron Microscopy (TEM) was carried out using a Hitachi Model -600 transmission electron microscope. To prepare the sample for TEM observation, carbon-coated copper grids (Ted Pella) were dipped into a 1% aqueous poly-lysine solution (Sigma) for 5 minutes and subsequently rinsed with deionized water. A drop of silicate nano-shell suspension was placed on the grid and allowed to dry until all the solvent evaporated. TE micrographs were recorded at 150,000X or higher magnification, corresponding to about 75 kV/cm^2.

2.3 Absorption and Fluorescence Spectrophotometry.

UV-Vis absorption spectroscopy was carried out at room temperature using a Cary 50 Bio absorption spectrophotometer (Varian), and a 1-cm path length Suprasil quartz cuvette. Fluorescence spectrophotometry was performed at room temperature using an SLM8000C spectrofluorimeter (SLM Instruments).

2.4. Preparation of Colloidal Gold.

Gold nanoparticles were prepared as follows: Five milliliters of 1% $HAuCL_4$ solution was added to 200 ml of water and the solution heated to boiling while magnetically stirred. Twent -five ml of 1% aqueous sodium citrate solution at room temperature was added to the boiling solution with vigo rous magnetic stirring. Stirring was allowed to continue until the solution became a deep red color, approximately 20 minutes, at which point the total volume was adjusted to 250 ml. To remove excess citrate ions, the gold solution was treated with 0.5 m l of Amberlite MB-150 mixed ion exchange resin (Sigma) (1 gram resin per 50 ml water) for about thirty minutes. The conductivity of the solution was measured using a Radiometer Model-CDM83 conductivity meter (Copenhagen). Individual particles of colloida l gold prepared in this way were about 15 nm ± 2 nm in diameter as confirmed using TEM.

Gold particles ~85 nm in diameter were prepared using a seeded growth method [9]. In brief, 0.83 ml of 0.2 M NH_2OH-HCl and 0.92 ml of 1% $HAuCL_4$ solution was added under vigorous magnetic stirring at room temperature to 10 ml of the aqueous 15 nm colloidal gold stock solution that had been diluted to 100 ml. After 20 minutes reaction time, the sample was dialyzed against water at pH 7.0 to remove un -reacted gold and hydroxylamine. The size of the particles was verified using TEM to be 85 nm ± 5 nm.

Colloidal gold suspension was stored in the dark at 4°C and warmed to room temperature before use. The UV-Vis absorption spectrum was taken at room temperature following this, and the absorbance of the colloidal gold

plasmon band, at 520 nm for 15 nm diameter particles and 540 nm for 85 nm particles was used to determine the final concentration of gold particles in the solution after manipulation. Assumi ng all the gold had been reduced into uniformly sized particles, the particle concentration in the colloidal gold stock solution was about 3×10^{15} particles L^{-1}.

2.5. Encapsulation of Dye Molecules in Silica Shells.

Silicate shells around Cascade Blu e (MW= 548 dalton) and Sulforhodamine-G (MW= 553 dalton) were prepared in the following manner: To reduce the degradation of the fluorescents dyes, all manipulations were carried out in dim light and containers covered with aluminum foil. Aqueous solutions containing 3×10^{-4} M Cascade Blue, and 3×10^{-4} M Sulforhodamine-G were prepared, and pH was adjusted to pH 7.0 using 0.1 M NaOH. The concentrations of the APS and sodium silicate solutions were adjusted to 7.3×10^{-3} M and 0.27 wt%, respectively. The pH of 15 ml of the 85 nm diameter colloidal gold suspension was adjusted to about pH 9.0 using 0.1 M NaOH. The typical absorbance of the colloidal gold was approximately 0.8 to 1.0.

Eight microliters of dye solution were added to the colloidal gold under vigorous magnetic stirring. After abou twenty minutes reaction time, the solution pH was adjusted to approximately pH 5 using 0.1M HCl solution, and eight microliters of 7.3×10^{-3} mol L^{-1} APS solution were added. After an additional twenty minutes, the solution pH was adjusted once more to about pH 10.5, and 1 ml of sodium silicate solution was added in one step to the suspension under vigorous magnetic stirring. After stirring for twent -four hours, 4 ml of 100% ethanol wer added quickly and vigorous stirring was continued an additional 24 hours at room temperature. The sample was dialyzed using 10,000 MWCO Snakeskin dialysis tubing (Fisher) against water at pH 7.0 overnight and concentrated by centrifugation at 5000 RPM using a Sorvall Model T3100 Superspeed tabletop centrifuge with fixed angle rotor at 25°C for twenty-five minutes. The particles were re-suspended in two ml of water at pH 7.0.

2.6. Removing the Gold Core.

To dissolve the gold core, 0.2 ml of slightly acidic 40 mM NaCN were added to 1 ml of the suspension in a fume hood. The pH, U -Vis absorption spectrum, fluorescence spectrum, and TEM of the sample were checked periodically during the dissolving process in order to assure the presence of silicate nano -shells throughout the dissolution process. Following removal of the gold template the resulting silicate nano-shells were dialyzed against slightly acidic water overnight.

2.7. Preparation of Encased Enzyme in Silica Shells.

An aqueous solution containing 1×10^{-6} M enzyme was prepar d at room temperature using water at pH =7.0. Enzyme activity was verified at room temperature using the standard assay for alcohol dehydrogenase [10]. In short, 0.2 ml of 0.5 M glycine buffer at pH 9.0 was added to 1 ml of enzyme solution to be assayed. To 1.1 ml of sample was added 1 ml of 1×10^{-6} M of NAD, and 0.1 ml of 0.01M ethanol, under gentle magnetic stirring. The appearance of NADH reaction product was monitored by its absorption at 340 nm or its fluorescence emission at 450 nm as a function of time after mixing. Assay results were compared to that of a standard solution containing 1 $\times 1^{-7}$ M of alcohol dehydrogenase in deionized water at pH 8.0 prepared at the same time.

Silicate shells containing yeast alcohol dehydrogenase w ere prepared as follows: Ten milliliters of freshly prepared 1×10^{7} M enzyme solution was added to 50 milliliters of the 15 nm colloidal gold solution adjusted to pH 8.0 and the mixture gently stirred at room temperature for 15 minutes. The reactant was centrifuged at 10,000 RPM for thirty minutes at 15°C in the Sorvall Model T3100 Superspeed tabletop centrifuge. The enzyme activities of the supernatant and sediments were determined as described before. The pH of 5 ml of the 0.27% sodium silicate stock s olution was adjusted to pH 8.0 and added to the suspension. The resulting solution was stirred gently at room temperature for twent -four hours, and then dialyzed to remove un-reacted species. The gold core was removed as described previously and the enzyme activity of the control and encased enzyme at pH 9.0 were determined.

3. RESULTS

Transmission electron micrographs of the uniform-sized 85-nm and 15-nm colloidal gold particles are shown in **Figure 1.** The UV-Vis absorption and fluorescence emis sion spectra of 1.6 x 10^{-7}M Cascade Blue and 1.6 x 10^{-7}M Sulforhodamine-G at pH 6.5 are shown in **Figure 2.** The maximum absorption wavelength for Cascade Blue is 399 nm and that for Sulforhodamine-G is 529 nm. Unless specified otherwise, these absorption maxima were used as the excitation wavelengths for fluorescence spectrophotometry. The emission maxima of Cascade Blue and Sulforhodamine - G are 419 nm and 533nm, respectively.

The fraction of dye bound to the colloidal gold was determined in the following manner: Two 15 ml portions of 85 nm colloidal gold stock solution that had been previously incubated with of 1.6×10^{-7} M dye for 20 minutes at room temperature at pH 6.5 were centrifuged and th fluorescence intensity of the supernatant was determined. This value was subtracted from the fluorescence intensity of the same concentration of dye. The results were converted into the percentage of bound dyes to the colloidal gold. The results demonstrated that only about 6% of the added Cascade Blue were attached to the colloidal gold, wherea 94% of the added Sulforhodamine -G were attached.

Assuming all of the HAuCl$_4$-3H$_2$O was used to form relatively uniform colloidal gold particles, 1.6 x 10^{-7}M of dye would correspond to approximately 5760 dye molecules per gold particle. Thus, for Cascade Blue there are on average approximately 345 dye molecules per particle, and for Sulforhodamine-G approximately 5414 dye molecules per particle of gold. Assuming the maximum surface area occupied by a single dye molecule is 2 nm^2, these values are well below the estimated maximum binding capacity of approximately 11343 dye molecules per colloidal particle of this size.

Presented in **Figure 3A** are TEM of gold-silicate core-shell particles containing Cascade Blue and Sulforhodamine-G dyes. After incubating these particles with 0.1 M NaCN to dissolve the gold cores, the hollow silicate structures shown in **Figure 3B** were obtained.
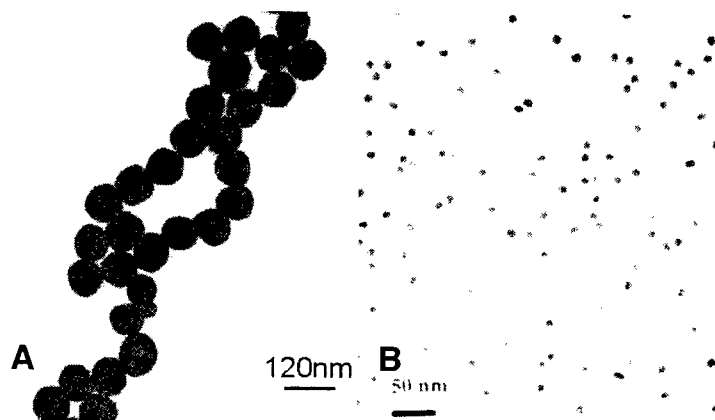
Figure 1. Transmission electron micrographs showing colloidal gold particles A.) 85 nm in diameter,and B.) 15 nm in diameter
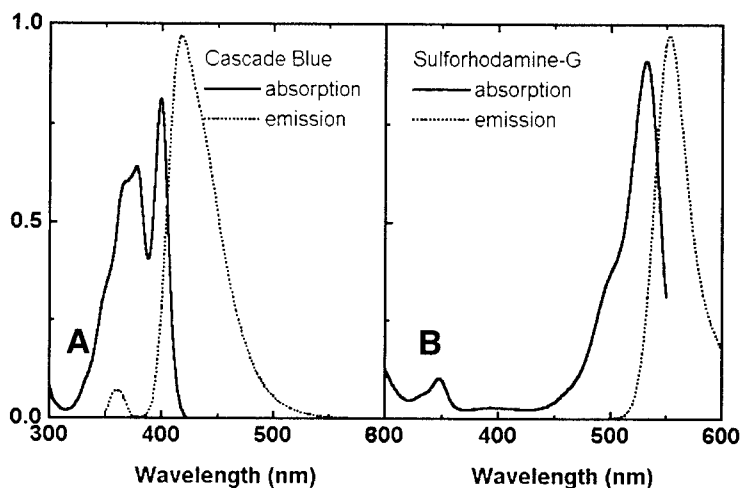
Figure 2. Absorption and emission spectra ofA.) 1.6 x 10-7M Cascade Blue (at pH 6.5 and λexc = 399 nm) in deionized water, and B.) 1.6 x 1 7M Sulforhodamine-G (at pH 6.5 and λexc = 529nm) .
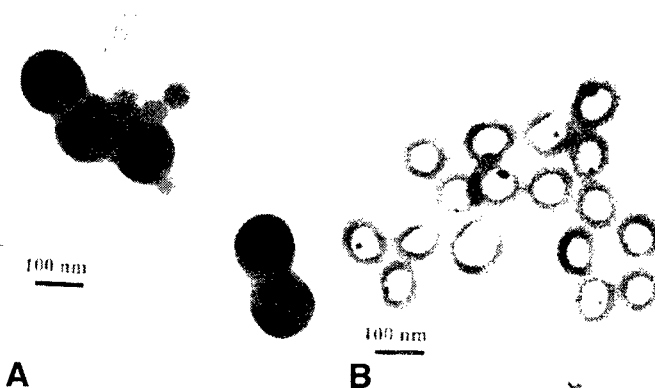
Figure 3. Transmission electron micrographs of A.) gold-silicate core-shell particles containing 15 molecules of Cascade Blue per particle or 243molecules of Sulforhodamin -G per particles, B.) After removal of the 85 nm diameter colloidal gold core

The plasmon absorption of colloidal gold with 85-nm diameter is found at 536 nm (**Figure 4A**, solid line). The plasmon absorption peak shifted to 546 nm in the presence of sodium silicate and 1.6 x 10^7M of Cascade Blue (**Figure 4A**, dotted line) and to 551 nm with the same concentration of Sulforhodamine -G and sodium silicate (**Figure 4A**, dashed line).
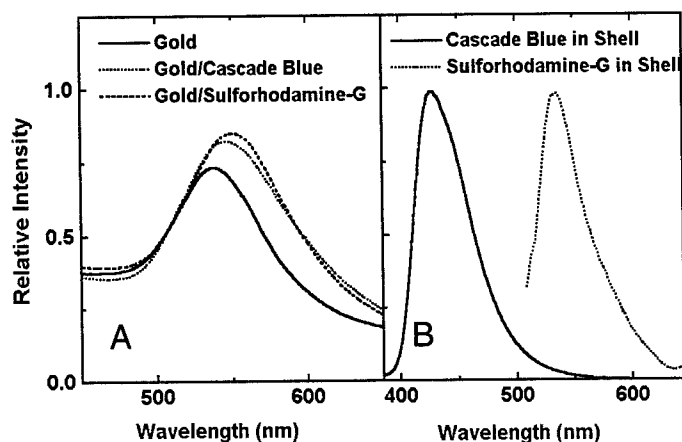

Figure 4. A.) Gradual shift of the plasmon absorption spectru of 85 nm diameter colloidal gold in water at pH 6.5 with addition of Cascade Blue Blue and Sulforhodamine-G, and sodium silicate. B.) Fluorescence emission spectra of encased Cascade Blue (λexc = 390) and Sulforhodamine-G (λexc = 529)
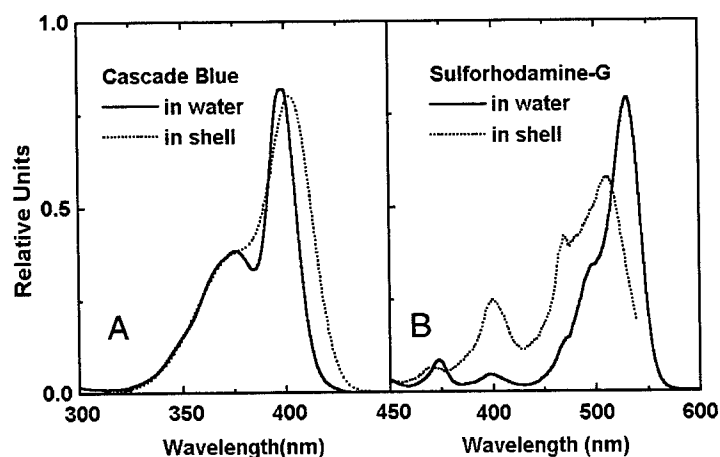
Figure 5. Excitation fluorescence spectra of A.) Cascade blue an B.) Sulforhodamin -G in water at pH 6.5 (solid line) and encased in gold-free silicate shells (dotted line).

Following the removal of colloidal gold by incubating with NaCN, the fluorescence emission of the encased dyes became detectable with significant wavelength shifts from those observed in solution (**Figure 4B**). For Cascade Blue, at pH 6.5, the fluorescence emission red-shifted from 419 nm to 429 nm, while the fluorescence emission peak of Sulforhodamine-G, when excited at 510 nm, blue-shifted from 553 nm to 538 nm. These changes reflec shifts in the excitation fluorescence maxima of dyes interacting with silicate shells (**Figure 5**). The absorption maximum of Cascade Blue in water is 399 nm, while the excitation fluorescence maximum is at 405 nm - a red shift. For encase Sulforhodamine-G, the excitation fluorescence maximum is blue shifted from 529 nm to 513 nm.

Turning attention to the encapsulation of yeast alcohol dehydrogenase in silicate shells, its enzyme activity was determined at pH 9.0 by observing the absorbance and fluorescence emission change of NADH at 340 nm and 450 nm, respectively. At pH 8.0 the enzyme was first bound to the 15 nm colloidal gold, which exhibited the plasmon absorption at 520 nm before addition of the enzyme (**Figure 6A**). A slight red shift of the plasmon peak was observed for colloidal gold bound with alcohol dehydrogenase. Like Casc ade Blue, the fluorescence of the enzyme encased within silicate shells demonstrated a small red shift (**Figure 6B**). The excitation wavelength used for ADH was 275 nm. **Figure 7** is a TEM micrograph of encased alcohol dehydrogenase, with 15-nm gold core still intact.
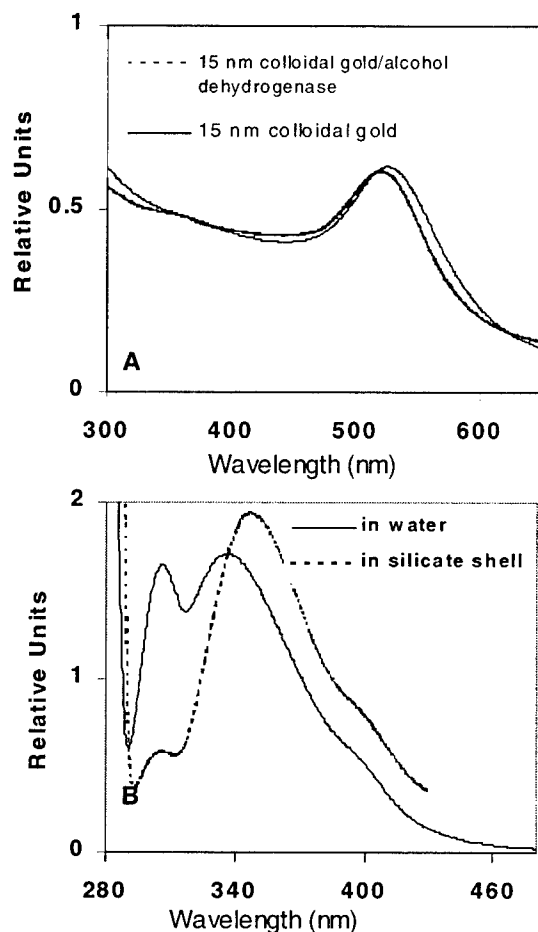
Figure 6. A.) The plasmon absorption spectra of 15nm colloidal gold at pH 6.5 (solid line) and with 1 x 10-7 M alcohol dehydrogenase (dotted line). B.) Fluorescence emission of 1 x 10⁷ M alcohol dehydrogenase in water at pH 6.5 (solid line) and inside silicate shells (dotted line).
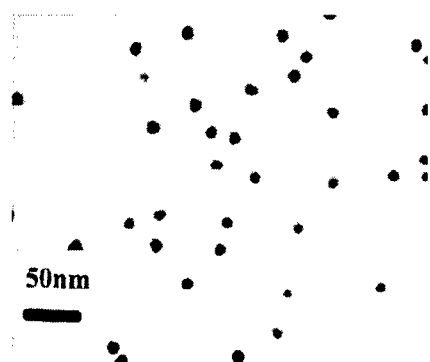

Figure 7. Transmission electron micrographs of typical gold-silicate core-shell particles containing approximately 50 molecules of alcohol dehydrogenase per particle.

Using the spectrophotometric and centrifugal methods described previously, the amounts of bound alcohol dehydrogenase were estimated after incremental addition of the enzyme to a colloidal gold suspension. The results are plotted as the number of alcohol dehydrogenase molecules per colloidal gold particl against total alcohol dehydrogenase added (**Figure 8**). It is anticipated that if the binding of alcohol dehydrogenase to the gold particle is strong, the plot will be linear until the maximum allowed binding on the colloidal gold takes place. The figure demonstrates such a linear correlation up to an alcohol dehydrogenase concentration of 2.7×10^{-7} M and the maximum binding is 95 alcohol dehydrogenase molecules per colloidal particle. The result is in good agreement for the estimated surface area available on a 15 nm colloidal gold particle for alcohol dehydrogenase molecules, each of which will likely occupy an area of about 9 nm^2. Since th concentration of alcohol dehydrogenase used in this study was 1.5×10^{-7} M, nearly 50% of the colloidal particle surface area was occupied by alcohol dehydrogenase. The activity of the alcohol dehydrogenase was assayed throughout the encapsulation procedure.

The survivability of alcohol dehydrogenase activit was determined to be best at pH 8.0 (**Figure 9**).). The remaining experiments were done using this pH. Samples of unbuffered alcohol dehydrogenase were incubated at several pH values between 5 and 10 for thirty minutes at room temperature prior to beginning the assay. The initial velocity of appearance of NADH fluorescence at 450 nm, normalized to that observed in aqueous solution at pH 8.0 is plotted. The highest rate of appearance of NADH was observed for alcohol dehydrogenase solutions incubated at pH 8.0, whereas the pH at which a maximum turn-over rate is observed for this enzyme is pH 9.0,.
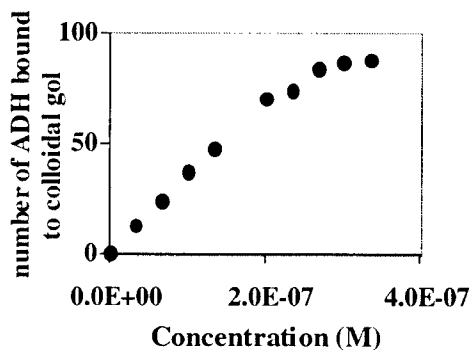
Figure 8. Number of alcohol dehydrogenase molecules bound per colloidal gold particle against the tota concentration of alcohol dehydrogenase added at pH 6.5.

The loss of enzyme activity is apparent at the time of enzyme binding to gold and subsequent silicate shell formation. The observed enzyme activities obtained various times after the start of incubation and shell growth are shown in **Figure 10**. The initial velocity of appearance of NADH fluorescence at 450 nm, normalized to that observed in aqueous solution at pH 8.0 is plotted. In both cases, it is evident that the immediate loss of about 20% of original activity is followed with much slower rate of loss of activity, which is similar to that in water. Addition of APS to the enzyme already attached to colloidal gold showed little effect on the activity.

4. DISCUSSION

As shown in **Figures** , **3** and **7**, the sizes of colloidal gold and the silicate casing are quite uniform, while removal of colloidal gold with NaCN proves to be quite effective. The amount of dye that binds to colloidal gold appears to depend on the nature of the dyes, and the two dyes used in this study demonstrate the potentially large differences in the affinity among many forms of dyes to the gold colloid. In the mean time, affinity of alcohol dehydrogenase to the colloidal gold appears to be significantly high (**Figure 8**). Assuming that the amount of dye and enzyme initially bound to the colloidal gold particle has all been encased the approximate molar concentration in a spherical volume of 100 nm in diameter (about 5.2×10^{-19} L) is 1.1 mM for Cascade Blue, 17.3 mM for Sulforhodamine -G, and 16 mM for alcohol dehydrogenase.

Upon reacting with colloidal gold, fluorescence of both dyes and ADH quenched most likely due to the loss of electrons from fluorescence chromophores to the colloidal gold [8,11]. After removing the colloidal gold, the fluorescence reappeared (**Fig. 6B.**) Upon binding any of the three molecules studied, the plasmon absorption peak was shifted to red. The fluorescence peak of Cascade Blue in E-Pure water was 419 nm, but in the silicate casing it was red - shifted to 429 nm. (**Figure 4B**), whereas the shift of Sulforhodamine G was from 553 nm to 538 nm, a

Figure 9. Survivability of alcohol dehydrogenas plotted as the initial velocity of the appearance of fluorescence intensity of NADH at 450 nm for 1 x 10-7M alcohol dehydrogenase samples incubated fo eighty minutes at various pH. Data are normalized to the observed activity observed from alcoho dehydrogenase at pH 9.0

Figure 10. Activity of alcohol dehydrogenase measured as the initial velocity of appearance o fluorescence of NADH at 450 nm as a function of incubation time at room temperature in water at p 8.0, attached to 15 nm colloidal gold particles, and during silicate shell growth. Data are normalized to th initial activity observed from alcohol dehydrogenase in aqueoud solution at p 9.0.

blue-shift. These shifts are reflection of the shifts in absorption spectra upon binding of these dyes to colloidal gold. Since determination of absorption spectra of these dyes in silicate-encased form was impractical, due to light scattering, the excitation spectra were obtained instead (**Figure 5**). The peak of excitation spectrum of encased Cascade Blue is at 405 nm and is red shifted from that in E-Pure water at 399 nm. On the other hand, the peak excitation spectrum of encased Sulforhodamine G is at 513 nm and is blue shifted from that in E-Pure water at 529 nm. A similar shift in fluorescence spectra is observed in ADH.

Within less than 10 minutes of binding to gold, the alcohol dehydrogenase activity is lost by 27% and then the rat of decrease of activity becomes similar to that found in water (**Figure 10**). This behavior seems to suggest that th loss in activity is due to the process of ADH binding to the colloidal gold and that the binding does not contribute
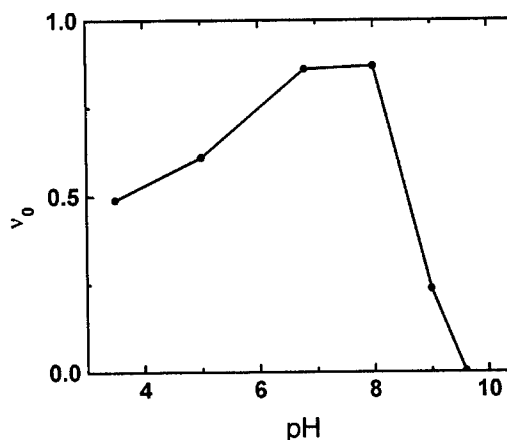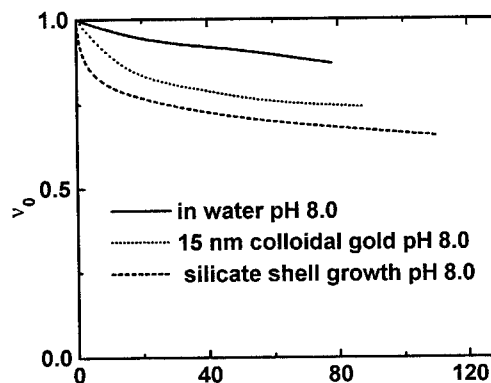
either to protect or enhance the enzyme activity. Similar conclusions may be drawn for the process of encasing with silicate, but there are a few addition factors should be taken into consideration. For example, how does the silicate shell affect the transport of the co-factor NAD and the substrate ethanol? What is the pH inside the silicate shell? Knowing that the thickness of silicate shell increases as the incubation in silicate continues, and the fact that the rate of loss of activity is similar to that in water, it may be concluded that the rate of kinetics is still limited by the intrinsic activity of the enzyme. As a consequence, encasing alcohol dehydrogenase in a silicate shell ha resulted in the retention of about 65% of the original activity. Whether or not the enzymes encased within silicate shells are protected from other solutes and environment remains to be examined.

5. CONC USIONS

Silicate has been used in the past as a matrix substance for sol-gel encapsulation of reactive molecules[6,7]. Encasing reactive molecules in nano-sized shells of silicate offers some advantages over the above-mentioned methods. The casing provides a protective shield to the reactants inside, and allows them to be dissolved in desired solvents at relatively high concentrations. A preferred casing size may be attained by adjusting the size of colloidal gold while the permeability of the casing may be controlled by the extent of silicate polymerization. Thi study has demonstrated that the encased dyes exhibit both absorption and fluorescent properties after removing the colloidal gold core, and that the activity of encased alcohol dehydrogenase is significantly retained in the silicate shell, though somewhat reduced.

ACKNOWLEDGEMENTS

REFERENCES

[1] F. Caruso, H. Lichtenfeld, M. Giersig et al., "Electrostatic Self-Assemby of Silica Nanoparticle-Polyelectrolyte Multilayers on Polystyrene Latex Particles." Journal of the American Chemical Society 120, 852 -8524, 1998.

[2] P. Mulvaney, L. M. Liz-Marzan, M. Giersig et al., "Silica Encapsulation of Quantum Dots and Metal Clusters." Journal of Materials Chemistry 10, 1259-1270, 2000.

[3] Thearith Ung, Liz-Marzan, L. M., Mulvaney, P., "Controlled Method for Silica Coating of Silver Colloids. Influence of Coating on the Rate of Chemical Reactions." Langmuir 14 (14), 3740-3748, 1998.

[4] P. Buining, B. Humbel, A. Philipse et al., "Preparation of Functional Silane-Stabilized Gold Colloids in the (Sub) nanometer Size Range." Langmuir 16 (22), 8285-8290, 1997.

[5] C. A. McKelvey, E. W. Kaler, J. A. Zasadzinski et al., "Templating Hollow Polymeric Spheres from Cationic Equilibrium Vesicles: Synthesis and Characterization." Langmuir 16 (22), 8285-8290, 2000.

[6] A. K. Williams and J. T. Hupp, "Sol-Gel Encapsulated Alcohol Dehydrogenase as a Versatile Environmentally Stabilized Sensor for Alcohols and Aldehydes." Journal of the American Chemical Society 120, 436 -4371, 1998

[7] D. Avnir, S. Braun, O. Lev et al., "Enzymes and Other Proteins Entrapped in Sol -Gel Materials." Chemical Materials 6, 160 -1614, 1994.

[8] O. Makarova, A. Ostafin, D. Meisel et al ., "Adsorption and Encapsulation of Fluorescence Probes in Nanoparticles." Journal of Physical Chemistry, B 103 (43), 9080-9084, 1999.

[9] K. Brown, D. Walter, and M. Natan, "Seeding of Colloidal Au Nanoparticle Solutions. 2. Improved Control of Particle Size and Shape." Chemical Materials 12 (2), 306-313, 2000.

[10] D. Jones, J. D. Gerber, and W. Drell, "A Rapid Enzymatic Method for Estimating Ethanol in Body Fluids." Clinical Chemistry 16, 402, 1970.

[11] P. M. Whitmore, H. J. Robota, and C. B. Harris, "Mechanisms for Electronic Energy Transfer Between Molecules and Metal Surfaces: A Comparison of Silver and Nickel." J. Chem. Phys. 77, 156 -8, 1982.

Addendum

The following papers were announced for publication in this proceedings but have been withdrawn or are unavailable.

[4258-01] **Methods of detection of quantum dots in biological applications**
S. A. Empedocles, W. Molenkamp, J. Jin, R. Daniels, J. Jiang, Quantum Dot Corp. (USA)

[4258-04] **Nanocrystals as multicolor single-excitation probes for flow and image cytometry**
W. Hyun, Univ. of California/San Francisco (USA); R. Daniels, C. Z. Hotz, M. P. Bruchez, Jr., Quantum Dot Corp. (USA)

[4258-05] **Simultaneous detection of multiple cellular markers by quantum dot semiconductor nanocrystals**
R. Daniels, J. Jiang, E. Y. Wong, Quantum Dot Corp. (USA); J. Kononen, O. Kallioniemi, National Institutes of Health (USA); M. P. Bruchez, Jr., Quantum Dot Corp. (USA)

[4258-08] **Surface-enhanced resonant Raman scattering: theory and experiment**
S. Schultz, J. Mock, D. A. Schultz, D. R. Smith, Univ. of California/San Diego (USA); P. M. Platzman, Lucent Technologies/Bell Labs. (USA)

[4258-14] **Nanostructured metallic substrates for surface-enhanced Raman scattering (SERS) applications**
T. Vo-Dinh, Oak Ridge National Lab. (USA)

[4258-15] **SERS as a single-molecule effect: a report from the near field**
M. Moskovits, L.-L. Tay, J. Yang, D. Anderson, Univ. of Toronto (Canada)

[4258-20] **Application of photocatalytic oxidation on titanium dioxide surfaces to disinfection, surface cleaning, and indoor air purification**
D. M. Blake, E. Wolfrum, J. Huang, Z. Huang, P. Maness, National Renewable Energy Lab. (USA); W. Jacoby, National Renewable Energy Lab. (USA) and Univ. of Missouri/Columbia (USA)

[4258-22] **Photochemical processing of known endocrine disruptors on heterogeneous metal oxide surfaces**
J. L. Ferry, L. Kong, R. Ozer, S. Walse, Univ. of South Carolina/Columbia (USA)

Author Index